EPFL

Thèse n° 9437

Molecularly Engineered Functional Materials for High Performance Perovskite Solar Cells

Présentée le 18 février 2022

Faculté des sciences de base
Groupe SCI SB MN
Programme doctoral en chimie et génie chimique

pour l'obtention du grade de Docteur ès Sciences

par

Cansu IGCI

Acceptée sur proposition du jury

Prof. K. Sivula, président du jury
Prof. M. K. Nazeeruddin, directeur de thèse
Prof. E. Palomares, rapporteur
Prof. G. Pozzi, rapporteur
Prof. W. L. Queen, rapporteuse

École
polytechnique
fédérale
de Lausanne

2022

Abstract

Over the last few years, the rapid development of molecular engineering and perovskite composition has allowed extremely promising solar energy conversion to achieve a certified power conversion efficiency (PCE) of over 25% for perovskite solar cells (PSCs). However, there is always room for improvement in research for the long-term stability and high cost of PSCs, which are major obstacles to the commercialization process, which can also be caused by organic materials and dopants. Thus, the work presented in this thesis is focused on synthesis, characterization and use of novel organic functional materials for PSCs. In addition, the work is aimed at finding synthetic guidelines that show how thoughtful molecular design, such as different atoms in the molecular structure, different functional groups can have different effects on photovoltaic performance and long-term stability of PSCs.

This work, introduces three novel hole-transporting materials (HTMs) with donor–π-bridge–acceptor (D–π–A) design principle. Triazatruxene-based donor units were functionalized with terthiophene conjugated arms as π unit, then differentiated into CI-B1, CI-B2 and CI-B3 HTMs by linking strong electron-accepting units. All three HTMs showed intermolecular aggregation by π-π stacking, especially CI-B3 molecules are packed in favor of a well-ordered edge-on stacking. PSCs with triple cation perovskite in n-i-p architecture with dopant-free HTM CI-B3 showed an impressive PCE of 17.54% with a small hysteresis and improved long-term stability.

Following up this work, the novel dopant-free HTM, CI-TTIN-2F, based on D–π–A, have been demonstrated for all-inorganic $CsPbI_3$ PSCs. CI-TTIN-2F features intermolecular aggregation formed by π-π stacking both face-on and edge-on orientation. Molecular dynamics (MD) calculations revealed the passivation effect of CI-TTIN-2F with Pb on the perovskite surface with different contact types. All-inorganic $CsPbI_3$ PSCs with dopant-free CI-TTIN-2F HTM demonstrate a high PCE of 15.9%, along with 86% efficiency retention after 1000 hours. Moreover, the largest all-inorganic perovskite solar module was fabricated using the CI-TTIN-2F HTM, and exhibited PCE of 11.0% with an area of 27 cm^2.

As the next part of our work, three benzodipyrrole-based organic small-molecules functionalized with 4-methoxyphenyl (CB-1), 3-fluorophenyl (CB-2), and 3-trifluoromethylphenyl (CB-3) have been introduced as HTMs for PSCs. PL characteristics and MD simulations revealed the passivation effect of the CB-2 and CB-3 molecules on top of perovskite surface. The PSC using the highly planar CB-2 achieved the highest PCE of 18.23% with excellent long-term storage stability in the air without encapsulation, and the molecular hydrophobicity of the fluorinated HTMs ensured that the devices showed no degradation of their PCEs over 6 months.

Finally, the novel passivation molecule tris(5-((tetrahydro-2*H*pyran-2-yl)oxy)pentyl)phosphine oxide (THPPO), has been employed at the HTM/perovskite interface. THPPO effectively passivated the undercoordinated Pb^{2+} defect on the surface of the perovskite layer by forming a coordinate bond with P=O that act as a Lewis base. The HTM-free devices have confirmed a significant increase in PCE from 5.84% to 13.31% with a significant improvement of the stability. Further, THPPO boosted the device's PCE from 19.87% to 20.70% when combining the device with spiro-OMeTAD as an HTM.

Keywords

Photovoltaic, perovskite solar cell, molecular engineering, hole transporting material, triazatruxene, benzodipyrrole, organic synthesis, interface, Lewis base, passivation.

Résumé

Au cours des dernières années, grâce au développement rapide de l'ingénierie moléculaire et de la composition de la pérovskite, il a permis une conversion de l'énergie solaire extrêmement prometteuse pour atteindre un rendement de conversion de puissance certifié (PCE) de plus de 25% pour les cellules solaires à pérovskite (PSC). Cependant, il y a toujours place à l'amélioration dans la recherche pour la stabilité à long terme et le coût élevé des PSC, qui sont des obstacles majeurs au processus de commercialisation, qui peuvent également être causés par des matières organiques et des dopants. Ainsi, les travaux présentés dans cette thèse sont axés sur la synthèse, la caractérisation approfondie et l'utilisation de nouveaux matériaux organiques fonctionnels pour les PSC. De plus, mon objectif est de trouver des lignes directrices synthétiques qui montrent comment une conception moléculaire réfléchie, telle que différents atomes dans la structure moléculaire, différents groupes fonctionnels peuvent avoir des effets différents sur les performances photovoltaïques et la stabilité à long terme des PSC.

Dans ce travail, j'ai introduit trois nouveaux matériaux de transport de trous (HTM) avec le principe de conception donneur-π-pont-accepteur (D-π-A). Les unités donneuses à base de triazatruxène ont été fonctionnalisées avec des bras conjugués au terthiophène en tant qu'unité, puis différenciées en HTM CI-B1, CI-B2 et CI-B3 en liant de fortes unités acceptant les électrons. Les trois HTM ont montré une agrégation intermoléculaire par empilement π-π, en particulier les molécules CI-B3 sont emballées en faveur d'un empilement de bord bien ordonné. Les PSC avec pérovskite triple cation dans une architecture n-i-p avec HTM CI-B3 sans dopant ont montré un PCE impressionnant de 17,54 % avec une petite hystérésis et une stabilité à long terme améliorée.

Suite à ce travail, le roman HTM sans dopant, CI-TTIN-2F, basé sur D–π–A, a été démontré pour les CSP $CsPbI_3$ entièrement inorganiques. Le CI-TTIN-2F présente une agrégation intermoléculaire formée par l'empilement π-π à la fois de face et de bord. Les calculs de dynamique moléculaire (MD) ont révélé l'effet de passivation du CI-TTIN-2F avec du plomb sur la surface de la pérovskite avec différents types de contact. Les PSC $CsPbI_3$ entièrement inorganiques avec CI-TTIN-2F HTM sans dopant présentent un PCE élevé de 15,9 %, ainsi qu'une rétention d'efficacité de 86 % après 1000 heures. De plus, le plus grand module solaire en pérovskite entièrement inorganique a été fabriqué à l'aide du CI-TTIN-2F HTM et présentait un PCE de 11,0 % avec une superficie de 27 cm^2.

Dans la suite de notre travail, trois petites molécules organiques à base de benzodipyrrole fonctionnalisées avec du 4-méthoxyphényle (CB-1), du 3-fluorophényle (CB-2) et du 3-trifluorométhylphényle (CB-3) ont été introduites en tant que HTM. Les caractéristiques PL et les simulations MD ont révélé l'effet de passivation des molécules CB-2 et CB-3 sur la surface de la pérovskite. Le PSC utilisant le CB-2 hautement planaire a atteint le PCE le plus élevé de 18,23% avec une excellente stabilité de stockage à long terme dans l'air sans encapsulation, et l'hydrophobie moléculaire des HTM fluorés a garanti que les dispositifs ne présentaient aucune dégradation de leurs PCE sur 6 mois.

Enfin, une nouvelle molécule de passivation avec un groupe oxyde de phosphine fournissant une base de Lewis, l'oxyde de tris(5-((tétrahydro-2*H*pyran-2-yl)oxy)pentyl)phosphine (THPPO), a été employée à l'interface HTM/pérovskite. THPPO a effectivement passivé le défaut Pb^{2+} sous-coordonné à la surface de la couche de pérovskite en formant une liaison coordonnée avec la base de Lewis fonctionnelle P=O. Les appareils sans HTM ont confirmé une augmentation significative du PCE de 5,84 % à 13,31 % avec une amélioration significative de la stabilité. En outre, THPPO a augmenté le PCE de l'appareil de 19,87 % à 20,70 % en combinant l'appareil avec spiro-OMeTAD en tant que HTM.

Mots-clés

Photovoltaïque, cellule solaire pérovskite, ingénierie moléculaire, matériaux de transport de trous, triazatruxène, benzodipyrrole, synthèse organique, interface, base de Lewis, passivation.

Symbols and Abbreviations

°C: degree Celsius

<τ>: average lifetime

α: field dependence parameter

2D: two-dimensional

3D: three-dimensional

Å: angstrom

A: electron acceptor

aq.: aqueous solution

AFM: atomic force microscopy

a.u.: arbitrary unit

AM: 1.5G Reference solar spectral irradiance according to ASTM G173-03

c-TiO_2: compact-TiO_2

C_{60}: fullerene

CB: conduction band

cm: centimeter

CV: cyclic voltammetry

D: electron donor

DCM: dichloromethane

DFT: density functional theory

DMF: dimethylformamide

DMSO: dimethyl sulfoxide

DSSC: dye-sensitized solar cell

E: electric field

E_g: band gap

eq.: equivalent

E_{HOMO}: ground-state oxidation potential

E_{LUMO}: excited-state redox potential

EQE: external quantum efficiency

ETL: electron-transporting layer

ETM: electron-transporting material

eV: electronvolt

FA: formamidinium

FAI: formamidinium iodide

Fc: Ferrocene

FF: fill factor

FK209: tris(2-(1*H*-pyrazol-1-yl)-4-tert-butylpyridine)cobalt(III) tri[bis(trifluoromethane)sulfonimide]

FTO: fluorine-doped tin oxide

GIWAXS grazing incidence wide-angle X-ray scattering

GWh: gigawatt-hour

h: Planck constant

h: hour

HI: hysteresis index

HOMO: highest occupied molecular orbital

HRMS: high resolution mass spectrometry

HTL: hole-transporting layer

HTM: hole-transporting material

Hz: hertz

I-V: current-voltage

ICT: intramolecular charge transfer

IN-2F: 2-(5,6-difluoro-3-oxo-2,3-dihydro-1*H*-inden-1-ylidene)malononitrile

IP: ionization potential

IPA: isopropanol

IPCE: incident photon-to-electron conversion efficiency

I_{ph}: photocurrent

ITO: indium-doped tin oxide

J-V: current density-voltage

J_{SC}: short-circuit current density

K: Kelvin

k_B: Boltzmann constant

kV: kilovolt

L: liter

Li-TFSI: Li-bis(trifluoromethanesulphonyl) imide

LUMO: lowest unoccupied molecular orbital

M: molar

m: meter

MA: methylammonium

MABr: methylammonium bromide

MAI: methylammonium iodide

MALDI: matrix-assisted laser desorption/ionization

MD: molecular dynamics

meV: millielectronvolt

mg: milligram

MHz: megahertz

min: minutes

mM: millimolar

mmol: millimol

mp-TiO_2: mesoporous-TiO_2

MPP: maximum power point

MPPT: maximum power point tracking

MS: mass spectrometry

NBS: *N*-bromosuccinimide

NHE: normal hydrogen electrode

nm: nanometer

NMR: nuclear magnetic resonance

ns: nanosecond

OFET: organic field effect transistor

p-: para-

PCBM: phenyl-C61-butyric acid methyl ester

PCE: power conversion efficiency

PEDOT:PSS: poly(3,4-ethylenedioxythiophene) polystyrene sulfonate

PL: photoluminescence

PMA: phenylmethylammonium

P_{max}: maximum power

PMMA: poly(methyl methacrylate)

ppm: part per million

ps: picosecond

PSC: perovskite solar cell

PTAA: poly[bis(4-phenyl)(2,4,6-trimethylphenyl)amine]

PV: photovoltaic

PWh: petawatt-hour

q_{xy}: scattering observed in the plane of the substrate

q_z: scattering observed out-of-plane with respect to the substrate

r: radius

RH: relative humidity

rpm. rotation per minute

RS: reverse scan

s: second

S: siemens

SCLC: space-charge limited current

SEM: scanning electron microscopy

spiro-OMeTAD: 2,2,7,7-tetrakis(N,N-di-p-methoxyphenylamine)-9,9-spirobifluorene

T: temperature

t: time

TAT: Triazatruxene

tBP: 4-tert-butylpyridine

T_d: decomposition temperature

t_G: Goldschmidt tolerance factor

TGA: thermogravimetric analysis

THF: tetrahydrofuran

THP: tetrahydropyran

T_m: melting temperature

TOPO: tri-n-octylphosphine oxide

TrPL: transient photoluminescence

UPS: ultraviolet photoelectron spectroscopy

UV: ultraviolet

UV-vis: ultraviolet-visible

v: frequency

V: Volt

v/v: volume per volume ratio

VB: valence band

VBM: valence band maximum

V_{OC}: open-circuit voltage

W: watt

w/v: weight per volume ratio

XPS: X-ray photoelectron spectroscopy

XRD: X-ray diffraction

XTOF: xerographic time-of-flight

θ: diffraction angle

λ: wavelength

μ: charge mobility

μ_0: charge mobility at zero field strength

μg: microgram

μL: microliter

μm: micrometer

Contents

List of Figures

List of Tables

List of Schemes

Chapter 1 Introduction

This chapter has parts based on the published review article: K. Rakstys C. Igci and M. K. Nazeeruddin. Chem. Sci., 2019, 10, 6748. DOI:https://doi.org/10.1039/C9SC01184F.

Increasing population, technological developments and rising living standards have led to an increase in energy needs. According to the International Energy Agency (IEA), the global electrical energy consumption in 2020 was more than 25 Petawatt hours (PWh).[1] In addition, IEA estimated nearly 50% growth in the world energy consumption by 2050. However, according to 2020 data, 88.3% of the world's electrical energy needs are still produced from non-renewable energy sources.[2] Traditional fossil-based fuels, such as coal, oil and gas, have direct negative impact to the environment such as climate change, warming of the earth, air pollution and acid rain. Considering the environmental effects and unsustainability of fossil fuels, renewable energy sources stand out as an important alternative. For this reason, the need for the development of renewable energy technologies is increasing day by day in order to cope with the political, economic and environmental problems involved in electricity generation. Research in renewable energy is moving to the forefront and becoming indisputably relevant for the future security of energy needs. Solar energy is an incredibly abundant, clean and sustainable resource among various renewable energy technologies, which remains underexploited to date. It shows us that solar cells' efficient and inexpensive energy conversion is vital for the global transition to a low-carbon society.

In the most general sense, solar cells are electronic devices that convert the energy of electromagnetic waves into electrical energy. This conversion is called the photovoltaic effect and was first observed in 1839 by the French physicist A. Edmond Becquerel.[3] Becquerel's named the work as the generation of electric current when platinum or gold plates immersed in acidic, neutral or alkaline solutions are exposed to solar radiation. The photovoltaic effect is based on the fact that an absorbed photon passes to a higher energy state by excitation of a charge carrier in the material. Although it took more than a century from the discovery of the photovoltaic effect to the construction of the first solar cell as a module, it has led to the rapid development of silicon based solar cells, both theoretically and experimentally. The first silicon solar cell in the literature was reported by Chapin, Fuller and Pearson in 1954 and showed an efficiency of only 6%.[4] In the 1970s, with the impact of wars and oil storage crises on scientific research, advances were made in photovoltaic (PV) technology and high-efficiency Si-based inorganic PVs began to be produced. Today, although silicon-based solar cells are commercially dominant, they are insufficient to meet production costs and some industrial demands due to high production cost and high energy demanding fabrication process. For this reason, the search for many different materials and methods for the production of cheaper and high-performance solar cells is increasing day by day.

Perovskite solar cells (PSCs) are considered a promising and burgeoning technology for solar energy conversion with the power conversion efficiency, currently exceeding 25%.[5] Instead of costly production of crystalline silicon, perovskite material, which is inexpensive and abundant, is obtained from a relatively very simple synthesis and is coated with conventional solution processing techniques. Dieter Weber first reported the unique structure and properties of the 3D perovskites of methylammonium lead triiodide ($MAPbI_3$) in 1978.[6] Then, the organic-inorganic hybrid halide perovskites were widely studied in the 1990s for the application in transistor technology and light emitting diodes, and further developed by Mitzi *et al.* due to their unique optoelectronic properties and easy solution process.[7] The first perovskite solar cell just reported in 2009 with 3.8% PCE by Miyasaka *et al.* and $MAPbI_3$ organic-inorganic hybrid perovskite was used as a light absorbing material with a liquid electrode in dye-sensitized solar cells

(DSSCs).[8] Perovskite-based solar cells have rapidly become the hottest topic in photovoltaics due to their unique optical and electrical properties. A pioneering works in the design of conventional perovskite solar cells have been reported in 2012 by Kim et al.[9] and Lee at al.[10] The efficiency of the PSCs has jumped to 9.7% due to dramatical improvement by utilizing spiro-MeOTAD as the hole transporting material (HTM) and mesoporous TiO_2 as the electron transport material (ETM) resulting in the solid-state meso-superstructured perovskite solar cell. In addition, the lifetime of perovskite-based devices extended to 500h stable device operation with the help of new configuration. This golden step has triggered the start of the intensive studies of perovskite solar cells. The fast development of device engineering and perovskite composition allowed to improve up-to-date solar cells with over 25% PCE certified by National Renewable Energy Laboratory (NREL).[5] In addition to achievement in the device performance, outperforming commercialized crystal semiconductor and other thin-film photovoltaic systems, the cost-effectiveness of perovskite material and solution processed device manufacturing makes the perovskite solar cell technology inevitable. Today, it is promising to see the commercialization of perovskite material in the world with high efficiencies by creating perovskite-silicon tandem solar cells.

Although perovskite solar cells have reached high power conversion efficiency, there are still several challenges limiting the industrial realization. The actual bottleneck for real uptake in the market still remains the cost-ineffective components and instability, where doping-induced degradation of charge selective layers may contribute significantly. The other important key factors could be lists as hygroscopic nature of HTMs, pinholes in film morphology, humidity and thermal induced instabilities, interfacial degradation between HTM/Au interface and undesirable chemical interactions of HTM with the perovskite layer. One promising avenue to stabilize perovskite solar cells could be the appropriate choice of the dopant-free and the highly hydrophobic hole transporting materials or passivation material, acting as a protection layer from the moisture and prevent the diffusion into perovskite layer. In addition, perovskite is very sensitive to water and humidity, it requires a very robust encapsulation process. Another criticism is the toxic effects of lead, which is frequently used in the perovskite. Another key factor that plays a major role in the commercialization potential is the cost-ineffectiveness of HTM. To date, spiro-OMeTAD and PTAA are the hole transporting materials of choice routinely employed in order to maintain the highest efficiency. However, its prohibitively high price prevents progress towards low-cost perovskite solar cell manufacturing. The reason resides in the complicated multi-step synthetic procedure, which is affordable in small quantities but is hardly scalable. It is directly related to the development of organic materials in the way of further advancement of perovskite technology and overcoming the problems. A deeper understanding of the relationship between small organic molecular structures and performance in perovskite devices is the most important goal placed in the focus of this thesis.

1.1 Perovskite Solar Cells

Perovskite solar cell devices generate photocurrent by interface engineering consisting mainly of five thin-layer materials. Initially, incident photons interact with the photoactive perovskite light-absorbing material to form predominantly free electrons and holes. After photoexcitation, the electrons in the perovskite layer are transferred to the conduction band of the electron transporting layer (ETL) and the holes in the perovskite material are injected into the highest occupied molecular orbital (HOMO) level of the transporting layer (HTL). Finally, the electrons are collected on the anode, which is a transparent conductive oxide deposited on glass substrate. On the back side, the holes are gathered into the cathode, which is a metallic electrode with high working function. In the meantime, it is expected that the kinetic processes of intrinsic radiative recombination, contact characteristics of electrode, charge accumulation and diffusion lengths of the charge carriers greatly control the limit of photovoltaic conversion efficiency of the perovskite devices.

1.1.1 Perovskite Materials

Perovskite minerals first discovered in the Ural Mountains of Russia in 1839 as $CaTiO_3$ is named after the Russian mineralogist Lev Perovski. In fact, it is found in abundance and in various forms and a yellow, brown, or black mineral of in the mantle layer of the world in inorganic form. The lattice structures of perovskites are in cubic phase. The general form of inorganic perovskites is indicated by ABO_3 and has a crystallographic structure. In this structure, the A mono-valent cation (A = Ca, Sr, Ba, Pb) is shared with 12 O monovalent anions and this part forms the cubic octahedral crystal structure. The smaller B bi-valent cation (Ti) is shared by 6 O anions and forms the octahedral crystal structure side.[11,12] Perovskite minerals began to attract attention in research in the 1940s, after the discovery of the dielectric and ferroelectric properties of the perovskite material $BaTiO_3$. In 1920s, the first perovskite in ABX_3 composition was identified in Goldsmith's tolerance factor studies.[13] An ideal stable three-dimensional (3D) perovskite structure has cubic symmetry and the cubic octahedral holes between voids of the crystal are filled with A cations (Figure 1.1). If the A cations are small or the B cations are too large, the tolerance factor falls below one and orthorhombic, rhombohedral or tetragonal structures are formed instead of the ideal cubic structure. In the other case, if the A cation is too large, two-dimensional (2D) superstructures or compositions have been described in the literature. Recently, 2D and 2D-3D mixtures have also been used in solar cell studies, as they show greater resistance to moisture compared to 3D perovskite structures.[14] The bulky organic cations in 2D perovskites can provide a steric barrier for surface water adsorption, which improves the long-term stability of PSCs. Because 2D perovskites have wide optical bandgap and limited charge transport, they are generally not a good choice as an absorber for solar cell application. Instead, 3D perovskite structures are generally used as solar cell absorbers for the devices that can generate electricity efficiently.

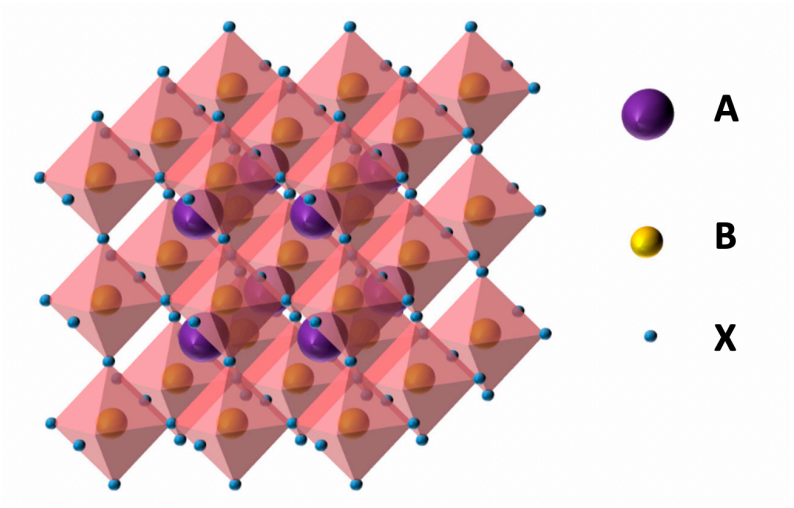

Figure 1.1 Schematic illustration of 3D perovskite structure.

1.1.2 Organic-Inorganic Perovskites

The organic-inorganic hybrid perovskite structure has crystals with general stoichiometry ABX_3 and ideally has a cubic symmetry configuration wherein A site is a monovalent organic methylammonium ($CH_3NH_3^+$, MA^+), formamidinium (NH_2=$CH_3NH_2^+$, FA^+) or inorganic cation (Cs^+, Rb^+), B is a divalent metal cation (Pb^{2+}, Sn^{2+}, or Ge^{2+}) and X stands for halide anion (I^-, Br^-, or Cl^-). The pure $MAPbI_3$ form has a band-gap of 1.57 eV with the optical absorption onset is at 800 nm and its absorption coefficient is extremely

high throughout the visible spectrum and part of the infrared.[15] Although pioneering work in perovskite structure was $MAPbI_3$ due to its excellent optoelectrical properties such as broad absorption spectrum, high absorption coefficient, high charge carrier mobility, low exciton binding energy, long electron and hole diffusion length, current research is evident that the increase in efficiency and stability of the perovskite-based solar cells (PSCs) is possible by combining more complex multi-cation and mixed-anion compositions of the perovskite absorber layer.[16, 17] The cation and anion tuning on the perovskite structure can effectively change optoelectronic properties of the organic-inorganic hybrid perovskite structure. One of the important modifications of metal-organic perovskite compounds is that the band gap can be adjusted by changing or mixing the halide groups in the structure. As the ionic diameter of the halogen atom used decreases, the band gap of the perovskite increases.[18] This enables smart perovskite designs according to the applications in tandem or organic light-emitting diode (OLED) devices. The effects of tuning the organic cations with different molecules on the perovskite system have been studied in the literature. It has been observed that $FAbI_3$ exhibits higher photocurrents when a slightly larger FA cation is used instead of MA cation in perovskite structure.[19] The larger the cation, the more energy is required for the cation to settle between the PbI_2 layers. Therefore, $FAPbI_3$ compounds are annealed at higher temperatures than $MAPbI_3$ and they are unstable at room temperature with α-FAPbI3 phase. However, stability was achieved using the FA/MA mixture with $(FAPbI_3)_{0.85}(MAPbBr_3)_{0.15}$ perovskite formulation and the perovskite devices performed better than the single cation counter-part.[20] After, the triple cation formulation was developed by Saliba *et al.* with the addition of cesium cation, and the perovskite formulation of $[CsPbI_3]_x[(FAPbI_3)_{0.85}(MAPbBr_3)_{0.15}]_{1-x}$ was examined.[21] With further increased complexity in (Cs/FA/MA) triple cation-based perovskite materials, it showed higher efficiency, improved photovoltaic performance, better reproducibility and higher long-term stability compared to FA/MA mixture. Cesium-containing triple cation perovskites are attracting significant attention and are used in our research as they have been validated in improving not only the stability but also the photovoltaic performance of PSCs.

1.1.3 Inorganic Perovskites

As a solution to the poor thermal stability of hybrid organic-inorganic perovskite materials, all-inorganic perovskite structures without volatile organic components have become an important research topic.[22] The thermal stability of $CsPbX_3$ (X = Cl, Br, and I) materials which may be compositionally stable even at temperatures exceeding 400°C, is significantly improved by replacing the organic ions in region A with inorganic cesium ions. Among the various inorganic monovalent cations, Cs^+ is reported to be the most feasible candidate to substitute the organic cations.[23] The size of Cs^+ satisfies the geometrical constraints of the perovskite structure to establish the continuous array of corner-sharing PbI_6 octahedra.[24] In literature, the efficiencies of all-inorganic Pb-halide PSCs have exceeded 20% in an n-i-p structure, which was achieved by the tetragonal (β) $CsPbI_3$ perovskite with an ideal bandgap of 1.68 eV for photovoltaic application.[25] However, the imperfect Goldschmidt tolerance factor of black phase $CsPbI_3$ determines that their PbI_6 octahedra tends to rotate when catalyzed by H_2O, which induces a rapid phase transition to the non-photovoltaic yellow δ phase.[26] Since the photoactive black phase of these perovskites can be stabilized at high temperature, many studies are carried out aiming to stabilize the black phase α-CsPbI3 at room temperature, such as additive engineering, interfacial passivation and nanocrystal growth.[24,27,28] However, the results of the strategies applied to increase the stability and obtain a high-efficiency device show that research on the subject needs to be continued. In the third chapter of the thesis, a new strategy for all-inorganic perovskite devices was discussed with a dopant-free HTM, which provides high efficiency and high stability at room temperature.

1.2 PSC Architectures and Operating Mechanism

Hybrid lead halide perovskites can cumulate the function of light absorption with n- and p-type conductions.[29] This ambipolar charge transport property of perovskite makes the design of PSCs quite versatile. The common device architecture is composed of five layers, which allow several combinations of materials: transparent electrode, n-type semiconducting electron transporting material (ETM), photoactive perovskite, p-type semiconducting hole transporting material and metallic electrode. Depending on the structure of the n-type layer, PSCs can be catalogued into mesoscopic or planar heterojunction structures, where both can be further divided into two categories variating on the position of the p-type and n-type selective contact materials.[30] Up to now, two different single junction architectures for perovskite solar cells have been developed, conventional (n-i-p) and inverted (p-i-n) configuration (Figure 1.2a). Perovskite is an intrinsic semiconductor (i), the HTM is p-doped and the ETM is n-doped layer.[31] The mesoscopic n-i-p and inverted p-i-n PSC device configurations show the highest performance reaching over 25%.[5] In conventional mesoscopic architecture, typically the glassy transparent electrode fluorine-doped tin oxide (FTO) is coated with the compact ETL made from TiO_2 and the additional mesoscopic TiO_2 scaffold is used on top, following by infiltration with photoactive perovskite material. A hole transporting layer is deposited on top of the perovskite, followed by the evaporation of a metallic top electrode, usually made of a high work function metal, such as gold, whereas inverted planar architecture has swapped charge selective contacts (Figure 1.2a). Although inverted perovskite devices typically have a higher stability with hysteresis-free behaviour, conventional devices have demonstrated to be superior in terms of power conversion efficiency. Moreover, since the perovskites have been proved to be ambipolar semiconductors, device architectures of PSCs that employ only one of the two selective contacts, such as ETM-free or HTM-free have been demonstrated.[32] However, these typically fail to produce high PCE, therefore it is generally agreed with the view that both the electron and hole selective contact materials are vital to reach high performance in PSCs.

The simplified operating mechanism and key charge-transfer processes of the typical PSCs are shown in Figure 1.2b Incident photons excite the perovskite light harvesting layer through the transparent electrode, leading to the photogeneration of electron-hole pairs in the material. Electrons are separated (1) from the holes and injected (2) into the conduction band (CB) of the electron transporting material before migrating to the anode. Meanwhile, the holes generated in the perovskite are transferred (3) to the HOMO level of the hole transporting material, before injection of the hole into the cathode. Electron and hole injections occur quite efficient due to the high diffusion lengths of charge carriers. Undesirable charge transfer (CT) processes such as back CT recombination of the charge carriers at three ETM/perovskite/HTM interfaces also occur (4-6), including non-radiative recombination (7). In the meantime, it is expected that the kinetic processes of intrinsic radiative recombination, contact characteristics of the electrode, charge accumulation and diffusion lengths of the charge carriers greatly control the limit of photovoltaic conversion efficiency of the perovskite devices.[16,17]

The applied technique for the evaluation of the photovoltaic performance of perovskite solar cell is the current density-voltage (*J-V*) measurement and determines the photovoltaic parameters of PSCs. *J-V* measurement is done by applying an external potential bias to the cell while measuring the current response. The photovoltaic parameters for PSCs can be listed as short-circuit current photocurrent density (J_{SC}), open circuit voltage (V_{OC}), fill factor (*FF*), incident photon-to-current conversion efficiency (IPCE) and maximum power (P_{max}). The *J-V* measuring of perovskite solar cells should be performed under illumination with standard test conditions so that test results can be reliably compared with each other. The standard test conditions are defined as 1 sun intensity, which means the total irradiance of the light source is 1000 W/m^2 with the air mass (AM) 1.5G illumination.

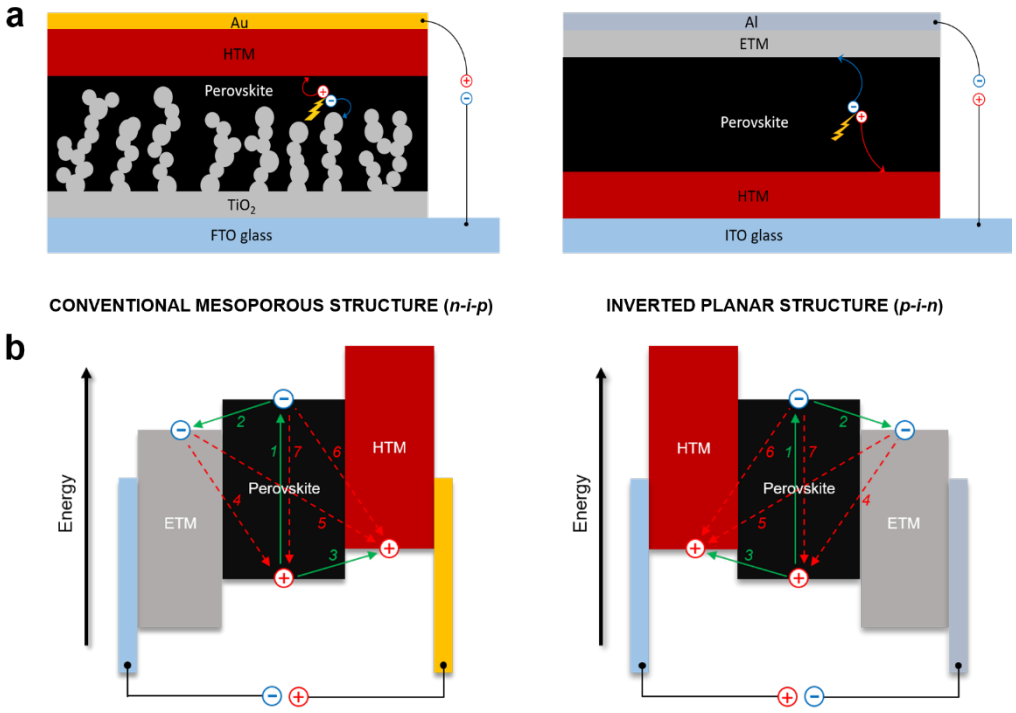

Figure 1.2 a) Structure of conventional mesoscopic n-i-p and inverted planar p-i-n device configurations; b) schematic illustration of energy levels and charge-transfer processes in different architecture PSCs.

1.3 Hole Transporting Materials for PSCs

HTM is important active material in PSC, responsible for efficient hole extraction at the perovskite/HTM interface and preventing undesirable charge recombination processes, leading to improvement in the performance of the device. For efficient device operation, well-aligned energy level of HTM with perovskite is crucial: HOMO level must be less negative than that of perovskite for efficient hole injection, while the high-lying LUMO level will ensure low electron affinity enabling beneficial electron blocking properties. An ideal HTM candidate should also have high hole mobility to reduce losses during hole transport to the contact, as well as sufficient conductivity. HTM has to be well soluble and should not require strong polar and protic solvents, as such solvents may dissolve the perovskite layer. Furthermore, since perovskites are known to be sensitive to moisture and oxygen, the hole transporting layer should act as protection from the air and prevent the diffusion of external moieties, therefore high thermal and photochemical stability, as well as high hydrophobicity, are desirable properties of HTM to resist from degradation factors and ensure long-term durable PV operation. On the other hand, to ensure low-cost perovskite solar cell manufacturing, an ideal HTM candidate has to be easily affordable by simple synthetic schemes with a minimized number of steps and easy workup and purification procedures for cost-effective upscale.

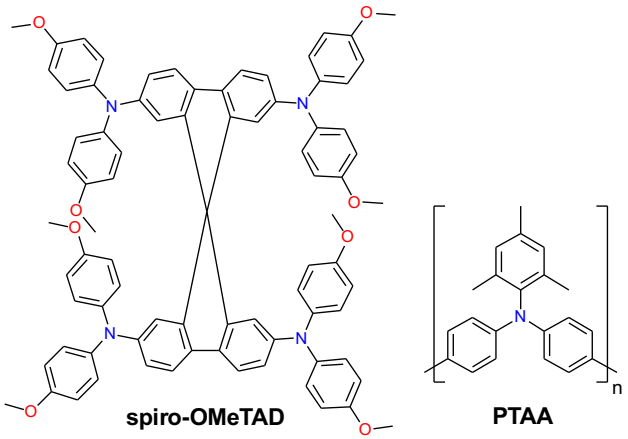

Figure 1.3 Chemical structures of 2,2',7,7'-tetrakis-(*N*,*N*'-di-*p*-methoxyphenylamine)-9,9'-spirobifluorene (spiro-OMeTAD) and poly[bis(4-phenyl)(2,4,6-trimethylphenyl)amine] (PTAA).

To date, 2,2',7,7'-tetrakis-(*N*,*N*'-di-*p*-methoxyphenylamine)-9,9'-spirobifluorene (spiro-OMeTAD) and poly[bis(4-phenyl)(2,4,6-trimethylphenyl)amine] (PTAA) are is still dominating the field and has been selected as the benchmark HTM to achieve high PCE values for PSCs.[33] Organic p-type semiconductor spiro-OMeTAD is the first report as HTM in ssDSSC two decades ago. It has a HOMO level around -5.1 eV, exhibits a hole mobility in the range of 10^{-5} to 10^{-4} cm^2 V^{-1} s^{-1} and has high solubility in organic solvents such as toluene or chlorobenzene, giving almost colourless thin films. However, the tedious multi-step synthesis of spiro-OMeTAD makes it prohibitively expensive and cost-ineffective. Typically, high-purity sublimation-grade spiro-OMeTAD is required to obtain high-performance devices. Moreover, it has been demonstrated as a limiting factor for the long-term stability of the device.[34] Among the polymers, p-doped PTAA has also become popular and been used to achieve record efficiencies.[35] The superior performance of PTAA arises from the exceptional hole mobility (10^{-3} – 10^{-2} cm^2 V^{-1} s^{-1}). However, it is extremely expensive reaching the price of ~2000 $/g. The hole transporting materials of choice routinely employed in order to maintain the highest efficiency, however, its prohibitively high price hinders progress towards low-cost perovskite solar cell manufacturing and may contribute to more than 30% of the overall module price. The reason resides in the complicated multi-step synthetic procedure, which is affordable in small quantities but is hardly scalable. Another key factor that plays a major role in the commercialization potential is the stability of the device. Additionally, wide bandgap hole transporting materials typically require doping in order to match necessary electrical conductivity and the use of additives is problematic, since hygroscopic nature of doping makes the hole transporting layer highly hydrophilic leading to chemical degradation and negatively influences the stability of the entire device. One promising avenue to stabilize perovskite solar cells could be the appropriate choice of the dopant-free and the highly hydrophobic hole transporting materials, acting as a protection layer from the moisture and prevent the diffusion of external moieties. To improve the gaps in the field, a huge research interest directed into new HTM candidates has been raised to find a better understanding in relationship between the HTM and PSC performance. A large number and different types of HTMs have been reported so far, based on organic and inorganic nature, where organic HTMs can further be divided into small-molecules and conducting polymers.

1.3.1 Chemical Doping for Hole Transporting Materials

Chemical doping is an important method in organic electronics to enhance device efficiency by controlling the energy levels, increasing the conductivity, and reducing ohmic losses in charge transport layers and injection barriers at the interface with the electrodes.[36] The basic principle of p-doping in organic semiconductors is that additional mobile charge carriers are generated by electron acceptors, which remove electrons from the HOMO to generate holes of an intrinsic HTM by chemical oxidation.[37] The introduction of additional charge carriers leads to an increased charge carrier density in the organic semiconductor by redox reactions, resulting in higher conductivity. The key requirement for efficient doping process is the suitable electron affinity of the dopant with respect to the energy levels of an organic semiconductor. When the HTM oxidized by dopant, the singly occupied molecular orbital (SOMO) level of the dopant material become slightly deeper than HOMO level of the undoped material. In this case, electrons able to flow from pristine material to dopant material by charge hopping. The existing trap states of the materials also can be filled with additives, resulting in improved conductivity. With the increase in the conductivity of dopant HTL, the series resistance of the material also decreases, which causes an increase in the fill factor in solar cells.

Traditionally, the hole transporting layer of PSCs is heavily doped with p-type dopants to provide the necessary electrical conductivity for the state-of-art spiro-OMeTAD and another wide bandgap HTMs. Numerous p-type dopants have been developed and realized including 2,3,5,6-tetrafluoro-7,7,8,8-tetracyanoquinodimethane (F4TCNQ), benzoyl peroxide, copper (II), and cobalt (III) complexes (Figure 1.4). To date, the combination of second-generation cobalt complex-based tris(2-(1*H*-pyrazol-1-yl)-4-*tert*-butylpyridine)cobalt(III) tri[bis(trifluoromethane)sulfonimide] (FK209) and lithium bis(trifluoromethanesulfonyl)imide (LiTFSI) with additive of 4-*tert*-butylpyridine (tBP) as morphology controller are routinely employed to improve the conductivity of HTMs.[38,39] Recently, incorporation of $ZnTFSI_2$ as a dopant showed increased hole mobility and long-term operational stability.[40]

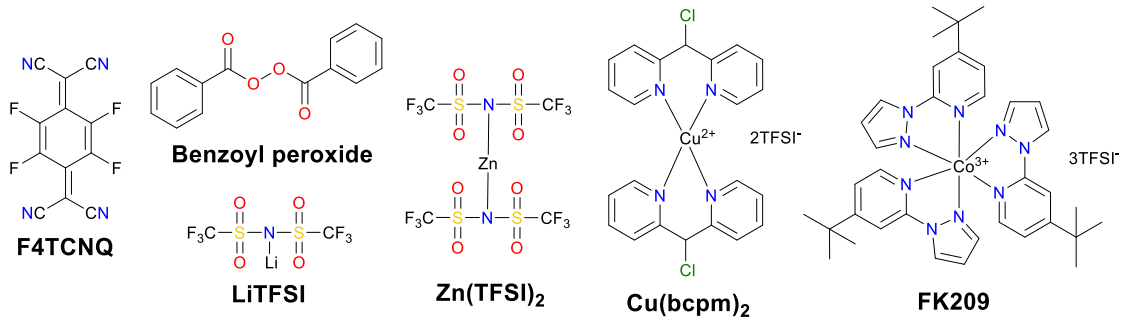

Figure 1.4 Chemical structures of different p-type dopants for HTMs employed in PSCs.

1.3.2 Molecular doped HTMs

It is worth noticing that the first novel hole transporting materials for perovskite solar cells have started to be published in 2014, about a year after perovskite photovoltaic topic has started. Up to now, various HTM-based articles were reported, including inorganic, organic molecular and polymeric materials. Spiro-OMeTAD is dominating the field and despite the high price (~350 $/g) routinely employed as highly efficient reference material for the research interests. This comes mainly because it is widely available and well-studied since it was commercialized decades ago. However, the cost-effective industrial potential for practical applications is hardly probable. Therefore, huge research interest directed into new HTM candidates has been raised to find an ideal HTM, which would be easily scalable for reasonable cost as well as for a better understanding the relationship between the HTM structure and PSC performance. As a result of spiro-OMeTAD, many research groups have been focused on spiro-type compounds and tried to improve the PCE with slight structural modifications. Some representative examples of these modifications are listed (Fig-

ure 1.5). Xu et al. have reported X60, where the spirobifluorene central core is replaced by spiro[fluorene-9,9'-xanthene] (SFX), which is synthesized by a one-pot approach condensing 4-bromophenol and 2,7-dibromo-9-fluorenone as the starting materials. This allowed to reduce the price of the final product by thirty times comparing with that of spiro-OMeTAD. Moreover, the insert of oxygen bridge into the structure leads to improved hole mobility and device performance of 19.8%.[41] Chiykowski et al. judiciously studied redox and thermal properties of SFX-based HTMs bearing TPA groups. It was determined that TPA groups positioned about the conjugated fluorene moiety increase the free energy change for hole-extraction from the perovskite layer, while TPAs about the xanthene unit governs the T_g values and hole mobility. 4-fold HTM-FX and HTM-FX' exhibited PCE of 19.5% and 20.8%, respectively.[42] Also, fluorene-terminated spiroOMeTAD alternative DM has been reported reaching the efficiency of 23.2%. Such high PCE is achieved by the careful optimization of the different amounts of additives (LiTFSI and tBP) in the HTL. Without additives, or with only small amounts of additives, the PCE of the device is very low because the conductivity of DM is not high enough. Encapsulated device using DM maintained 92.6% of its initial PCE value after 310 h under continuous illumination condition proving its enhanced thermal stability comparing with spiro-OMeTAD.[43] Two-fold dimethoxydiphenylamine-substituted X59 was reported with an identical device performance as predecessor X60 and almost no hysteric behaviour, showing that diphenylamine units on the xanthene do not play a major role, therefore it was further functionalized with covalently linked differently substituted pyridine groups.[44] This allowed to realize 4-*t*-butylpyridine (tBP)-free PSCs with improved stability compared with that of spiro-OMeTAD-based solar cell that contained tBP as an additive. *Para*-position substituted pyridine-based XPP showed the highest performance of 19.5% among the series, due to the fact that both nitrogen atoms in XPP can easily form a strong chemical bonding with the Pb atoms, while the *ortho*- and *meta*-anchored molecules can only contribute with one nitrogen atom binding to the Pb.[45] However, the pyridine anchors slightly lowered the performance once compared with X59. Zhu and co-workers reported carbazole incorporating spiro core. Carbazole-based single-spiro-HTM named SCZF-5 reached PCE of 20.1%.[46] Carbazole derivatives have been intensively studied since it has interesting features such as the low-cost of the 9*H*-carbazole starting material, good chemical and environmental stability provided by the fully aromatic unit, as well as easy incorporation of a wide variety of functional groups into the nitrogen atom that allows better solubility and fine tuning of the electronic and optical properties.[47] 3,6-Dimethoxydiphenylamine-substituted carbazoles as donor units in the periphery were widely used to tune the HOMO level of the molecule.

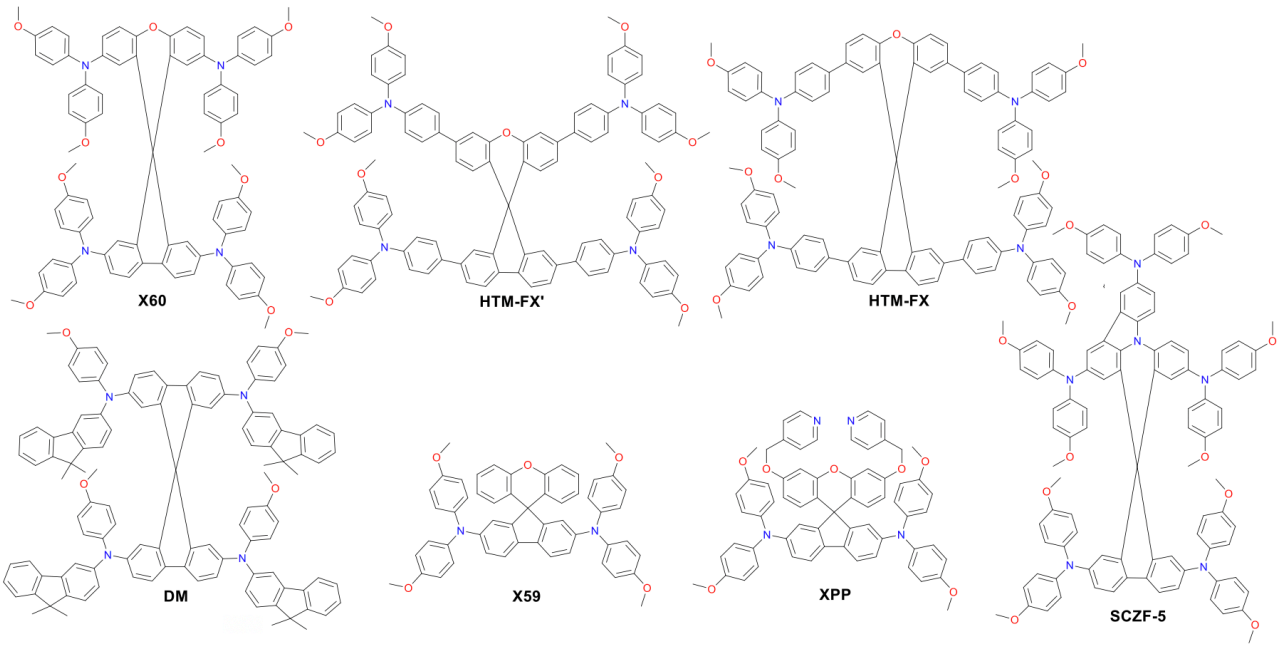

Figure 1.5 Chemical structures of different spiro-based HTMs.

In HTM literature another important design strategy is come from nitrogen-containing central scaffolds (Figure 1.6). Among them, PCE has been further improved with aniline-based enamines using the same straightforward synthetic protocol. Three diphenylethenyl moieties containing V1091 showed excellent hole mobility of 1.7×10^{-2} cm^2 V^{-1} s^{-1} leading to the PCE of 20.2%, while V1056 showed the slightly lower performance of 18.7%.[48] Triazatruxene (TAT) is a star-shaped, planar structure consisting of three indole units fused to a benzene ring. TAT has become a widely used core structure for HTMs due to its strong electron donating properties, strong π–π intermolecular interactions, easily modifiable photophysical and electrochemical properties, and high hole mobility. Planar and large aromatic surface of TAT core can overlap with each other for efficient intermolecular charge transfer. It also able to stabilize the oxidized radical cation by the nitrogen atom of indole moiety during operation.[49] TAT core derivatives can be obtained by two different synthetic approach. One of the approaches for the synthesis of TAT core is carried out by cyclotrimerization reaction of indole starting material with bromine reagent. Then, reductive dehalogenation can be applied to obtain triazatruxene under mild conditions.[50] The other approach is that TAT can be obtained in one step by $POCl_3$–promoted trimerization of 2-indolinone. The tribrominated TAT derivative (3), obtained in three steps from 2-indolinone as shown in Scheme 1.1, is a versatile starting material for the synthesis of TAT-based HTMs. For the preparation, the commercially available 2-indolinone has a trimerization reaction with heat in the presence of phosphoryl chloride to able to obtain tris-*N*-unsubstituted-TAT (1). This is followed by the alkylation reaction to increase the solubility of the final HTM, performed under basic conditions with excess alky halide. Then, bromination reaction performed with regioselectivity in the presence of *N*-bromosuccinimide (NBS) to finally obtain to 3,8,13-tribromotriazatruxene (3), which could be further functionalized by Ullmann, Suzuki and Buchwald–Hartwig coupling reactions.[51] This approach provides the optimal synthetic approach for the preparation of TAT in terms of yield and reaction time. In one of the earliest reports, 18.3% device performance was achieved employing triazatruxene-based KR131, which exhibited surface interaction with perovskite material resulting efficient hole injection from the valence band of perovskite into the HOMO of HTM and outperforming the reference spiro-OMeTAD.[50] Another triazatruxene HTM TAT-^{t}BuSty was reported reaching PCE of 20.3%.[52] Cho and co-workers reported fluorinated indolo[3,2-*b*]indole-based derivative IDIDF.[53] A planar π-conjugated backbone linked with a flexible alkyl chain enabled a formation of the molecular stacked arrangement by strong π-π interaction, leading to improved hole mobility, and PCE of 19.8%.

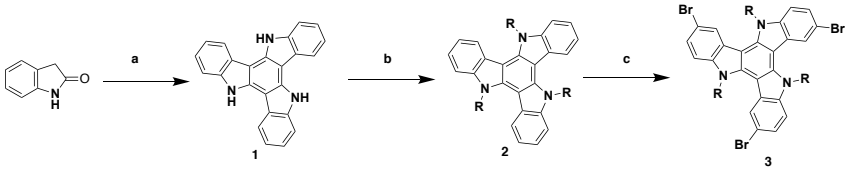

Scheme 1.1 The preparation of the triazatruxene derivative (3) as a central core. a) $POCl_3$, 100 °C; b) 1-iodohexane, NaH, DMF, 120 °C; c) NBS in DMF, $CHCl_3$, 25 °C.

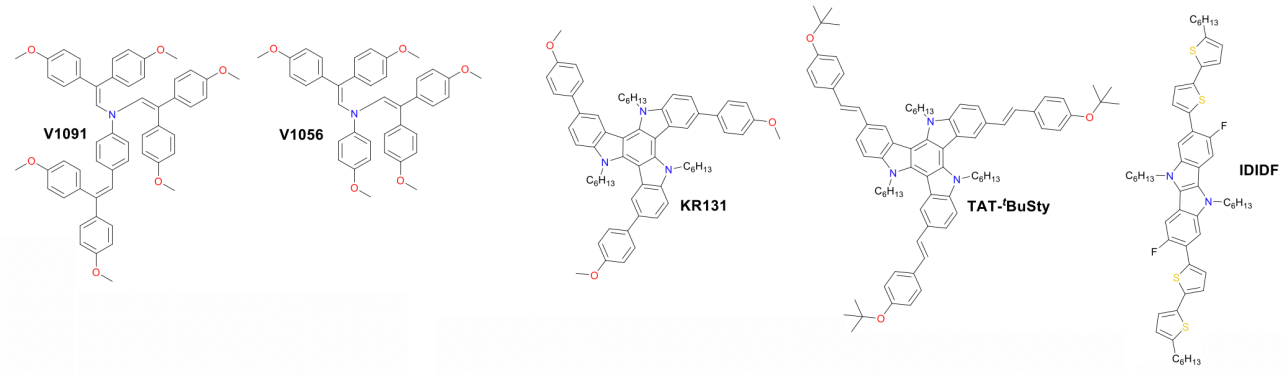

Figure1.6 Chemical structures of from nitrogen-containing central scaffold HTMs.

HTMs based on sulfur-rich benzotrithiophene (BTT) core was intensively studied as such fused systems are known to maximize the π-orbital overlap, inducing face-to-face π-stacking and facilitating charge transport through intermolecular hopping (Figure 1.7). Star-shaped BTT-3 was firstly reported with optimized HOMO level, showing an excellent band alignment with the perovskite, leading to the PCE of 18.2%.[54] Encouraged by this result, Garcia-Benito et al. have further studied the impact of isomerism on BTT-based HTMs.[55] It was found that *cis* arrangement of the sulfur atoms facing each other in the core of BTT-4 may further benefit the interaction with the perovskite, leading to impressive PCE of 19%, while the 4-fold isomeric form of BTT-5 showed 18.2%, respectively. Heteroatom effect (N, O, and Se) was studied yielding benzotripyrrole (BTP), benzotrifuran (BTF), and benzotriselenophene (BTSe) central cores, respectively. From single-crystal diffraction, it was found that BTF-1 shows tighter molecular π–π interactions than BTT-3 and BTSe-1. However, the best PSC performance of 18.5% was achieved with BTSe-1, while BTF-1 showed the slightly lower result of 18.2%.[56] Benzodithiophene (BDT) and more extended sulfur-rich core anthratetrathiophene (ATT) were also used as scaffolds for novel HTMs. Sandoval-Torrientes et al. reported TTPA-BDT molecule with four-fold substitution bringing the performance (η = 18.1%) close to BTT analogs.[57]

The benzo[1,2-*b*:4,5-*b*0]dipyrrole (BDP) is a pyrrole-based heterocyclic small molecule. The OLED application of the BDP-based materials showed that the high molecular planarity of BDP core can facilitate the intermolecular π-π interaction and can enhance the charge transport properties. In addition, the BDP unit has a good carrier mobility and compatible energy level with perovskites, which can further promote hole extraction.[58] Although BDT core is widely studied for high efficiency perovskite solar cells, BDP, the nitrogen analog of the sulfur-based heterocycle, core has only one example in the HTM literature.[59] The study applied 2,3,6,7-tetraphenylbenzodipyrrole core with alkanediylsulfonate anion side chains (BDPSOs) on the inverted-structure perovskite solar cell. Sulfonate salts of alkylated BDPs were shown to have transparent films, well aligned HOMO levels with the perovskite (-5.21/-5.37 eV), with hole mobility reasonably close to or slightly higher than spiro-OMeTAD. The position of fluorine atoms on the aryls was changed and the best compound, 3F-br-4C, showed a PCE of 17.2% with minimal hysteresis. The solar cell devices fabricated using BDPSOs showed good storage and operational stability, with PCE retention >90% while stored in a glove box under nitrogen.[59]

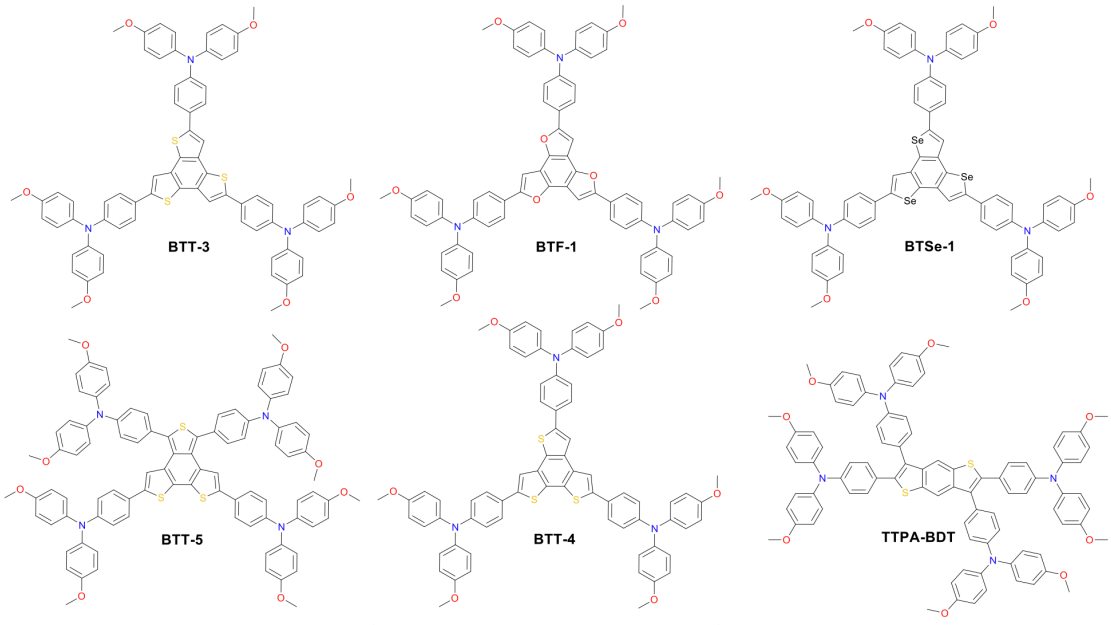

Figure 1.7 Chemical structures of benzodithiophene (BDT), benzotrithiophene (BTT), benzotrifuran (BTF), benzotriselenophene (BTSe) core based HTMs.

As a result, tremendous efforts have been made to develop new alternative low-cost and efficient HTMs to replace Spiro-OMeTAD. Organic small molecule doped HTMs are the most widely developed group in PSCs due to their synthetic diversity, tunable properties, high purity and simple solution. Among them, selected HTMs were examined and summarized photovoltaic parameters are listed in Table 1.1. However, although the performance of PSCs is dramatically enhanced, most of the reported high-efficiency doped HTMs are suffering from rapid degradation and are limited to a very short operation lifetime up to a few months.

ID	J_{SC} (mA cm^{-2})	V_{OC} (V)	*FF*	PCE (%)	Ref. PCE (%)[a]
TTPA-BDT	23.0	1.07	0.736	18.1	17.7
BTT-5	22.50	1.10	0.733	18.17	18.9
BTF-1	21.31	1.106	0.772	18.2	18.0
BTT-3	21.9	1.065	0.767	18.2	18.1
KR131	20.7	1.145	0.77	18.3	17.9
BTSe-1	21.88	1.065	0.795	18.5	18.0
V1056	22.1	1.07	0.79	18.7	20.2
3-F-br-4C[b]	20.2	1.06	0.80	17.2	-
BTT-4	23.04	1.090	0.753	18.97	18.9
HTM-FX[d]	-	-	-	19.5	20.4
XPP[c,d]	23.18	1.12	0.75	19.5	16.5

X59	23.4	1.13	0.73	19.8	20.8
IDIDF	23.6	1.06	0.792	19.8	16.8
X60	24.2	1.14	0.71	19.84	-
SCZF-5[d]	24.40	1.11	0.74	20.1	19.11
V1091[d]	22.5	1.11	0.81	20.2	20.2
TAT-^{t}BuSty[d]	22.1	1.15	0.8	20.3	20.3
HTM-FX'[d]	-	-	-	20.8	20.4
DM	24.91	1.144	0.812	23.2	21.3

Table 1.1 Photovoltaic performance of the perovskite devices employed with selected doped small molecule-based HTMs sorted by PCE of champion device. [a]Spiro-OMeTAD or PTAA were used as the reference in most of the cases; [b]p-i-n device architecture; [c]tBP-free composition; [d]planar device architecture.

1.3.3 Molecular doped-free HTMs

The long-term stability of PSCs is one of the critical issues that need to be addressed for their commercial applications. A promising solution for stabilizing PSCs is the appropriate choice of dopant-free HTMs. Removing the dopants has already been demonstrated to be very effective towards improved device stability. Therefore, many research groups have been focused on dopant-free HTMs and tried to improve the PCE with higher device stability. Some representative examples of these modifications are listed (Figure 1.8) and summarized photovoltaic parameters of the HTMs are showed in Table 1.2. Huang et al. presented dopant-free truxene-based HTM decorated with three diarylamine groups, and six hexyl side chains, adopting a planar, rigid, and fully conjugated molecular geometry. PSCs fabricated under p-i-n architecture using Trux-OMeTAD showed a high PCE of 18.6% with minimal hysteresis.[60] Anthanthrone dye based molecule TPA-ANT-TPA has been reported by Pham et al. and reached 17.5% PCE using no regular doping.[61] Hazmi et al. reported dopant-free molecules, based on dibenzothienopyrrole equipped with diphenylamine donors tuned with differently positioned methoxy groups.[62] Meta-substituted mDPA-DBTP showed the highest performance among the series reaching PCE over 18%. Notably, devices based on dopant-free mDPA-DBTP retained 81% of its original PCE after 33 days of storage, during which the doped spiro-OMeTAD devices lost their PCE completely. m-MTDATA has been reported to reach a PCE as high as 18.12% for simple solution-processed inverted PSCs with J_{SC} of 22.50 mA/cm^2, V_{OC} of 1035 mV and *FF* of 0.778. Furthermore, m-MTDATA based devices without any encapsulation showed significantly better stability than the PEDOT: PSS based devices after 1000 h exposure to the ambient environment with a humidity of 30 RH%.[63] Another commercial example TAPC has been demonstrated as an efficient HTM in p-i-n configuration PSC. By adopting TAPC as the HTL, the best device achieved a PCE of 18.80% with minor hysteresis and increased stability device without any encapsulation.[64] Li with co-workers presented a simple polycyclic 2,5,9,12-tetra(*tert*-butyl)diacenaphtho[1,2-*b*:1',2'-*d*]thiophene dopant-free HTM coded as PCA-1 with PCE of 18.17%.[65] Simple design of TPAC3M dopant-free HTM has been reported by Park et al.[66] Fabricated p-i-n inverse type planar PSCs with configuration ITO/TPAC3M/$CH_3NH_3PbI_3$/PCBM/ZnO/Al exhibited 17.54%.

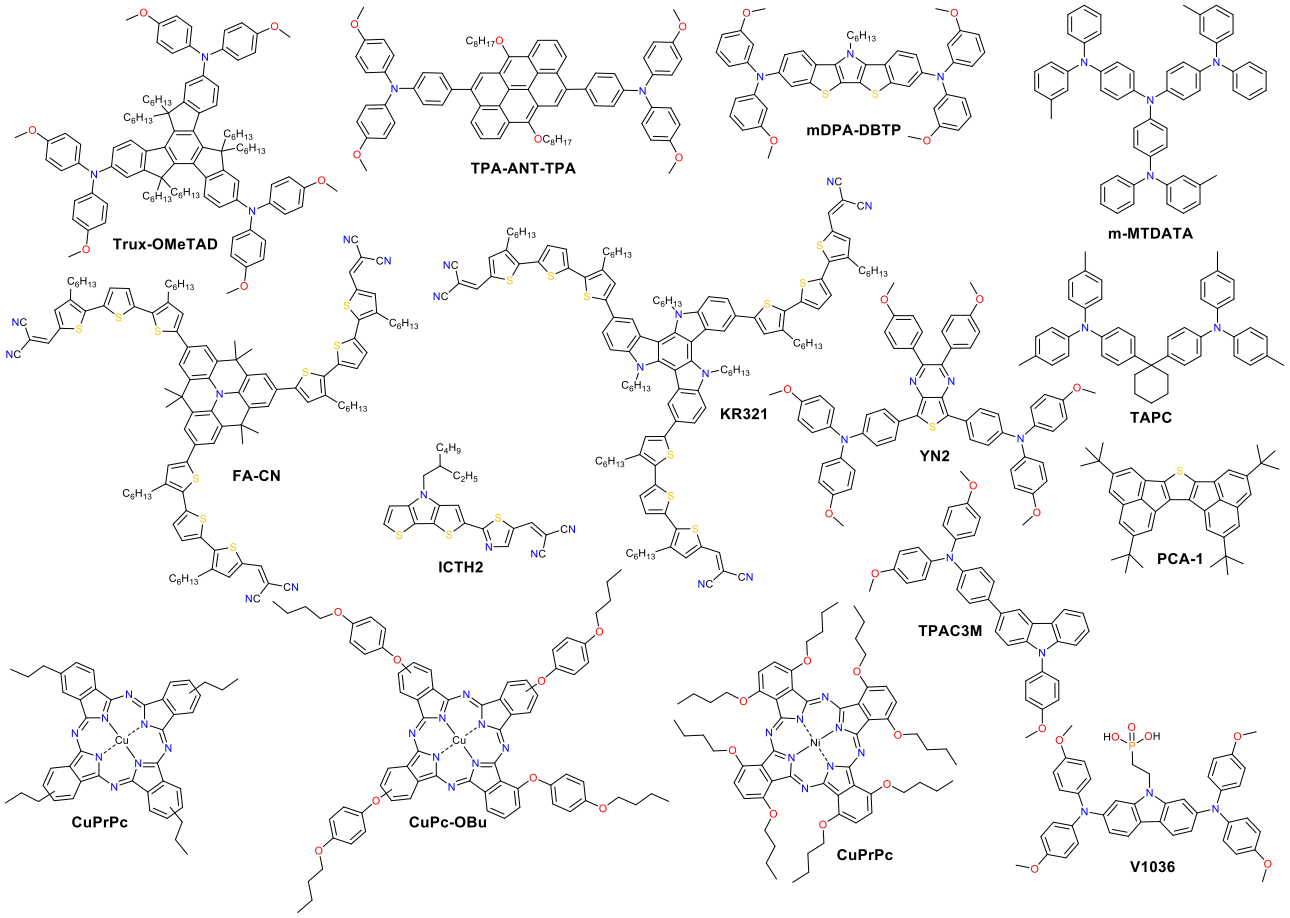

Figure 1.8 Chemical structures of the efficient dopant-free hole transporting materials applied in PSC.

Donor – π-bridge – acceptor (D–π–A) type dopant-free HTMs have great potential to show high charge carrier mobility due to strong dipolar intermolecular interaction, minimizing ohmic losses of the contact. Moreover, they combine the advantages of both small molecules like well-defined structures, and polymers, like good thermal, electrochemical and photochemical stability, together with high solubility and suitable wetting on the perovskite. Typically, they are composed of planarized central unit inducing the formation of the molecular stacked arrangement by strong π-π interaction linked to a strong accepting unit and equipped with flexible alkyl chains leading to improved hole mobility. D–π–A-type HTM coded as FA-CN was reported, incorporating a fused quinolizino acridine donor with alkyl-substituted terthiophenes and malononitriles as acceptors. Optimized devices with dopant-free FA-CN showed an impressive PCE of 18.9% with superior long-term stability under full illumination for 1300 h.[67] Changing the quinolizino acridine central core to triazatruxene yielded KR321 HTM with slightly improved performance of 19% due to highly ordered characteristic face-on organization leading to increased vertical charge carrier transport.[68] Bharath et al. reported D–π–A type ICTH2 HTM based electron-donating dithieno[3,2-*b*:2′,3′-*d*]pyrrole and electron-accepting dicyanovinylene moieties imparting high intramolecular charge transfer nature and eliminating the need of additives or dopants during the fabrication of solar cell devices.[69] PSCs with ICTH2 HTM showed PCE of 18.75% with an active area of 2.04 cm^2. D–A–D type HTM YN2 featuring triphenylamine as the donor along with thienopyrazine unit as the acceptor has been presented by Xu et al. The YN2-based PSCs affords an impressive PCE value of 19.27% with V_{OC} of 1.11 V, a J_{SC} of 23.15 mA cm^{-2} and an *FF* of 0.75.[70] D–A type and branched structures have been proven as two major design strategies to prepare high performance dopant-free HTMs. Such molecules enable better intermolecu-

lar interactions towards the increase of the charge mobility. In general, the doping process is not required for efficient hole transport and collection if HTM can exhibit hole mobility as high as 10^{-4} – 10^{-3} cm^2 V^{-1} s^{-1}.

ID	J_{SC} (mA cm^{-2})	V_{OC} (V)	*FF*	PCE (%)	Ref. PCE (%)[a]
TPA-ANT-TPA	21.07	1.03	0.796	17.5	16.8
TPAC3M[b]	22.79	1.00	0.78	17.54	12.6
CuPc-OBu	22.8	1.06	0.73	17.6	18.8
CuPrPc[c]	23.2	1.01	0.76	17.8	17.5
V1036[b]	21.9	1.09	0.81	17.8	19.2
mDPA-DBTP[c]	21.13	1.12	0.76	18.09	17.82
m-MTDATA[b]	22.50	1.035	0.78	18.12	13.44
PCA-1[c]	22.30	1.062	0.767	18.17	18.30
NiPc-$(OBu)_8$	23.1	1.08	0.734	18.3	19.4
Trux-OMeTAD[b]	23.2	1.02	0.79	18.6	16.3
ICTH2	24.78	1.03	0.735	18.75	14.74
TAPC[b]	22.32	1.04	0.811	18.8	12.9
FA-CN	21.71	1.13	0.77	18.9	19.2
KR321	21.70	1.13	0.78	19.03	19.01
YN2	23.15	1.11	0.75	19.27	17.80

Table 1.2 Photovoltaic performance of the perovskite devices employed with dopant-free small molecule-based HTMs sorted by PCE of champion device. [a]Doped spiro-OMeTAD or PEDOT: PSS were used as the reference in most of the cases; [b]p-i-n device architecture; [c]planar device architecture.

1.3.4 Polymeric doped-free HTMs

Polymers are potentially attractive HTM candidates in perovskite solar cells since they typically present good stability, processability, mechanical flexibility and film uniformity with tunable energy levels. Both, high density and hydrophobicity of polymers are also very important for protecting the perovskite layer from moisture in the ambient, therefore enhancing PSC lifetime. Three different kinds of polymers are mostly used as HTMs for perovskite solar cells including homopolymer, copolymer, and D–A copolymer types. The class of polymeric HTMs have been found as very effective for highly efficient and stable PSC. Chemical structures of the selected D–A copolymer types dopant-free polymeric hole transporting materials applied in PSCs are listed in Figure 1.9 and summarized photovoltaic parameters of the HTMs are showed in Table 1.3. D–A type copolymers have been found as very effective dopant-free HTMs as such design strategy can ensure high hole mobility and enhanced device stability by rationally implementing different donors and acceptors. In addition, the introduction of suitable side chains into their conjugated backbones may form two-dimensional polymers with effectively tuned morphological properties. Lee at al. reported D–A type copolymer asy-PBTBDT comprising benzo[1,2-*b*:4,5:*b*']dithiophene (BDT) and benzothiadiazole (BT) as donor and acceptor units, respectively.[71] Introduction of asymmetric alkoxy substituents on BT units produced irregularity within a repeating unit of the polymer resulting that it is not only

soluble in common organic solvents, but also highly soluble in the green solvent 2-methylanisole, which is known food additive. The best device employing dopant-free asy-PBTBDT reached a PCE of 18.3%, which is equivalent to the results obtained by the best control device employing doped spiro-OMeTAD. The performance was significantly improved using another BDT and BT based copolymer PTEG reported by Kim and co-workers.[72] Here, side chains were further engineered by installing tetraethylene glycol (TEG) chains on BT units. TEG groups improve solubility by enhancing dipole-dipole interaction with the solvent. Moreover, flexible TEG groups can affect hole mobility by preventing backbone twisting and increasing π-π stacking. An improvement in the contact between perovskite and PTEG occurs because the surface energy of TEG groups is higher than that of alkyl groups. Dopant-free PTEG-based device achieved an impressive efficiency of 19.8% with a J_{SC} of 22.5 mA cm^{-2}, a V_{OC} of 1.14 V, and a *FF* of 0.77 in planar PSC. Cai et al. reported three HTMs comprising a carbazole donor moiety, flanked by two thienyl groups that are co-polymerized with a pristine or functionalized BT unit with two methoxy or octyloxy substituents, resulting PCDTBT, PCDTBT1, PCDTBT8.[73] It was found that the device performance strongly depends on the chemical structure of the conjugated polymer side chains. Dopant-free polymers have been shown to achieve both high efficiency and device stability, however, they typically suffer few drawbacks as batch-to-batch reproducibility, purity, and high synthetic cost.

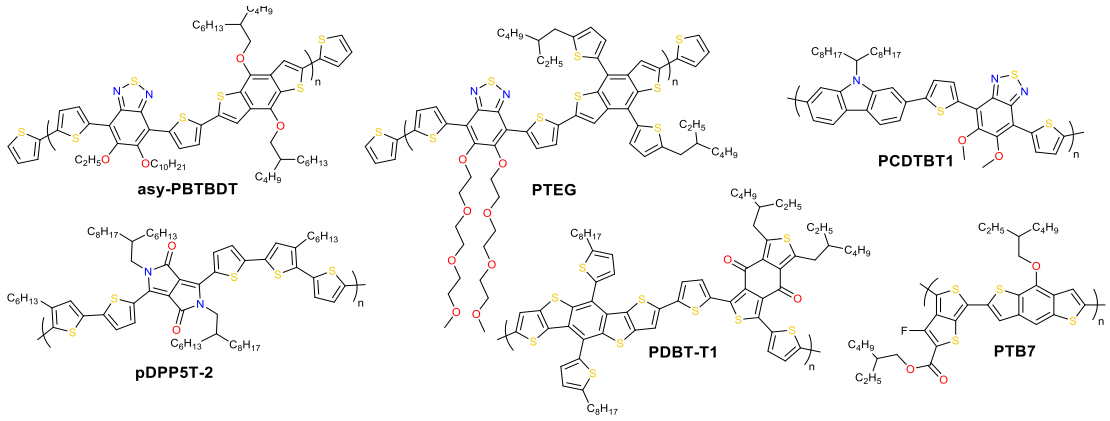

Figure 1.9 Chemical structures of the D–A copolymer types dopant-free polymeric hole transporting materials applied in PSC.

ID	J_{SC} (mA cm^{-2})	V_{OC} (V)	*FF*	PCE (%)	Ref. PCE (%)[a]
asy-PBTBDT	22.4	1.11	0.732	18.3	18.5
PTB7[b]	22.6	1.13	0.71	18.5	13
pDPP5T-2[b]	21.5	1.15	0.76	18.9	13
PCDTBT1[b]	22.2	1.1	0.782	19.1	19.4
PDBT-T1[b]	22.2	1.17	0.77	19.8	13
PTEG[b]	22.5	1.14	0.77	19.8	17.9

Table 1.3 Photovoltaic performance of the perovskite devices employed with dopant-free polymeric HTMs sorted by PCE of champion device. [a]Doped spiro-OMeTAD or PTAA were used as the reference in most of the cases; [b]planar device architecture.

1.4 PSC Interface Engineering

Interface engineering, which plays an important role for highly efficient and stable PSCs, develops methods for solving high density defects likely to exist in the bulk and on the surface of the perovskite film. Several types of surface defects may exist on the perovskite surface, such as Pb cluster, organic A cation vacancy, under-coordinated I^- ions, under-coordinated Pb^{2+} ions, iodine vacancies, can cause in charge recombination via non-radiative channels. Therefore, it may degrade device performance and lead to rapid degradation of the perovskite solar cells. Because the ionic nature of the perovskite lattice enables the concept of molecular passivation, interface engineering can be an effective strategy to reduce the defects.

1.4.1 Defect Types of PSCs

The defects are introduced by impurities or lattice defects and show different energy states within the band structure. The defects can trap photo-generated charge carriers, causing non-radiative recombination and preventing the carriers from contributing to the energy produced from the active layer. In solar cell architectures, defects act as recombination centers in the bulk of the material, in addition, grains and grain boundaries affect carrier transport adversely. Intrinsic defects and traps can also cause undesirable phenomena such as hysteresis in the current–voltage characteristics and instability, which remains another area of concern in terms of the commercialisation and reproducibility of devices.[74] Many defect trap states or carrier transport barriers are most likely to exist at the interfaces between each functional layer, the material's surface and at the grain boundaries of the perovskite solar cells. Generally, types of the defects could generalize as point defects, impurity defects, morphology defects including two-dimensional grain boundaries and surface. Defects can appear due to crystal growth or device fabrication conditions and three-dimensional defects such as lead aggregations.[75]

Non-radiative charge recombination in semiconductor materials usually can occurs via deep trap levels or Auger recombination when the concentration of charge carriers is high. When defects create deep trap levels, electrons and holes that cannot escape the aid of thermal activation and counter-charged carriers will be trapped, which will be destroyed by non-radiative radiation as defined by Shockley Read Hall theory.[76] The formation of deep trap levels via Shockley Read Hall theory recombination has been identified as a decisive pathway for the loss of charge carriers in perovskite materials. Uncoordinated halide ions and Pb^{2+} ions defects such as Pb-I can cause deep traps.

Some intrinsic defects of organometallic perovskite materials are point defects, which occur at the core of the material and cause shallow level traps with low defect formation energy. Unlike deep-level traps, they are point defects that occur easily like shallow traps and are not as harmful to photovoltaics as deep-level traps. Due to the ionic nature of organometallic perovskite materials and their high ion migration rates, these charged point defects can propagate to the interfaces under an electric field and cause a deposition of charged ions at the interfaces.[77] This creates involuntary doping effects at the interfaces and can affect the photovoltaic performance of the PSC. The other point defect could be created by the lattice imperfection as the crystallographic defects, such as anti-site, vacancy, and interstitial.[74,78] An anti-site defect occurs when an atom occupying a wrong site of the lattice with the displacement of one atom by another atom. The vacancy defects are formed when there is no atom in the proper lattice site. The interstitial defects can occur where ions are in interstitial positions (in between the atom sites) of a lattice. These defects can trigger the degradation caused by the presence of oxygen, moisture, and light. In addition, ionic defect diffusion is also accelerated under illumination in combination with heat, which strongly decrease the long-term stability of the devices.[78] *J-V* hysteresis in cells, phase separation, degradation of perovskite materials, and degradation of metal electrodes are due to the formation, migration or redistribution of these defects through grain boundaries of perovskite.[74] To eliminate the negative effects of the defects, a deep understanding of defect chemistry in perovskite is required, which is important for the long-term stability of the devices and further material optimisation.

1.4.2 Passivation Methods of PSCs

Perovskites defects continue to be treated as they detrimentally influence the photophysical and photoelectrical properties of films and devices. Therefore, it is important to disable or reduce the charge trap density by passivation. Passivation can change the contact resistance at the perovskite/charge transfer layer interface and also can cause *FF*-led changes by reducing defects of the film, the holes on the surface and changing the shunt path.[79] This has led to the development of passivation materials with many different functions and approaches that can reduce the interface and surface defect states in perovskite solar cells. Various passivation techniques can be applied between the electron transport material and the perovskite, between perovskite grains (grain boundaries), between the perovskite and the hole transport layer, between the hole transport layer and the electrode, and between the electrode material and the atmospheric environment.[80] Here, effective state-of-the-art passivation strategies aimed at minimizing the formation of a wide variety of defects during the annealing and solution processes are classified under two groups as passivation during perovskite formation and surface passivation by post-treatment.

One of the important passivation strategies during the film formation is excess PbI_2 in the perovskite film which resulted in self-passivation by non-stoichiometric precursors of perovskite. The passivation mechanism of excess PbI_2 and the existing position of residual PbI_2 in perovskite film have been studied extensively. The excess PbI_2 was found to passivate the grain boundaries, helps to improve the crystallinity and increase the particle size in perovskite film, resulting in large and homogeneous grain formation.[81] The non-stoichiometric perovskite film with excess PbI_2 showed higher photoluminescence (PL) intensity and slower PL degradation as a proof of the reduction in trap-assisted recombination due to grain recovery of the perovskite. The excess PbI_2 in halide perovskite is found to lead to high efficiency and stable PSCs with improved carrier lifetime and suppressed hysteresis.[82] In addition, a great deal of research has been done to induce perovskite self-passivation through the use of organic ammonium halides. During the formation of the perovskite layer, a little excess of amine salt, is beneficial for passivation of grain boundaries defects, crystalline properties, and film quality.[83] Ammonium salts are able to passivate the anion and cation defects on the perovskite. Long-chain alkylammonium halides can also induce low-dimensional (2D or quasi-2D) perovskite formation. Another perovskite passivation method during formation is employing a graded 2D/3D perovskite structure with dimensional engineering. 2D perovskites with larger bandgaps can energetically envelop 3D grains, transforming defect-rich boundaries into layered 2D perovskites.[84] The designed long-chain ammonium salts are used as good effective passivators as well as to improve the hydrophobicity of perovskites and provide stability to devices.

Another category for effective passivation of perovskite can be recovered under surface treatment. By surface treatment, passivation agents can bind to defects on the perovskite surface through ionic bonds, covalent bonds or other chemical interactions and optimize interface contact through intermolecular forces. The application of an additional hydrophobic organic thin layers after perovskite formation can not only passivate the hybrid perovskite surface, but can also improve the water stability of the device. This hydrophobic structure can be provided by amine-functional graphene, long organic chain silane, or organic molecules with a fluorinated side chain, increasing the moisture resistance property to make water-resistant perovskite films.[85] Recent studies showed that fluorinated-based molecules are promising surface passivation materials to improve the light stability of the perovskite solar cells. The fluoride ions with extremely high electronegativity are very effective in passivating simultaneously both the organic cation and halide anion vacancies as shown by Li et al.[86] They found that the fluoride ion, with the smallest radius among halide ions, can form strong hydrogen bonds (N–H···F) with the organic cations of the perovskite (MA, FA) as well as can form the strong ionic bonding with Pb^{2+}. The effective vacancy defect passivation is also useful for inactivating the diffusion of organic cations and halide anions. The ability of some organofluorinated compounds to function as a barrier layer and eventually prevent the cation releasing from the perovskite layer has been also verified.[87,88] Thus, deposition of 1H,1H,2H,2H-perfluorooctyltriethoxysilane (PFOTES) was demonstrated to increase the light stability of perovskite solar cells by suppressing the Pb^0 formation at the perov-

skite surface and maintaining carrier dynamics. Trichloro (3,3,3-trifluoropropyl)silane coated as thin-layer for an effective passivation and the surface modification, resulted with water-resistant perovskite films because of extremely hydrophobic trifluoromethyl groups. Also, Li et al. reported effective surface passivation of perovskite layers by graphene oxide modified with 4-fluorophenyl substituents.[88] The passivation effect was mainly due to the interaction between 4-fluorophenyl units and undercoordinated Pb^{2+} ions, as suggested by the behavior of the electron localization function and further supported by the reduction of the deep trap states in t-DOS distribution.

Lewis acid–base chemistry has been extensively employed for surface passivation through post-treatment. Lewis acid and base can form covalent bonds and form acid-base complexes by sharing electron pairs through Lewis base donating a pair of electrons, while Lewis acid gains a pair of electrons. Electron-rich defects such as undercoordinated I^- ions and Pb–I anti-site substitutions can be passivated by Lewis acids that can accept lone pairs. Fullerene (C_{60}) and its derivatives are well-known Lewis acid passivators, which decrease the non-radiative recombination at the perovskite/TiO_2 heterojunction because of its optoelectronic properties.[84,89] Iodopentafluorobenzene (IPFB) and tris(pentafluorophenyl)phosphine (TPFP) as multifunctional Lewis acid additives have been incorporated to the surface of perovskite films to passivate the under-coordinated I^- and to enhance hydrophobicity by fluorine substitution.[90,91] Small molecules with fluorine atoms can inductively withdraw electron density from the aromatic ring, thus more readily accepting electrons from the coordinated I^- to form a halogen bond.

On the other hand, electron-deficient defects like undercoordinated Pb^{2+} ions or Pb clusters can be passivated by Lewis bases that donate electron pairs.[92] The presence of heteroatom in organic molecule such as oxygen (O), nitrogen (N), sulfur (S), or phosphorus (P) atoms and halide ions in perovskite can be combined to form the Lewis adducts. The lone pair electrons of these heteroatoms or amines, carboxyl, hydroxyl, carbonyl, and phosphine oxides functional groups could passivate the undercoordinated Pb^{+2} defects in metal–halide perovskites.[93] Especially, thiophene and pyridine groups are mostly used in the literature because of their good passivation effects on defects, which stems from the covalent bond of Pb^{2+} to this species. The effective surface defect passivation via a Lewis acid-base interaction can result in larger grain size, reduce the non-radiative recombination centers, and provide a longer carrier lifetime with extended photoluminescence (PL) lifetime.[94] An important example among them, tri-n-octylphosphine oxide (TOPO) molecule with Lewis base containing phosphine oxide (P=O) group has been applied as passivator, which is widely reported for passivation effect on perovskite film surface via mono-bonding with defect sites. The P=O electron-donor group has a relatively larger difference in electronegativity between P and O compared to the carboxyl and sulfinyl groups commonly used for perovskite passivation. Thus, oxygen atom of P=O can exhibit stronger electron donating and coordination ability with metal atoms. DeQuilettes et al. Reported that TOPO showed extended PL lifetime especially at the grain boundaries of the perovskite layer.[95] In addition, improvement in device efficiency was observed with the help of passivation effect of TOPO ligands applied to the $MAPbI_3$ perovskite surface. And moisture stability of the devices was significantly improved due to the three hydrophobic long alkyl chains in TOPO.[96] These developments shed light on the subject that more research is needed to better understand the mechanism of passivation, to identify the types of defects and to select the suitable functional groups for passivation.

1.5 PSC Stability

Perovskite solar cells have reached high power conversion efficiency in a short period of time, however, there are still several challenges limiting the industrial realization. Long-term stability of PSCs is one of the important issues to be resolved. The perovskite layer is prone to rapid decomposition when the device exposure to high temperature, humidity, oxygen, and full solar illumination. The degradation of PSCs is a complex and multilateral process and can result in changes of the perovskite materials in terms of crystal structure, thin-film morphology, composition and optoelectronic properties.[97]

Moisture stability is a major issue affecting PSC performance and it has been the subject of a number of investigations. Prolonged exposure to water vapor and high relative humidity, which is unavoidable in the outdoor environment, has highly detrimental effects on the perovskite lattice structure. The mechanism of water interaction with methylammonium lead iodide has been mostly highlighted. In this case, perovskite crystals easily decompose and convert into the precursor PbI_2 with irreversible degradation. This deleterious effect is enhanced in the presence of heat, electrical field or UV light.[98] Perovskite decomposition of unencapsulated $MAPbI_3$ films when exposed to ambient air can be evidenced by a visually distinct colour change from black to yellow. On the other hand, water vapor exposure leads to hydrated the crystal phase ($CH_3NH_3PbI_3{\cdot}H_2O$) due to hydrophilic properties of perovskite, which is reversible process only with dehumidification.[99] Instability of HTMs, especially caused by hygroscopic doping, is an important issue to be resolved for the long-term stability of PSCs. Particularly, wide bandgap hole transporting materials such as spiro-OMeTAD typically require doping in order to match necessary electrical conductivity. The use of additives is problematic since hygroscopic nature of doping makes the hole transporting layer highly hydrophilic leading to chemical degradation and negatively influences the stability of the entire device.[100]

Thermal stability is another important issue limiting the commercialization of PSCs. The module temperature can easily reach ~50°C when solar modules are operating under direct sunlight. In addition, modules can be exposed to extreme temperature conditions ranging from -40°C to +85°C, depending on the environment and weather conditions. Therefore, it is crucial for a PSC to have long-term thermal stability. It was observed that $MAPbI_3$ undergoes a tetragonal to cubic phase transformation at ~56°C.[101] Many studies have also shown that perovskite layers can thermally decompose when annealed for extended periods of time above 100°C, which can provide sufficient thermal energy to overcome the activation barriers of chemical processes for the decomposition.[102] In addition to perovskite decomposition, increased ionic mobility in the lattice because of high temperatures can also lead to poor performance of the devices. Thermal decomposition studies showed that organic cations like MA and FA are not stable at high temperature. Research efforts to improve long-term thermal stability of PSCs have been continued. One of the highlighted modifications in the composition of perovskite material is replacing them with inorganic cations like the caesium (Cs^+) or rubidium (Rb^+) cation may improve the thermal stability of the resulting perovskite solar cells.[103] Zhang et al. showed that $CsPbBr_3$ nanocrystals can be stable up to 417°C under vacuum, and they begin to sublime above 417°C.[104] The other compositional modifications are engineering of interfaces with the creation of 2D/3D perovskite combination which improve the stability performance of the solar cell more than one year without any loss in efficiency.[84] One of the other possible solutions for thermal instabilities is thermally and chemically stable metal-organic complexes. Due to their excellent hole transport properties, metal-organic complex HTMs have been incorporated into perovskite solar cells, but high PCE has not been achieved. Another approach to enhance stabilization is through interface engineering with HTMs. Introducing a thin (10 nm) chromium layer between the spiro-MeOTAD and the top gold electrode reduced the dramatic device degradation associated with increased temperature. Basically, the addition of the Cr layer prevents gold migration through the HTM to the perovskite layer.[105] Besides, it is revealed that the integrated Al_2O_3 mesoporous buffer layer in the HTM preserves the metal electrode migration during the ageing process, and Al_2O_3 buffer layer eliminates pinholes induced instability of HTM by protecting the perovskite layer.[106]

Light stability is another important test for a high-performance PSC. There is a substantial amount of work describing photo-induced changes in PSC performance and perovskite structure. In devices exposed to long-term irradiation, both reversible and irreversible degradation of perovskite material can be observed due to photo-induced ion dissociation, light-activated trap states formation, photo decomposition and photo-induced atom/ion migration. [97,107] The light-induced decomposition of $MAPbI_3$ films causes a black to grey colour change when illuminated with white light in a vacuum. Light-induced changes in film morphology were also investigated, where $MAPbI_3$ had a major change in surface morphology from a smooth surface to a rough surface containing cracks and large pores, under light illumination.[108]

1.6 Conclusion and Outlook

Here I have summarized the great research effort and rapid development of molecular engineering of organic materials for perovskite solar cells. The research results in the literature will be guided by shedding light on the future developments. In particular, it is of great importance for the field of PSC to continue research to improve the disadvantages such as the long-term stability and high cost of PSCs, which are the biggest obstacles to the commercialization process. In addition, it has been demonstrated that interface engineering is of great importance in determining the photovoltaic performance of devices. The presence of defects on the perovskite surface can be passivated by interface engineering by adding an interlayer molecule or an HTM with passivation capability. Therefore, I have extensively designed, synthesized and investigated small molecule organic materials for perovskite solar cell applications. I investigated the reasons behind the improving photovoltaic performance and stability of PSCs through structural, chemical, optical, and photovoltaic analysis. Specifically, most of the work described in the thesis has focused on the design and molecular engineering of various low-cost small molecule HTMs with or without dopant perspectives. In addition, interlayer engineering was applied to the designed HTMs with the integration of passivation capability. Finally, I designed and developed an interfacial layer for the interface of the perovskite/hole transport material with the p-type Lewis base passivation molecule. These organic materials applied to perovskite solar devices have been extensively researched to provide a clear understanding of how the working mechanism of organic materials can be tuned to improve the photovoltaic performance and long-term stability of the devices.

Chapter 2 D-π-A Type Triazatruxene-based Dopant-free Hole Transporting Materials

Three donor–π-bridge–acceptor (D–π–A) type organic small molecules coded CI-B1, CI-B2 and CI-B3 are designed, synthesized and used as dopant-free hole transporting materials (HTMs) for perovskite solar cells (PSCs). The strong electron-donating triazatruxene central core (D), terthiophene conjugated arms (π) and three different strong electron-accepting units (A) provide high intramolecular charge transfer nature and eliminate the need of dopants during the fabrication of PSCs. HTMs are designed with 1,3-indandione, *N*-ethyl rhodanine, and dicyanovinylene *N*-ethyl rhodanine strong acceptor units to understand the effect of terminal functional groups on dopant-free PSC performance. The effects of end-capped acceptors in D-π-A structured HTMs on molecular and photovoltaic properties were investigated via photophysical and electrochemical experiments, especially GIWAX. Interestingly, due to the change of end-capping, three different organization of self-assembly with π-π stacking are observed in the solid thin films. Dopant-free CI-B1, CI-B2, CI-B3 and spiro-OMeTAD with dopants are used with triple cation perovskite composition $Cs_{0.1}(MA_{0.15}FA_{0.85})_{0.9}Pb(I_{0.85}Br_{0.15})_3$ (MA: $CH_3NH_3^+$, FA: $NH=CHNH_3^+$) in n-i-p architecture. The cells prepared with CI-B3, end-capped with dicyanovinylene *N*-ethyl rhodanine acceptor unit, showed deeper HOMO level compared to spiro-OMeTAD and produced higher V_{OC} value. Superiority of the CI-B3 device performance can be explained by its better morphology in the thin film and well-ordered edge-on aggregation by π-π stacking. CI-B3 based devices not only exhibits a comparable power conversion efficiency (PCE) of 17.54 % to the state-of-art of spiro-OMeTAD with dopants (18.02%), but also demonstrates improved long-term stability, maintaining 88% of its original PCE after 1000 h of illumination, while the performance of spiro-OMeTAD-based device dropped by 70% of initial data. Therefore, this study provides a new material design strategy for the efficient and highly stable dopant-free HTMs. The superior photovoltaic performance, synthetic simplicity, dopant-free nature, high durability and edge-on molecular orientation of CI-B3 show its great perspective as HTM candidate for efficient and stable PSCs.

This chapter is based on the published work: Igci et al. Sol RRL, 2020, 2000173. DOI: 10.1002/solr.202000173.

Authors: Cansu Igci, Sanghyun Paek, Kasparas Rakstys, Hiroyuki Kanda, Naoyuki Shibayama, Vygintas Jankauskas, Cristina Roldán Carmona, Hobeom Kim, Abdullah Mohamed Asiri, and Mohammad Khaja Nazeeruddin.

In this work I contributed as first author. I synthesized and characterized all organic materials, performed data analysis, designed the experiments.

2.1 Introduction

Among several *p*-type materials of different categories (organic small molecules, inorganic molecules and polymeric materials), spiro-OMeTAD has demonstrated well-aligned HOMO level with the valence band (VB) of the perovskite, high solubility in organic

solvents and high homogeneity of its thin films.[33] Yet, spiro-OMeTAD needs chemical dopants to obtain higher efficiency because of its weak intermolecular electronic coupling and wide band gap.[109] Among the many *p*-type dopants developed today, the combination of cobalt complex-based tris(2-(1*H*-pyrazol-1-yl)-4-*tert*-butylpyridine)cobalt(III)tri[bis(trifluoromethane)sulfonimide] (FK209) and lithium bis(trifluoromethanesulfonyl)imide (LiTFSI) are commonly employed to improve the mobility and conductivity of HTMs by radical cation generation.[110] Also, 4-*tert*-butylpyridine (tBP) has morphological benefits and improves the homogeneity of the layer by preventing phase segregation of LiTFSI.[111] However, these dopants have several drawbacks such as their high hygroscopicity, which accelerates device degradation, and the high diffusion of lithium ions, which reduces the effect of dopant over time, both contributing to the long-term device degradation.[112] The logical solution for stabilizing PSCs must therefore involve dopant-free HTMs, which essentially requires revealing the relationship between the structure of dopant-free molecules and cell performance towards highly efficient and stable cells.

Among the high-performance dopant-free HTMs applied in PSCs, a very important molecular design for small organic molecules is the donor–π-bridge–acceptor (D–π–A) architecture, which provides high charge carrier mobility, strong dipolar intermolecular interaction and intramolecular charge delocalization.[67] Focusing in the donor core unit, a planar nitrogen-containing triazatruxene (TAT) is a good candidate due to the excellent optical and electronic properties, strong π-π intermolecular interaction, high hole mobility and wide synthetic variety with tunable properties.[52] In addition, the nitrogen atom of the indole unit helps to stabilize the oxidized radical cation formed during device operation, and from a synthetic perspective, it can also be prepared from low cost precursors synthesized from abundant natural products.[52] On the other hand, thiophene π-bridge units can stabilize the molecule increasing the double-bond character, and D-π-A molecules containing them have shown lowered band gaps, higher hole mobility and higher photovoltaic performance compared with furan-bridged molecules.[113] Rakstys *et al.* reported a dopant-free HTM based on terthiophene π-bridging unit, which aggregates as highly ordered face-on columnar stacks within the thin layer.[68] This resulted in increased carrier transport through the oriented π-π stacks and enhanced cell efficiency, questioning the role of molecular structure on the interfacial interactions and final cell performance. For example, such molecules are typically end-capped with strong acceptor units that may act as Lewis base blocks, enhancing intermolecular charge transfer and may passivate the perovskite surface, reducing crystal defects.[114] Early investigations also showed that these additives lead to a better crystallization and growth of the films, or that passivation treatment within the film could improve non-radiative recombination.[115]

Inspired by these results, we have made use of the Lewis base functional blocks in the HTM structure to create a cost-effective solution for optimizing the performance of the device without the need of adding an extra passivation layer.[116] Herein, we have developed three novel D–π–A type molecules to deeper investigate the design strategy of dopant-free HTM. A planar triazatruxene central core (D), alkylated terthiophenes as conjugated arms (π) and various strong electron acceptor units (A) are introduced into the molecules. Different electron-accepting moieties were carefully selected and investigated to understand the effect of acceptor strength. For that, 1,3-indandione, *N*-ethyl rhodanine, and dicyanovinylene *N*-ethyl rhodanine were used, yielding end-capped HTMs coded as CI-B1, CI-B2, and CI-B3, respectively (Figure 2.1). We have investigated the intermolecular interaction and orientation of the various HTMs, and inferred that this affects the performance and stability of the device. All dopant-free molecularly engineered HTMs were successfully applied in n-i-p PSCs, and those prepared with highly oriented dopant-free CI-B3 achieved an encouraging PCE of 17.54%, a very comparable performance to that of the reference spiro-OMeTAD with dopants (18.02%). More importantly, devices containing CI-B3 exhibit a substantial improvement in long-term device stability, outperforming that of spiro-OMeTAD with dopants under the same experimental conditions.

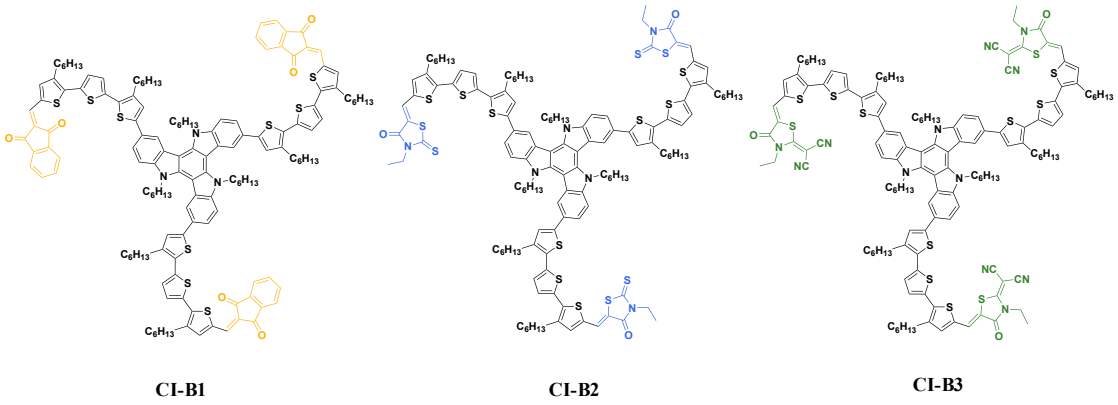

Figure 2.1 Chemical structures of CI-B1, CI-B2, and CI-B3 HTMs.

2.2 Result and Discussion

2.2.1 Design and Synthesis of CI-B HTMs

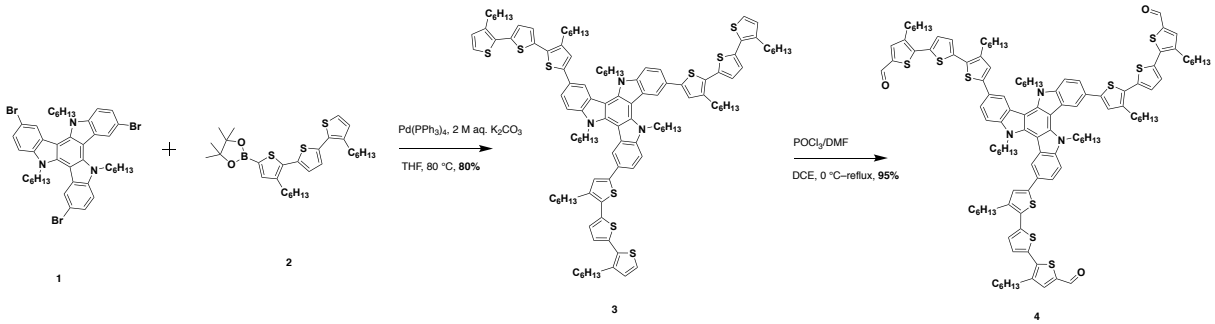

Scheme 2.1 Synthetic route for *5*'',*5*''''',*5*'''''''''-(5,10,15-trihexyl-10,15-dihydro-5*H*-diindolo[3,2-*a*:3',2'-*c*]carbazole-3,8,13-triyl)tris(3,3''-dihexyl-[2,2':5',2''-terthiophene]-5-carbaldehyde) (4).

The three novel triazatruxene-based dopant-free HTMs were successfully synthetized. At the beginning of synthesis, the alkylated terthiophene conjugated arms were introduced into the triazatruxene core by Suzuki cross-coupling reaction. Then, the Vilsmeier formylation reaction gave the carbaldehyde intermediate (4) (Scheme 2.1). Compound *5*'',*5*''''',*5*'''''''''-(5,10,15-trihexyl-10,15-dihydro-5*H*-diindolo[3,2-*a*:3',2'-*c*]carbazole-3,8,13-triyl)tris(3,3''-dihexyl-[2,2':5',2''-terthiophene]-5-carbaldehyde) (4) 4 was accomplished starting from commercially available and inexpensive precursor 2-indolinone according to previous reports with small modifications.[68]

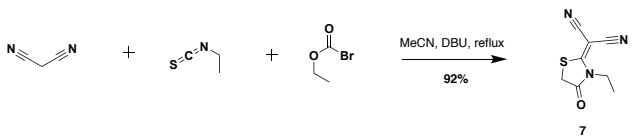

Scheme 2.2 Synthetic route for 2-(3-ethyl-4-oxothiazolidin-2-ylidene)malononitrile (7).

In terms of design, Alkylated triazatruxene donor core and alkylated terthiophene conjugated arm were preserved throughout the series, while the acceptor unit was modulated with commercially available 1*H*-indene-1,3(2*H*)-dione (5), 3-ethyl-2-thioxothiazolidin-4-one (6), and synthesized 2-(3-ethyl-4-oxothiazolidin-2-ylidene)malononitrile (7), respectively, to obtain CI-B1, CI-B2, and CI-B3. The designed acceptor unit, 7 was isolated after cyclization reaction of malononitrile with ethyl isothiocyanate and ethyl bromoacetate in the presence of DBU (Scheme 2.2).[117] The final products CI-B1, CI-B2 and CI-B3 were synthesized condensing obtained aldehyde and selected acceptor under Knoevenagel reaction conditions in the presence of piperidine as shown in Scheme 2.3.

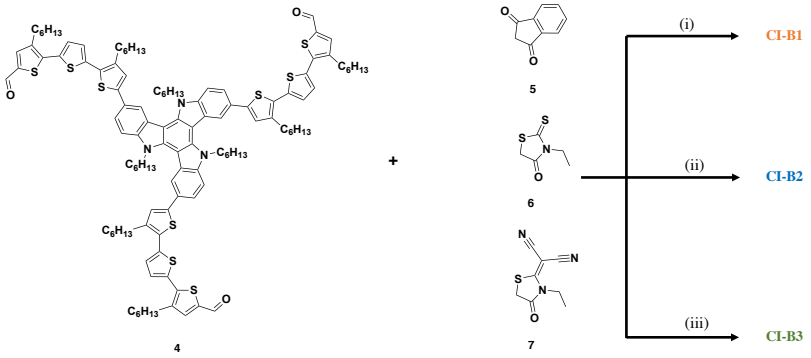

Scheme 2.3 Synthetic route for CI-B1, CI-B2 and CI-B3 molecules. i) Et_3N, chloroform, reflux, 50% ii) Piperidine, chloroform, reflux, 48% iii) Piperidine, chloroform, reflux, 52%.

CI-B HTMs were characterized by mass spectroscopy and elemental analysis methods (Appendix A). CI-B HTMs showed the best solubility in tetrachloroethane, followed by THF and DCM. NMR experiments were conducted under various conditions. 800 MHz and 600 MHz high field NMR analysis was performed in *d*-THF (the best solvent) and long experiment time was tried to increase peak intensities. In order to receive bigger signals, the analysis at high temperature up to 55 °C were made. However, the peaks of the spectra were buried in the baseline and the intensities were very low for each experiment. To improve the signal, the concentration of the samples was increased using 3 mM, 5 mM and 10 mM in *d*-THF. For those that are more concentrated were stirred at high temperature to obtain a homogeneous dark-red solution. However, even in this case any improvement in the peak intensity was not observed. The strong π- π interactions and the intermolecular aggregation in solution might reduce the degree of freedom of proton spin, as well as promote their precipitation after certain period.

2.2.2 Thermal, Optical, and Electrochemical Properties

To confirm the thermal stability of the new HTMs, we performed thermogravimetric analysis (TGA). As shown in Figure 2.2a, high decomposition temperatures (T_d) determined at the 5% weight loss of CI-B1, CI-B2, and CI-B3 are detected, reaching 360 °C, 327 °C, and 434 °C respectively. According to these results, CI-B3 possess exceptional thermal stability. The optical properties of the new molecules were investigated by ultraviolet-visible (UV-Vis) absorption and photoluminescence (PL) spectroscopy (Figure 2.2b) and the obtained data are summarized in Table 2.1. CI-B1, CI-B2, and CI-B3, which contain strong acceptor units, exhibit two absorption bands ranging between 350 and 700 nm. The first absorption band, centred between 350 and 450 nm, originates from the localized aromatic π-π* transition of the D-π-A type conjugation system. The second absorption bands, centred at 550, 500, 522 nm for CI-B1, CI-B2, and CI-B3 respectively, are assigned to the intermolecular charge transfer (ICT). Note that the position of the ICT band is

considerably red-shifted with increasing the strength of the electron acceptors, which is given based on their absorption profiles: CI-B1 > CI-B3 > CI-B2. The emission peaks of CI-B1, CI-B2, and CI-B3 are centred at 726, 712 and 733 nm, respectively. We next calculated the optical energy band gap (E_g) values from the intersection of the absorption and photoluminescence spectra, that are determined to be 649, 601, and 626 nm, which corresponds to E_g of 1.91, 2.06 and 1.98 eV, respectively. Compared to spiro-OMeTAD (E_g ~ 3.0 eV), the new molecules have a smaller band gap, favouring the thermal population of the conduction band, and thus increasing the number of intrinsic charge carriers.[118, 119]

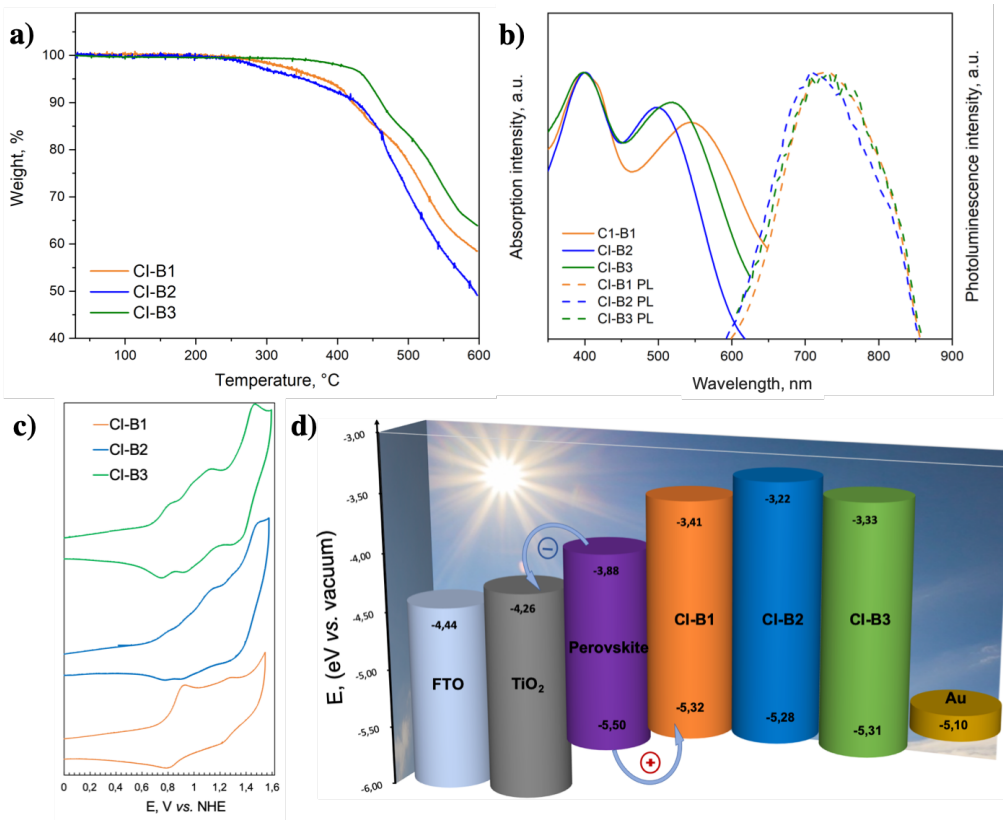

Figure 2.2 a) TGA curves of CI-B1, CI-B2 and CI-B3. b) UV-Vis absorption and PL spectra normalized at the peak value. c) Cyclic voltammograms of the HTMs and d) schematic energy level diagram of components used in the devices.

The experimental HOMO levels were derived from the ground-state oxidation potential E_{HOMO} estimated from cyclic voltammetry with a standard three-electrode configuration, shown in Figure 2.2c. The HTMs were tested in dichloromethane containing 0.1 M *n*-Bu_4NPF_6 as a supporting electrolyte. The E_{HOMO} values were calculated to be -5.32, -5.28, and -5.31 eV vs. vacuum for CI-B1, CI-B2, and CI-B3, respectively, that is less negative than VB of the perovskite, facilitating the hole extraction. Consequently, no big differences were observed between the three HTMs, which is also expected as the HOMO orbitals are mostly localized in the triazatruxene central core along with terthiophene bridges.[68] The LUMO energy levels were calculated from E_g and E_{HOMO}. The obtained values are -3.41, -3.22 and -3.33 eV for CI-B1, CI-B2, and CI-B3, respectively. Given that the LUMO levels of the HTMs are below -4 eV, a beneficial electron blocking from perovskite to Au electrode is ensured. A schematic energy levels are shown in Figure 2.2d. All thermal, optical, and electrochemical properties are summarized in Table 2.1.

HTM	λ_{abs}[a] (nm)	λ_{em}[a] (nm)	E_{HOMO}[b] (eV)	E_g[c] (eV)	E_{LUMO}[d] (eV)	T_d[e] (°C)
CI-B1	398, 550	726	-5.32	1.91	-3.41	365
CI-B2	401, 500	712	-5.28	2.06	-3.22	333
CI-B3	398, 522	733	-5.31	1.98	-3.33	434

Table 2.1 Thermal, optical and electrochemical properties of CI-B1, CI-B2 and CI-B3 HTMs. [a)] Absorption and emission spectra measured in dichloromethane; [b)] Measured in 0.1 M n-Bu_4NPF_6/DCM solution using glassy carbon working electrode, Pt reference electrode and Pt counter electrode calibrated by Fc/Fc^+ as an external reference. Potentials were converted to the normal hydrogen electrode (NHE) by addition of +0.624 V and -4.44 eV to the vacuum, respectively; [c)] Evaluated from the intersection of normalized absorption and emission spectra; [d)] $E_{LUMO} = E_g + E_{HOMO}$; [e)] Degradation temperature observed from TGA (5% weight loss at 10 °C/min).

2.2.3 Surface Geometry and Film Forming Investigation of HTM layers

2-dimensional grazing incidence wide-angle X-ray scattering (2D GIWAXS) was employed to investigate the crystallization of the three novel HTMs influenced by the different acceptors. The samples, prepared by spin-coating a tetrachloroethane solution on silicon wafers, showed diffractions assignable to the π-π stacking structure ($q \approx 1.6$ Å^{-1}) and the Lamellar structure ($q \approx 0.35$ Å^{-1}) for the three systems (experimental details in Appendix A). The azimuthally integrated intensity profile (Figure 2.3a) was calculated from 2D GIWAXS measurements, shown in Figure 2.4a-d. The d-spacings for the π–π stacking structure (d_π) and the intercolumnar organization (d_{io}) were calculated to be 3.9 and 18 Å, respectively. We also calculated the angular dependence of the peak intensity (Figure 2.3b) at $q = 1.6$ Å^{-1}, which corresponds to π-π stacking. The χ is the angle with respect to the q_z axis (out-of-plane), while χ = 90° is q_{xy} axis (in-plane).[120,121]

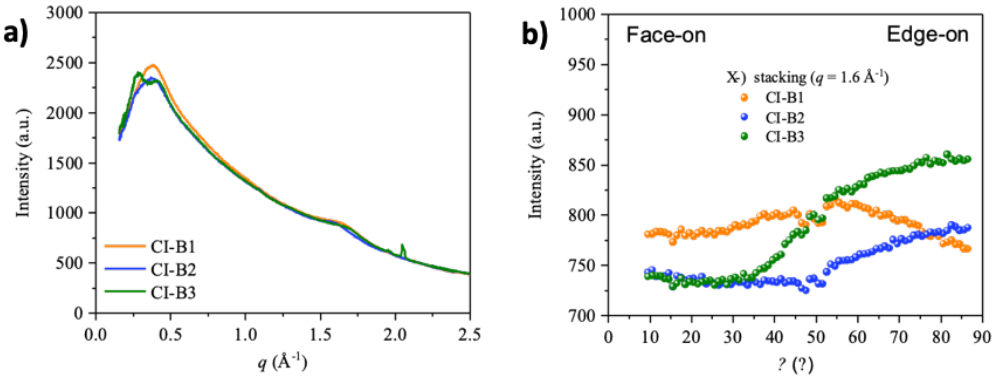

Figure 2.3 (a) The azimuthally integrated intensity profile obtained from 2D GIWAXS measurements of CI-B1, CI-B2, and CI-B3. (b) The angular dependence of the peak intensity at $q = 1.6$ Å^{-1} for the π–π stacking structure.

According to 2D GIWAXS patterns, all three HTMs undergo π-π stacking interaction, however, the self-assembly orientation between the compounds are varying significantly. As presented in Figure 2.4e, the intensity of CI-B1 shows slight change as a function of χ, which means that CI-B1 is isotropic. The π-π stacking peak at 1.6 Å^{-1} shows isotropic orientation and its stacking phase is randomly arranged according to the broad out-of-plane peak at 0.3-0.4 Å^{-1}. Therefore, it has both a face-on and an edge-on stacking molecular orientation with random phase. On the other hand, for CI-B2 film (Figure 2.4b) the same π-π stacking peak was seen in-plane at 1.6 Å^{-1}, meaning the edge-on stacking interaction. However, the broad out-of-plane peak at 0.3-0.4 Å^{-1} shows a randomly stacked phase as illustrated at Figure 2.4f. In addition, for CI-B3 (Figure 2.4c), two strong and dispersive diffractions were observed at 0.3 and 0.4 Å^{-1} out-of-plane, which is probably due to the well aligned molecule stacking phase.[122,123] The CI-B3 molecules are thus packed in favor of an edge-on stacking fashion with well-order as schematically shown at Figure 2.4g.

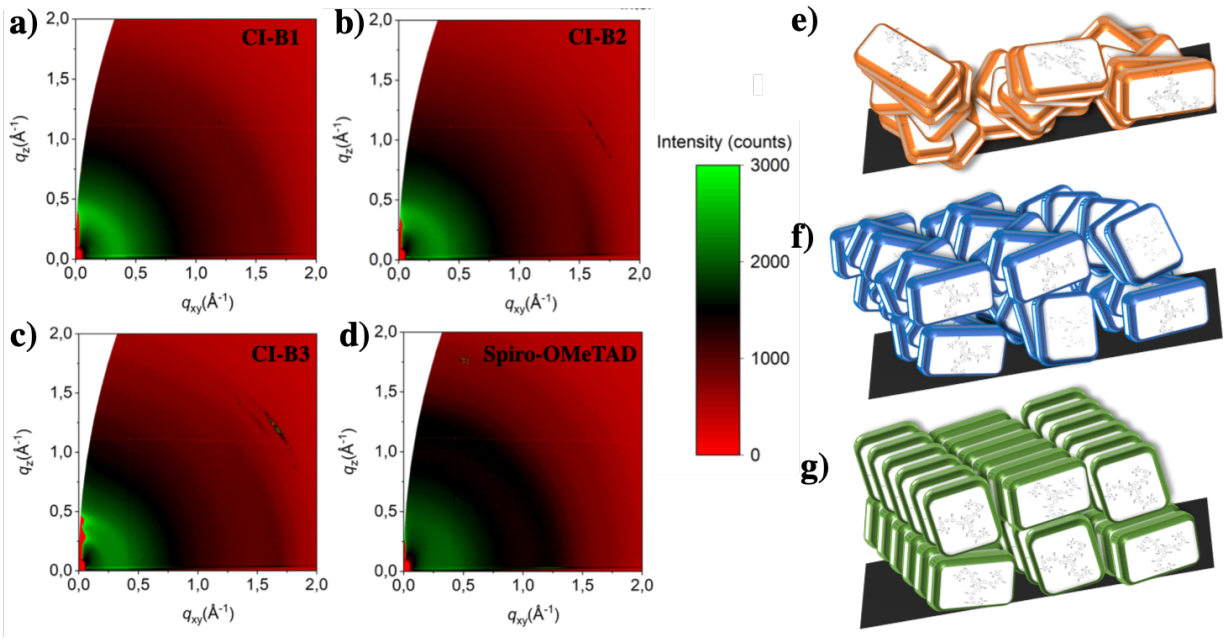

Figure 2.4 GIWAXS patterns of the films coated from tetrachloroethane on a silica wafer a) CI-B1, b) CI-B2, c) CI-B3, d) spiro-OMeTAD. Orientation phase of e) CI-B1, f) CI-B2, g) CI-B3.

The morphology of the HTM film and perovskite/HTM interface is of great importance since it can considerably affect the interfacial hole transfer and charge recombination processes. Thus, the morphology of the dopant-free HTM films coated onto the perovskite was investigated by scanning electron microscopy (SEM), as shown in Figure 2.5a-d. All HTM layers were measured at low voltage in order to reduce the penetration volume and keep electrons close to the surface. As presented in the Figure 2.5b and Figure 2.5c, both CI-B2 and CI-B3 HTMs form smooth and homogeneous films, with CI-B3 presenting better surface coverage. However, a rod-like structure was detected for CI-B1 (Figure 2.5a), which prevents from a good film coverage. Such large aggregates, observed exclusively on the CI-B1 film, may be formed due to the hydrogen bonding ability of 1,3-indandione end capping acceptor unit.[124,125] Similarly, despite CI-B2 resulted in a more homogeneous morphology and better surface coverage than CI-B1, it has a substantial presence of pin holes that could deteriorate the device performance. Consequently, the poor film coverage for CI-B1 and CI-B2 could be the main factors for the low V_{OC} and *FF* achieved for these systems, suggesting that end-capped acceptors could greatly affect the surface morphology and have important consequences for the photovoltaic performance.

We then examined the performance of PSCs fabricated with the dopant-free triazatruxene based molecules in n-i-p configuration consisting of FTO/TiO_2/$Cs_{0.1}(MA_{0.15}FA_{0.85})_{0.9}Pb(I_{0.85}Br_{0.15})_3$/HTM/Au. The cross-sectional SEM image of entire PSC with CI-B3 HTM is displayed in Figure 2.5d. The device was made using ~500 nm thick perovskite atop a ~200 nm thick mesoporous TiO_2 layer, which was deposited on FTO glass coated with ~30 nm of compact TiO_2. Finally, it was completed by depositing a ~70 nm thick HTM layer and ~70 nm of gold as the counter electrode, therefore we employed a thinner than that usually required for Spiro-OMeTAD. Note that for a dopant-free HTM, the thickness plays a crucial role as the current extraction is strongly limited by its inferior charge-transporting capability. [126] Therefore, the thinner the layer, the better hole-transport will be achieved.

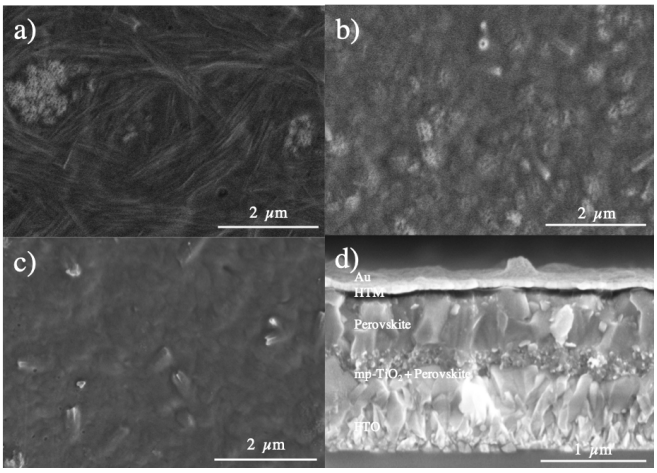

Figure 2.5 Top surface SEM images of a TiO_2/perovskite/HTM a) CI-B1, b) CI-B2, c) CI-B3, d) cross-sectional SEM micrographs of perovskite devices containing CI-B3 HTM.

2.2.4 Thin-layer Characteristics of HTMs

To understand the interfacial processes and the hole-extraction capability induced by the different strong electron acceptors, we investigated the perovskite/HTM interface by using steady-state photoluminescence (PL) and time-resolved photoluminescence (TRPL), and compared the results with those achieved for spiro-OMeTAD (Figure 2.6a, b). In all cases, the bilayer perovskite/HTM showed reduced PL intensity than the bare perovskite (experimental details in Appendix A). In particular, CI-B2 and CI-B3 show very similar behaviour compared to spiro-OMeTAD, while on the contrary, strong PL quenching occurred for the CI-B1, suggesting it has the highest hole-extraction ability corresponds to perovskite/CI-B1 bilayer (Figure 2.6a). The time constant of TRPL measurements 25.7, 30.8 and 32.9 ns were retrieved for CI-B1, CI-B2 and CI-B3 HTM-coated perovskite films, and a slightly slower process with τ = 36.8 ns was obtained for the spiro-OMeTAD/perovskite interface (Figure 2.6b). This further demonstrates that the HTMs exhibit more efficient hole extraction ability than spiro-OMeTAD.

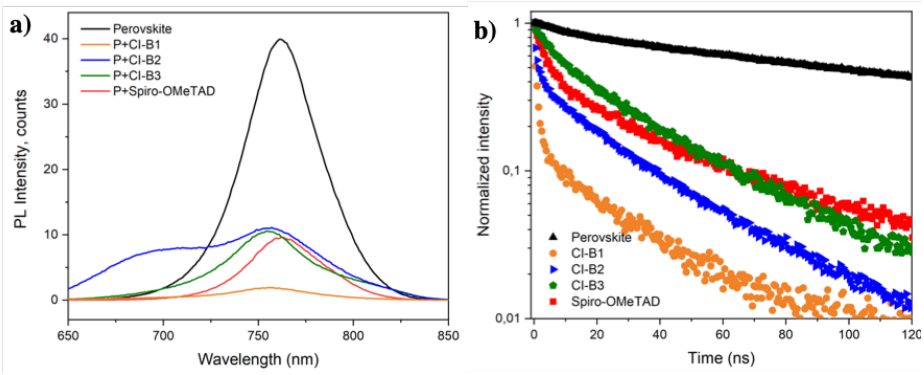

Figure 2.6 a) PL spectra of the pristine perovskite and perovskite/HTM film excited at 450 nm from HTM side; b) Normalized PL decay in the first 120 ns time window.

To investigate the charge transport and hole collection properties of the HTMs, their lateral thin-film conductivity was measured. For that, we spin coated dopant-free HTMs films on organic field effect transistor (OFET) substrates containing interdigitated contacts with different channel lengths (experimental details in Appendix A). Results, summarized in Figure 2.7, demonstrate that CI-B3 shows a higher conductivity (9.60 x 10^{-7} S cm^{-1}) than either CI-B1 (7.98 x 10^{-8} S cm^{-1}) or CI-B2 (5.33 x 10^{-7} S cm^{-1}). Therefore, the well-ordered edge-on stacking molecular orientation characteristic in CI-B3 might result in more efficient π–π stacking in the hole transporting films. Also, the conductivity of spiro-OMeTAD w/o dopant was determined to be σ = 1.07 x 10^{-6} S cm^{-1}, as previously reported in literature.[127]

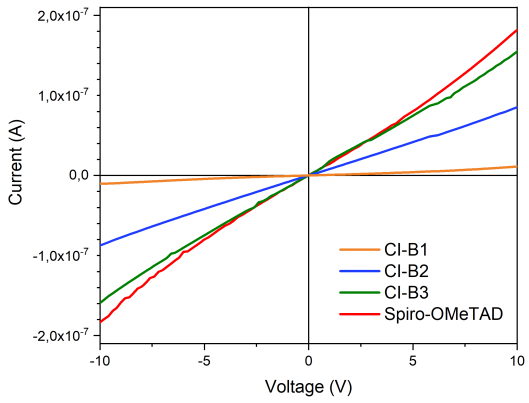

Figure 2.7 The conductivity measurements on OFET substrates of CI-B1, CI-B2 and CI-B3.

We also characterized the charge transport ability of CI-B1, CI-B2 and CI-B3 films by using xerographic time-of-flight (XTOF) technique.[68,128] Due to the specific D- π -A structure present in these HTMs, the type of transported carriers had to be verified. The kinetics of the photo discharge analysis was performed in the layers of sufficient thickness for the surface photogeneration. As expected, it showed a photo response only for positive charging, confirming that holes are the unique carriers transported in the three materials (Figure 2.8, Appendix A).

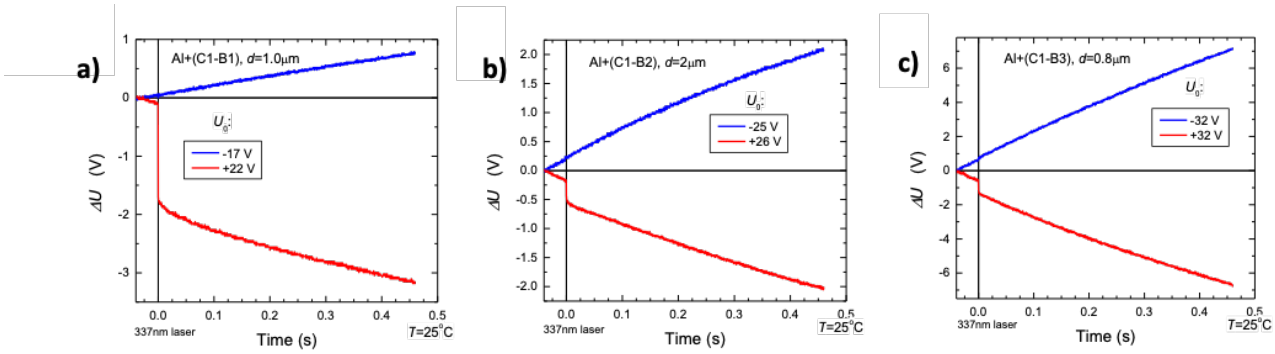

Figure 2.8 Integral discharge transients in xerographic mode in layers of a) C1-B1, b) C1-B2 and c) C1-B3.

However, due to the dispersive nature of the holes under high degree of molecular aggregation, the hole drift mobility of C1-B1 could not be obtained. Note that for thin films the region involved in charge generation corresponds practically to the entire thickness, therefore the transient kinetics exhibit noticeable change of slope. When the slope changes, a hole transit occurs, which can only be determined within a relatively narrow range of electric fields. The hole mobility results are shown in standard plot for organic compounds (Figure 2.9). We estimated that the hole mobility of the C1-B2 and C1-B3 thin films are $8x10^{-5}$ and $1.3\ x10^{-4}$ cm^2/Vs, respectively and CI-B3 showed one order of magnitude higher mobility.

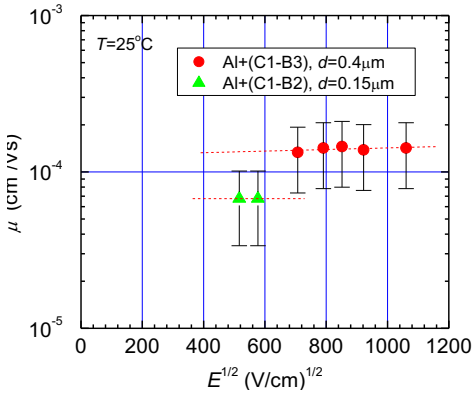

Figure 2.9 The hole drift mobility plot vs electric field for C1-B2 and C1-B3.

2.2.5 Device Characteristics

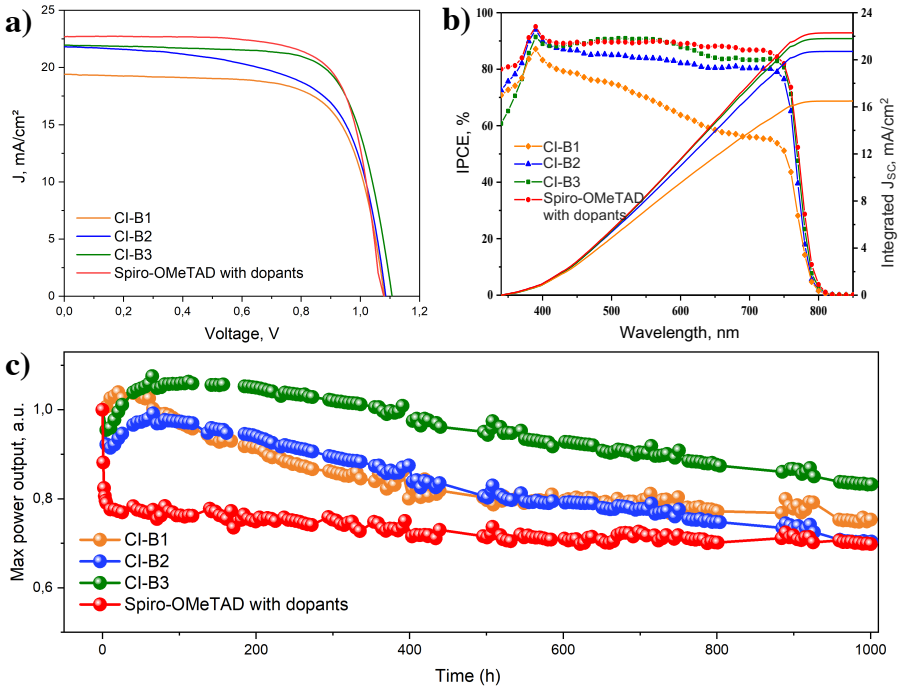

Figure 2.10 a) Current–voltage curves of the best-performing devices. b) IPCE spectra of the devices using CI-B1, CI-B2, CI-B3 and spiro-OMeTAD with dopants as HTMs. c) normalized maximum power point tracking of perovskite solar cells for 1000h.

To explore the performance of the three novel compounds, PSCs were fabricated using the following device configuration: fluorine-doped tin oxide (FTO)/compact-TiO_2/mesoporous-TiO_2/perovskite/HTM/Au. A triple-cation $Cs_{0.1}(MA_{0.15}FA_{0.85})_{0.9}Pb(I_{0.85}Br_{0.15})_3$ perovskite formulation was used as light absorber and each HTM was coated using a 0.15 M solution in tetrachloroethane (experimental details in Appendix A). Figure 2.10a shows the typical current–voltage (*J-V*) curves of the solar cells based on C1-B HTMs. The corresponding photovoltaic parameters are summarized in Table 2.2, and the device statistics are shown (Figure 2.11). We also prepared devices using spiro-OMeTAD with dopants as the reference cells, together with spiro-OMeTAD w/o dopants for comparison. As expected, the pristine spiro-OMeTAD limits considerably the cell performance, becoming mandatory the use of chemical dopants to improve PCE towards 18%. In contrast, thanks to the strong contribution of molecular aggregation the molecules, they are able to exhibit high device efficiencies over 14% without the addition of any dopant.

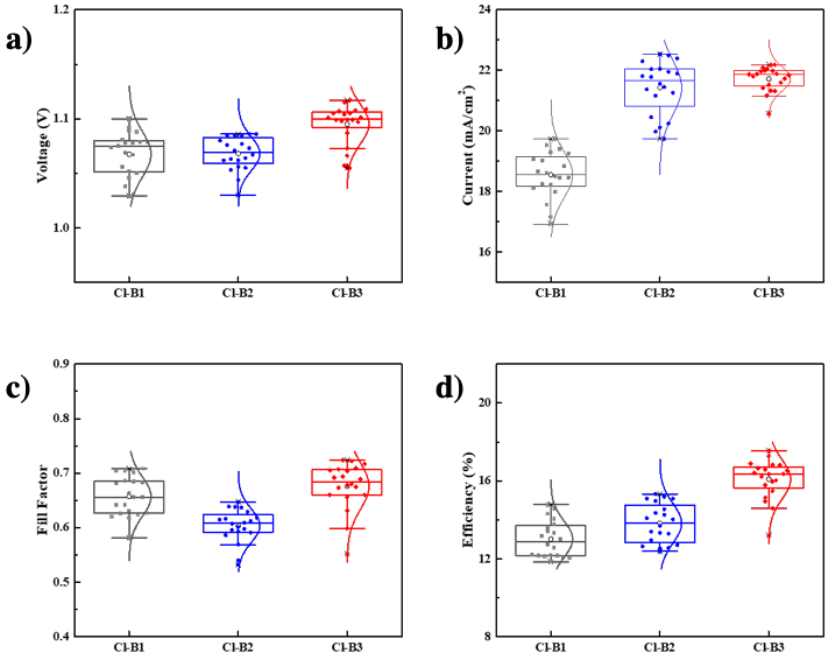

Figure 2.11 Metrics statistics of the photovoltaics parameters obtained from 20 PSCs based on CI-B1, CI-B2 and CI-B3 HTMs. a) open-circuit voltage, b) short-circuit current density, c) fill factor, and d) power conversion efficiency.

As summarized in Table 2.2, devices containing CI-B1, yielded a moderate photovoltaic performance of 14.78%, with an open circuit voltage (V_{OC}) of 1.08 V, short circuit current density (J_{SC}) of 19.4 mA cm^{-2}, and fill factor (*FF*) of 0.705. Note that CI-B1 organizes in a very random-type orientation, promoting the presence of numerous film inhomogeneities and pin-holes. Similarly, devices containing CI-B2 exhibit PCE values of 15.33% with V_{OC} of 1.09 V, J_{SC} of 21.8 mA cm^{-2}, *FF* of 0.647. Such remarkable improvement in device efficiency is mainly the consequence of an enhanced J_{SC} achieved for CI-B2, plausibly attributed to its better ability to organize in a preferred crystal orientation. Importantly, the edge-on surface organization observed for CI-B3 allows an impressive improvement in photovoltaic performance towards 17.54%, leading to V_{OC} values of 1.11 V, J_{SC} of 22.0 mA cm^{-2}, and enhanced *FF* of 0.722. Note that this device efficiency is competitive with the heavily doped spiro-OMeTAD-based device, which reached 18.02% under the comparable conditions. In addition, the reason for the improved V_{OC} observed for CI-B3 molecule could be due to its deeper HOMO level, in contrast to devices containing CI-B2 or spiro-OMeTAD. This is further supported by the faster PL decay observed for CI-B3 compared to CI-B2, which suggests a more efficient charge extraction at the perovskite/HTM interface, also facilitated by a better

film homogeneity and surface morphology. All these advantages, together with its improved hole mobility, might promote CI-B3 towards higher J_{SC} and FF values compared to CI-B1 and CI-B2.[60,129] As a remark, CI-B solar devices also presented small hysteresis between the forward and reverse *J–V* curves at 0.01 V s^{-1} scan speed (Figure 2.12).

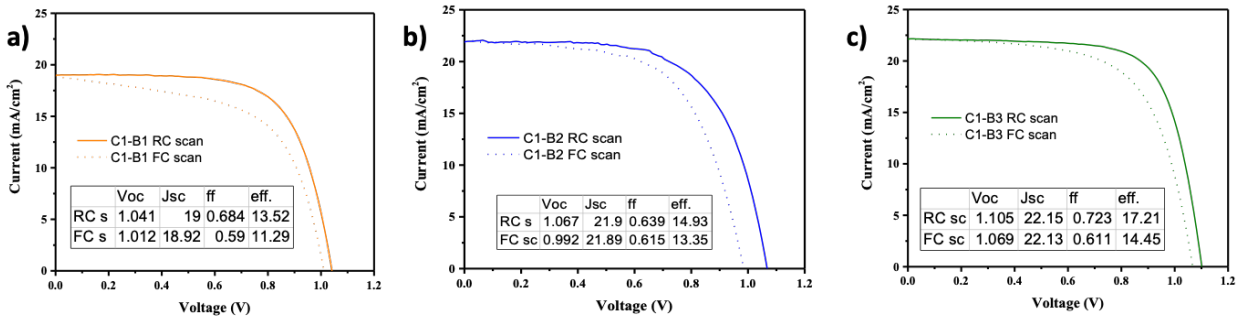

Figure 2.12 The photovoltaic performance of the devices based on a) CI-B1, b) CI-B2 and c) CI-B3 under AM 1.5G illumination (100 mW cm^{-2}). The active area of devices is 0.16 cm^2. The curves were recorded scanning at 0.01 V s^{-1} from forward bias to short circuit condition and *vice versa.*

ID	J_{SC} *(mA/cm²)*	V_{OC} (V)	*FF*	*PCE (%)*
CI-B1	19.4	1.081	0.705	14.78
CI-B2	21.8	1.086	0.647	15.33
CI-B3	22.0	1.107	0.722	17.54
Spiro-OmeTAD	22.7	1.079	0.736	18.02

Table 2.2 Photovoltaic performance of the devices based on CI-B1, CI-B2, CI-B3 and spiro-OMeTAD with dopants under AM1.5G illumination (100 mW cm^{-2}).

We further investigated the series resistance (R_S) and shunt resistance (R_{SH}) exhibited by the PSCs with dopant-free HTMs by estimating the slope of the *J–V* curves near V_{OC} and J_{SC}, respectively (Table 2.3). The CI-B2-based device showed the highest R_S (9.3 Ω cm^2) and lowest R_{SH} (560.1 Ω cm^2), whereas CI-B3-based device had lowest R_S (5.9 Ω cm^2) and highest R_{SH} (864.2 Ω cm^2) values. Significant reduction of *FF* for solar cells based on CI-B2 can therefore be attributed to the relatively higher R_S and lower R_{SH}. Besides, the better performance of CI-B3 based device may be rationalized in terms of the increased *FF* value through a lower R_S and a higher R_{SH}.[130,131]

HTM	CI-B1	CI-B2	CI-B3
R_S (ohm.cm^2)	6.6	9.3	5.9
R_{SH} (ohm.cm^2)	719.4	560.1	864.2

Table 2.3 R_S and R_{SH} values for PSCs based on CI-B HTMs.

The incident photon-to-current efficiency (IPCE) spectra of the best performing PSCs are also shown in Figure 2.10b which exhibits a consistent trend with the characteristic *J–V* curve. The integrated current density (J_{int}), calculated from the integration of the IPCE spectrum for CI-B1, CI-B2, CI-B3 and spiro-OMeTAD with dopants, respectively, agrees with the value obtained from the *J–V* curve, within 5% deviation. Interestingly, CI-B3 based PSCs demonstrated high photon-to-electron conversion over 85% ranging from 400 to 750 nm. Such a behaviour, and the overall improved photovoltaic parameters observed for CI-B3, is therefore ascribed to the combination of enhanced hole mobility, better film morphology, deeper HOMO level and well-order π–π stacking.

Finally, we also examined the long-term stability of perovskite devices containing the new CI-B series and compared it with spiro-OMeTAD with dopants. The tests, conducted at maximum power point (MPP) tracking, were performed without encapsulation, in argon ambient under a constant light illumination of 100 mW cm^{-2}. Current-voltage curves were recorded every 3 h for 42 days (Figure 2.10c). As seen from the results, the performance of cells containing spiro-OMeTAD with dopants decreased dramatically within the first 10h. This effect, previously related with the migration and intercalation of dopants through the device interlayers, results in a maximum power output drop of 30%.[132,133] Such a rapid drop, which remained lost during the next 1000 h of operation, is in contrast with the behaviour observed for the dopant-free CI-B devices. As presented in the Figure 2.10c, in all cases dopant-free CI-Bs began to regain its maximum efficiency 7-hour after the first PCE drop, showing a considerable enhancement of device performance during the first hours of operation. Such effect is mainly attributed to an improvement in *FF* and the V_{OC} during light soaking.[134,135] In addition, CI-B molecules contain nine alkyl chains providing high hydrophobicity to the system, which may additionally act as a good barrier to slow down perovskite degradation.[136,137] The best among the series CI-B3 showed the excellent stability, maintaining 88% of its original PCE after 1000 h of device operation, thus combining both high performance and stability in a single material.

2.3 Conclusion

In summary, we have reported three D-π-A type triazatruxene-core based new organic hole transporting materials, namely CI-B1, CI-B2 and CI-B3, which are obtained by simple synthesis from inexpensive starting materials. Our results demonstrate that using different strong electron acceptors, the morphology and molecular packing of the HTM layer can be strongly modified, which has strong consequences in the carrier transport and charge recombination at the interface, avoiding the need of incorporating instable chemical dopants. Among them, dopant-free CI-B3, which contains dicyanovinyl-substituted rhodanine, exhibited a remarkable PCE of 17.54%, on par with doped spiro-OMeTAD (18.02%), resulting in a more efficient and stable material. According to GIWAXS results, such improved performance is achieved thanks to the formation of a well-ordered edge-on aggregates of π-π stacking, which are induced by the specific nature of the acceptor. Interestingly, the devices containing CI-B3 exhibited excellent long-term stability under MMP tracking, maintaining 88% of its original PCE after 1000 h of illumination. This contrasts with the behaviour of devices containing spiro-OMeTAD with dopants, which dropped rapidly to 70% of the initial value. These results emphasize the versatility of organic small molecules as dopant-free HTMs, providing a prospect for future material design towards efficient and highly stable transporting layers.

2.4 Synthetic methods and Procedures

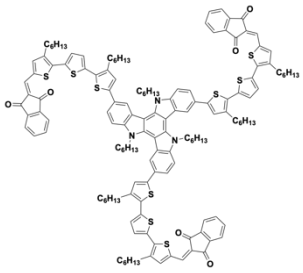

2,2',2''-(((5,10,15-trihexyl-10,15-dihydro-5*H*-diindolo[3,2-*a*:3',2'-*c*]carbazole-3,8,13-triyl)tris(3,3''-dihexyl-[2,2':5',2''-terthiophene]-5'',5-diyl))tris(methaneylylidene))tris(1*H*-indene-1,3(2*H*)-dione) (CI-B1). 5'',5''''',5'''''''-(5,10,15-trihexyl-10,15-dihydro-5*H*-diindolo[3,2-*a*:3',2'-*c*]carbazole-3,8,13-triyl)tris(3,3''-dihexyl-[2,2':5',2''-terthiophene]-5-carbaldehyde) (4) (0.5 g, 0.26 mmol, 1eq.) and commercially available 1*H*-indene-1,3(2*H*)-dione (0.38 g, 2.60 mmol, 10 eq.) were dissolved in chloroform (50 mL) and a few drops of triethylamine base were added. The reaction mixture was stirred overnight at reflux temperature. The reaction was quenched with water and was acidified with few drops of conc. HCl. The organic layer was extracted with DCM, dried over anhydrous magnesium sulfate, filtered and concentrated under reduced pressure. The resulting residue was purified by column chromatography on silica gel (2% ethanol in chloroform) to yield dark red solid. Yield 0.30 g (50%). Due to low solubility with intermolecular aggregation and strong π- π interaction, ^{1}H and ^{13}C NMR spectra could not be obtained. $C_{144}H_{153}N_3O_6S_9[M^+]$ Exact Mass = 2307.9246, MS (ESI-QTOF) = 2307.926. Elemental analysis calcd (%) for $C_{144}H_{153}N_3O_6S_9$: C, 74.86; H, 6.67; N, 1.82. Found: C, 74.84; H, 6.55; N, 1.83.

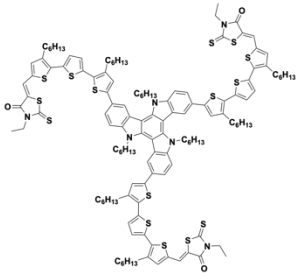

(5*Z*,5'*Z*,5''*Z*)-5,5',5''-(((5,10,15-trihexyl-10,15-dihydro-5*H*-diindolo[3,2-*a*:3',2'-*c*]carbazole-3,8,13-triyl)tris(3,3''-dihexyl-[2,2':5',2''-terthiophene]-5'',5-diyl))tris(methaneylylidene))tris(3-ethyl-2-thioxothiazolidin-4-one) (CI-B2). Aldehyde compound (4) (0.5 g, 0.26 mmol, 1eq.) and commercially available 3-ethyl-2-thioxothiazolidin-4-one (0.42 g, 2.60 mmol, 10 eq.) were dissolved in chloroform (50 mL) and a few drops of Et_3N base were added. The reaction mixture was stirred overnight at reflux temperature. The reaction was quenched with water and was acidified with few drops of conc. HCl. The organic layer was extracted with DCM, dried over anhydrous magnesium sulfate, filtered and concentrated under reduced pressure. The resulting residue was purified by column chromatography on silica gel (2% ethanol in chloroform) to yield dark red solid. Yield 0.29 g (48%). Due to low solubility with intermolecular aggregation and strong π- π interaction, ^{1}H and ^{13}C NMR spectra could not be obtained. $C_{132}H_{156}N_6O_3S_{15}[M^+]$ Exact Mass = 2352.8049, MS (ESI-QTOF) = 2352.814. Elemental analysis calcd (%) for $C_{132}H_{156}N_6O_3S_{15}$: C, 67.30; H, 6.67; N, 3.57. Found: C, 67.03; H, 6.48; N, 3.42.

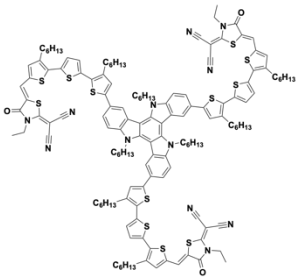

2,2',2''-((5*Z*,5'*Z*,5''*Z*)-(((5,10,15-trihexyl-10,15-dihydro-5*H*-diindolo[3,2-*a*:3',2'-*c*]carbazole-3,8,13-triyl)tris(3,3''-dihexyl-[2,2':5',2''-terthiophene]-5'',5-diyl))tris(methaneylylidene))tris(3-ethyl-4-oxothiazolidine-5,2-diylidene))trimalononitrile (CI-B3). Compound (4) (0.5 g, 0.26 mmol, 1eq.) and 2-(3-ethyl-4-oxothiazolidin-2-ylidene)malononitrile (5) (0.5 g, 2.60 mmol, 10 eq.) were dissolved in chloroform (50 mL) and a few drops of piperidine were added. The reaction mixture was stirred overnight at reflux temperature. The reaction was quenched with water and was acidified with few drops of conc. HCl. The organic layer was extracted with DCM, dried over anhydrous magnesium sulfate, filtered and concentrated under reduced pressure. The resulting residue was purified by column chromatography on silica gel (2% ethanol in chloroform) to yield dark red solid. Yield 0.33 g (52%). Due to low solubility with intermolecular aggregation and strong π- π interaction, ^{1}H and ^{13}C NMR spectra could not be obtained. $C_{141}H_{156}N_{12}O_3S_{12}[M^+]$ Exact Mass = 2448.9072, MS (ESI-QTOF) = 2448.907. Elemental analysis calcd (%) for $C_{141}H_{156}N_{12}O_3S_{12}$: C, 69.08; H, 6.41; N, 6.86. Found: C, 69.03; H, 6.20; N, 6.71.

Chapter 3 Dopant-free Hole Transport Materials Afford Efficient and Stable Inorganic Perovskite Solar Cells and Modules

Inorganic perovskites especially for triiodides are quite sensitive to the moisture, due to their undesirable Goldschmidt tolerance factor. Such inferior stability could be improved by doping, surface energy tuning, additive engineering, and interfacial passivation, while the implementation of these strategies is limited due to the potential impact on device performance. Within this context, the construction of an efficient water proofer is a key issue for enhancing the stability of inorganic perovskite photovoltaics and promoting their large-scale application. The emerging $CsPbI_3$ perovskites are highly efficient and thermally stable materials for wide-bandgap perovskite solar cells (PSCs), but the doped hole transport materials (HTMs) accelerate the undesirable phase transition of $CsPbI_3$ in ambient. The donor – π-bridge – acceptor (D–π–A) design for small organic molecules stands out with a planar nitrogen-containing triazatruxene (TAT) core with alkyl chains was employed as the donor (D) due to its, excellent charge transporting ability and strong π-π stacking ability. Alkylated terthiophene conjugated arm 3,3''-dihexyl-2,2':5',2''-terthiophene was integrated as π-bridge module of the new molecule to increase hole-mobility properties by increased conjugation length. A strong Lewis base electron-withdrawing acceptor (A) unit, 2-(5,6-difluoro-3-oxo-2,3-dihydro-1*H*-inden-1-ylidene)malononitrile (IN-2F) was armed. Herein, a dopant-free D-π-A type HTM named CI-TTIN-2F has been developed which overcomes the stability problem. The suitable optoelectronic properties and energy-level alignment endow CI-TTIN-2F with excellent charge collection properties. Moreover, CI-TTIN-2F provides multisite defect-healing effects on the defective sites of $CsPbI_3$ surface. Inorganic $CsPbI_3$ PSCs with CI-TTIN-2F HTM feature high efficiencies up to 15.9%, along with 86% efficiency retention after 1000 h under ambient conditions. Inorganic perovskite solar modules were also fabricated that exhibiting an efficiency of 11.0% with a record area of 27 cm^2. The PCE of the module is among the highest PCEs for $CsPbI_3$ solar modules. This work confirms that using efficient dopant-free HTMs is an attractive strategy to stabilize inorganic PSCs for their future scale-up.

This chapter is based on published work: C. Liu, C. Igci, Y. Yang, O. A. Syzgantseva, M. A. Syzgantseva, K. Rakstys, H. Kanda, N. Shibayama, B. Ding, X. Zhang, V. Jankauskas, Y. Ding, S. Dai, P. J. Dyson, M. K. Nazeeruddin, Angew. Chem. Int. Ed. 2021, 60, 20489. doi.org/10.1002/anie.202107774.

Authors: Cheng Liu, Cansu Igci, Yi Yang, Dr. Olga A. Syzgantseva, Dr. Maria A. Syzgantseva, Dr. Kasparas Rakstys, Dr. Hiroyuki Kanda, Prof. Naoyuki Shibayama, Dr. Bin Ding, Xianfu Zhang, Dr. Vygintas Jankauskas, Dr. Yong Ding, Prof. Songyuan Dai, Prof. Paul J. Dyson, Prof. Mohammad Khaja Nazeeruddin. In this work I contributed equally with Cheng Liu and Yi Yang as first author, we conceptualized the idea and designed the experiments. Specifically, I performed the synthesis and characterization all organic materials, and the data analysis.

3.1 Introduction

Inorganic perovskites especially for triiodides are quite sensitive to the moisture. Several strategies were reported to address stability issue of all-inorganic perovskites including surface energy tuning, additive engineering, and interfacial passivation.[24,27,28,138] However, the implementation of these strategies for improving stability is limited due to the potential impact on device performance. For instance, the amount of the additive is normally low in order to maintain crystallinity and charge mobility of the perovskite film.[139] Similarly, the thickness of the surface passivation layer must be a few nanometers to maintain charge extraction from the active layers to the charge transport layers.[140] For these reasons, highly hydrophobic hole transport materials (HTMs) have received attention, as they have the potential to block the moisture-driven phase transition of black phase $CsPbI_3$.[141]

At present, state-of-the-art $CsPbI_3$ PSCs still use 2,2′,7,7′-tetrakis(*N*,*N*-di-*p*-methoxyphenyl-amino)-9,9′-spi-robifluorene (spiro-OMeTAD) doped with lithium bis(trifluoromethane)sulfonamide (LiTFSI), cobalt complex and 4-*tert*-butyl pyridine (TBP) additives as the HTM.[38,39] However, we observed very fast phase transitions in the black phase $CsPbI_3$ films covered with standard doped spiro-OMeTAD layers, with these transitions being even faster than that of bare $CsPbI_3$ films under the same conditions. Hence, the hygroscopic nature of the dopants eliminates the advantage of the hydrophobicity of the upper hole transport layers and significantly accelerates the phase transition of $CsPbI_3$ leading to device degradation.[142,143] Therefore, developing dopant-free, efficient, and stable HTMs is highly desirable and could lead to practical applications of inorganic perovskites in PSCs.

Herein, we described the design and synthesis of a dopant-free D-π-A type HTM, namely CI-TTIN-2F, employing a triazatruxene (TAT) as the electron-rich donor, alkylated terthiophene as π-bridges, and a fluorinated electron-deficient acceptor (Figure 3.1). Benefiting from intramolecular charge transfer (ICT) and strong dipolar intermolecular interactions, CI-TTIN-2F shows excellent optoelectronic properties, ideal energy-level alignment, and good charge collection properties. In addition, joint experimental and theoretical studies suggest that CI-TTIN-2F provides multisite defect-healing effects on the surface of the $CsPbI_3$ films due to the presence of various heteroatoms (N, O, S, F) in the HTM structure, which effectively reduces the trap densities and charge recombination at the interface. As a dopant-free HTM for the all-inorganic $CsPbI_3$ PSCs, CI-TTIN-2F impressively delivers high PCEs of 15.9% on small-area cells and 11.0% on modules with a record area of 27 cm^2. Furthermore, the device employing CI-TTIN-2F maintains over 86% of its initial performance for 1000 h after storage in ambient conditions.

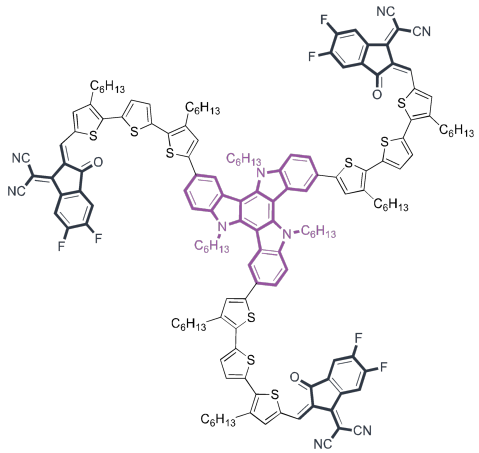

Figure 3.1 Chemical structure of the CI-TTIN-2F molecule.

3.2 Result and Discussion

3.2.1 Design and Synthesis of CI-TTIN-2F HTM

A planar nitrogen-containing triazatruxene (TAT) core with alkyl chains was employed as the donor (D) due to its excellent charge transporting and strong π-π stacking ability.[52] The alkylated terthiophene conjugated arms, 3,3''-dihexyl-2,2':5',2''-terthiophene, were modulated as π-bridge to increase hole-mobility properties of the molecule by increasing the double-bond character.[68] A strong Lewis base electron-withdrawing acceptor (A) unit, 2-(5,6-difluoro-3-oxo-2,3-dihydro-1*H*-inden-1-ylidene)malononitrile (IN-2F), was selected based on D-π-A type architecture to decrease the LUMO levels without causing strong steric hindrance, enhance inter/intramolecular non-covalent interactions, and increase hydrophobicity leading to a long-term stability. Synthesis of the intermediate 5'',5'''',5'''''''-(5,10,15-trihexyl-10,15-dihydro-5*H*-diindolo[3,2-*a*:3',2'-*c*]carbazole-3,8,13-triyl)tris(3,3''-dihexyl-[2,2':5',2''-terthiophene]-5-carbaldehyde) compound 4 was accomplished starting from commercially available and inexpensive precursor 2-indolinone according to the reported method with a small modification (Scheme 3.1).[68] The designed acceptor unit was synthesized from commercially available 5,6-Difluoro-2-benzofuran-1,3-dione as previously described in the literature.[144] It reduced in the presence of tert-butyl acetoacetate and triethyl amine at room temperature to difluorinated indanedione. Then, it followed by dicyanovinylene moiety incorporation in one of the carbonyl with sodium acetate under reflux to get 2-(5,6-difluoro-3-oxo-2,3-dihydro-1*H*-inden-1-ylidene)malononitrile (Scheme 3.2). The final product was synthesized by condensing the obtained aldehyde (4) and the acceptor in the presence of pyridine under Knoevenagel reaction conditions (Scheme 3.3). Moreover, CI-TTIN-2F is soluble in tetrachloroethane, and reasonably soluble in tetrahydrofuran and dichloromethane, allowing solution processing. The expected structure of CI-TTIN-2F was confirmed by MALDI-TOF mass spectrometry and elemental analysis (Appendix B).

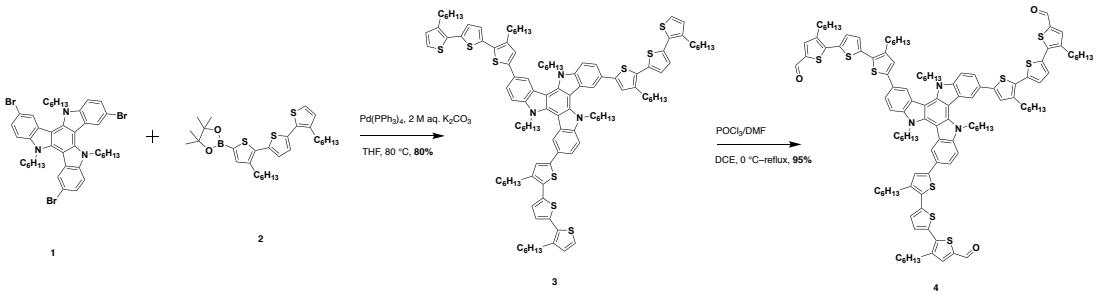

Scheme 3.1 Synthetic route of 5'',5'''',5'''''''-(5,10,15-trihexyl-10,15-dihydro-5H-diindolo[3,2-a:3',2'-c]carbazole-3,8,13-triyl)tris(3,3''-dihexyl-[2,2':5',2''-terthiophene]-5-carbaldehyde).

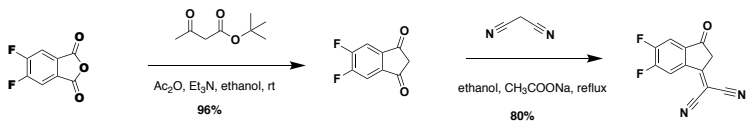

Scheme 3.2 Synthetic route of 2-(5,6-difluoro-3-oxo-2,3-dihydro-1*H*-inden-1-ylidene)malononitrile.

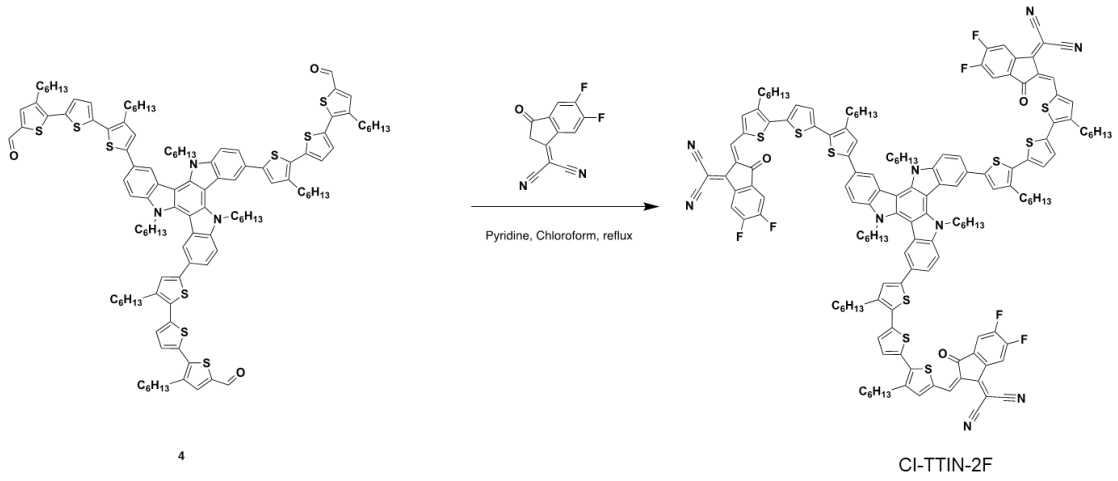

Scheme 3.3 Synthetic routes of CI-TTIN-2F.

3.2.2 Thermal, Optical, and Electrochemical Properties

To evaluate the thermal properties of CI-TTIN-2F thermogravimetric analysis (TGA) was carried out under a nitrogen atmosphere (Figure 3.2a). The decomposition temperature (T_{dec}) corresponding to a weight loss of 5% occurs above 300 °C, indicating that CI-TTIN-2F has sufficient thermal stability for application as an HTM in PSCs. The optical properties of CI-TTIN-2F were investigated by ultraviolet-visible (UV-Vis) spectroscopy in the solid state and in tetrachloroethane solution (Figure 3.2b). The UV-vis spectra of the CI-TTIN-2F film and solution show multimodal absorption (Figure 3.2c). Absorption bands were observed between 350 and 500 nm, which may be attributed to the localized aromatic π-π* transition of the D-π-A structure. More importantly, an additional NIR absorption peak centred at around 660 nm indicates ultra-strong intermolecular charge transfer from the TAT electron-donating unit to the IN-2F electron-withdrawing group. Note that the position of the ICT band is slightly red-shifted as the solution transitions to the solid-state, which is characteristic of many organic semiconductors.[8] The optical energy bandgap (*E*g) estimated from the onset of the absorption peak is determined to be 1.52 eV for CI-TTIN-2F, which would increase the intrinsic carrier concentration through the thermal population in the conduction band (experimental details in Appendix B).

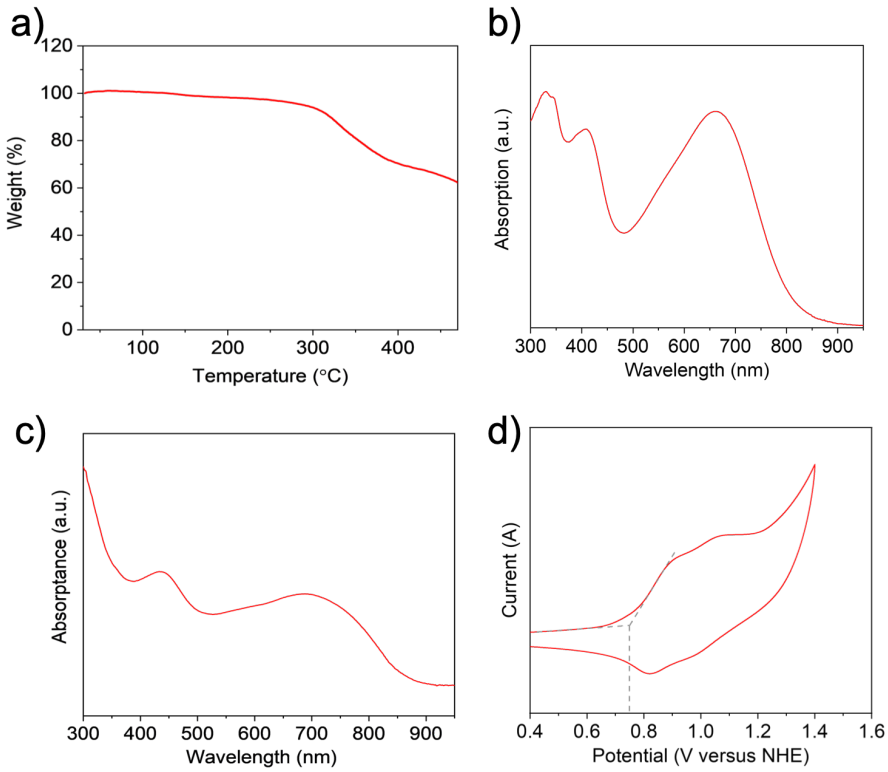

Figure 3.2 a) TGA curves of CI-TTIN-2F under nitrogen atmosphere with a heating rate of 20°C/min. b) UV-vis absorption spectra of CI-TTIN-2F in dilute tetrachloroethane solution. c) . UV-Vis absorption spectra of CI-TTIN-2F thin films. d) Cyclic voltammograms of the CI-TTIN-2F HTMs measured in 0.1 M n-Bu4NPF6 solution in tetrahydrofuran.

To investigate HOMO energy level (E_{HOMO}) of CI-TTIN-2F, electrochemical cyclic voltammetry (CV) was first performed with a standard three-electrode configuration (Figure 3.2d). The material was tested in tetrahydrofuran containing 0.1 M *n*-Bu_4NPF_6 as a supporting electrolyte, and the oxidation potential was calibrated against an internal ferrocene standard. The E_{HOMO} value was calculated as -5.37 eV vs. vacuum for CI-TTIN-2F. The HOMO level is well aligned with the valence band energy level of the $CsPbI_3$ inorganic perovskite so that the photogenerated charge carriers should be efficiently transferred at the interface.[145] The lowest unoccupied molecular orbital (LUMO) energy levels were calculated to be -3.85 eV by subtracting the optical bandgap and HOMO energy level. These results are consistent with the trend estimated from density functional theory (DFT) calculations (Table 3.1).

	HOMO	LUMO
PBE-D3	-4.60	-3.58
PBE0@PBE-D3	-5.23	-3.29
PBE0	-5.23	-3.22

Table 3.1. Energy levels (in eV) of CI-TTIN-2F, computed with different density functionals.

3.2.3 Intrinsic Properties of CI-TTIN-2F

The localization and energies of frontier molecular levels of CI-TTIN-2F have been assessed using density functional theory calculations, employing various functionals, including Perdew-Burke-Ernzerhof (PBE) density functional with Grimme's D3 dispersion cor-

rection and hybrid PBE0 density functionals (experimental details in Appendix B). The molecular structures were optimized by using PBE-D3 density functional. The localization and energies of the frontier molecular levels of CI-TTIN-2F for the HOMO are delocalized primarily in the TAT core and spread along the entire molecule, while LUMO are localized in the acceptor moiety and π-bridge of the HTM (Figure 3.3a). Figure 3.3b shows the schematic of the energy band diagram. The energy bands of the $CsPbI_3$ perovskite were characterized by ultraviolet photoelectron spectroscopy (UPS) and UV-vis spectroscopy. The energy level alignment implies that the fluorinated IN-2F acceptor unit with stronger electron-withdrawing properties endows CI-TTIN-2F with much deeper HOMO energy levels by 0.40 eV compared to spiro-OMeTAD. The lower HOMO of CI-TTIN-2F is expected to ensure more efficient interfacial hole-transport kinetics and improve the open-circuit voltage (V_{OC}) for $CsPbI_3$ PSCs.[146]

The space-charge limited current (SCLC) measurements were carried out on the hole-only devices to evaluate the charge transport properties of CI-TTIN-2F, and the hole mobilities were extracted following the Mott-Gurney Law (Figure 3.3c). Encouragingly, with the D-π-A molecular structure, CI-TTIN-2F exhibits high hole mobility of 3.7×10^{-4} $cm^2 \cdot V^{-1} \cdot s^{-1}$, significantly higher than that of spiro-OMeTAD (6.1×10^{-5} $cm^2 \cdot V^{-1} \cdot s^{-1}$), attributed to the higher degree of conjugation and better intermolecular interactions.[67] Grazing incidence wide-angle X-ray scattering (GIWAXS) was performed to investigate the molecular organization in the HTM film (Figure 3.3d). The pole plots of the azimuth angle integrated around q_z = 3.5 $Å^{-1}$ (Figure 3.3e) indicate that CI-TTIN-2F possess multiple orientations in the films. Besides the face-on orientation, CI-TTIN-2F exhibits edge-on stacking that favor charge transport.[147]

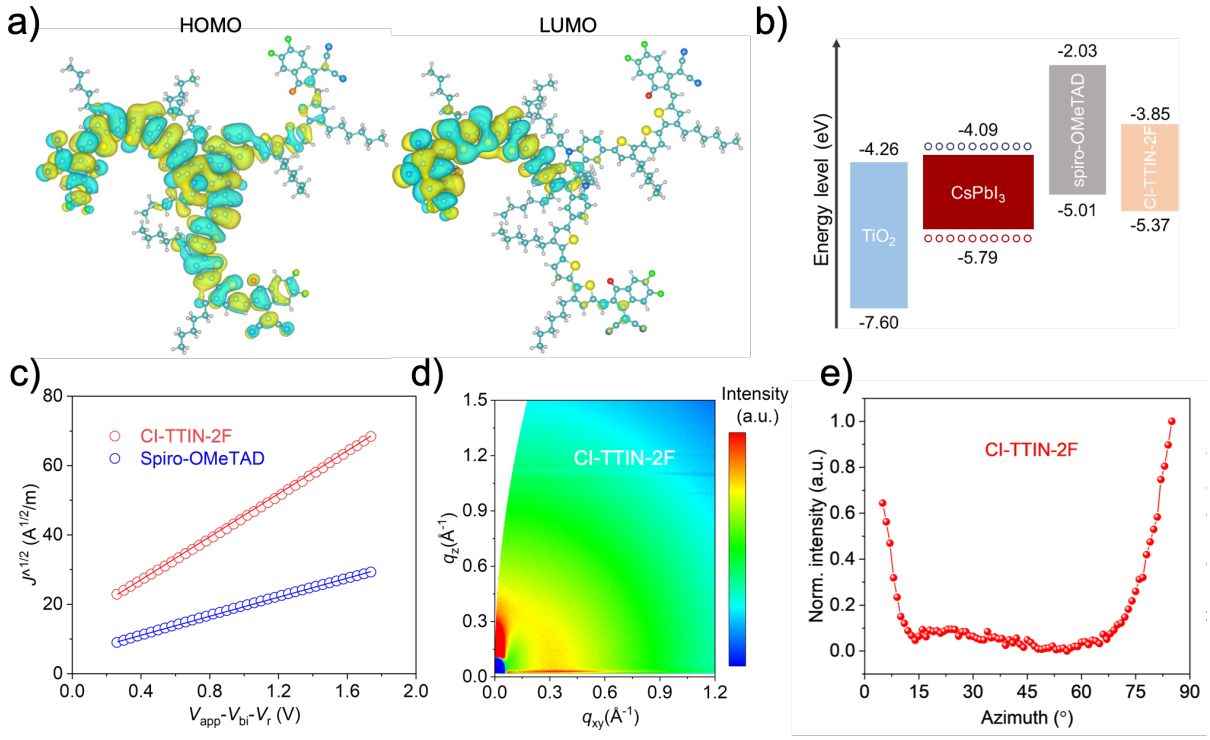

Figure 3.3 a) Spatial distribution of HOMO and LUMO orbitals in CI-TTIN-2F. C, O, N, H, F and S atoms are colored in cyan, red, blue, white, green and yellow, respectively. b) Molecular energy level alignments. c) The hole injection characteristics measured by the SCLC method of dopant-free HTMs. d) 2D GIWAXS patterns of pristine hole CI-TTIN-2F HTM. e) The pole plots of the azimuth angle integrated around q_z = 3.5 $Å^{-1}$ of CI-TTIN-2F.

3.2.4 Characterization of Perovskite/HTM Interfaces

To investigate the potential interactions occurring between the CI-TTIN-2F HTM and the perovskite surface, Born Oppenheimer molecular dynamics (MD) calculations of CI-TTIN-2F deposited on top of a slab of tetragonal β-$CsPbI_3$ perovskite were performed and the 0 ps and 4 ps of the simulation was shown in Figure 3.4 (experimental details in Appendix B). The MD simulations show that CI-TTIN-2F can form Pb contacts of different types with the perovskite surface, specifically: i) The CN groups of the acceptor units interact with the Pb^{2+} cations of the surface, in particular forming relatively short Pb···N contacts of 2.8-3.0 Å (Figure 3.5a), evidencing strong coordination interactions. ii) The F atoms of the acceptor can interact weakly with the surface; however, average Pb-F distances are longer to be > 4 Å (Figure 3.5b). This is partially due to the face-on configuration of CI-TTIN-2F CN groups within 2FIN which coordinate with the perovskite surface, as malononitrile unit can rotate. Consequently, coordination of the CN group with the surface rotates the conjugated 5,6-difluoro-3-oxo-2,3-dihydro-1*H*-inden-1-ylidene moiety having a quasi-planar geometry (Figures 3.4), lifting the F atoms and thus elongating the Pb-F distances. However, the weak Pb-F contacts (Figure 3.5c) contribute to more intimate interactions between the HTM and the perovskite surface. iii) The lone pairs of electrons on sulfur atoms of the π-bridges interact with the Pb^{2+} cations of the surface, which are similar to previously reported oligothiophene HTMs.[148] The Pb-S distances around 3.7 Å are below the sum of van der Waals radii of Pb and S, evidencing coordination interactions. iv) The average Pb-O distances in the stabilized molecular conformation are about 3.0-3.5 Å, which is below or close to the sum of van-der-Waals radii of the interacting atoms. The average distances of the shortest contacts I-X (X = O, N, S, F) are longer, being about 4 Å. In the face-on configuration the hexyl units also tend to orient along the perovskite surface, which allows the site-specific non-covalent Pb-X interactions to be maximized, since the corresponding parts of HTM can sufficiently approach the surface. Some hexyl units are unable to orient parallel to the surface due to the steric hindrance produced by other parts of CI-TTIN-2F (Figure 3.4), and sometimes the hexyl chains provide steric hindrance.

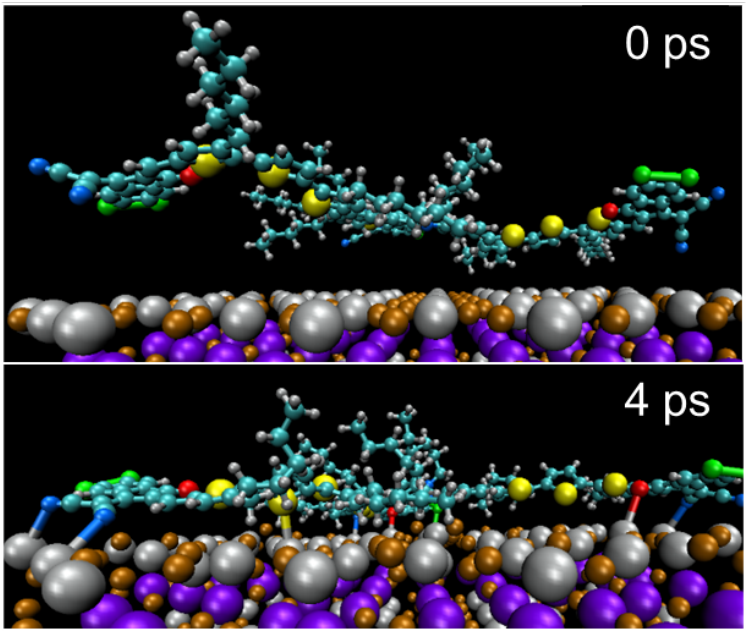

Figure 3.4 Molecular dynamics calculations of the CI-TTIN-2F molecule deposited on top of the slab of $CsPbI_3$ perovskite.

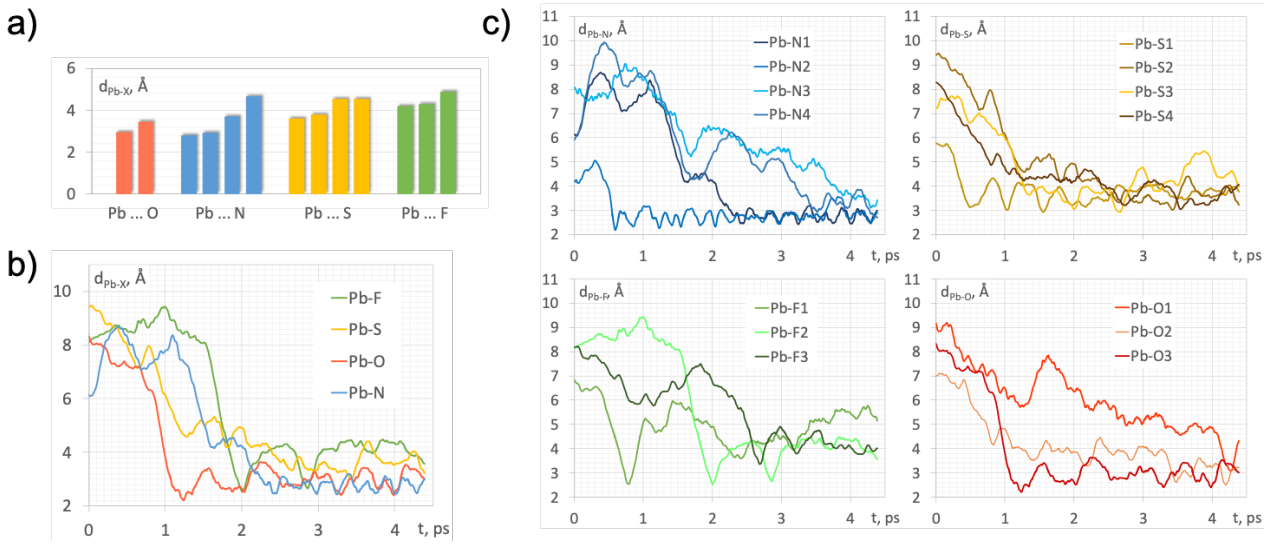

Figure 3.5 a) Average distances Pb-X, where X = O, N, S, F of the HTM deposited on perovskite surface. b) Evolution of distances Pb-X (X = O, N, S, F) during the process of CI-TTIN-2F deposition on top of the perovskite surface: comparison between different contacts. c) Evolution of distances Pb-X (X = O, N, S, F) during the process of CI-TTIN-2F deposition on top of the perovskite surface: several contacts of the same type Pb-Xi.

To elucidate the impact of CI-TTIN-2F on the electronic structure of the interface, a representative snapshot during the MD trajectory was selected to simulate the electronic structure using PBE0 density functional (Figure 3.6). The perovskite surface was represented by PbI_2-terminated slab, in which each Pb^{2+} ion can be considered as unsaturated, representing a defect. In the absence of CI-TTIN-2F on the perovskite surface, Pb-centered trap-like states were observed at the bottom of the conduction band of the perovskite (Figure 3.6a). Interestingly, upon coverage of the perovskite with CI-TTIN-2F, these states disappear, with the contribution of the Pb^{2+} ions being "merged" with the continuous manifold of states at the bottom of the conduction band (Figure 3.6b). Moreover, the empty CI-TTIN-2F-centered states are situated below the conduction band manifold (Figure 3.6c). Consequently, an electron from the bottom of the perovskite conduction band at the interface can migrate on the CI-TTIN-2F instead of recombining with the holes. Moreover, the participation of CI-TTIN-2F orbitals in the formation of the bottom of the conduction band favors electron delocalization over the perovskite/HTM interface, which in turn facilitates electron migration.

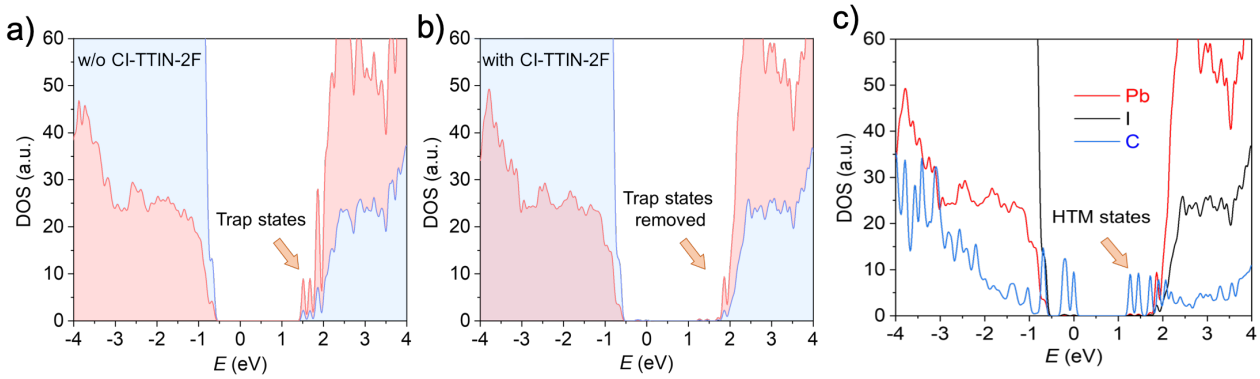

Figure 3.6 Electronic structure of the PbI_2-terminated surface a) without and b) with CI-TTIN-2F HTMs, calculated using PBE0 density functional. c) Electronic structure of the CI-TTIN-2F/perovskite interface, calculated using PBE0 density functional.

Since charge extraction properties are crucial for HTMs, we examined the charge-carrier dynamics in pristine $CsPbI_3$ and $CsPbI_3$/HTM films using steady-state photoluminescence (PL) and time-resolved photoluminescence (TRPL) spectroscopy. The pristine $CsPbI_3$ film exhibits the strongest PL emission centered around 725 nm (Figure 3.7a). Significant quenching was observed in the presence of the HTM, and CI-TTIN-2F has the lowest PL intensity, suggesting rapid hole extraction across the interface and a superior hole extraction ability of CI-TTIN-2F compared to spiro-OMeTAD. TRPL spectroscopy was used to delineate the carrier dynamics quantitatively (Figure 3.7b). The pristine $CsPbI_3$ film shows a longer lifetime (τ_1 = 2.11 ns), which was reduced by the HTM due to the charge extraction. The $CsPbI_3$/CI-TTIN-2F junction presents faster hole transfer (0.69 ns) than the $CsPbI_3$/spiro-OMeTAD interface (0.76 ns), most likely due to the deeper valence band maximum of CI-TTIN-2F and the stronger interfacial interactions between the Pb^{2+} ion on the perovskite surface and 2FIN units of CI-TTIN-2F compared to spiro-OMeTAD.[149]

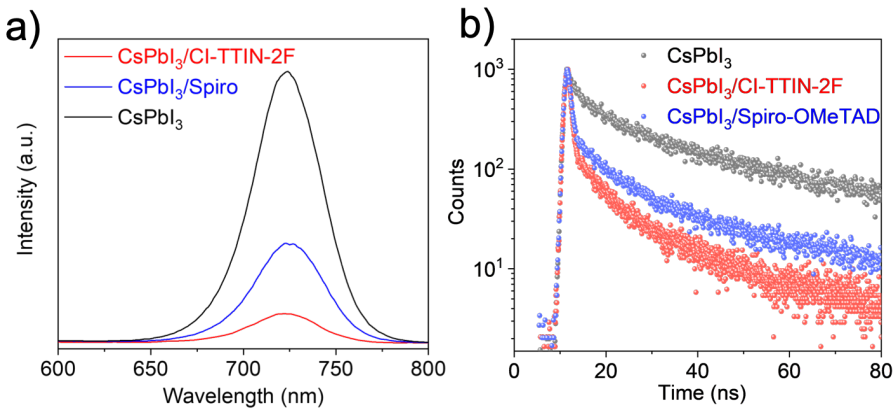

Figure 3.7 a) Steady-state photoluminescence (PL) spectra of $CsPbI_3$ films without and with different HTMs. b) TRPL spectra of $CsPbI_3$ films on glass substrate capping without and with different HTMs.

3.2.5 Device Characteristics

The cross-section SEM image of the complete PSC was shown with an n-i-p structure comprising FTO/TiO_2/$CsPbI_3$/CI-TTIN-2F/Au, in which the thickness of the CI-TTIN-2F hole transport layer (HTL) was optimized at ~50 nm (Figure 3.8a) (experimental details in Appendix B). The best-performing CI-TTIN-2F-based device shows a PCE of 15.91% under reverse scan conditions, with a short-circuit photocurrent density (J_{SC}) of 18.82 mA·cm^{-2}, a V_{OC} of 1.10 V, and a fill factor (*FF*) of 77.50%, and a PCE of 15.29% in forward scan condition, with a J_{SC} of 18.82 mA·cm^{-2}, a V_{OC} of 1.06 V, and an *FF* of 76.90% (Figure 3.8b). The device performance is higher than that of the spiro-OMeTAD-based PSC with an efficiency of 11.44% under reverse scan and 8.68% in forward scan (Figure 3.8c), reflecting the lower-lying HOMO levels as well as the improved hole mobility and extraction for CI-TTIN-2F HTM. The two devices exhibit similar integrated photocurrent values (Figure 3.8d), and the main difference in efficiency derives from the V_{OC} and *FF*. The CI-TTIN-2F-based device demonstrates reduced trap states compared with the spiro-OMeTAD-based device over the whole defect energy region. This reduction derives from the effective surface passivation of CI-TTIN-2F, which is confirmed by the removal of trap states (Figure 3.6). Hence, CI-TTIN-2F gives rise to advantageously accelerated interface charge transfer, diminishes surface defects, and suppresses trap-assisted recombination, which reduces energy loss and thus enhances device performance, especially for V_{OC} and *FF*.

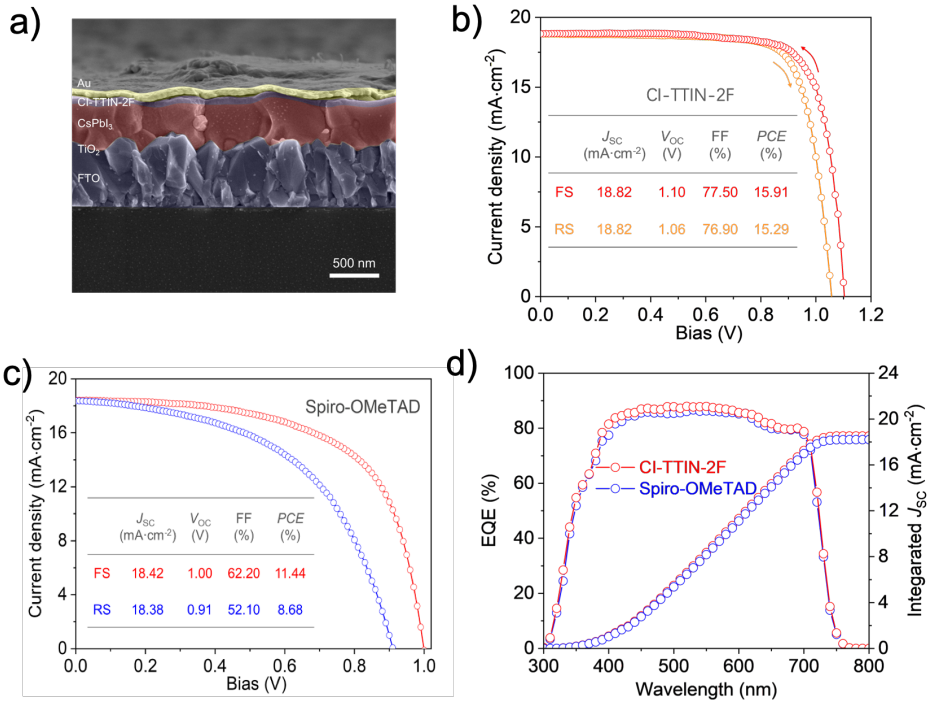

Figure 3.8 a) Cross-section SEM image of the device with CI-TTIN-2F HTMs. b) The *J-V* curves of the CI-TTIN-2F-based champion device. c) **.** *J-V* curves of $CsPbI_3$ PSCs with dopant-free spiro-OMeTAD HTMs. d) EQE of perovskite solar cells with various HTMs.

To demonstrate large-scale application of the CI-TTIN-2F HTM, inorganic $CsPbI_3$ perovskite modules with an active area of 27 cm^2 were fabricated (Figure 3.8a). The modules were patterned by the P1, P2, and P3 laser-scribing method (Figure 3.9b), consisting of nine sub-cells. Notably, the $CsPbI_3$ PSC module achieves a PCE of 10.98% employing the CI-TTIN-2F HTM, with a J_{SC} of 1.96 $mA{\cdot}cm^{-2}$, a V_{OC} of 9.36 V, and an *FF* of 60%. The similar V_{OC} of each sub-cell with a single cell implies the good uniformity of the HTM layer over a large area. The reduced J_{SC} and *FF* can be attributed to the greater series resistance because of the longer carrier transport paths and the device nonuniformities. Moreover, the perovskite solar module with the CI-TTIN-2F HTM shows a steady output PCE of 10.80% under the AM 1.5 G illumination for 250 s, which is consistent with that calculated from *J-V* scanning (Figure 3.10a). The performance of the reported inorganic perovskite modules versus device area are summarized in Figure 3.10b.[150] The efficiency of the CI-TTIN-2F-based module is comparable with that of previous reports while showing the largest module area.

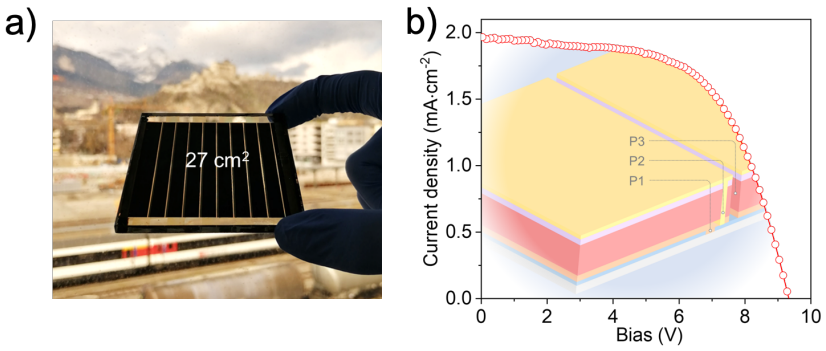

Figure 3.9 a) Photograph of the CI-TTIN-2F-based mini module. b) The *J-V* curve of the best-performing module. The inset is the schematic illustration of the mini-module device structure.

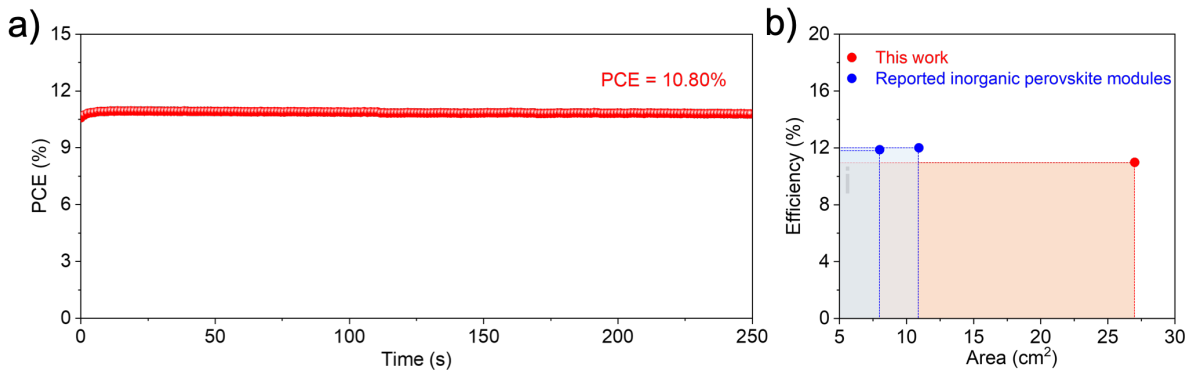

Figure 3.10 a) PCE output at a maximum power point of 6 V for the CI-TTIN-2F-based perovskite solar module. b) PCEs of all-inorganic perovskite modules versus module area from this work and previous reports.

3.2.6 Stability Characteristics

Moisture-induced phase transitions of the perovskite film are a critical degradation path for all-inorganic PSCs. To examine the effects of HTL incorporation on phase stability of perovskite films, we tracked the absorbance evolution of $CsPbI_3$ films under a controlled relative humidity (RH) of ~50% and photographs of the perovskite films stored for different time are shown in Figure 3.11a. Remarkably, the $CsPbI_3$ film covered with doped spiro-OMeTAD is bleached within only 20 min, which is even more rapid than that of the bare $CsPbI_3$ film (100 min). The degradation onset is significantly retarded to 180 min when the hydrophilic dopants were removed from the spiro-OMeTAD HTL composition. Specially, no obvious change in color is observed from the $CsPbI_3$ film with the CI-TTIN-2F HTM after aging for 480 min. To probe surface property of the HTLs, contact angles of water droplets on the $CsPbI_3$/HTLs samples were measured (Figure 3.11b). The CI-TTIN-2F HTL showed a much higher contact angle of ~99° than those of spiro-OMeTAD with (~75°) and without dopants (~88°), and the improved hydrophobicity can be in part attributed to the introduced fluorinated 1,1-dicyanomethylene-3-indanone acceptor units in the D-π-A structure. The stability of unencapsulated $CsPbI_3$ PSCs employing different HTMs was monitored in an ambient atmosphere with a RH of ~20% for 1000 hours. Figure 3.11c presents the normalized PCEs of the devices as a function of storage time and the device performances were periodically measured in ambient air. the ambient stability monitored under ambient conditions reveals that the doped spiro-OMeTAD-based device suffers a sharp drop up to <10% of the initial PCE within only 100 h due to the moisture-sensitive dopants. Furthermore, the dopant-free spiro-OMeTAD-based device retains 66% of the pristine performance after 1000 hours. Encouragingly, the CI-TTIN-2F-based device maintains 86% of its initial PCE after 1000 h exposure. Moreover, we examined the operational stability of the unencapsulated CI-TTIN-2F-based device under a constant one sun illumination (AM1.5G) at 25°C in a nitrogen atmosphere at the maximum power point (Figure 3.11d). The $CsPbI_3$ PSC with CI-TTIN-2F maintains over 80% of the initial PCE under light soaking for 800 h, demonstrating a superior photochemical stability based on this new CI-TTIN-2F HTM.

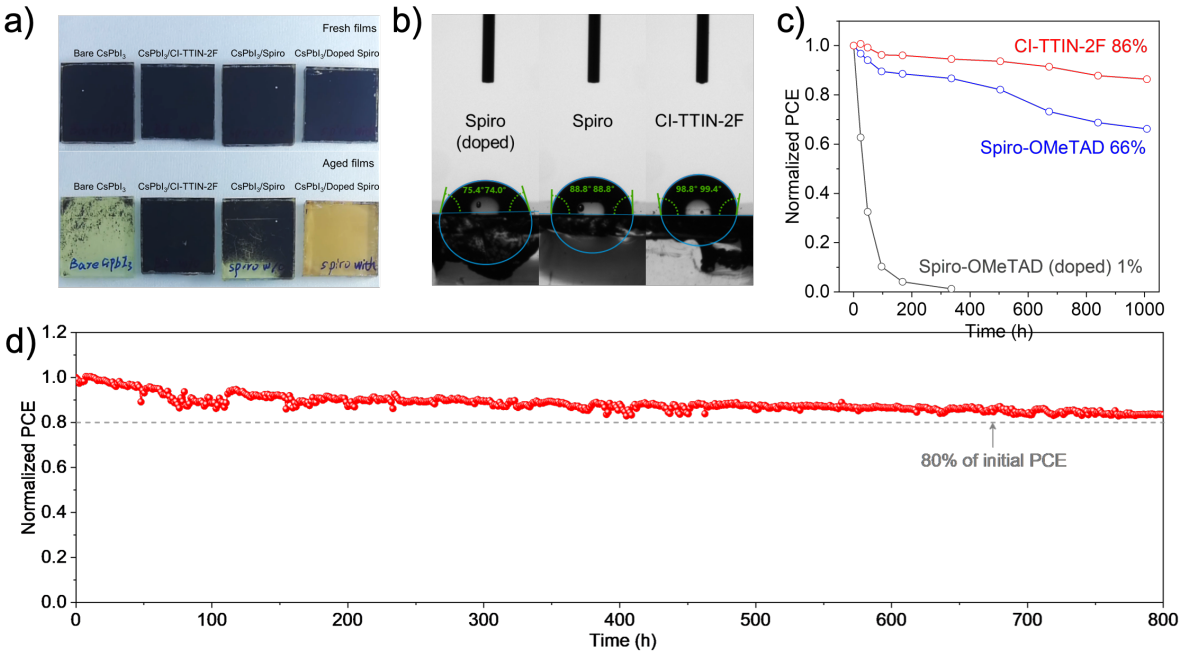

Figure 3.11 a) Photos of the $CsPbI_3$ films with and without different HTMs before and after exposure to RH of ~50% for 480 min. b) Water contact angles of different HTLs on the perovskite layer. c) Stability under ambient (~20% RH) for the unencapsulated $CsPbI_3$ PSCs with different HTMs. d) Operational stability of the $CsPbI_3$ device with CI-TTIN-2F HTMs under a constant one sun illumination at the maximum power point without a UV filter in nitrogen atmosphere.

3.3 Conclusion

We synthesized a new dopant-free HTM named CI-TTIN-2F with a D-π-A molecular configuration. The suitable optoelectronic properties and energy-level alignment endow CI-TTIN-2F with excellent charge collection properties. In addition, joint experimental and theoretical studies suggest that CI-TTIN-2F has the capacity for multisite passivation effects on defective $CsPbI_3$ surfaces due to the presence of various heteroatoms. As a result, all-inorganic $CsPbI_3$ PSCs with dopant-free CI-TTIN-2F HTM demonstrate a high PCE of 15.9%, along with 86% efficiency retention after 1000 hours under ambient conditions. These results indicate an excellent compatibility of CI-TTIN-2F with all-inorganic PSCs. Notably, the largest all-inorganic perovskite solar module was fabricated using the CI-TTIN-2F HTM, and exhibited an efficiency of 11.0% with an area of 27 cm^2. This study provides a new design strategy toward efficient dopant-free HTMs with multisite passivation effects that stabilize all-inorganic PSCs to facilitate future scale-up.

3.4 Synthetic methods and Procedures

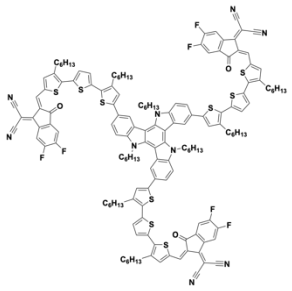

2,2',2''-((2*Z*,2'*Z*,2''*Z*)-(((5,10,15-trihexyl-10,15-dihydro-5H-diindolo[3,2-*a*:3',2'-*c*]carbazole-3,8,13-triyl)tris(3,3''-dihexyl-[2,2':5',2''-terthiophene]-5'',5-diyl))tris(methaneylylidene))tris(5,6-difluoro-3-oxo-2,3-dihydro-1*H*-indene-2,1-diylidene))trimalononitrile (CI-TTIN-2F). Intermediate compound 5'',5'''',5'''''''-(5,10,15-trihexyl-10,15-dihydro-5*H*-diindolo[3,2-*a*:3',2'-*c*]carbazole-3,8,13-triyl)tris(3,3''-dihexyl-[2,2':5',2''-terthiophene]-5-carbaldehyde) (0.25 g, 0.13 mmol, 1eq.) and 2-(5,6-difluoro-3-oxo-2,3-dihydro-1*H*-inden-1-ylidene)malononitrile (0.29 g, 1.30 mmol, 10 eq.) were dissolved in chloroform (30 mL) and a few drops of pyridine base were added. The reaction mixture was stirred overnight at reflux temperature. The reaction was quenched with water and was acidified with few drops of conc. HCl. The organic layer was extracted with chloroform, dried over anhydrous magnesium sulfate, filtered and concentrated under reduced pressure. The resulting residue was purified by column chromatography on silica gel (2% ethanol in chloroform) to yield dark green solid. CI-TTIN-2F was obtained with a good yield (0.18 g, 53%). Due to intermolecular aggregation and strong π- π interaction, ^{1}H and ^{13}C NMR spectra could not be obtained. $C_{153}H_{147}F_6N_9O_3S_9$ [M^+] Exact Mass =2559.90, MS (MALDI-TOF) =2560.274 Elemental analysis calcd (%) for $C_{153}H_{147}F_6N_9O_3S_9$: C, 71.72; H, 5.78; N, 4.92; S, 11.26. Found: C, 70.86; H, 5.28; N, 4.73; S, 10.51.

Chapter 4 Highly Planar Benzodipyrrole-based Hole Transporting Materials with Passivation Effect for Efficient Perovskite Solar Cells

Three benzodipyrrole (BDP)-based organic small molecules with substituted 4-methoxyphenyl (CB-1), 3-fluorophenyl (CB-2), and 3-trifluoromethylphenyl (CB-3) are designed, synthesized, and used as a hole-transporting material (HTM) for perovskite solar cells (PSCs). The electrochemical, optical, thermal, electronic, and optoelectronic properties of the HTMs are characterized to verify their suitability for PSCs. The terminal functional groups of the HTMs having different heteroatoms mainly target effective defect passivation of perovskites. Photoluminescence (PL) studies support the notion that the fluorinated moieties of CB-2 and CB-3 can contribute to the defect passivation via interaction with Pb of the perovskite. This is further strengthened by Molecular dynamic (MD) simulations. The molecular planarity of CB-2 was confirmed by the simulation and the calculation of small dihedral angle between the BDP unit and the 3-fluorophenyl of CB-2. In particular, a highly planar conformation of CB-2 on the perovskite surface can facilitate more efficient hole transfer at the interface and thus facilitate the hole extraction with the help of intermolecular π–π interaction. Thus, the PSCs employing CB-2 achieve the highest power conversion efficiency (PCE) of 18.23% while the devices using CB-1 and CB-3 exhibit a lower PCE of 16.78% and 16.74%, respectively. Furthermore, the molecular hydrophobicity of the fluorinated HTMs enabled the devices to demonstrate excellent long-term storage stability in the air without encapsulation. PSCs with the BDP-based HTMs demonstrate excellent long-term storage stability without degradation in their PCEs over 6 months. The highly planar geometry, defect passivation effect, and hydrophobicity of CB-2 show its great potential as an HTM for efficient and stable PSCs.

This chapter is based on the manuscript under-revision by Solar RRL.

Authors: Cansu Igci, Hiroyuki Kanda, So-Min Yoo, Albertus Adrian Sutanto, Olga A. Syzgantseva, Maria A. Syzgantseva, Vygintas Jankauskas, Kasparas Rakstys, Hobeom Kim, Abdullah M. Asiri, and Mohammad Khaja Nazeeruddin. In this work I contributed as first author. I conceptualized the idea, designed the experiments, synthesized and characterized all organic materials, performed data analysis.

4.1 Introduction

Benzodipyrrole (BDP) is a pyrrole-based heterocyclic small molecule, and there has been interest in the BDP-based organic molecules for application in organic field-effect transistors (OFETs) and organic light-emitting diodes (OLEDs) as a hole injection material.[151-154] However, the use of the BDP-based HTMs in PSCs has rarely been studied.[58,155] The presence of the heteroatom in the BDP core can facilitate the intermolecular non-covalent interaction and increase the molecular planarity while extending π-electron delocalization along the molecular backbone, which can enhance the charge transport properties.[156-160] In addition, a tunable energy level of the BDP unit is promising to design a well-aligned energy level with perovskites, which can further promote hole extraction.[156] Moreover, the functionalization of the BDP unit with the heteroatom integration can target effective defect passivation of perovskites resulting in a reduced charge recombination loss, thereby improving device performance.[73,161,162]

Herein, we developed three novel BDP-based organic small molecules as a HTM in PSCs, 1,5-dihexyl-2,6-bis(4-methoxyphenyl)-1,5-dihydropyrrolo[2,3-*f*]indole, 2,6-bis(3-fluorophenyl)-1,5-dihexyl-1,5-dihydropyrrolo[2,3-*f*]indole and 1,5-dihexyl-2,6-bis(3-(trifluoromethyl)phenyl)-1,5-dihydropyrrolo[2,3-*f*]indole named CB-1, CB-2, and CB-3, respectively (Figure 4.1). 4-methoxyphenyl, 3-fluorophenyl and 3-trifluoromethylphenyl functional groups were attached in the BDP-based HTM structure to examine the heteroatom effects on PSC performance. We investigated the HTMs in terms of electrochemical energy levels, optical properties of absorption and photoluminescence (PL), thermal stability, and electronic properties of hole mobility and film conductivity. Furthermore, molecular dynamic (MD) simulations revealed an interaction between the heteroatoms of the molecules and Pb atom of the perovskite, which proves an impact of the HTMs on the defect passivation effect. We employed the HTMs to fabricate PSCs and the use of CB-2 achieved the highest PCE of 18.23 % mainly based on its strong defect passivation effect and intermolecular interaction owing to a high degree of molecular planarity. Meanwhile, the use of CB-1 and CB-3 resulted in a lower PCE of 16.78% and 16.74%, respectively, mainly due to the absence of the passivation effect of CB-1 and the inferior hole-transporting capability of CB-3 despite its defect passivation effect. Lastly, we demonstrated significantly stable device performance during long-term storage using the HTMs with improved hydrophobicity, particularly in fluorinated CB-2 and CB-3 HTMs based PSCs.

4.2 Results and Discussion

4.2.1 Design and Synthesis of BDP-based HTMs

In the molecular design of the HTMs, the alkylated BDP core was preserved as a donor unit while functional groups were modulated with 4-methoxyphenyl, 3-fluorophenyl, and 3-trifluoromethylphenyl for CB-1, CB-2, and CB-3, respectively (Figure 4.1). The solubility of the compounds was adjusted by adding long *N*-alkyl chains in the BDP unit, which improve hydrophobicity and solubility in an organic solvent, thus making the HTM solution-processable and protecting perovskite from degradation by moisture.[163] The methoxyphenyl substitution in the CB-1 was chosen due to the electron-donating effect to adjust the HOMO level and to improve the hole mobility and film quality of the HTM layer.[164] CB-2 and CB-3 containing fluorine atoms have been employed to decrease the LUMO levels without causing strong steric hindrance, enhance inter/intramolecular non-covalent interactions, and increase hydrophobicity leading to a long-term stability.[74,53]

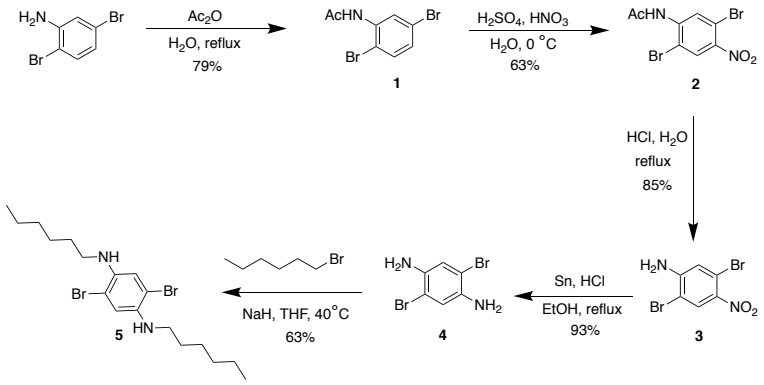

Scheme 4.1 Synthetic route for 2,5-dibromo-N^1,N^4-dihexylbenzene-1,4-diamine (5).

The three novel BDP-based HTMs were successfully synthesized in a in a linear 7-step effort with good overall yield. Synthesis of the intermediate 2,5-dibromobenzene-1,4-diamine (4) was accomplished starting from commercially available and inexpensive precursor 2,5-dibromoaniline according to the method reported by Moroni *et al*. with a small modification (Scheme 4.1).[165] The synthesis started with acetylation reaction of amine substitute of 2,5-dibromoaniline with acetic anhydride to obtain compound 1. Then, nitro group was introduced by adding concentrated H_2SO_4 and HNO_3 to the compound 1. Deacetylation of compound 2 followed by nitro reduction with stannous chloride in acidic environment to get compound 4. Finally, selective mono-*N*-alkylation of both amino groups of the compound (4) with 1-bromohexane in the presence. of sodium hydride in tetrahydrofuran solution gave 2,5-dibromo-N^1, N^4-dihexylbenzene-1,4-diamine (5).

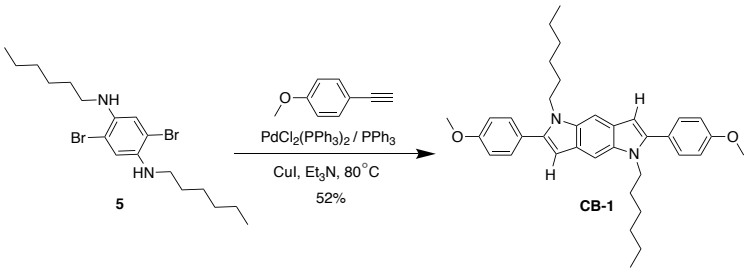

Scheme 4.2 Synthetic route for 1,5-dihexyl-2,6-bis(4-methoxyphenyl)-1,5-dihydropyrrolo[2,3-*f*]indole (CB-1).

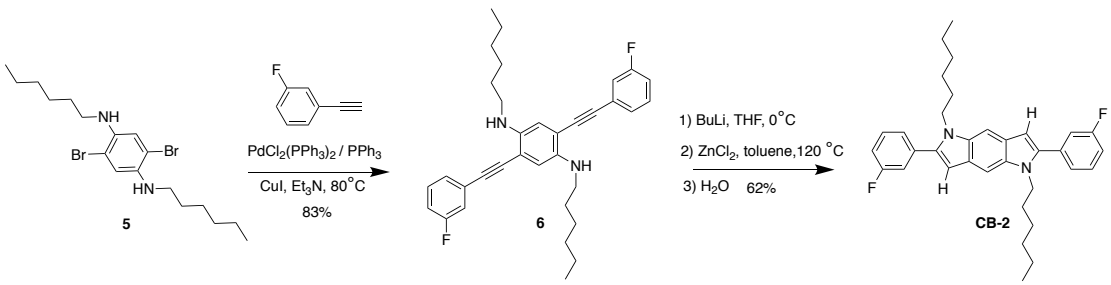

Scheme 4.3 Synthetic route for 2,6-bis(3-fluorophenyl)-1,5-dihexyl-1,5-dihydropyrrolo[2,3-*f*]indole (CB-2).

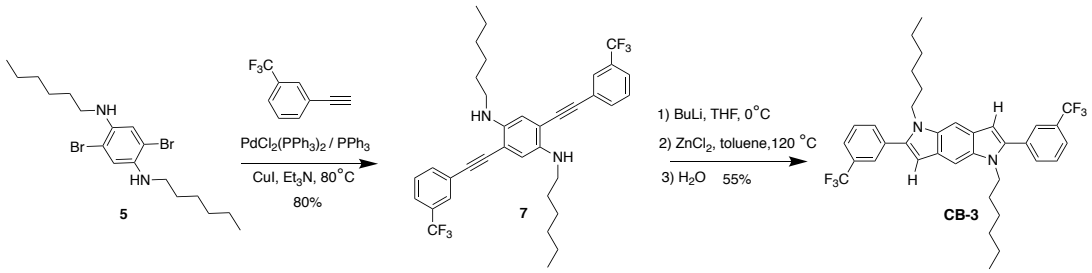

Scheme 4.4 Synthetic route for 1,5-dihexyl-2,6-bis(3-(trifluoromethyl)phenyl)-1,5-dihydropyrrolo[2,3-*f*]indole (CB-3).

For the target compounds CB-1, CB-2, and CB-3, compound 5 were coupled with 3 different alkyn units, 1-ethynyl-4-methoxybenzene, 1-ethynyl-3-fluorobenzene and 1-ethynyl-3-(trifluoromethyl)benzene, respectively, by Sonogashira coupling reaction using $PdCl_2(PPh_3)_2$, CuI and PPh_3 (Scheme 4.2, 4.3, 4.4). After the reaction, the crude materials were purified by column chromatography method on silica gel with hexane/dichloromethane as eluent. While the fluorobenzene substituted intermediate 6 and trifluoromethylbenzene substituted intermediate 7 could be successfully purified and characterized, the methoxybenzene substituted intermediate could not be isolated. In column chromatography with the acidic medium and water content of silica gel, it was observed that the double cyclization reaction was continued and the desired CB-1 compound was directly obtained with a good yield (Scheme 4.2). For compound 6 and 7, synthesis followed by zinc-mediated intramolecular cyclization reaction. First, it was deprotonated with *n*-BuLi, followed by transmetalation using $ZnCl_2$. The double cyclization reaction was completed by quenching the reaction mixture with water (Scheme 4.3 and 4.4). Purification of the final compounds was performed by column chromatography without the need for high-pressure vacuum distillation. The synthesized chemical structures were verified by ^{1}H and ^{13}C NMR spectroscopy and mass spectrometry (Appendix C). All the final compounds are well-soluble in common organic solvents such as tetrahydrofuran, chloroform, toluene, and chlorobenzene, typically used for HTM processing on perovskite absorbers.

4.2.2 Density Functional Theory Calculation

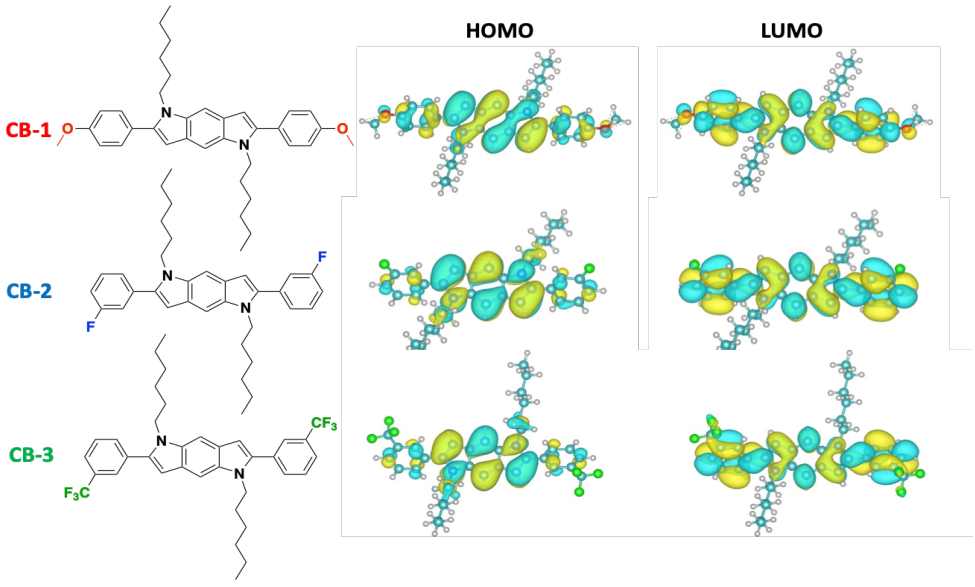

Figure 4.1 Molecule structure and spatial distribution of HOMO and LUMO orbitals in CB-1, CB-2 and CB-3, computed with PBE-D3 density functional on top of PBE-D3 optimized geometry (isosurface value – 0.015). C, O, N, H and F atoms are colored in cyan, red, blue, white and green.

To investigate the energy levels and spatial distribution of frontier orbitals of CB-1, CB-2, and CB-3, the density functional theory (DFT) calculations were carried out, and the benchmarking of the different density functionals was performed (Figure 4.1). The molecular structures were optimized by using either the PBE-D3 density functional or hybrid PBE0 density functional, and the HOMO and LUMO energies were calculated by using PBE-D3, B3LYP, and PBE0 density functionals (Table 4.1). The obtained orbital energy values correlated well with each other, and the same trend was observed for all cases: E_{HOMO} (CB-1) > E_{HOMO} (CB-2) > E_{HOMO} (CB-3) and E_{LUMO} (CB-1) > E_{LUMO} (CB-2) > E_{LUMO} (CB-3). When the BDP core is functionalized with electron-donating methoxyphenyl unit in CB-1, the positive mesomeric effect of the methoxy side group increased the electron density in the benzene ring and expanded the conjugation in the molecule, resulting in a higher HOMO/LUMO level. In addition, the trifluoromethylphenyl group of CB-3 has a stronger electron-withdrawing group than the fluorophenyl group of CB-2, which produced the negative inductive effect of CB-3 with deeper HOMO/LUMO levels. The molecular orbital spatial distribution of HOMO and LUMO were similar for all molecules. The electron density in the HOMO of CB-1, CB-2, and CB-3 was primarily distributed on the BDP unit while that of LUMO was spread along the entire molecule. These results hint that the planar structural geometry of the molecules may be the cause of the larger extent of the orbital delocalization and better conjugated system.[166]

	PBE-D3		B3LYP*		PBE0	
	HOMO (eV)	LUMO (eV)	HOMO (eV)	LUMO (eV)	HOMO (eV)	LUMO (eV)
CB-1	-3.96	-1.55	-4.45	-0.80	-4.80	-0.75
CB-2	-4.30	-2.05	-4.80	-1.31	-5.14	-1.31
CB-3	-4.45	-2.29	-4.94	-1.55	-5.30	-1.57

Table 4.1 Energies in eV of HOMO and LUMO calculated with different density functionals. *For the case of B3LYP calculation, geometries optimized at PBE-D3 level are used.

4.2.3 Thermal, Optical, and Electrochemical and Properties

To confirm the thermal stability of the new HTMs, we performed thermogravimetric analysis (TGA) recorded under the nitrogen atmosphere at the heating rate of 10 °C/min. The decomposition temperatures (T_d) determined at 5% weight loss of CB-1, CB-2 and CB-3 were 337 °C, 302 °C, and 251 °C, respectively, indicating that the new HTMs have good thermal stability (Figure 4.2a). The optical properties of the molecules were investigated by ultraviolet-visible (UV-Vis) absorption and PL spectroscopy in DCM solutions (Figure 4.2b). The absorption spectra of the HTMs showed two intense bands in the region of 240 and 340 nm. The first absorption band for CB-1, CB-2 and CB-3 originated from the localized aromatic π-π* transition of the conjugation system and center at 247, 244, 235 nm, respectively. The strong absorption bands at 333, 336, 338 nm, respectively of CB-1, CB-2 and CB-3 were ascribed to n-π* transition. All molecules showed a shoulder-like transition around 400 nm, which may be due to the extension of π–conjugation because of additional phenyl units.[151] The PL emission peaks of CB-1, CB-2 and CB-3 are centered at 440, 447 and 455 nm, respectively. The optical bandgap (E_g) values, estimated from the corresponding intersections of absorption and emission onsets, were determined to be 398, 410, and 415 nm, which corresponds to E_g of 3.12, 3.02 and 2.99 eV, respectively. The redshift both in the absorption and PL spectra can be attributed to the electron-withdrawing of F in CB-2 and CF_3 in CB-3, which resulted in narrow E_g.

We performed cyclic voltammetry with a standard three-electrode configuration to experimentally investigate HOMO energies of CB-1, CB-2 and CB-3 (Figure 4.2c). The materials were tested in dichloromethane containing 0.1 M n-Bu_4NPF_6 as a supporting electrolyte and the oxidation potential was calibrated against ferrocene internal standard. The E_{HOMO} values were calculated to be -5.24, -5.30, and -5.34 eV vs. vacuum for CB-1, CB-2 and CB-3, respectively, showing the same trend with the result of DFT calculation. The HOMO levels are well aligned with the valence band energy level of the typical lead iodide-based perovskites so that the photogenerated charge carriers are efficiently transferred at the interface. LUMO levels were calculated from the optical bandgap and HOMO level differences. CB-2 and CB-3 showed lower LUMO levels to -2.28 and -2.35 eV, respectively, while CB-1 is -2.12 eV. The large offset between the LUMO of the HTMs and the conduction band energy of the perovskite can effectively block the back-electron transfer. A schematic of the energy band diagram is shown in Figure 4.2d. All electrochemical, optical and thermal properties of the materials are summarized in Table 4.2.

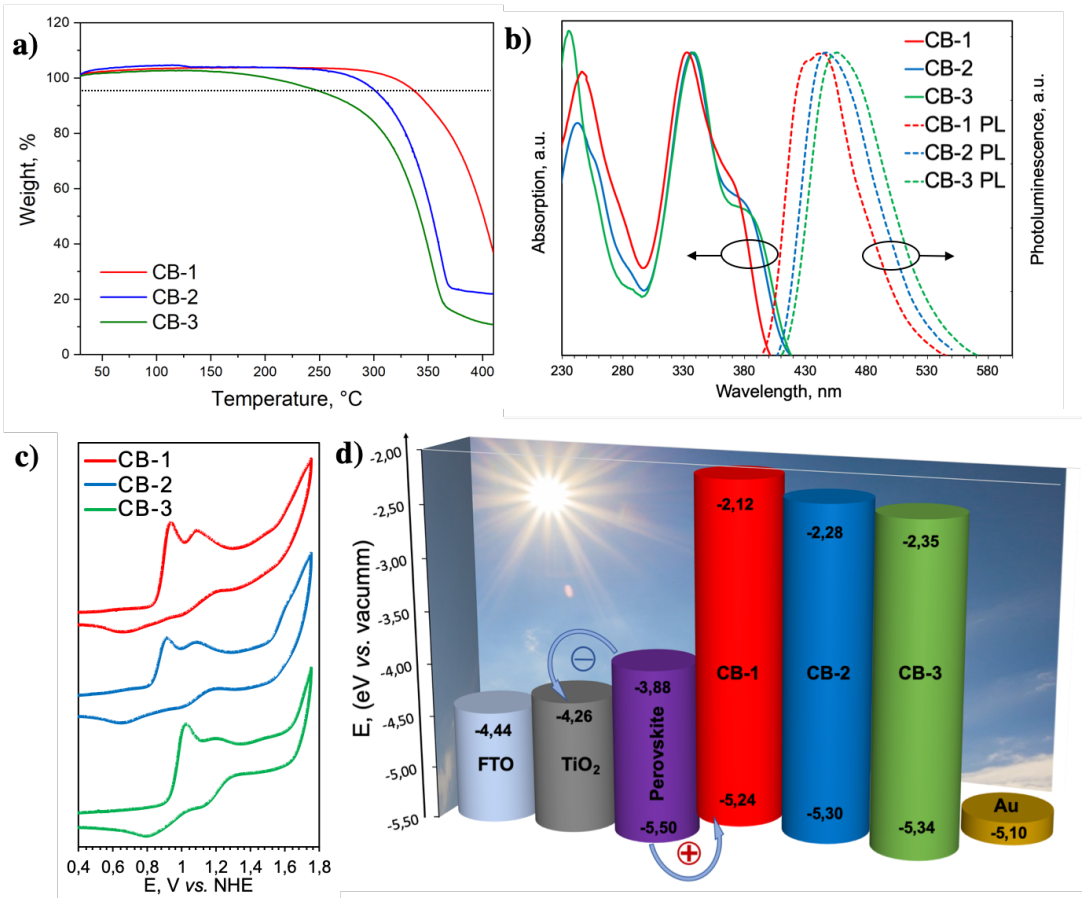

Figure 4.2 a) Thermogravimetric analysis curves for CB-1, CB-2, CB-3 HTMs. b) Normalized UV-Vis absorption and PL spectra of BDP-based HTMs in DCM solution. c) Cyclic voltammograms of the HTMs in DCM solution. d) Schematic energy level diagram of components used in the devices.

4.2.4 Hole Collection Properties

To investigate charge transport and hole collection properties of the BDP-based HTMs, the xerographic time-of-flight (XTOF) method was used (Figure 4.3a, Appendix C). Samples were prepared under drop casting technique on Al coated glass plates using chlorobenzene as a solvent with 0.54-1.2 µm film thickness (experimental details in Appendix C). The room-temperature zero-field hole-drift mobility (μ_0) of CB-1, CB-2 and CB-3 was measured to be 1.1×10^{-5} cm^2 V^{-1} s^{-1}, 0.63×10^{-5} cm^2 V^{-1} s^{-1} and 0.56×10^{-5} cm^2 V^{-1} s^{-1}, respectively. Among the HTMs, CB-1 exhibited a higher hole mobility than that of CB-2 and CB-3, which can be attributed to a

higher degree of conjugation and better intermolecular interaction of the molecule.[167,168] In addition, lateral thin-film conductivity of the HTMs was measured with OFETs (Figure 4.3b).[169] Similar to the result of the hole mobility measurement, CB-1 showed a higher conductivity (4.72×10^{-4} S cm^{-1}) than CB-2 (4.06×10^{-4} S cm^{-1}) and CB-3 (1.58×10^{-4} S cm^{-1}). The conductivity of the doped spiro-OMeTAD as a reference was determined to be 6.25×10^{-4} S cm^{-1}. The results of the hole-mobility and conductivity measurements are summarized in Table 4.2.

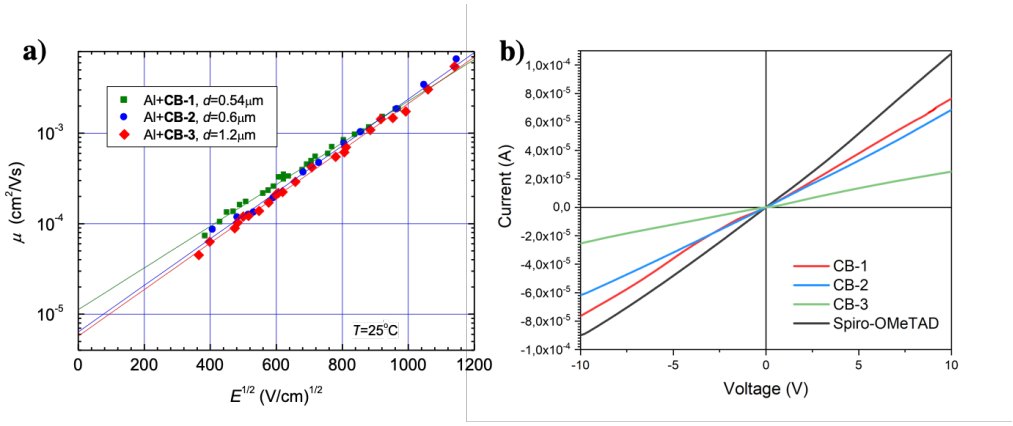

Figure 4.3 a) Holes drift mobility field dependencies for CB-1, CB-2, CB-3 HTMs. b) The conductivity of CB-1, CB-2, CB-3 and spiro-OMeTAD measured on OFET substrates.

Compound	T_d [°C][a]	λ_{abs} [nm][b]	λ_{em} [nm][b]	HOMO [eV][c]	LUMO [eV][d]	ΔE_g [eV][e]	σ [S cm^{-1}][f]	μ_0 [cm^2 V^{-1} s^{-1}][g]
CB-1	337	247, 333	440	-5.24	-2.12	3.12	4.72×10^{-4}	1.1×10^{-5}
CB-2	302	244, 336	447	-5.30	-2.28	3.02	4.06×10^{-4}	0.63×10^{-5}
CB-3	251	235, 338	455	-5.34	-2.35	2.99	1.58×10^{-4}	0.56×10^{-5}

Table 4.2 Thermal, optical, electrochemical and electronic properties of CB-1, CB-2 and CB-3. [a] Decomposition temperature corresponding to 5% weight loss determined from TGA; [b] Absorption and emission spectra measured in dichloromethane; [c] Measured in 0.1 M *n*-Bu_4NPF_6/DCM solution using glassy carbon working electrode, Pt reference electrode and Pt counter electrode calibrated by Fc/Fc^+ as an external reference. Potentials were converted to the normal hydrogen electrode (NHE) by addition of +0.624 V and -4.44 eV to the vacuum, respectively; [d] LUMO = HOMO + ΔE_g; [e] $\Delta E_g = 1240/\lambda_{onset}$; [f] Conductivity values; [g] Mobility values at zero field.

4.2.5 Thin-layer Characteristics

As the film morphology of an HTM is of great importance to realize efficient charge transfer, we performed scanning electron microscopy (SEM) to investigate surface morphology of the HTMs on a perovskite film $[(FAPbI_3)_{0.87}(MAPbBr_3)_{0.13}]_{0.92}(CsPbI_3)_{0.08}$, which we used as a light absorber of PSCs (Figure 4.4a) (experimental details in Appendix C). CB-1 presented a highly well-oriented fibril-like structure with sparsely distributed aggregates. The highest hole mobility and conductivity of CB-1 can be attributed to the fiber-like structure, but the large aggregates and the pinholes on the film can obstruct charge carriers to be efficiently collected to the top electrode in PSCs. On the other hand, CB-2 and CB-3 exhibited more homogeneous layer formation than CB-1.

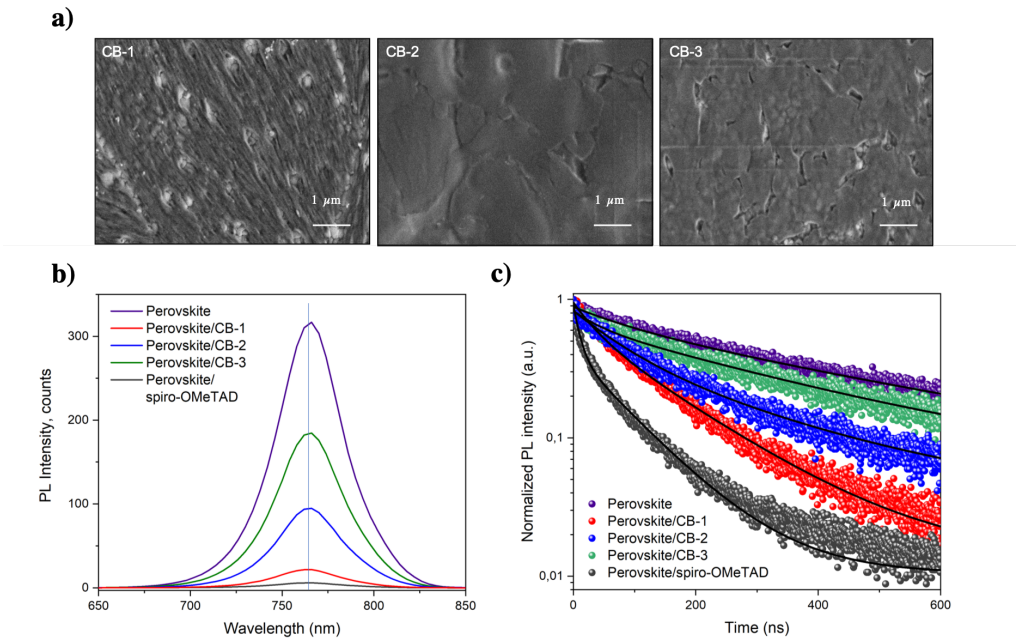

Figure 4.4 a) Top surface SEM images of HTMs on perovskite. b) Steady-state PL spectra of the pristine perovskite and perovskite/HTM films (CB-1, CB-2, CB-3 and spiro-OMeTAD) upon excitation at 475 nm. c) Transient PL spectra in the first 600 ns time window of the pristine perovskite and perovskite/HTM films upon excitation at 640 nm.

We investigated PL characteristics of the HTM deposited perovskite films, which can give insights about charge-carrier dynamics that can closely link to the hole transfer as well as defect state of the perovskite (Figure 4.4b) (experimental details in Appendix C). For steady-state PL measurements, the films were excited with 475 nm light. The bare perovskite film showed a PL emission peak at 767 nm with the highest intensity.[170] The deposition of the HTMs on top of the perovskite resulted in a strong quenching of the PL emission compared to the bare perovskite film, indicating the effective hole transfer from the perovskite to the HTMs. The stronger PL quenching upon the deposition of CB-1 than CB-2 and CB-3 implies that more efficient hole transfer can occur at the interface with the use of CB-1. On the other hand, the deposition of CB-2 or CB-3 on the perovskites resulted in a less strong quenching of the PL emission. While the PL quenching can occur due to the efficient hole extraction from the perovskites to an HTM, defects in perovskites can also lead to the PL quenching due to nonradiative recombination of charge carriers. Especially, undercoordinated Pb^{2+} in the perovskites can significantly influence charge-carrier dynamics acting as a nonradiative recombination center. Nevertheless, the defects could be effectively passivated thanks to the fluorinated aryl units of CB-2 and CB-3, which could suppress the PL quenching.[88] To gain a better understanding, we also performed time-resolved PL (TrPL) measurements of the films, which were excited by 640 nm light. For the neat perovskite film, the PL decay curve was fitted to a mono-exponential decay function, which resulted in the PL lifetime as 338.4 ns (Figure 4.4c). Meanwhile, the decay curves of the HTMs deposited perovskites were fitted to a bi-exponential decay function which takes account of radiative recombination in the bulk perovskite as well as non-radiative recombination at the interface.[171] We summarized the detailed PL lifetime parameters in Table 4.3. The average PL lifetime (τ_{ave}) of the films with the HTMs exhibited the same trend to the result of the steady-state PL intensity of the films. The PL lifetime of the neat perovskite film (τ_1 = 338.4 ns) was significantly decreased upon the deposition of CB-1, CB-2, CB-3, and spiro-OMeTAD resulting in τ_{ave} = 105.9, 166.3, 263.1, and 46.0 ns, respectively, indicating the efficient hole-transfer from the perovskite to the HTMs. As mentioned above, the suppressed PL quenching and the retarded PL decay of the films with CB-2 and CB-3 suggest that the fluorinated aryl units present in these molecules efficiently contribute to defect passivation.

Condition	A_1	τ_1[ns]	A_2	τ_2[ns]	τ_{Ave}[ns]	χ^2
Perovskite	0.760	338.4	-	-	-	0.986
Perovskite/CB-1	0.328	36.0	0.608	143.6	105.9	0.995
Perovskite/CB-2	0.422	78.1	0.377	265.0	166.3	0.989
Perovskite/CB-3	0.178	41.9	0.598	328.9	263.1	0.981
Perovskite/Spiro-OMeTAD	0.512	10.8	0.392	91.9	46.0	0.993

Table 4.3 Mono-exponential decay function, $y = A_1 e^{-t/\tau_1}$ fitted result of PL lifetime curve of the perovskite, and bi-exponential decay function, $y = A_1 e^{-t/\tau_1} + A_2 e^{-t/\tau_2}$ for the perovskites with HTMs.

4.2.6 Characterization of Perovskite/HTMs Interfaces

To obtain more insight into the interface and the passivation effect, first-principles Born-Oppenheimer MD simulations have been performed (Figure 4.5). In the computational experiments, the HTMs were placed on the perovskite surface and allowed to interact at 300 K constant temperature (experimental details in Appendix C). While CB-1 did not have a specific interaction with the perovskite, the fluorine atom of CB-2 exhibited a strong interaction with the Pb atoms at the perovskite surface. Therefore, the undercoordinated Pb^{2+} in the perovskite can be effectively passivated by CB-2, leading to the higher intensity and the longer lifetime of PL of the films than those using CB-1.[172-175] Meanwhile, in addition to BDP core planarity, the geometry of CB-2 also allowed for realization of the benzene rings conformation parallel to the perovskite surface, resulting in a higher planar molecular orientation of CB-2 than CB-1. The distribution of dihedral angles between BDP core and substituted phenyl units along the MD trajectory was analyzed according to occurrences percentage of CB-1, CB-2 and CB-3 (Figure 4.6). CB-2 revealed a higher occurrence at smaller dihedral angle between 20° and 40° than CB-1 (40°-60°) and CB-3 (60°-80°), as the fluorine atom did not produce a steric hindrance for the rotation of the benzene in the presence of hexyl chains. The higher planarity and smaller dihedral angles of CB-2 may allow better intermolecular π–π stacking of HTM, resulting in a better hole transfer capacity.[161] On the other hand, the greater number of fluorine atoms of CB-3 also favored the strong interaction with the Pb atoms in the perovskite that gave rise to the highest intensity and the longest lifetime of PL among the use of the three HTMs. But unlike CB-2, the benzene rings of CB-3 systematically have an out-of-plane orientation with respect to the perovskite surface, resulting in a reduced planarity of the molecular configuration with a higher dihedral.

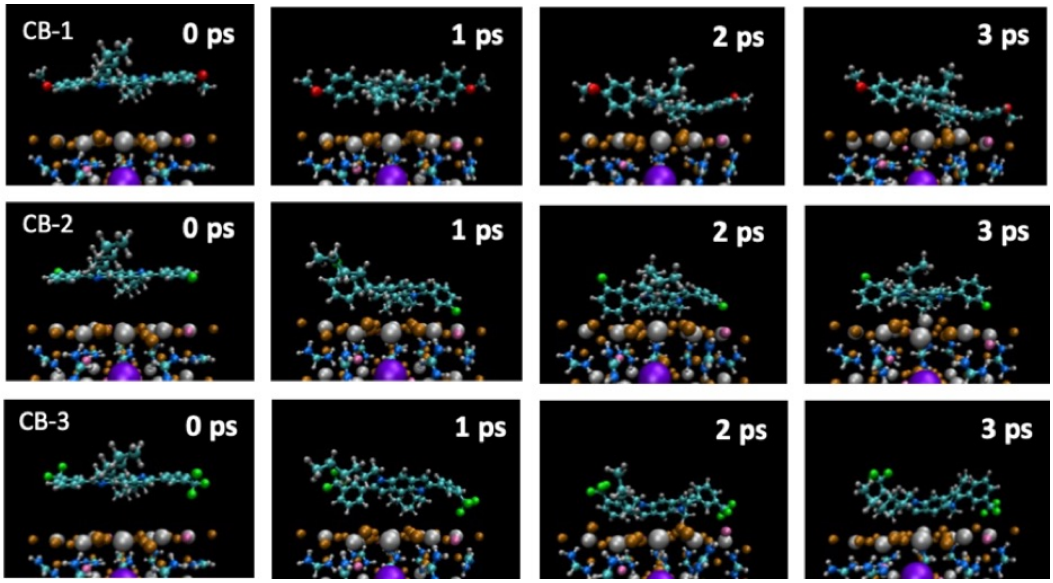

Figure 4.5 Interaction of CB-1 (top), CB-2 (middle) and CB-3 (bottom) HTMs with perovskite surface. C, O, N, H, F, Br, I, Pb and Cs atoms are colored in cyan, red, blue, white, green, mauve, brown, grey and purple, respectively.

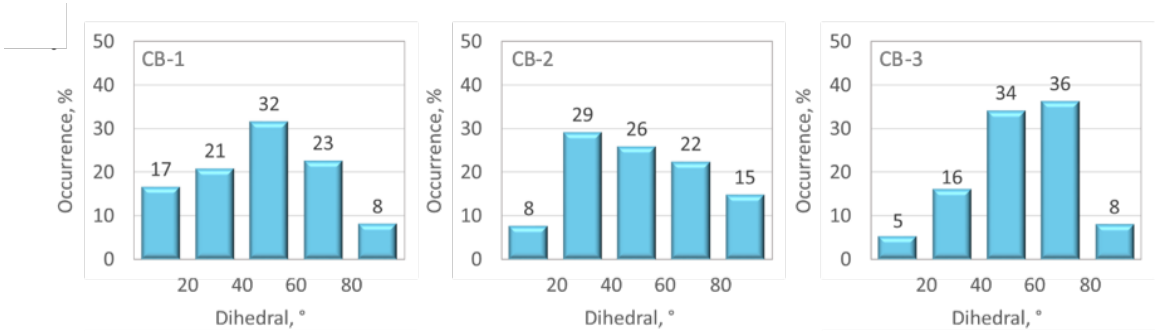

Figure 4.6 The distribution of dihedral angles of CB-1, CB-2 and CB-3 between BDP core and substituted phenyl units along the MD trajectory.

4.2.7 Device Characteristics

We employed the three BDP-based HTMs to fabricate PSCs consisting of fluorine-doped tin oxide (FTO)/ compact TiO_2 (c-TiO_2)/ mesoporous TiO_2 (mp-TiO_2)/ SnO_2/ perovskite $[(FAPbI_3)_{0.87}(MAPbBr_3)_{0.13}]_{0.92}(CsPbI_3)_{0.08}]$ / HTM/ Au. We observed the device structure via cross-sectional SEM which confirmed the formation of ~70 nm-thick HTLs (Figure 4.7) (experimental details in Appendix C).

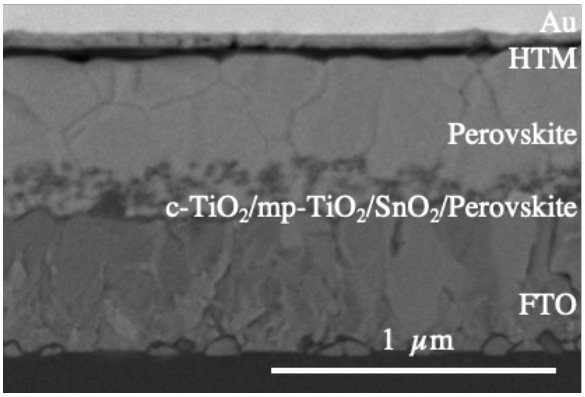

Figure 4.7 Cross-section SEM images of PSCs employing of CB-2 as HTMs.

Among the HTMs, CB-2 resulted in the best-performing PSCs having a PCE of 18.23%, open-circuit voltage (V_{OC}) of 1.025V, short-circuit current (J_{SC}) of 23.19 mA cm^{-2}, and fill factor (*FF*) of 0.767 in a champion device while the device using spiro-OMeTAD showed a PCE of 20.26% (Figure 4.8a). However, the PSCs using CB-1 and CB-3 exhibited lower PCEs; the PSC using CB-1 showed a PCE of 16.78% having V_{oc} of 1.004V, J_{SC} of 23.31 mA cm^{-2} and *FF* of 0.717, and CB-3 showed a PCE of 16.74% having V_{OC} of 1.003V, J_{SC} of 22.35 mA cm^{-2} and *FF* of 0.747 in each champion device. The highest PCE of the devices using CB-2 can be attributed to the effective defect passivation by the fluorine atom, which can interact with the undercoordinated Pb^{2+} in the perovskite.[172-175] In addition, the highly planar molecular configuration might particularly improve V_{OC} based on the increase in the molecular ionization potential, thereby increasing built-in potential of the device.[176] Furthermore, the strong intermolecular π–π interaction based on the molecular planarity can contribute to the improvement in *FF* by decreasing the interfacial resistance. On the other hand, the degradation in the device performance using CB-1 might result from the absence of the passivation effect as well as the inhomogeneous film morphology despite its high conductivity and hole mobility (Figure 4.4a). Although CB-3 exhibited the passivation effect with the presence of trifluoromethyl group, the lowest film conductivity and hole mobility only allowed the limited J_{SC} and non-planar molecular configuration allowed limited V_{OC}, resulting in the lowest PCE among the devices. We also measured external quantum efficiency (EQE) of the devices and the integrated J_{SC} exhibited a consistent trend and value with that of the *J-V* curves (Figure 4.8b). Detailed photovoltaic parameters are summarized in Table 4.4 and also the statistics of 20 individual devices for each HTM are presented in Figure 4.9.

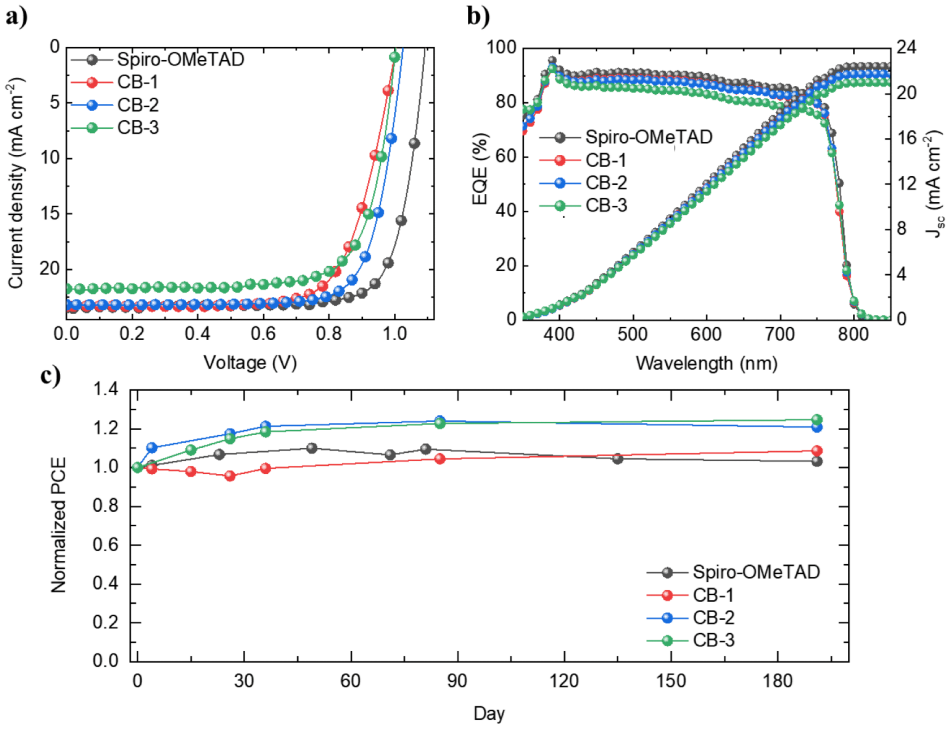

Figure 4.8 a) *J-V* curves of champion PSCs and b) EQE spectra of the devices using CB-1, CB-2, CB-3 and spiro-OMeTAD as HTMs. c) long-term air-storage stability of PSCs under constant 1 sun illumination using spiro-OMeTAD and CB series as an HTM.

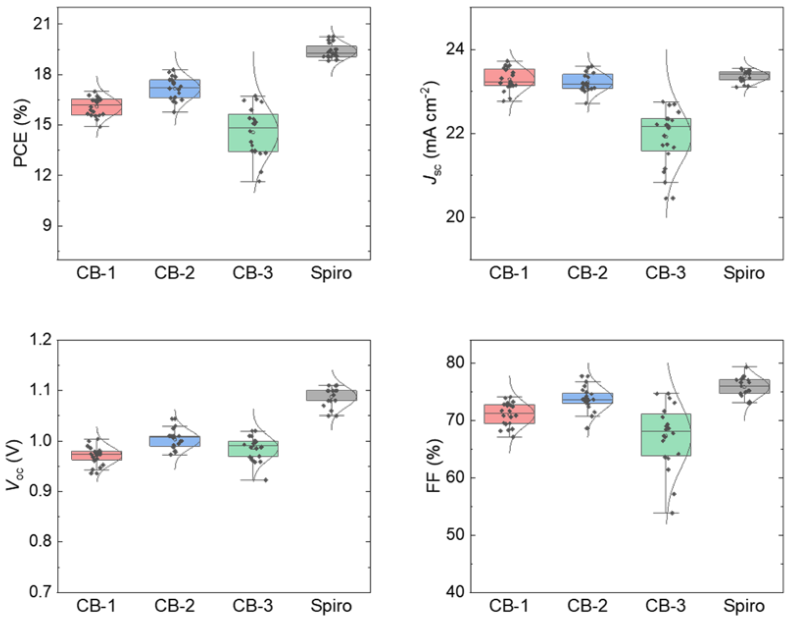

Figure 4.9 Statistics of PCE, J_{SC}, V_{OC}, and *FF* of PSCs with spiro-OMeTAD, CB-1, CB-2, and CB-3 as an HTM.

We carried out the long-term air-storage stability test of the devices without encapsulation that have been stored in dark under the relative humidity below 10 % (Figure 4.8c). All the devices basically proved being super stable with the use of the CB HTMs and not showing a degradation of PCEs over 6 months. The normalized PCEs of the device using CB-2 (121%) or CB-3 (125%) were higher than that of the device using spiro-OMeTAD (103%), which can be ascribed to the fluorine-containing functional groups of CB-2 and CB-3. Although the device using CB-1 showed slightly lower normalized PCEs than that using CB-2 or CB-3, it was still comparable to the device using spiro-OMeTAD by maintaining almost 109% of its initial PCE over 6 months. To investigate the excellent stability of the devices having the CB HTMs, we measured a water contact angle of the HTMs deposited on the perovskite (Figure 4.10) (experimental details in Appendix C). The water contact angle of CB-1, CB-2 and CB-3 were 67.9°, 88.9°, and 101.8°, respectively, which were larger than that of spiro-OMeTAD (64.6°). Especially, the much larger contact angles of CB-2 and CB-3 indicated their strong hydrophobicity that arose from the fluorophenyl and trifluoromethylphenyl, respectively.[74] The superior hydrophobicity of CB-2 and CB-3 can effectively prevent moisture penetration into the perovskite layer leading to superior device stability.

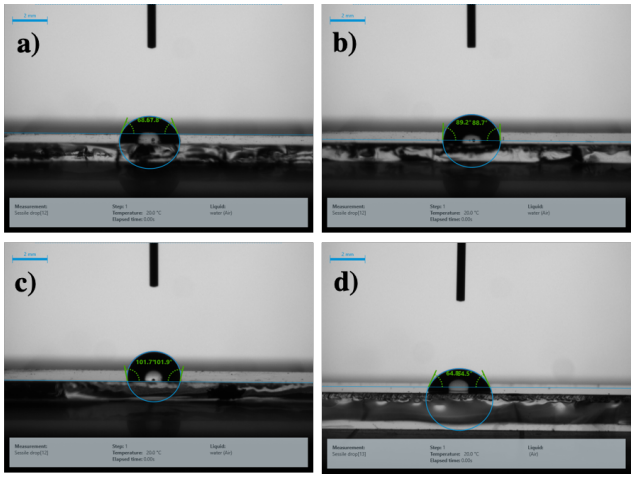

Figure 4.10 Water contact angle measurement on top of (a) CB-1, (b) CB-2, (c) CB-3 and (d) spiro-OMeTAD films on the top of perovskite.

HTM	V_{OC} (V)	J_{SC} (mA cm^{-2})	*FF*	PCE (%)
CB-1	1.004	23.31	0.717	16.78
CB-2	1.025	23.19	0.767	18.23
CB-3	1.003	22.35	0.747	16.74
spiro-OMeTAD	1.092	23.43	0.792	20.26

Table 4.4 Photovoltaic performance of the champion PSCs based on CB-1, CB-2 and CB-3 and spiro-OMeTAD.

4.3 Conclusion

We successfully designed and synthesized three BDP core-based organic HTMs, CB-1, CB-2, and CB-3, and demonstrated efficient and stable PSCs using the HTMs. The BDP core unit was functionalized by 4-methoxyphenyl, 3-fluorophenyl, and 3-trifluoromethylphenyl, respectively, that intended passivation of defects in perovskites. The molecules were examined by various characterization methods in terms of electrochemical, optical, thermal, electronic, and optoelectronic properties. Our results presented that the functionalization of the BDP unit can lead to the effective defect passivation and molecular planarity according to

the substituents. We found out that the fluorinated derivatives of CB-2 and CB-3 can suppress non-radiative recombination at the interface indicated by the PL characteristics, which can be attributed to the passivation of the undercoordinated Pb^{2+} by fluorine. MD simulations also verified the passivation interactions of fluorinated CB-2 and CB-3 with the Pb atoms of the perovskite. Also, the molecular planarity of CB-2 was confirmed by the simulation and the calculation of small dihedral angle between the BDP unit and the 3-fluorophenyl of CB-2, which can lead to the intermolecular π–π interaction and thus facilitate the hole extraction. Therefore, the PSC using CB-2 achieved the highest PCE of 18.23%. However, CB-3 showed the lower PCE of 16.74% because of the inferior hole-transporting capability and non-planar molecular configuration despite the passivation effect. Also, CB-1 without the passivation effect resulted in the lower PCE of 16.78% despite the high mobility and film conductivity. Furthermore, the molecular hydrophobicity of the fluorinated HTMs enabled the devices to demonstrate excellent long-term storage stability in the air without encapsulation and showed no degradation of their PCEs over 6 months. We believe this study provides a prospect for future materials design of efficient and highly stable HTMs by enriching the chemistry of BDP-based organic small molecules.

4.4 Synthetic methods and Procedures

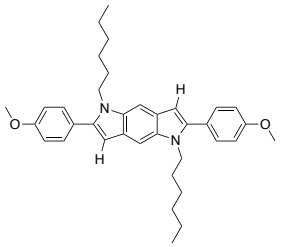

1,5-dihexyl-2,6-bis(4-methoxyphenyl)-1,5-dihydropyrrolo[2,3-f]indole; CB-1 : 2,5-dibromo-N^1,N^4-dihexylbenzene-1,4-diamine (5) (0.5 g, 1.15 mmol, 1eq.) were added in 30 min. degassed triethylamine (30 mL). CuI (22 mg, 0.12 mmol, 10 mol %), PPh_3 (30 mg, 0.12 mmol, 10 mol %) and 1-ethynyl-4-methoxybenzene (0.37 mL, 2.88 mmol, 2.5 eq.) was added to the reaction mixture and degassed for additional 10 min. The mixture was stirred at 80 ºC for overnight after addition of $PdCl_3(PPh_3)_2$ (40 mg, 0.06 mmol, 5 mol %). The reaction mixture was quenched with water after cooling it to room temperature. The organic layer was extracted with DCM, dried over anhydrous magnesium sulfate, filtered and concentrated under reduced pressure. The resulting residue was purified by column chromatography on silica gel (3:1, hexane: DCM) and cyclization was completed during the chromatography to give final product CB-1 as a white solid in 52% yield (0.32 g, 0.60 mmol). ^{1}H NMR (400 MHz, $CDCl_3$, δ): 7.55 (s, 2H), 7.51 (td, 4H), 7.05 (td, 4H), 6.56 (s, 2H), 4.20 (t, J = 7.6 Hz, 4H), 3.92 (s, 6H), 1.79 (p, 4H), 1.28 – 1.21 (m, 12H), 0.88 (t, J = 6.7 Hz, 6H). ^{13}C NMR (100 MHz, $CDCl_3$, δ): 159.25, 141.87, 134.94, 130.56, 126.39, 125.91, 113.88, 100.53, 98.95, 55.36, 44.22, 31.41, 29.52, 26.61, 22.60, 14.03. HRMS (ESI) m/z: [M^+] calcd for $C_{36}H_{44}N_2O_2$, 536.3403, found, 536.3420.

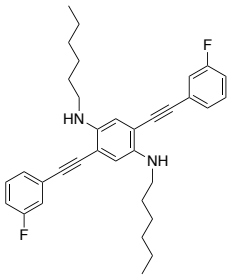

2,5-bis((3-fluorophenyl)ethynyl)-N^1,N^4-dihexylbenzene-1,4-diamine; 6: 2,5-dibromo-N^1,N^4-dihexylbenzene-1,4-diamine (5) (0.5 g, 1.15 mmol, 1eq.) were added in 30 min. degassed triethylamine (30 mL). CuI (22 mg, 0.12 mmol, 10 mol %), PPh_3 (30 mg, 0.12 mmol, 10 mol %) and 1-ethynyl-3-fluorobenzene (0.3 mL, 2.65 mmol, 2.3 eq.) was added to the reaction mixture and degassed for additional 10 min. The mixture was stirred at 80 ºC for overnight after addition of $PdCl_3(PPh_3)_2$ (40 mg, 0.06 mmol, 5 mol %). The reaction mixture was quenched with water after cooling it to room temperature. The organic layer was extracted with DCM, dried over anhydrous magnesium sulfate, filtered and concentrated under reduced pressure. The resulting residue was purified by column chromatography on silica gel (3:1, hexane: DCM) to give product 6 as orange solid in 83% yield (0.49 g, 0.96 mmol). ^{1}H NMR (400 MHz, $CDCl_3$, δ): 7.37 – 7.31 (m, 4H), 7.27 – 7.21 (m, 2H), 7.14 – 7.02 (m, 2H), 6.75 (s, 2H), 4.13 (s, 2H), 3.18 (t, J = 7.1 Hz, 4H), 1.71 (p, J = 7.2 Hz, 4H), 1.51 – 1.44 (m, 4H), 1.41 – 1.33 (m, 8H), 0.94 (t, J = 6.7, 6H).^{13}C NMR (100 MHz, $CDCl_3$, δ): 163.68, 161.23, 141.23, 130.05, 129.96, 127.34, 127.31, 125.13, 125.03, 118.28, 118.05, 115.71, 115.50, 113.93, 109.75, 94.79, 94.76, 87.57, 44.58, 31.66, 29.53, 26.88, 22.67, 14.05.

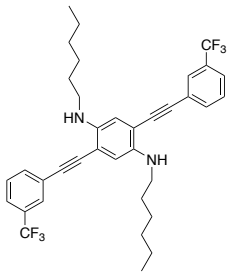

N¹,N⁴-dihexyl-2,5-bis((3-(trifluoromethyl)phenyl)ethynyl)benzene-1,4-diamine; 7 : 2,5-dibromo-*N*¹,*N*⁴-dihexylbenzene-1,4-diamine (5) (0.3 g, 0.69 mmol, 1eq.) were added in 30 min. degassed triethylamine (15 mL). CuI (13 mg, 0.07 mmol, 10 mol %), PPh_3 (18 mg, 0.07 mmol, 10 mol %) and 1-ethynyl-3-(trifluoromethyl)benzene (0.29 g, 1.73 mmol, 2.5 eq.) was added to the reaction mixture and degassed for additional 10 min. The mixture was stirred at 80 ºC for overnight after addition of $PdCl_3(PPh_3)_2$ (24 mg, 0.035 mmol, 5 mol %). The reaction mixture was quenched with water after cooling it to room temperature. The organic layer was extracted with DCM, dried over anhydrous magnesium sulfate, filtered and concentrated under reduced pressure. The resulting residue was purified by column chromatography on silica gel (3:1, hexane: DCM) to give product 7 as dark orange solid in 80% yield (0.34 g, 0.55 mmol). ^{1}H NMR (400 MHz, $CDCl_3$, δ): 7.80 (s, 2H), 7.71 (d, *J* = 7.7 Hz, 2H), 7.61 (d, *J* = 7.9 Hz, 2H), 7.51 (t, *J* = 7.8 Hz, 2H), 6.77 (s, 2H), 4.14 (s, 2H), 3.19 (t, *J* = 7.1 Hz, 4H), 1.71 (q, *J* = 7.3 Hz, 4H), 1.51 – 1.44 (m, 4H), 1.40 – 1.34 (m, 8H), 0.92 (t, *J* = 6.6, 6H).^{13}C NMR (100 MHz, $CDCl_3$, δ): 134.47, 131.57, 131.25, 130.93, 130,60, 128.98, 128.24, 128.20, 128.16, 128,12, 125.07, 124.83, 124.79, 124.15, 122.36, 114.09, 109.74, 94.52, 88.13, 44.59, 31.63, 29.45, 26.86, 22.64, 14.01.

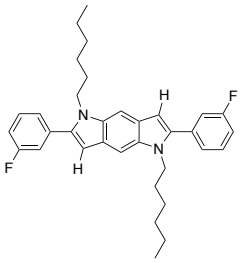

2,6-bis(3-fluorophenyl)-1,5-dihexyl-1,5-dihydropyrrolo[2,3-f]indole; CB-2: 2,5-bis((3-fluorophenyl)ethynyl)-*N*¹,*N*⁴-dihexylbenzene-1,4-diamine 6 (0.2 g, 0.39 mmol, 1eq.) in THF (3 mL) was cooled to 0 ºC and BuLi in hexane (0.35 mL, 2.5 M, 0.86 mmol, 2.2 eq.) was added dropwise to the suspended solution. The reaction mixture was allowed to reach room temperature and stirred for 30 min. Then, it followed by addition of zinc chloride in 2-methyltetrahydrofuran (0.45 mL, 1.9 M, 0.86 mmol, 2.2 eq.) and toluene (3 mL) solution to the reaction mixture. The reaction mixture was heated to 120 ºC and stirred for 3 h. After cooling to room temperature, the resulting mixture were quenched with water. The phases were extracted with EtOAc and sat. NaH_4Cl solution, dried over anhydrous magnesium sulfate, filtered. The solvent was removed in vacuo and the residue was purified by silica gel column chromatography (6:1 hexane: DCM) to give product CB-2 as a yellow solid in 62% yield (0.12 g, 0.24 mmol). ^{1}H NMR (400 MHz, $CDCl_3$, δ): 7.58 (s, 2H), 7.47 (q, *J* = 7.3 Hz, 2H), 7.33 (dd, *J* = 27.3, 8.2 Hz, 4H), 7.14 (t, *J* = 8.6 Hz, 2H), 6.64 (s, 2H), 4.23 (t, *J* = 7.6 Hz, 4H), 1.77 (p, *J* = 7.8, 7.3 Hz, 4H), 1.27 – 1.17 (m, 12H), 0.86 (t, *J* = 6.6 Hz, 6H). ^{13}C NMR (100 MHz, $CDCl_3$, δ): 163.97, 161.52, 141.01, 140.98, 135.93, 135.84, 135.34, 130.02, 129.93, 126.15, 124.92, 124.89, 116.18, 115.96, 114.59, 114.38, 101.82, 99.49, 44.33, 31.32, 29.45, 26.53, 22.55, 13.98. HRMS (ESI) *m/z*: [M⁺] calcd for $C_{34}H_{38}F_2N_2$, 513.3076, found, 513.3075.

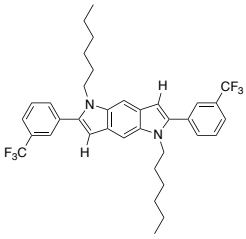

1,5-dihexyl-2,6-bis(3-(trifluoromethyl)phenyl)-1,5-dihydropyrrolo[2,3-f]indole; CB-3 : *N*¹,*N*⁴-dihexyl-2,5-bis((3-(trifluoromethyl)phenyl)ethynyl)benzene-1,4-diamine 7 (0.14 g, 0.23 mmol, 1eq.) in THF (2 mL) was cooled to 0 ºC and BuLi in hexane (0.20 mL, 2.5 M, 0.50 mmol, 2.2 eq.) was added dropwise to the suspended solution. The reaction mixture was allowed to reach room temperature and stirred for 30 min. Then, it followed by addition of zinc chloride in 2-methyltetrahydrofuran (0.26 mL, 1.9 M, 0.50 mmol, 2.2 eq.) and toluene (2 mL) solution to the reaction mixture. The reaction mixture was heated to 120 ºC and stirred for 3 h. After cooling to room temperature, the resulting mixture were quenched with water. The phases were extracted with EtOAc and sat. NaH_4Cl solution, dried over anhydrous magnesium sulfate, filtered. The solvent was removed in vacuo and the residue was purified by silica gel column chromatography (6:1 hexane: DCM) to give product CB-3 as a yellow solid in 55% yield (78 mg, 0.127 mmol). ^{1}H NMR (400 MHz, $CDCl_3$, δ): 7.85 (s, 2H), 7.76 (d, *J* = 7.6 Hz, 2H), 7.67 (dd, *J* = 20.6, 7.9 Hz, 4H), 7.59 (s, 2H), 6.67 (s, 2H), 4.20 (t, *J* = 7.5 Hz, 4H), 1.79 (p, *J* = 6.9 Hz, 4H), 1.21 – 1.18 (m, 12H), 0.83 (t, *J* = 6.6 Hz, 6H). ^{13}C NMR (100 MHz, $CDCl_3$, δ): 140.73, 135.44, 134.52, 132.36, 131.47, 131.15, 130.82, 130.50, 128.99, 128.16, 126.26, 125.96, 125.92, 125.88, 125.85, 125.45, 124.30, 124.26, 122.74, 102.17, 99.60, 44.41, 31.28, 29.52, 26.51, 22.49, 13.91. HRMS (ESI) *m/z*: [M⁺] calcd for $C_{36}H_{38}F_6N_2$, 613.3012, found, 613.3012.

Chapter 5 Phosphine Oxide Derivative as a Passivating Agent to Enhance Perovskite Solar Cells Performance

Defects of metal-halide perovskites detrimentally influence the optoelectronic properties of the thin film and, ultimately, the photovoltaic performance of perovskite solar cells (PSCs). Especially, defect-mediated non-radiative recombination that occurs at the perovskite interface significantly limits the power conversion efficiency (PCE) of PSCs. In this regard, interfacial engineering or surface treatment of perovskites has become a viable strategy for reducing the density of surface defects thereby improving PCE of PSCs. An important method among the surface treatment is to aim to passive under-coordinated Pb^{2+} defects using Lewis bases or electron donation materials. validate significantly increased carrier lifetimes and improved open circuit voltages in the devices reduced undercoordinated ions in the perovskite layer. Here, an organic molecule, tris(5-((tetrahydro-2*H*-pyran-2-yl)oxy)pentyl)phosphine oxide (THPPO), is synthesized and introduced as a defect passivation agent in PSCs. The P=O terminal group of THPPO, a Lewis base, can passivate perovskite surface defects such as under-coordinated Pb^{2+}. We observed significant improvements in PL characteristics of films by introducing THPPO and attributed the improvements to defect passivation effect which reduced undesirable non-radiative recombination in PSCs. Furthermore, the passivation mechanism of THPPO on under-coordinated Pb^{2+} defects was examined by XPS, XRD and ^{31}P-NMR, GIWAXS analysis. Two different device application strategies were used to fabricate the passivation molecule, the HTL-free and HTL-based PSCs device configurations. Consequently, improvement of PCEs from 19.87% to 20.70 % and from 5.84% to 13.31% are achieved in n-i-p PSCs and hole transporting layer (HTL)-free PSCs, respectively.

This chapter is based on published work: ACS Appl. Energy Mater., 2021, 4, 2, 1259–1268, DOI:10.1021/acsaem.0c02472.

Authors: Albertus Adrian Sutanto, Cansu Igci, Hobeom Kim, Hiroyuki Kanda, Naoyuki Shibayama, Mounir Mensi, Valentin I.E. Queloz, Cristina Momblona, Hyung Joong Yun, Henk J. Bolink, Aron J. Huckaba, and Mohammad Khaja Nazeeruddin. In this work I contributed equally with Albertus Adrian Sutanto as first author, we conceptualized the idea and designed the experiments. Specifically, I performed the synthesis and characterization of the passivation molecule.

5.1 Introduction

To date, various defect passivation strategies in PSCs have been reported by using inorganic,[177-179] organic molecules,[180-183] and polymers,[184,185] also through additive engineering,[186,187] grain-boundary engineering,[188] and multi-dimensional engineering,[170,189-191]

which can result in reduced non-radiative charge recombination, efficient charge collection, and thereby improving device performance. One of the effects that defect passivation can exert is to reduce the under-coordinated Pb^{2+} in the perovskite by taking advantage of Lewis base materials that have validated the improvement of carrier dynamics and device performance.[91,95,115, 192-195] Among the Lewis base materials, molecules including phosphine oxide such as tri-*n*-octylphosphine oxide (TOPO), triphenylphosphineoxide (TPPO), and tetraisopropyl methylenediphosphonate (TMPP) have been regarded as promising passivation agents due to their electron-donating ability.[91,95,196]

In this study, we synthesized a new Lewis base organic molecule containing a phosphine oxide group, ((tetrahydro-2*H*-pyran-2-yl)oxy)pentyl)phosphine oxide (THPPO), as a passivating agent on top of a perovskite layer (Figure 5.1a). The P=O group of THPPO led to the formation of a chemical bond with under-coordinated Pb^{2+} on the surface of the perovskite. The perovskite film treated with THPPO showed reduced non-radiative carrier recombination and improved PCE of PSCs. We incorporated THPPO in two different types of devices: one is a device with a n-i-p configuration (Figure 5.1b) and the other is a hole-transporting layer (HTL)-free device for the development towards simplified and cost-effective PSCs. The introduction of THPPO led to an improvement in PCE from 19.87% to 20.70% of the n-i-p devices and 5.84% to 13.31% of the HTL-free devices.

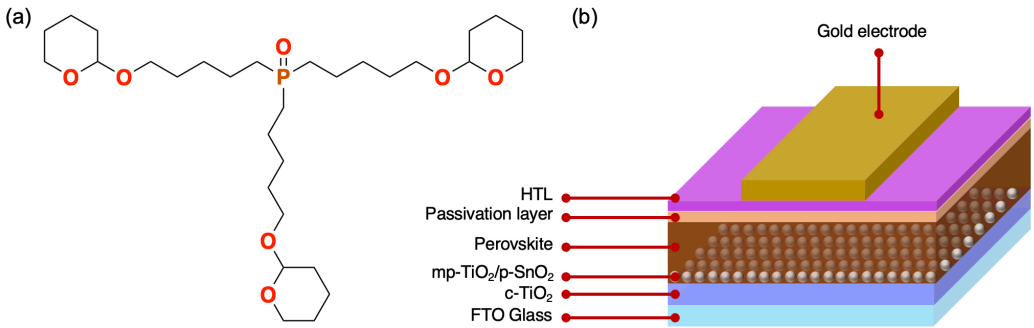

Figure 5.1 a) Molecular structure of THPPO. b) device structure of n-i-p PSCs employing fluorine-doped tin oxide (FTO), compact TiO_2 (c-TiO_2), mesoporous TiO_2 (mp-TiO_2), SnO_2, perovskite, THPPO as a passivation layer, HTL, and gold electrode.

5.2 Result and Discussion

5.2.1 Design and Synthesis of THPPO

In the molecular design of THPPO, the phosphine oxide group that provides a Lewis base was chosen as an active passivation agent for perovskites. It was functionalized with a five-carbon alkyl substituent chain to make it soluble in common organic solvents. The tetrahydropyranyl ether units were introduced to serve as likely anchors at the interface between perovskite and HTL.[197] The synthesis of THPPO began with a carboxylic acid reduction reaction of commercially available 5-bromopentanoic acid by borane-tetrahydrofuran complex to the corresponding primary alcohol.[198] Obtained 5-bromopentan-1-ol was then attached to tetrahydropyran (THP) group in the presence of *p*-toluenesulfonic acid in dichloromethane to attain tetrahydropyranyl ether functional group.[199] As a last step 2-((5-bromopentyl)oxy)tetrahydro-2*H*-pyran with magnesium formed a Grignard reagent, which reacted with phosphorous trichloride to furnish alkyl-phosphine intermediate product. Then, the intermediate product was oxidized with hydrogen peroxide in dichloromethane with high yield to obtain novel passivation molecule THPPO (Scheme 5.1).[200,201] Purification of the final compound was performed by column chromatography without the need for high-pressure vacuum distillation. The

synthesized product chemical structure was verified by ^{1}H, ^{13}C, and ^{31}P NMR spectroscopy and mass spectroscopy (Appendix D). THPPO is soluble in common organic solvents such as tetrahydrofuran (THF), chloroform, toluene, and chlorobenzene, typically used for deposition of a passivation layer in PSCs.

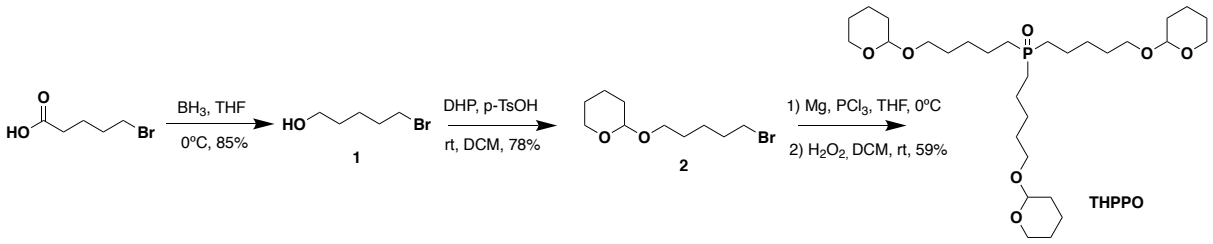

Scheme 5.1 a) Synthetic route for tris(5-((tetrahydro-2*H*-pyran-2-yl)oxy)pentyl)phosphine oxide, THPPO.

5.2.2 THPPO Thin-films Characteristics

We deposited THPPO solution dissolved in chlorobenzene with various concentrations (0.005, 0.010, 0.020, and 0.030 M) on top of a triple cation-based perovskite layer $[(FAPbI_3)_{0.87}(MAPbBr_3)_{0.13}]_{0.92}(CsPbI_3)_{0.08}$. Figure 2a shows the steady-state photoluminescence (PL) spectra of the control and THPPO-treated perovskite thin films. The films were excited with 550 nm light from the top side of the film. Emission spectra of all the films show a peak at 767 nm regardless of the concentration of THPPO while the PL intensity was improved by increasing the concentration of THPPO (Figure 5.2a) (experimental details in Appendix D). The improvement of PL intensity can be attributed to the passivation effect of THPPO, which can lead to a reduction of the density of trap states in the perovskite with enhanced radiative recombination. Meanwhile, the unchanged position of PL emission peak and absorption onset implies that the deposition of THPPO did not degrade or modify the crystal structure of underlying perovskite. To gain a better understanding of the carrier dynamics of the films, we performed time-resolved PL (TrPL) measurement of the films upon excitation at 480 nm (Figure 5.2b). The TrPL decay curves were fitted to a bi-exponential decay function (Table 5.1). All the THPPO treated perovskite thin films exhibited significantly prolonged PL lifetimes for the fast and slow components of the PL decay (t_1 and t_2, respectively). For example, the film with 0.030 M THPPO had t_1= 19.0 ns and t_2= 192.3 ns while the control film had t_1=12.6 ns and t_2 = 96.4 ns indicating that THPPO can effectively reduce the density of traps on the surface of perovskites by passivation.

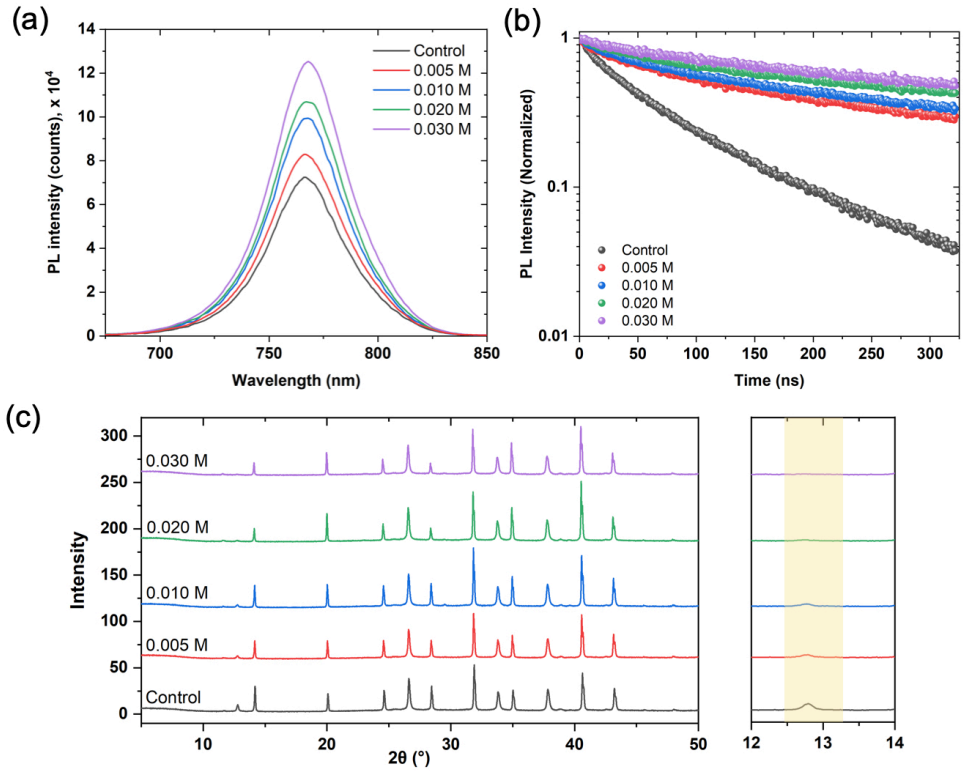

Figure 5.2 a) Steady-state PL spectra (λ_{exc}= 550 nm). b) time-resolved PL spectra (λ_{exc}= 480 nm). c) XRD patterns of control perovskite film and passivated films with various concentrations of THPPO.

THPPO Concentration [M]	t_1 [ns]	t_2 [ns]
Control	12.6	96.4
0.005	18.0	146.3
0.010	19.6	184.6
0.020	19.4	193.4
0.030	19.9	192.3

Table 5.1 Bi-exponential decay function, $y = y_0 + A_1 e^{-x/t1} + A_2 e^{-x/t2}$ fitted PL lifetime curves of perovskite films.

X-ray diffraction (XRD) of the perovskite films showed the typical pattern of triple-cation and mixed-halide perovskites.[21] The deposition of THPPO did not cause an additional formation of a new pattern indicating that it did not alter the crystalline structure of perovskites (Figure 5.2c). As we used an excessive amount of PbI_2 in the perovskite, the pristine film accordingly showed a noticeable peak at 12.7° that can be assigned to the residual PbI_2. However, the peak intensity was reduced by the deposition of THPPO. As PbI_2 is a well-known Lewis acid, the reduction of the PbI_2 peak intensity of the THPPO-treated films can be explained by the formation of PbI_2·THPPO adduct (Figure 5.2c).[202,203]

5.2.3 Surface Characterization of THPPO

The surface morphology of the perovskite films treated with various concentrations of THPPO was observed by scanning electron microscopy (SEM) images (Figure 5.3a) (experimental details in Appendix D). The pristine film showed sparsely distributed bright

grains that can be attributed to the residual PbI_2. Upon the deposition of 0.005 M THPPO, the density of the bright grains decreased, and the color became darker as PbI_2 was transformed into PbI_2·THPPO adduct, which is consistent with the result of XRD.[202] The use of 0.010 M THPPO decreased the effective area of perovskite grains while increasing its occupation between the grains. Therefore, the surface contact area between the perovskite grains and THPPO was significantly increased possibly leading to more effective passivation. However, a further increase in the concentration of THPPO resulted in thicker and nonhomogeneous coverage on top of the perovskite grains showing a stronger contrast.

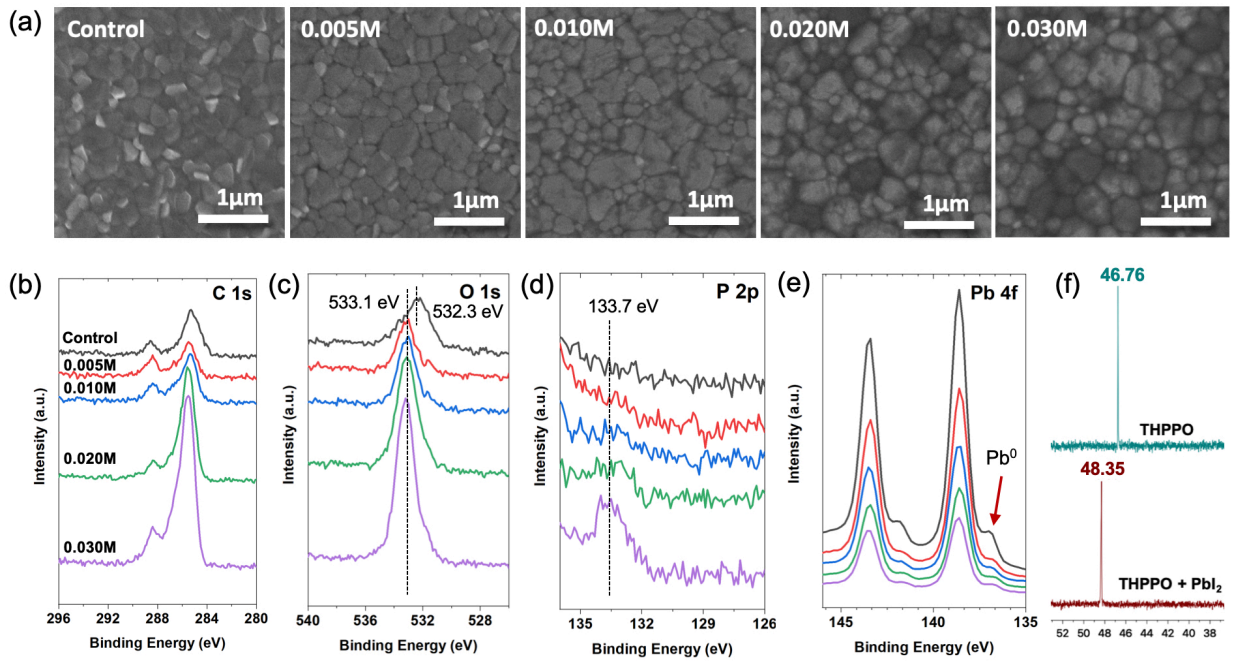

Figure 5.3 a) SEM images: surface morphology of control perovskite film and films with various concentrations of THPPO. Core level XPS spectra of b) C 1s, c) O 1s, d) P 2p, and e) Pb 4f of control perovskite film and films with various concentrations of THPPO. f) ^{31}P-NMR spectra of 0.01 mmol THPPO and THPPO mixed with 0.01 mmol PbI_2 in DMSO-d_6.

The presence of THPPO on the perovskite surface was characterized by X-ray photoelectron spectroscopy (XPS) (experimental details in Appendix D). The C 1s spectrum of the control film exhibited two main peaks at 285.5 and 288.4 eV, which can be attributed to C-C bond and C=O bond, respectively (Figure 5.3b).[204] The increase in THPPO concentration resulted in a significant increase in the peak intensity of the C-C bond because the deposited THPPO has an increasing number of C-C bonds of three pentyl chains with tetrahydropyran ether. The peak of C=O bond at 288.4 eV might originate from the contamination of the perovskite upon the exposure to the ambient air during the sample transfer for the measurement.[205] The peak at 532.3 eV of the control film in the O 1s spectra, can be also attributed to O=C bond formed by the surface oxidation (Figure 5.3c).[206,207] The deposition of THPPO caused an appearance of an additional peak at 533.1 eV that arose from tetrahydropyran and ether of THPPO showing a significant increase in the intensity as increasing the concentration of THPPO.[208] In the P 2p spectra, we confirmed a peak that originated from the P=O bond of THPPO at 133.7 eV (Figure 5.3d).[209,210]

The Pb 4f spectra verified the passivation effect of THPPO (Figure 5.3e). The pristine film showed four prominent peaks at 136.9, 138.6, 141.8, and 143.4 eV. Pb $4f_{7/2}$ and Pb $4f_{5/2}$ peaks at 138.6 and 143.4 eV can be attributed to lead halide bonds, while Pb $4f_{7/2}$ and Pb $4f_{5/2}$ peaks at 136.9 and 141.8 eV can be attributed to Pb^0. It is worth noting that Pb^0 peak can arise out of the under-

coordinated Pb^{2+}, which can act as a non-radiative recombination center leading to degradation of device performance.[211,212] Upon the deposition of THPPO, the apparent decrease in the intensity of Pb^0 was observed and confirmed by the quantitative analysis of Pb^0 (Table 5.2). The reduction in the Pb^0 ratio can be explained by the coordination between the under-coordinated Pb^{2+} and the lone pair electron from Lewis base of THPPO, which resulted in defect passivation.[115,213,214]

THPPO Concentration [M]	Ratio of Pb^0 out of the total Pb [%]
Control	10.16
0.005	5.75
0.010	5.75
0.020	6.34
0.030	6.50

Table 5.2 Quantitative analysis of Pb 4f spectra presenting the ratio of Pb^0 in perovskite films with various concentrations of THPPO.

To further elucidate the interaction between THPPO and the under-coordinated Pb^{2+} on the perovskite surface, we performed ^{31}P-NMR spectroscopy (Figure 5.3f). The measurement was carried out by using 0.01 mmol THPPO dissolved in 0.5 mL DMSO-d_6 followed by the addition of 0.01 mmol PbI_2. As the dissociation of PbI_2 in the solution can yield the under-coordinated Pb^{2+}, we can investigate the underlying mechanism of the passivation by examining its interaction with THPPO. While the phosphorous peak of pristine THPPO was at 46.76 ppm, the addition of PbI_2 shifted the peak to 48.35 ppm. The downfield shift indicates that the electron density of the phosphorous nucleus decreases as P=O functional group as a Lewis base donates electrons to Pb^{2+} triggering the passivation effect.[91,95,193]

5.2.4 GIWAXS Characterization of THPPO

To investigate the molecular stacking state of THPPO, we carried out grazing-incident wide angle X-ray scattering (GIWAXS) analysis (experimental details in Appendix D). The control film had a Debye-Scherrer ring at q_z = 1.0 $Å^{-1}$ which can be attributed to (100) crystal planes of the cubic phase of the perovskite (Figure 5.4a). Upon the deposition of THPPO on top of the perovskite layer, new peaks appeared at q_z = 0.40 and 0.79 $Å^{-1}$ that resulted from the out-of-plane orientation of THPPO on the perovskite layer (Figure 5.4b). Azimuthally integrated intensity profile of the film with THPPO also clearly showed the prominent peak at 0.40 $Å^{-1}$ having a lattice spacing of 15.9Å that corresponds to the size of THPPO simulated by a molecular mechanics force field (Figure 5.4c and 5.4d). The peak at 0.79 $Å^{-1}$ can be ascribed to the second diffraction peak of THPPO. We examined the angular dependence of the diffraction peak at 0.40 $Å^{-1}$ to obtain a detailed insight about the molecular stacking state of THPPO (Figure 5.4e). The intensity of the peak became prominently high at the low incident angle range below 20° indicating vertically well-aligned THPPO, so-called 'edge-on' stacking. Therefore, the P=O group can effectively interact with the under-coordinated Pb^{2+} of the perovskite octahedral that can lead to the formation of the Lewis adduct, which agrees well with the result of ^{31}P-NMR analysis. The illustration of tbe passivation mechanism was shown in Figure 5.4f.

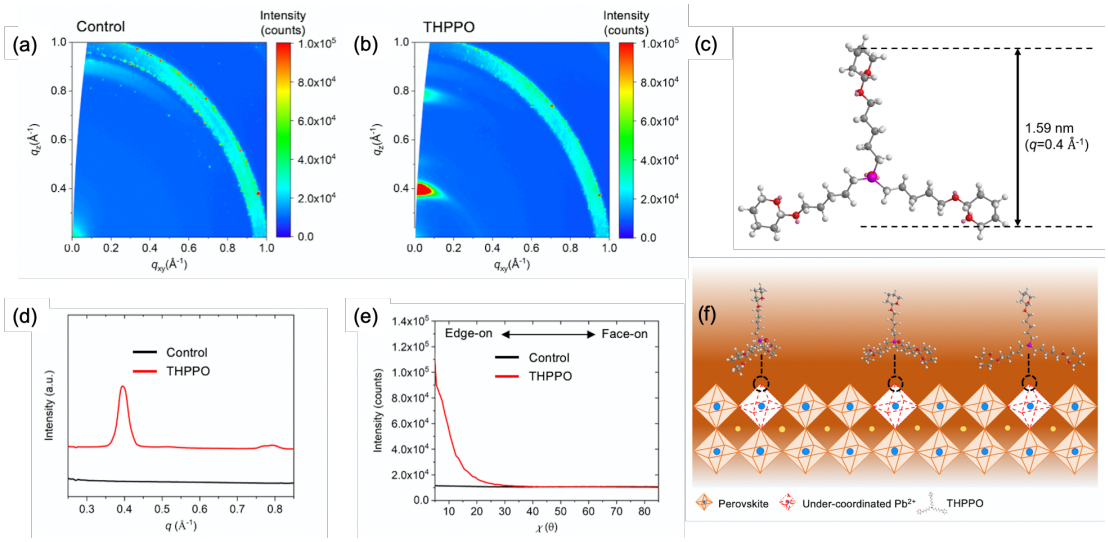

Figure 5.4 GIWAXS patterns of a) control perovskite film and b) THPPO-treated perovskite film. c) Molecular modelling of THPPO by molecular mechanics force field (MM2, Chem3D) method with the condition of molecular dynamics at 2.0 fs step interval and heating/cooling rate of 1.0 Kcal/atom/ps at 300 K.d) Azimuthally integrated intensity profile obtained from GIWAXS patterns. e) Angular dependence of the peak intensity at 0.40 Å^{-1}. f) Cartoon illustration of the proposed passivation mechanism. The concentration of THPPO is 0.030 M.

5.2.5 Energy Level Characterization of Layers

We performed ultraviolet photoelectron spectroscopy (UPS) to examine the energy level alignment of perovskites upon the surface modification using THPPO (Figure 5.5a and 5.5b). The control film exhibited -5.70 eV of valence band (VB) energy and the energies gradually increased to -5.60 eV, -5.59 eV, and -5.58 eV according to the deposition of 0.005, 0.010, and 0.020 M of THPPO on top of the perovskite film, respectively (Figure 5.5c). The positive shift in the VB edge by the THPPO treatment resulted in a favourable energetic alignment between perovskite and spiro-OMeTAD or gold electrode, which can facilitate hole transfer between the layers.

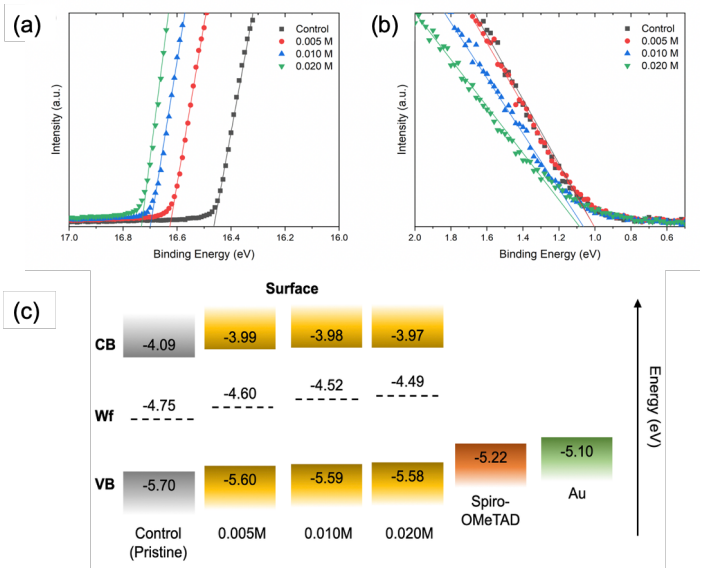

Figure 5.5 Ultraviolet photoelectron spectroscopy (UPS) spectra of control perovskite film and THPPO passivated perovskite films showing a) secondary cut-off and b) onset. c) Energy level diagram showing the valence band (VB), work function, and conduction band (CB) of the control and THPPO-passivated perovskite films.

5.2.6 Device Characteristics

We employed THPPO as a passivating agent in PSCs without HTL (fluorine-doped tin oxide (FTO)/compact-TiO_2 (c-TiO_2)/mesoporous-TiO_2 (mp-TiO_2)/SnO_2/perovskite/THPPO/Au). Various concentrations of THPPO from 0.005 M to 0.030 M were applied to find an optimal condition of THPPO treatment in PSCs (experimental details in Appendix D). Cross-sectional SEM images showed well-deposited electron transporting layers (compact-TiO_2/mesoporous-TiO_2/SnO_2) and perovskite layer (~500 nm) and top Au electrode. However, the THPPO layer was not easily recognized due to its very thin thickness (Figure 5.6).

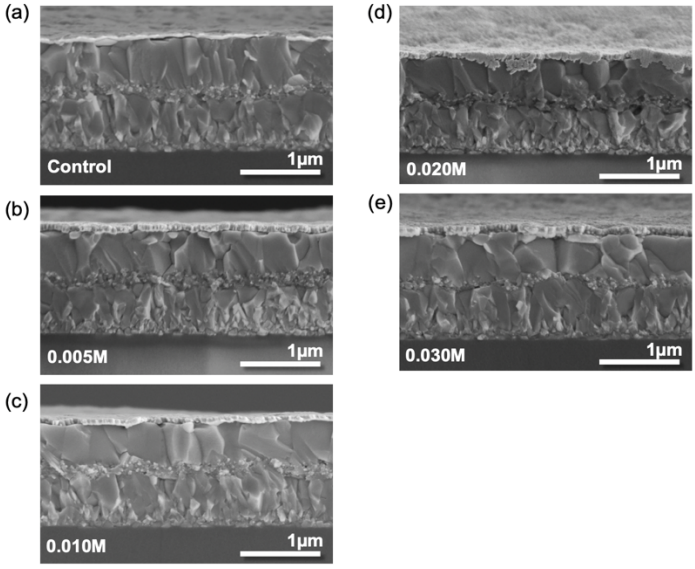

Figure 5.6 Cross-sectional SEM images of control device and HTL-free devices employing THPPO with various concentrations (FTO/compact TiO_2/mesoporous TiO_2/passivated SnO_2/perovskite/THPPO/Au).

All the THPPO-passivated devices showed improved photovoltaic performance compared to the control device (Figure 5.7a) (experimental details in Appendix D). Detailed device parameters were shown at Table 5.3. The best performing device was achieved upon the deposition of 0.010 M THPPO having open-circuit voltage (V_{OC}) of 0.866 V, short-circuit current density (J_{SC}) of 23.32 mA cm^{-2}, and fill factor (*FF*) of 0.689, resulting in a PCE of 13.31%. We also measured external quantum efficiency (EQE) of the device (Figure 5.7b). The statistical analysis of the 96 HTL-free devices with THPPO passivation layer was performed and the results are summarized in Figure 5.7c, d, e and Table 5.4. We statistically confirmed that the improvement of PCE by the THPPO treatment mainly resulted from the enhancement in V_{OC} (Figure 5.7d and Table 5.4). The average V_{OC} of the control device was 0.64 V and increased to 0.84 V with the use of 0.010 M of THPPO and it saturated with a further increase in the concentration of THPPO. The improvement in V_{OC} can be ascribed to the reduced non-radiative recombination owing to the defect passivation effect of THPPO that we confirmed by the PL analyses.[215] The average J_{SC} and *FF* of the devices also improved by applying 0.010 M of THPPO from 22.3 mA cm^{-2} to 23.1 mA cm^{-2} and from 0.31 to 0.62, respectively. The improvements can be explained by the reduced density of trap states owing to the passivation effect of THPPO. In addition, the favourable energetic band alignment between THPPO and Au can lead to the facilitation of charge transfer. However, a further increase in the THPPO concentration degraded both J_{SC} and *FF* because of the insulating nature of THPPO.[216] It can hinder efficient charge transfer by increasing series resistance at the interface (Figure 5.7e and Table 5.4,). We also fabricated the device to compare THPPO and trioctylphosphine oxide (TOPO), one of the most widely used phosphine oxide-based passivation agent.[95,196] The device employing 0.010 M TOPO resulted in a lower photovoltaic performance with a PCE of 9.36% compared to the device using 0.010 M THPPO (Figure 5.7f).

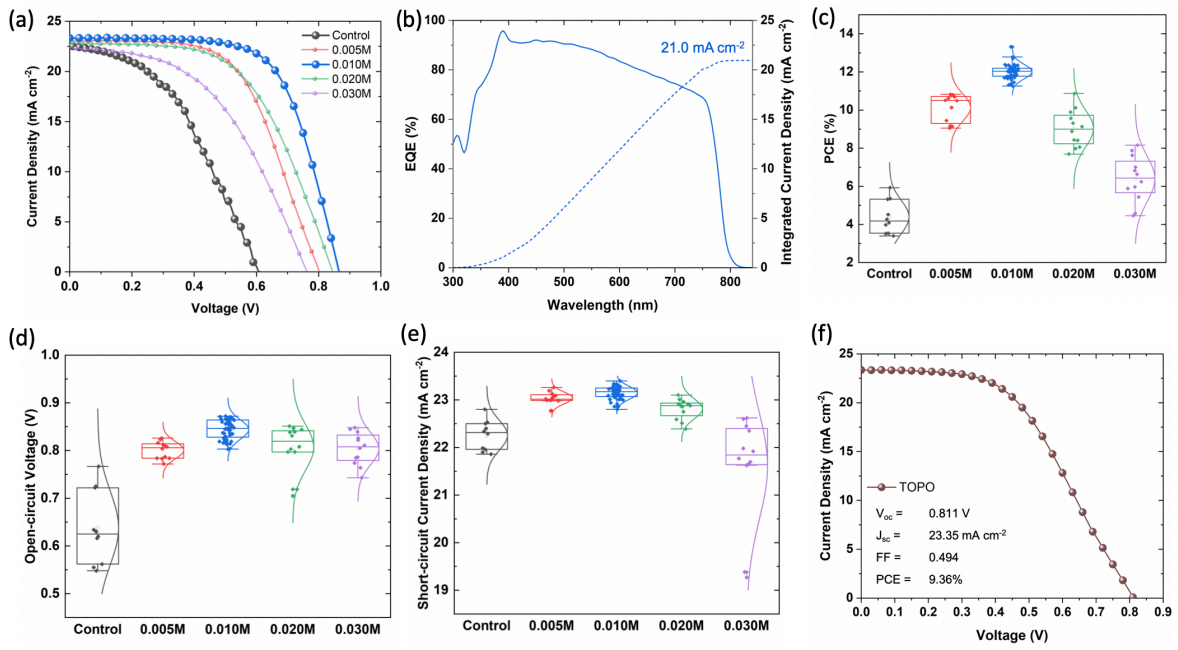

Figure 5.7 Photovoltaic characteristics of control and THPPO-passivated perovskite solar cells. a) Current density-Voltage (*J-V*) curves, f b) EQE spectrum and the integrated J_{SC} of the THPPO-passivated PSC with HTL. Statistics of 96 HTL-free devices for c) PCE, d) open-circuit voltage and e) short-circuit current density. f) *J-V* curve of the best performing HTL-free PSC using 0.010 M of trioctylphosphine oxide (TOPO) as a passivating agent.

THPPO Concentration [M]	V_{OC} [V]	J_{SC} [mA cm^{-2}]	*FF*	PCE [%]
Control	0.610	22.53	0.425	5.84
0.005	0.804	23.01	0.585	10.83
0.010	0.866	23.32	0.659	13.31
0.020	0.847	22.86	0.562	10.87
0.030	0.764	22.35	0.478	8.16

Table 5.3 PV parameters of the champions cells of PSCs employing THPPO as a passivation layer with various conditions.

THPPO Concentration [M]	V_{OC} [V]	J_{SC} [mA cm^{-2}]	*FF*	PCE [%]
Control	0.64 ± 0.08	22.3 ± 0.3	0.31 ± 0.05	4.4 ± 0.9
0.005	0.80 ± 0.02	23.0 ± 0.1	0.55 ± 0.04	10.1 ± 0.7
0.010	0.84 ± 0.02	23.1 ± 0.1	0.62 ± 0.02	12.0 ± 0.4
0.020	0.81 ± 0.05	22.8 ± 0.2	0.49 ± 0.04	9.0 ± 1.0
0.030	0.80 ± 0.03	21.6 ± 1.1	0.37 ± 0.06	6.4 ± 1.2

Table 5.4 Average values of PV parameters of 96 PSCs according to various conditions of THPPO.

We developed PSCs including spiro-OMeTAD as an HTL, while using the optimized THPPO treatment of 0.010 M with the configuration of FTO/c-TiO_2/mp-TiO_2/SnO_2/perovskite/THPPO/spiro-OMeTAD/Au. Prior to the device fabrication, we performed ^{31}P NMR spectroscopy to confirm the well-formed THPPO on top of the perovskite despite the deposition of spiro-OMeTAD that also uses chlorobenzene as a solvent (Figure 5.8). While the control device exhibited V_{OC} of 1.064 V, J_{SC} of 23.76 mA cm^{-2}, *FF* of 0.786, and PCE of 19.87%, the device with the THPPO passivation layer showed V_{OC} of 1.108 V, J_{SC} of 24.08 mA cm^{-2}, *FF* of 0.776, and PCE of 20.70%. (Figure 5.9a and Table 5.5). We measured EQE spectrum of the device with passivation (Figure 5.9b). Also, we evaluated *J-V* hysteresis of the THPPO-passivated device and the control device by measuring them under reverse and forward bias scans. The control device showed PCE of 19.85 % and 17.70 % under reverse and forward bias scans, respectively (Figure 5.9d). The calculated result in a hysteresis index (HI) is 0.11, defined as $\frac{PCE_{reverse}-PCE_{forward}}{PCE_{reverse}}$. Meanwhile, the THPPO-passivated device showed more stable *J-V* hysteresis behaviour having HI of 0.06 resulted from PCE of 20.67 % and 19.43 % under reverse and forward bias scans, respectively (Figure 5.9c). The improvement of the *J-V* characteristics can be attributed to the passivation effect and favourable band alignment for charge extraction.

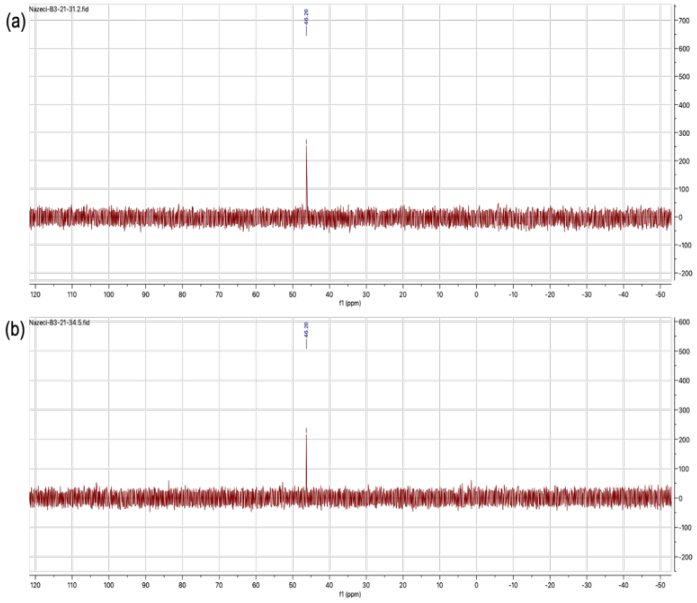

Figure 5.8 ^{31}P NMR spectra of 0.030M THPPO-treated perovskite films dissolved in DMSO-d_6 a) without chlorobenzene washing and b) with chlorobenzene washing.

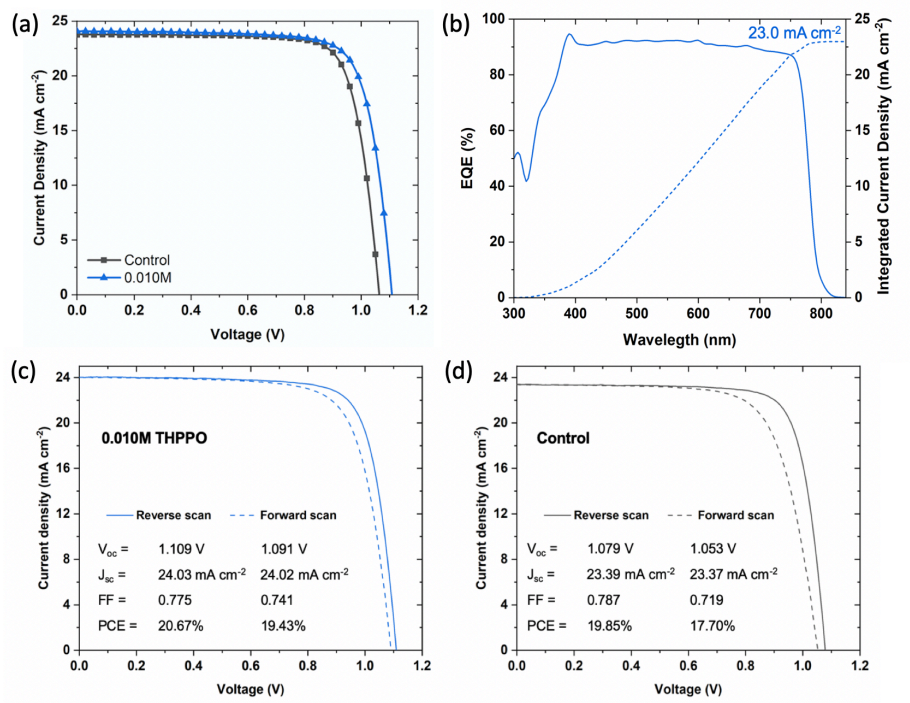

Figure 5.9 a) *J-V* curves of n-i-p devices using spiro-OMeTAD as an HTL. b) EQE spectrum and the integrated J_{SC} of the THPPO-passivated PSC with spiro-OMeTAD as an HTL. *J-V* hysteresis characteristics of

c) HTL-based PSCs with 0.010M THPPO passivation and d) control device.

THPPO Concentration [M]	V_{OC} [V]	J_{SC} [mA cm-2]	*FF*	PCE [%]
Control	1.059 ± 0.005	23.8 ± 0.2	0.781 ± 0.007	19.7 ± 0.2
0.010	1.106 ± 0.002	24.1 ± 0.1	0.768 ± 0.008	20.5 ± 0.2

Table 5.5 Average values of PV parameters of PSCs employing spiro-OMeTAD as an HTL.

Lastly, we performed stability measurement of the HTL-free devices by storing the devices under dark with relative humidity kept below 10 % (Figure 5.10a). A significant improvement of the stability was observed for the THPPO-passivated device that retained 96 % of its maximum efficiency after 360 hours however, the control device only retained 62 % of its maximum efficiency for the same time window. The improvement in the device stability might be correlated with the THPPO's high decomposition temperature (T_d) of 251 °C obtained from thermogravimetric analysis (Figure 5.10b).

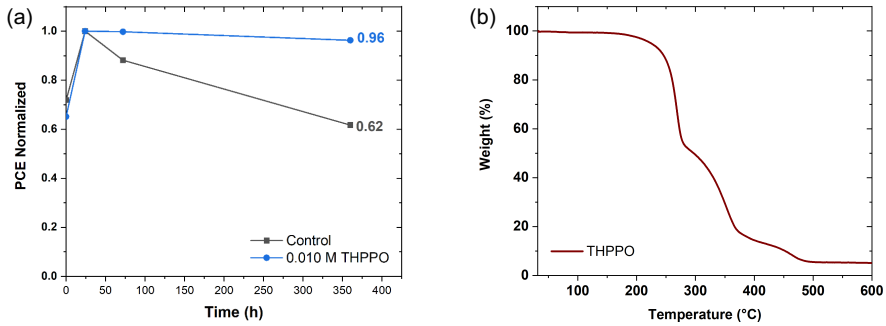

Figure 5.10 a) Stability measurement of HTL-free devices without THPPO and with 0.010 M THPPO for 360 h. The devices have been stored under dark with relative humidity (RH) below 10%. b) Thermogravimetric analysis (TGA) of THPPO. The high decomposition temperature (T_d) of 251 °C was determined at the 5 % weight loss of THPPO.

5.3 Conclusion

In conclusion, we successfully synthesized a new molecule, THPPO, based on phosphine oxide derivative and demonstrated its application as a passivating agent in PSCs. We observed significant improvements in PL characteristics of the perovskite films by introducing THPPO. It was attributed to defect passivation effect of THPPO, which reduced undesirable non-radiative recombination at the interface. Various analyses such as XPS, XRD, and ^{13}P-NMR spectroscopy verified the defect passivation effect in which a chemical interaction occurs between under-coordinated Pb^{2+} and P=O functional group of THPPO. It can lead to the formation of Lewis adduct based on well-aligned THPPO on top of the perovskite layer. Consequently, PCE of HTL-free device increased from 5.84 to 13.31% and that of the device with spiro-OMeTAD as an HTL increased from 19.87% to 20.70%. We believe this study provides insights about an important approach to design a new passivating molecule that can improve the performance of PSCs but also sheds light on the understanding of defect passivation mechanism.

5.4 Synthetic methods and Procedures

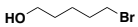

5-bromopentan-1-ol; 1. To a solution of 5-bromopentanoic acid (2 g, 11.0 mmol) in THF (15 mL) borane tetrahydrofuran complex solution (1 M, 13 mL, 13 mmol) was added at 0 °C under inert atmosphere. The mixture was stirred at rt for 3 h. Then, water/THF mixture (1:1, 20 mL) were added to the resulting mixture to quench reaction. The aqueous layer was extracted with diethyl ether (20 mL x 3), then combined organic layers were concentrated to give 1.57 g (9.38 mmol, 85 %) 5-bromopentan-1-ol 1 as a pale liquid. ^{1}H NMR (400 MHz, $CDCl_3$, δ): 3.66 (t, J = 6.4 Hz, 2H), 3.43 (t, J = 6.7 Hz, 2H), 1.95 – 1.86 (m, 2H), 1.64 – 1.49 (m, 4H, -CH_2). ^{13}C NMR (100 MHz, $CDCl_3$, δ): 62.55, 33.74, 32.51, 31.77, 23.45. HRMS (ESI) m/z: [M^+] calcd for $C_5H_{11}OBr$, 166.00, found, 165.99.

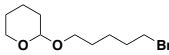

2-((5-bromopentyl)oxy)tetrahydro-2H-pyran; 2. A solution of the 5-bromopentan-1-ol **1** (1.2 g, 7.18 mmol), 3,4-dihydro-2*H*-pyran (1.0 mL, 10.9 mmol) and p-toluenesulfonic acid mono hydrate (13.6 mg, 0.07 mmol) in dichloromethane (10 mL) was stirred at rt for 3 h. After addition of diethyl ether (12 mL), washed with saturated $NaHCO_3$(aq) (15 mL) and brine solution (15 mL). The combined organic layers were dried with Na_2SO_4, filtered and concentrated under reduced pressure. The resulting residue was purified by silica gel column chromatography (1:9 EtOAc:hexane) to yield 2 (1.4 g, 5.60 mmol, 78 %) as a colourless oil. ^{1}H NMR (400 MHz, $CDCl_3$, δ): 4.59 (dd, J = 4.6, 2.7 Hz, 1H), 3.91 – 3.85 (m, 1H), 3.77 (dt, J = 9.7, 6.5 Hz, 1H), 3.55 – 3.49 (m, 1H), 3.48 – 3.38

(m, 3H), 1.96 – 1.49 (m, 12H). ^{13}C NMR (100 MHz, $CDCl_3$, δ): 98.93, 67.24, 62.40, 33.76, 32.64, 30.76, 28.90, 25.49, 25.01, 19.69. HRMS (ESI) *m*/*z*: [M^+] calcd for $C_{10}H_{19}BrO_2$, 250.05, found, 250.06.

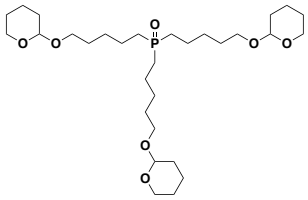

tris(5-((tetrahydro-2H-pyran-2-yl)oxy)pentyl)phosphine oxide; THPPO. Magnesium (0.19 g, 7.94 mmol) and dry THF (4 mL) were placed under inert atmosphere and 0.5 mL a solution of the total amount of 2-((5-bromopentyl)oxy)tetrahydro-2*H*-pyran **2** (1.2 g, 4.78 mmol) in THF (4 mL) were added followed by few drops of 1,2-dibromoethane. The mixture was cooled to 0 °C and remaining portion of the 2-((5-bromopentyl)oxy)tetrahydro-2*H*-pyran was added dropwise. The reaction mixture was stirred at rt for 2 h, then, it was cooled to 0 °C and a solution of PCl_3 (0.08 mL, 0.96 mmol) in THF (1 mL) was added over 10 min. After the mixture was stirred at rt overnight, saturated aqueous NH_4Cl (2 mL) was added. The solvent was removed under reduced pressure. The crude product was dissolved in dichloromethane (10 mL) and H_2O_2 (0.2 mL, 30% (w/w) in H_2O) was added. The solution was stirred for 1h, and 10 mL of water was added. Then, the phases extracted with DCM and sat. $NaCO_3$ solution. The solvent was removed in vacuo and the residue was purified by silica gel column chromatography (1:9 MeOH:DCM) to yield to yield THPPO as a yellow oil (1.58 g, 59% yield). ^{1}H NMR (400 MHz, $CDCl_3$, δ): 4.57 (t, *J* = 3.7 Hz, 3H), 3.87 (ddd, *J* = 10.9, 7.3, 3.4 Hz, 3H), 3.76 (dt, *J* = 9.6, 6.6 Hz, 3H), 3.51 (ddd, *J* = 10.7, 5.7, 3.3 Hz, 3H), 3.40 (dt, *J* = 9.6, 6.3 Hz, 3H), 1.88 – 1.79 (m, 3H), 1.76 – 1.45 (m, 39H). ^{13}C NMR (100 MHz, $CDCl_3$, δ): 98.98, 67.25, 62.49, 30.77, 29.34, 27.92, 27.56, 25.47, 21.64, 19.75. ^{31}P NMR (300 MHz, $CDCl_3$, δ): 46.76. HRMS (ESI) *m*/*z*: $[M+Na]^+$ calcd for $C_{30}H_{57}O_7P$, 583.37, found, 583.38.

Chapter 6 Conclusion

The focus of this thesis is the development of novel small-molecule organic materials for perovskite solar cells. Specifically, most of the work described in the thesis has focused on the design and molecular engineering of various low molecular weight hole transport materials. In addition, an interfacial layer was developed at the interface of the perovskite/hole transport material with the Lewis base passivation molecule. The main goal was to reveal the key roles of the synthesized novel organic materials in determining the performance and stability of PSC devices through structural, chemical, optical, and photovoltaic analyses. Thus, these organic materials applied to perovskite solar devices have been extensively researched to provide a clear understanding of how the working mechanism of organic materials can be tuned to improve the photovoltaic performance and long-term stability of the devices.

- In the second chapter, I have designed and synthesized three novel small-molecule HTMs with donor–π-bridge–acceptor (D–π–A) design principle. Triazatruxene-based donor units were functionalized with terthiophene conjugated arms as π unit, then differentiated into CI-B1, CI-B2 and CI-B3 HTMs by linking different strong electron-accepting units. HTMs were obtained from six linear steps synthetic effort with simple and inexpensive starting materials. I mainly investigated the role of strong acceptors such as 1,3-indandione, *N*-ethyl rhodanine, and dicyanovinylene *N*-ethyl rhodanine on these HTMs for the application of dopant-free perovskite solar cells. Research on HTMs through photophysical and electrochemical experiments showed that the molecules' HOMO and LUMO energy levels well-align with the energy levels of perovskite material. Moreover, GIWAXS results revealed that all three HTMs undergo π-π stacking interaction, although CI-B1 and CI-B2 are packed in random orientation, especially CI-B3 molecules are packed in favor of a well-ordered edge-stacking fashion. In parallel, when the hole extraction ability of the HTMs were investigated, CI-B3 was exhibited to have higher conductivity and hole mobility. CI-B1, CI-B2 and CI-B3 HTMs without any chemical additives or doping were applied on triple cation perovskite composition $Cs_{0.1}(MA_{0.15}FA_{0.85})_{0.9}Pb(I_{0.85}Br_{0.15})_3$ (MA: $CH_3NH_3^+$, FA: $NH{=}CHNH_3^+$) in n-i-p architecture of PSCs. The PSC with HTM CI-B3 showed an impressive power conversion efficiency of 17.54% with a small hysteresis and improved long-term stability. According to MMP tracking results, 88% of its original PCE was maintained after 1000 h of illumination, while device containing doped spiro-OMeTAD rapidly dropped to 70% of its initial value.

- In the third chapter, I have expanded the use of donor–π-bridge–acceptor (D–π–A) based dopant-free HTM for all-inorganic perovskite solar cells. I designed and synthesized novel HTM CI-TTIN-2F with triazatruxene-based donor unit and terthiophene conjugated arm and functionalized with a strong electron-withdrawing acceptor unit, 2-(5,6-difluoro-3-oxo-2,3-dihydro-1*H*-inden-1-ylidene)malononitrile (IN-2F). CI-TTIN-2F molecule were examined to understand its characteristics in optoelectronics. It showed good thermal stability, good hydrophobic property with the help of fluorine atoms, an additional NIR absorption for ultra-strong intermolecular charge transfer, and narrow optical bandgap. The HOMO level of CI-TTIN-2F found well aligned with the valence band energy level of the $CsPbI_3$ inorganic perovskite. Moreover, GIWAXS results revealed that CI-TTIN-2F possess multiple orientations in films, besides face-on orientation in π-π stacking, it also has edge-on stacking that supports charge transfer. We further investigated the HTM/inorganic perovskite interfaces with molecular dynamics calculations to reveal passivation effect of the molecule by the presence of various het-

eroatoms. According to MD simulations results, it was understood that Cl-TTIN-2F can interact with Pb on the perovskite surface with different types of contacts. Specifically, the CN groups of the acceptor units, the F atoms of the acceptor and the lone pairs electrons on sulfur atoms of the π-bridges can interact with the Pb^{2+} cations of the surface. In light of this information, we applied dopant-free and hydrophobic Cl-TTIN-2F HTM on the all-inorganic $CsPbI_3$ PSCs to able to improve undesirable phase transition of $CsPbI_3$ in ambient. As a result, all-inorganic $CsPbI_3$ PSCs with dopant-free Cl-TTIN-2F HTM demonstrate a high PCE of 15.9%, along with 86% efficiency retention after 1000 hours under ambient conditions. In particular, the largest all-inorganic perovskite solar module was fabricated using the Cl-TTIN-2F HTM, and exhibited an efficiency of 11.0% with an area of 27 cm^2.

- In chapter 4, I have designed and synthesized three benzodipyrrole-based organic small-molecules with substituted 4-methoxyphenyl (CB-1), 3-fluorophenyl (CB-2), and 3-trifluoromethylphenyl (CB-3). The synthesis was completed in a straightforward seven-step effort, conducting with simple and inexpensive materials. When the electrochemical, optical, thermal, electronic, and optoelectronic properties of the HTMs were characterized, it was concluded that they have planar structural geometry, good thermal stability, well aligned HOMO levels with the valence band energy level of the typical lead iodide-based perovskites, as well as good charge transport and hole collection properties. We further investigated the HTM/inorganic perovskite interfaces with PL characteristics and MD simulations to reveal passivation effect of the molecule on the perovskite surface. For CB-2 and CB-3 molecules, both suppressed PL quenching, retarded PL decay of the films and MD simulations showed the fluorinated aryl units present in these molecules efficiently contribute to defect passivation. In addition, the molecular planarity of CB-2 was confirmed by the simulation and the calculation of small dihedral angle between the BDP unit and the 3-fluorophenyl of CB-2, which can lead to the intermolecular π–π interaction and thus facilitate the hole extraction. CB-1, CB-2 and CB-3 HTMs were applied on triple cation perovskite composition $(FAPbI_3)_{0.87}(MAPbBr_3)_{0.13}]_{0.92}(CsPbI_3)_{0.08}$ in n-i-p architecture of PSCs. Among them, the PSC using CB-2 achieved the highest PCE of 18.23% with improved V_{OC} and *FF,* while the devices using CB-1 and CB-3 exhibit a lower PCE of 16.78% and 16.74%, respectively. The lack of passivation effect of CB-1 HTM and the inferior hole-transporting capability and non-planar molecular configuration of CB-3 HTM were found to be possible causes of poor performance in PSCs. Moreover, the molecular hydrophobicity of the fluorinated HTMs enabled the devices to demonstrate excellent long-term storage stability in the air without encapsulation and showed no degradation of their PCEs over 6 months.

- In chapter 5, I have designed and synthesized THPPO, a novel phosphine oxide derivative molecule obtained in a facile 3-step synthetic route. In the molecular design of THPPO, the phosphine oxide group that provides a Lewis base was chosen as an active passivation agent for perovskites. It was functionalized with a five-carbon alkyl substituent chain to make it soluble in common organic solvents. The tetrahydropyranyl unit was combined with the ether group as effective anchors at the interface between perovskite and HTL. Design principle was targeting to passivate the defect on the surface of the perovskite layer, especially the undercoordinated Pb^{2+} sites. With the integration of THPPO passivation layer on top of the perovskite layer, PL characteristics of films showed significant improvements due to the defect passivation effect by forming Lewis adduct, which reduces undesirable non-radiative recombination in PSCs. Furthermore, we validated interaction between under-coordinated Pb^{2+} and P=O functional Lewis base of THPPO by XPS, XRD and ^{13}P-NMR spectroscopy. Moreover, THPPO integrated perovskite films demonstrated a positive shift in the energy level alignment compared to the pristine film, facilitating hole transfer between the layers. Hence, two different device application strategies were used to fabricate the passivation molecule, the HTL-free and HTL-based PSCs device configurations. The HTL-free devices have confirmed a significant increase in PCE from 5.84% to 13.31% with the help of the passivation effect and improved energy level alignment. Further, THPPO boosted the device's PCE from 19.87% to 20.70% when combining the device with spiro-

OMeTAD as an HTM in n-i-p configuration. Also, a significant improvement of the stability was observed for the THPPO-passivated device that retained 96 % of its maximum efficiency after 360 hours.

Summarizing, I have extensively investigated small molecule organic materials for perovskite solar cell application and the reasons behind the improving photovoltaic performance and stability of PSCs. I designed and synthesized different HTM series and p-type passivation molecule throughout the thesis aiming to gain a basic understanding of the requirements of organic materials and lead to further improvement of photovoltaic performance. I believe my thesis paves the way for providing a fundamental understanding of the relationships between the molecular structure and performance of organic materials in operating devices. With the ultimate goal of commercialization of PSCs, research on applications of organic materials should increase so that it is possible to obtain high-performance, stable and low-cost PSCs. I hope that the well-performing materials presented in my thesis will provide further motivation for the development of new materials and contribute to the acquisition of PSCs for commercial application.

References

[1] International Energy Agency (IEA), World Energy Outlook 2020. https://www.iea.org/reports/world-energy-outlook-2020, (accessed October, 2021).

[2] British Petroleum (BP), Statistical Review of World Energy 2021, 70th edition. https://www.bp.com/content/dam/bp/business-sites/en/global/corporate/pdfs/energy-economics/statistical-review/bp-stats-review-2021-full-report.pdf, (accessed October, 2021).

[3] R. Williams, *J. Chem. Phys.*, 1960, **32**, 1505.

[4] D. M. Chapin, C. S. Fuller and G. L. Pearson, *J. Appl. Phys.*, 1954, **25**, 676.

[5] National Renewable Energy Laboratory (NREL), Best Research-Cell Efficiency Chart, https://www.nrel.gov/pv/cell-efficiency.html, (accessed October, 2021).

[6] D. Weber, *Z. Naturforsch.*, 1978, **33**, 1443.

[7] D. B. Mitzi, C. A. Feild, W. T. A. Harrison and A. M. Guloy, *Nature*, 1994, **369**, 467–469.

[8] A. Kojima, K. Teshima, Y. Shirai and T. Miyasaka, *J. Am. Chem. Soc.*, 2009, **131**, 6050–6051.

[9] H.-S. Kim, C.-R. Lee, J.-H. Im, K.-B. Lee, T. Moehl, A. Marchioro, S.-J. Moon, R. Humphry-Baker, J.-H. Yum, J. E. Moser, M. Grätzel and N.-G. Park, *Sci. Rep.*, 2012, **2**, 591.

[10] M. M. Lee, J. Teuscher, T. Miyasaka, T. N. Murakami and H. J. Snaith, *Science (80-.).*, 2012, **338**, 643–647.

[11] T. C. Sum, N. Mathews, *Energy Environ. Sci.*, 2014, **7**, 2518–2534.

[12] M. L. Moreira, E. C. Paris, G. S. do Nascimento, V. M. Longo, J. R. Sambrano, V. R. Mastelaro, M. I. B. Bernardi, J. Andrés, J. A. Varela and E. Longo, *Acta Materialia.*, 2009, **57**, 5174–5185.

[13] V.M. Goldschmidt, *Naturwissenschaften*, 1926, **14**, 477–485.

[14] F. Zhang, H. Lu, J. Tong, J. J. Berry, M. C. Beard and K. Zhu,*Energy Environ. Sci.*, 2020, **13**, 1154.

[15] T. Baikie, Y. Fang, J. M. Kadro, M. Schreyer, F. Wei, S. G. Mhaisalkar, M. Graetzel and T. J. White, *J. Mater. Chem. A,* 2013, **1**, 5628.

[16] T. J. Savenije, C. S. Ponseca, L. Kunneman, M. Abdellah, K. Zheng, Y. Tian, Q. Zhu, S. E. Canton, I. G. Scheblykin, T. Pullerits, A. Yartsev and V. Sundström, *J. Phys. Chem. Lett.*, 2014, **5**, 2189–2194.

[17] Q. Dong, Y. Fang, Y. Shao, P. Mulligan, J. Qiu, L. Cao and J. Huang, *Science (80-.).*, 2015, **347**, 967–970.

[18] Q. Dong, *Science*, 2015, **347**, 967-970.

[19] J.-W. Lee, D.-J. Seol, A.-N. Cho, and N.-G.Park, *Adv. Mater.*, 2014, **26**, 4991-4998.

[20] M. Pazoki, T. J. Jacobsson, A. Hagfeldt, G. Boschloo, and T. Edvinsson, *Physical Review B*, 2016, **93**, 144105.

[21] M. Saliba, T. Matsui, J.-Y. Seo, K. Domanski, J.-P. Correa-Baena, M. K. Nazeeruddin, S. M. Zakeeruddin, W. Tress, A. Abate, A. Hagfeldt and M. Grätzel, *Energy Environ. Sci.*, 2016, **9**, 1989–1997.

[22] J. Tian, Q. Xue, Q. Yao, N. Li, C. J. Brabec and H. L. Yip, *Adv. Energy Mater.,* 2020, **10**, 2000183.

[23] X. Sun, Z. Shao, Y. Rao, H. Meng, C. Gao, C. Chen, D. Liu, P. Lv, Z. Li and X. Wang, *Adv. Energy Mater.,* 2021, **11**, 2002754.

[24] C. Liu, Y. Yang, O. A. Syzgantseva, Y. Ding, M. A. Syzgantseva, X. Zhang, A. M. Asiri, S. Dai and M. K. Nazeeruddin, *Adv. Mater.* 2020, ***32***, 2002632.

[25] Y. Wang, M. I. Dar, L. K. Ono, T. Zhang, M. Kan, Y. Li, L. Zhang, X. Wang, Y. Yang and X. Gao, *Science,* 2019, **365**, 591-595.

[26] Z. Li, F. Zhou, Q. Wang, L. Ding and Z. Jin, *Nano Energy,* 2020, **71**, 104634.

[27] K. Wang, Q. Tian, G. Zhao, J. Wen, J. Huang, C. Gao, Z. Xu, Y. Liu, L. Liang and L. Meng, *Cell Rep. Phys. Sci.,* 2020, **1**, 100180.

[28] T. Wu, Y. Wang, Z. Dai, D. Cui, T. Wang, X. Meng, E. Bi, X. Yang and L. Han, *Adv. Mater.,* 2019, **31**, 1900605.

[29] Q. Ling, W. Huang, A. Baldwin and P. Jarvis, *Science (80-.).*, 2012, **338**, 655–659.

[30] S. S. Malia and C. K. Hong, *Nanoscale*, 2016, **8**, 10528-10540.

[31] Z. Liu, A. Zhu, F. Cai, L. Tao, Y. Zhou, Z. Zhao, Q. Chen, Y.-B. Cheng and H. Zhou, *J. Mater. Chem. A*, 2017, **5**, 6597–6605.

[32] D. Liu, J. Yang and T. L. Kelly, *J. Am. Chem. Soc.*, 2014, **136**, 17116–17122.

[33] U. Bach, D. Lupo, P. Comte, J. E. Moser, F. Weissörtel, J. Salbeck, H. Spreitzer and M. Grätzel, *Nature*, 1998, **395**, 583–585.

[34] A. Mei, X. Li, L. Liu, Z. Ku, T. Liu, Y. Rong, M. Xu, M. Hu, J. Chen, Y. Yang, M. Gratzel and H. Han, *Science (80-.).*, 2014, **345**, 295–298.

[35] W. S. Yang, B.-W. Park, E. H. Jung, N. J. Jeon, Y. C. Kim, D. U. Lee, S. S. Shin, J. Seo, E. K. Kim, J. H. Noh and S. Il Seok, *Science (80-.).*, 2017, **356**, 1376–1379.

[36] J. M. Kim, S. J. Yoo, C. K. Moon, B. Sim, J. H. Lee, H. Lim, J. W. Kim and J. J. Kim, *J. Phys. Chem. C*, 2016, **120**, 9475–9481.

[37] K. Walzer, B. Maennig, M. Pfeiffer and K. Leo, *Chem. Rev.*, 2007, **107**, 1233–1271.

[38] S. Wang, M. Sina, P. Parikh, T. Uekert, B. Shahbazian, A. Devaraj and Y. S. Meng, *Nano Lett.*, 2016, **16**, 5594–5600.

[39] A. Abate, T. Leijtens, S. Pathak, J. Teuscher, R. Avolio, M. E. Errico, J. Kirkpatrik, J. M. Ball, P. Docampo, I. McPherson and H. J. Snaith, *Phys. Chem. Chem. Phys.*, 2013, **15**, 2572–2579.

[40] J.-Y. Seo, H.-S. Kim, S. Akin, M. Stojanovic, E. Simon, M. Fleischer, A. Hagfeldt, S. M. Zakeeruddin and M. Grätzel, *Energy Environ. Sci.*, 2018, **11**, 2985-2992.

[41] B. Xu, D. Bi, Y. Hua, P. Liu, M. Cheng, M. Grätzel, L. Kloo, A. Hagfeldt and L. Sun, *Energy Environ. Sci.*, 2016, **9**, 873–877.

[42] V. A. Chiykowski, Y. Cao, H. Tan, D. P. Tabor, E. H. Sargent, A. Aspuru-Guzik and C. P. Berlinguette, *Angew. Chemie - Int. Ed.*,

2018, **57**, 15529–15533.

[43] N. J. Jeon, H. Na, E. H. Jung, T. Y. Yang, Y. G. Lee, G. Kim, H. W. Shin, S. Il Seok, J. Lee and J. Seo, *Nat. Energy*, 2018, **3**, 1–8.

[44] D. Bi, B. Xu, P. Gao, L. Sun, M. Grätzel and A. Hagfeldt, *Nano Energy*, 2016, **23**, 138–144.

[45] B. Xu, Z. Zhu, J. Zhang, H. Liu, C. C. Chueh, X. Li and A. K. Y. Jen, *Adv. Energy Mater.*, 2017, **7**, 1700683.

[46] X. Zhu, X. Ma, Y. Wang, Y. Li, C. Gao, Z. Wang, Z. Jiang and L. Liao, *Adv. Funct. Mater.*, 2018, 1807094.

[47] M. S. Kang, S. Do Sung, I. T. Choi, H. Kim, M. Hong, J. Kim, W. I. Lee and H. K. Kim, *ACS Appl. Mater. Interfaces*, 2015, **7**, 22213–22217.

[48] D. Vaitukaityte, Z. Wang, T. Malinauskas, A. Magomedov, G. Bubniene, V. Jankauskas, V. Getautis and H. J. Snaith, *Adv. Mater.*, 2018, **30**, 1803735.

[49] X.-C. Li, C.-Y. Wang, W.-Y. Lai and W. Huang, *J. Mater. Chem. C*, 2016, **4**, 10574–10587.

[50] M. Franceschin, L. Ginnari-Satriani, A. Alvino, G. Ortaggi and A. Bianco, *Eur. J. Org. Chem.*, 2010, **2010**, 134–141.

[51] K. Rakstys, A. Abate, M. I. I. Dar, P. Gao, V. Jankauskas, G. Jacopin, E. Kamarauskas, S. Kazim, S. Ahmad, M. Gratzel and M. K. Nazeeruddin, *J. Am. Chem. Soc.*, 2015, **137**, 16172–16178.

[52] A. Connell, Z. Wang, Y.-H. Lin, P. C. Greenwood, A. A. Wiles, E. W. Jones, L. Furnell, R. Anthony, C. P. Kershaw, G. Cooke, H. J. Snaith and P. J. Holliman, *J. Mater. Chem. C*, 2019, **7**, 5235-5243.

[53] I. Cho, N. J. Jeon, O. K. Kwon, D. W. Kim, E. H. Jung, J. H. Noh, J. Seo, S. Il Seok and S. Y. Park, *Chem. Sci.*, 2017, **8**, 734–741.

[54] A. Molina-Ontoria, I. Zimmermann, I. Garcia-Benito, P. Gratia, C. Roldan-Carmona, S. Aghazada, M. Graetzel, M. K. Nazeeruddin and N. Martin, *Angew. Chemie - Int. Ed.*, 2016, **55**, 6270–6274.

[55] I. García-Benito, I. Zimmermann, J. Urieta-Mora, J. Aragó, A. Molina-Ontoria, E. Ortí, N. Martín and M. K. Nazeeruddin, *J. Mater. Chem. A*, 2017, **5**, 8317–8324.

[56] I. García-Benito, I. Zimmermann, J. Urieta-Mora, J. Aragó, J. Calbo, J. Perles, A. Serrano, A. Molina-Ontoria, E. Ortí, N. Martín and M. K. Nazeeruddin, *Adv. Funct. Mater.*, 2018, **28**, 1801734.

[57] R. Sandoval-Torrientes, I. Zimmermann, J. Calbo, J. Aragó, J. Santos, E. Ortí, N. Martín and M. K. Nazeeruddin, *J. Mater. Chem. A*, 2018, **6**, 5944–5951.

[58] T. Akasaka, A. Osuka, S. Fukuzumi, H. Kandori and Y. Aso, *Chemical Science of π-Electron Systems*, Springer Japan, 2015.

[59] R. Shang, Z. Zhou, H. Nishioka, H. Halim, S. Furukawa, I. Takei, N. Ninomiya and E. Nakamura, *J. Am. Chem. Soc.* 2018, **140**, 5018–5022.

[60] C. Huang, W. Fu, C. Z. Li, Z. Zhang, W. Qiu, M. Shi, P. Heremans, A. K. Y. Jen and H. Chen, *J. Am. Chem. Soc.*, 2016, **138**, 2528–2531.

[61] H. D. Pham, T. T. Do, J. Kim, C. Charbonneau, S. Manzhos, K. Feron, W. C. Tsoi, J. R. Durrant, S. M. Jain and P. Sonar, *Adv. Energy Mater.*, 2018, **8**, 1703007.

[62] R. Azmi, S. Y. Nam, S. Sinaga, Z. A. Akbar, C.-L. Lee, S. C. Yoon, I. H. Jung and S.-Y. Jang, *Nano Energy*, 2017, **44**, 191-198.

[63] R. Chen, T. Bu, J. Li, W. Li, P. Zhou, X. Liu, Z. Ku, J. Zhong, Y. Peng, F. Huang, Y.-B. Cheng and Z. Fu, *ChemSusChem*, 2018, **11**, 1467–1473.

[64] L. Yang, F. Cai, Y. Yan, J. Li, D. Liu, A. J. Pearson and T. Wang, *Adv. Funct. Mater.*, 2017, **27**, 1702613.

[65] Y. Li, K. R. Scheel, R. G. Clevenger, W. Shou, H. Pan, K. V. Kilway and Z. Peng, *Adv. Energy Mater.*, 2018, **8**, 1801248.

[66] S. J. Park, S. Jeon, I. K. Lee, J. Zhang, H. Jeong, J. Y. Park, J. Bang, T. K. Ahn, H. W. Shin, B. G. Kim and H. J. Park, *J. Mater. Chem. A*, 2017, **5**, 13220–13227.

[67] S. Paek, P. Qin, Y. Lee, K. T. Cho, P. Gao, G. Grancini, E. Oveisi, P. Gratia, K. Rakstys, S. A. Al-Muhtaseb, C. Ludwig, J. Ko and M. K. Nazeeruddin, *Adv. Mater.*, 2017, **29**, 1606555.

[68] K. Rakstys, S. Paek, P. Gao, P. Gratia, T. Marszalek, G. Grancini, K. T. K. T. Cho, K. Genevicius, V. Jankauskas, W. Pisula and M. K. M. K. Nazeeruddin, *J. Mater. Chem. A*, 2017, **5**, 7811–7815.

[69] D. Bharath, M. Sasikumar, N. R. Chereddy, J. R. Vaidya and S. Pola, *Sol. Energy*, 2018, **174**, 130–138.

[70] P. Xu, P. Liu, Y. Li, B. Xu, L. Kloo, L. Sun and Y. Hua, *ACS Appl. Mater. Interfaces*, 2018, **10**, 19697–19703.

[71] J. Lee, M. Malekshahi Byranvand, G. Kang, S. Y. Son, S. Song, G.-W. Kim and T. Park, *J. Am. Chem. Soc.*, 2017, **139**, 12175–12181.

[72] G.-W. Kim, J. Lee, G. Kang, T. Kim and T. Park, *Adv. Energy Mater.*, 2018, **8**, 1701935.

[73] F. Cai, J. Cai, L. Yang, W. Li, R. S. Gurney, H. Yi, A. Iraqi, D. Liu and T. Wang, *Nano Energy*, 2018, **45**, 28–36.

[74] L. Fu, H. Li, L. Wang, R. Yin, B. Li and L. Yin, *Energy Environ. Sci.*, 2020, **13**, 4017–4056.

[75] F. Wang, S. Bai and W. Tress, *Nj Flex Electron,* 2018, **2,** 22.

[76] L. M. Pazos-Outón, T. P. Xiao, and E.Yablonovitch, *J. Phys. Chem. Lett.,* 2018, **9**, 1703–1711.

[77] W. Tress, N. Marinova, T. Moehl, S. M. Zakeeruddin, M. K. Nazeeruddin and M. Grätzel, *Energy Environ. Sci.*, 2015, ***8****, 995*-1004.

[78] Y. Chen and H. Zhou, *J. Appl. Phys.,* 2020, **128**, 060903.

[79] S. Shao and M. A. Loi, *Adv. Mater. Interfaces*, 2020, **7**, 1901469.

[80] E. Aydin, M. De Bastiani and S. De Wolf, *Adv. Mater.,* 2019, **31**, 1900428.

[81] C. Li, H. Li, Z. Zhu, N. Cui, Z. Tan and R. Yang, *Sol. RRL*, 2021, **5**, 2000579.

[82] C. Roldan-Carmona, P. Gratia, I. Zimmermann, G. Grancini, P. Gao, M. Graetzel and M. K. Nazeeruddin, *Energy Environ. Sci.*, 2015, **8**, 3550-3556.

[83] H. Lu, A. Krishna, S. M. Zakeeruddin, M. Grätzel and A. Hagfeldt, *iScience*, 2020, **23**, 101359.

[84] F. Gao, Y. Zhao, X. Zhang and J. You, *Adv. Energy Mater.,* 2020, **10**, 1902650.

[85] L. Fagiolari and F. Bella, *Energy Environ. Sci.*, 2019, **12**, 3437-3472.

[86] N. Li, S. Tao, Y. Chen, X. Niu, C. K. Onwudinanti, C. Hu, Z. Qiu, Z. Xu, G. Zheng, L. Wang, Y. Zhang, L. Li, H. Liu, Y. Lun, J. Hong, X. Wang, Y. Liu, H. Xie, Y. Gao, Y. Bai, S. Yang, G. Brocks, Q. Chen and H. Zhou, *Nat. Energy*, 2019, **4**, 408.

[87] H. Kanda, O. J. Usiobo, C. Momblona, M. Abuhelaiqa, A. A. Sutanto, C. Igci X. -X. Gao, J. -N. Audinot, T. Wirtz and M. K. Nazeeruddin, *Sol. RRL,* 2020, 2000650.

[88] H. Li, L. Tao, F. Huang, Q. Sun, X. Zhao, J. Han, Y. Shen and M. Wang, *ACS Appl. Mater. Interfaces,* 2017, **9**, 38967.

[89] X. Fang, J. Ding, N. Yuan, P. Sun, M. Lv, G. Ding and C. Zhu, P*hys. Chem. Chem. Phys.*, 2017, **19**, 6057-6063.

[90] A. Abate, M. Saliba, D. J. Hollman, S. D. Stranks, K. Wojciechowski, R. Avolio, G. Grancini, A. Petrozza and H. J. Snaith, *Nano Lett.,* 2014, **14**, 3247-3254.

[91] Z. Yang , J. Dou , S. Kou , J. Dang , Y. Ji , G. Yang , W.-Q. Wu , D.-B. Kuang and M. Wang , *Adv. Funct. Mater.*, 2020, **30**, 1910710.

[92] J. Kim, A. Ho-Baillie and S. Huang, *Solar RRL*, 2019, **3**, 1800302.

[93] T. Wu, X. Li, Y. Qi, Y. Zhang, and L. Han, *ChemSusChem*, 2021, **14**, 1–24.

[94] Y. Li, M. Dailey, P. J. Lohra and A. D. Printz, *J. Mater. Chem. A*, 2021, **9**, 16281-16338.

[95] D. W. deQuilettes, S. Koch, S. Burke, R. K. Paranji, A. J. Shropshire, M. E. Ziffer and D. S. Ginger, ACS Energy Lett., 2016, **1**, 438-444.

[96] G. Huang, C. Wang, H. Zhang, S. Xu, Q. Xu and Y. Cui, *J. Mater. Chem. A*, 2018, **6**, 2449-2455.

[97] S. Kundu, T. L. Kelly, *EcoMat*., 2020, **2**, e12025.

[98] L. Etgar, P. Gao, Z. Xue, Q. Peng, A. K. Chandiran, B. Liu, M. K. Nazeeruddin and M. Gratzel, *J. Am. Chem. Soc.*, 2012, **134**, 17396–17399.

[99] K.-C. Wang, J.-Y. Jeng, P.-S. Shen, Y.-C. Chang, E. W.-G. Diau, C.-H. Tsai, T.-Y. Chao, H.-C. Hsu, P.-Y. Lin, P. Chen, T.-F. Guo and T.-C. Wen, *Sci. Rep.*, 2015, **4**, 4756.

[100] X. Zhou, C. Bao, F. Li, H. Gao, T. Yu, J. Yang, W. Zhu and Z. Zou, *RSC Adv.*, 2015, **5**, 58543–58548.

[101] C. C. Stoumpos, C. D. Malliakas and M. G. Kanatzidis, *Inorg Chem*. 2013, **52**, 9019-9038.

[102] A. E. Williams, P. J. Holliman, M. J. Carnie, M. L. Davies, D. A. Worsley and T. M. Watson. *J Mater Chem A*., 2014, **2**, 19338-19346.

[103] M. Saliba, T. Matsui, K. Domanski, J.-Y. Seo, A. Ummadisingu, S. M. Zakeeruddin, J.-P. Correa-Baena, W. R. Tress, A. Abate, A. Hagfeldt and M. Gratzel, *Science.*, 2016, **354**, 206–209.

[104] C. Zhang, J. F. S. Fernando and K. L. Firestein, *APL Mater.*, 2019, **7**, 071110.

[105] Y. Han, S. Meyer, Y. Dkhissi, K. Weber, J. M. Pringle, U. Bach, L. Spiccia and Y.-B. Cheng, *J. Mater. Chem. A*, 2015, **3**, 8139-8147.

[106] N. Aristidou, I. Sanchez-Molina, T. Chotchuangchutchaval, M. Brown, L. Martinez, T. Rath and S. A. Haque, *Angew. Chem. Int. Ed.,* 2015, **54**, 8208-8212.

[107] M.Sayantan, Z. Ying and Z. Xiaodan, F*ront.Electron.*, 2021, **2**, 8.

[108] Q. M. Hong, R. P. Xu, T. Y. Jin, J. X. Tang and Y. Q. Li, *Org Electron.,* 2019, **67**, 19-25.

[109] J. Urieta-Mora, I. García-Benito, A. Molina-Ontoria and N. Martín, *Chem. Soc. Rev.,* 2018, **47**, 8541.

[110] H. J. Snaith and M. Grätzel, *Appl. Phys. Lett.,* 2006, **26**, 262114.

[111] E. J. Juarez-Perez, M. R. Leyden, S. Wang, L. K. Ono, Z. Hawash and Y. Qi, *Chem. Mater.,* 2016, **16**, 5702.

[112] T. Leijtens, T. Giovenzana, S. N. Habisreutinger, J. S. Tinkham, N. K. Noel, B. A. Kamino, G. Sadoughi, A. Sellinger and H. J. Snaith, *ACS Appl. Mater. Interfaces,* 2016, **8**, 5981.

[113] A. A. Raheem, S. Kamaraj, V. Sannasi and G. Praveen, *Org. Chem. Front*., 2018, **5**, 777.

[114] G. Yang, P. Qin, G. Fang and G. Li, *Sol. RRL,* 2018, **2**, 1800055.

[115] N. K. Noel, A. Abate, S. D. Stranks, E. S. Parrott, V. M. Burlakov, A. Goriely and H. J. Snaith, *ACS Nano,* 2014, **8**, 9815.

[116] C. Lu, M. Paramasivam, K. Park, C. H. Kim and H. K. Kim, *ACS Appl. Mater. Interfaces,* 2019, **11**, 14011.

[117] S. Higashijima, H. Miura, T. Fujita, Y. Kubota, K. Funabiki, T. Yoshida and M. Matsui, *Tetrahedron,* 2011, **67**, 6289.

[118] Z. Hu, W. Fu, L. Yan, J. Miao, H. Yu, Y. He, O. Goto, H. Meng, H. Chen and W. Huang, *Chem. Sci.,* 2016, **7**, 5007.

[119] J. Roncali, *Chem. Rev.,* 1997, **97**, 173.

[120] W. Ma, L. Ye, S. Zhang, J. Hou and H. Ade, *J. Mater. Chem. C,* 2013, **1**, 5023.

[121] P. Müller-Buschbaum, *Adv. Mater.,* 2014, **26**, 7692.

[122] Z. Wang, Y. Zhang, J. Zhang, Z. Wei and W. Ma, *Adv. Energy Mater.,* 2016, **6**, 1502456.

[123] F. Qi, X. Deng, X. Wu, L. Huo, Y. Xiao, X. Lu, Z. Zhu and A. K.-Y. Jen, *Adv. Energy Mater*., 2019, **9**, 1902600.

[124] A. M. Silski, J. P. Petersen, R. D. Brown, S. A. Corcelli and S. A. Kandel, *J. Phys. Chem. C,* 2018, **122**, 25467.

[125] L. A. Chetkina and V. K. Belsky, *Crystallogr. Rep.,* 2008, **53**, 579.

[126] X. Liu, F. Zhang, Z. Liu, Y. Xiao, S. Wang and X. Li, *J. Mater. Chem. C,* 2017, **5**, 11429.

[127] L. Wang, J. Zhang, P. Liu, B. Xu, B. Zhang, H. Chen, A. K. Inge, Y. Li, H. Wang, Y. B. Cheng, L. Kloo and L. Sun, *Chem. Commun.,* 2018, **54**, 9571.

[128] S. Grigalevicius, G. Buika, J.V. Grazulevicius, V. Gaidelis, V. Jankauskas and E. Montrimas, *Synth. Met.,* 2001, **122**, 311.

[129] S. Park, J. H. Heo, J. H. Yun, T. S. Jung, K. Kwak, M. J. Ko, C. H. Cheon, J. Y. Kim, S. H. Im and H. J. Son, *Chem. Sci.*, 2016, **7**, 5517.

[130] H. Baig, H. Kanda, A. M. Asiri, M. K. Nazeeruddin and T. Mallicka, *Sustainable Energy Fuels,* 2020, **4**, 528.

[131] Q. Hu, E. Rezaee, M. Li, Q. Chen, C. Li, S. Cai, H. Shan and Z. Xu, *Sol. RRL,* 2020, **4**, 1900340.

[132] Z. Hawash, L. K. Ono, S. R. Raga, M. V. Lee and Y. B. Qi, *Chem. Mater.*, 2015, **27**, 562.

[133] T. A. Berhe, W. N. Su, C. H. Chen, C. J. Pan, J. H. Cheng, H. M. Chen, M. C. Tsai, L. Y. Chen, A. A. Dubaleb and B. J. Hwang, *Energy Environ. Sci.*, 2016, **9**, 323.

[134] C. Zhao, B. B. Chen, X. F. Qiao, L. Luan, K. Lu and B. Hu, *Adv. Energy Mater.*, 2015, **5**, 1500279.

[135] F. Zhang, C. Yi, P. Wei, X. Bi, J. Luo, G. Jacopin, S. Wang, X. Li, Y. Xiao, S. M. Zakeeruddin and M. Grätzel, *Adv. Energy Mater.*, 2016, **6**, 1600401.

[136] Y. Wang, X. Liu, H. Shan, Q. Chen, T. Liu, X. Sun, D. Ma, Z. Zhang, J. Xu and Z.-X. Xu, *Dyes Pigm.*, 2017, **139**, 619.

[137] S. S. Reddy, K. Gunasekar, J. H. Heo, S. H. Im, C. S. Kim, D.-H. Kim, J. H. Moon, J. Y. Lee, M. Song and S.-H. Jin, *Adv. Mater.*, 2016, **28**, 686.

[138] T. Zhang, M. I. Dar, G. Li, F. Xu, N. Guo, M. Grätzel and Y. Zhao, *Sci. Adv.,* 2017, **3**, e1700841.

[139] C. Liu, Y. Yang, X. Liu, Y. Ding, Z. Arain, X. Li, Y. Li, Z. Zhou, S. Dai and M. K. Nazeeruddin, *J. Mater. Chem. A,* 2020, **8**, 10226-10232.

[140] C. Yan, Z. Li, Y. Sun, J. Zhao, X. Huang, J. Yang, Z. Ci, L. Ding and Z. Jin, *J. Mater. Chem. A,* 2020, **8**, 10346-10353.

[141] T. Miyasaka, A. Kulkarni, G. M. Kim, S. Öz and A. K. Jena, *Adv. Energy Mater.,* 2020, **10**, 1902500.

[142] W. Xiang and W. Tress, *Adv. Mater.,* 2019, **31**, 1902851.

[143] S. Oz, A. K. Jena, A. Kulkarni, K. Mouri, T. Yokoyama, I. Takei, F. Ünlü, S. Mathur and T. Miyasaka, *ACS Energy Lett.,* 2020, **5**, 1292-1299.

[144] S. Dai, F. Zhao, Q. Zhang, T.-K. Lau, T. Li, K. Liu, Q. Ling, C. Wang, X. Lu, W. You, X. Zhan, *J. Am. Chem. Soc.,* 2017, **139**, 1336-1343.

[145] C. Liu, L. Zhang, Y. Li, X. Zhou, S. She, X. Wang, Y. Tian, A. K. Jen and B. Xu, *Adv. Funct. Mater.,* 2020, **30**, 1908462.

[146] T. Niu, W. Zhu, Y. Zhang, Q. Xue, X. Jiao, Z. Wang, Y.-M. Xie, P. Li, R. Chen and F. Huang, *Joule,* 2021, **5**, 249-269.

[147] C. Igci, S. Paek, K. Rakstys, H. Kanda, N. Shibayama, V. Jankauskas, C. Roldán-Carmona, H. Kim, A. M. Asiri and M. K. Nazeeruddin, *Solar RRL,* 2020, **4**, 2000173.

[148] Q. Xiao, T. Sakurai, T. Fukino, K. Akaike, Y. Honsho, A. Saeki, S. Seki, K. Kato, M. Takata and T. Aida, *J. Am. Chem. Soc.,* 2013, **135**, 18268-18271.

[149] N. Arora, M. I. Dar, A. Hinderhofer, N. Pellet, F. Schreiber, S. M. Zakeeruddin and M. Grätzel, *Science,* 2017, **358**, 768-771.

[150] C. Liu, Y. Yang, C. Zhang, S. Wu, L. Wei, F. Guo, G. M. Arumugam, J. Hu, X. Liu and J. Lin, *Adv. Mater.,* 2020, **32**, 1907361.

[151] H. Tsuji, Y. Yokoi, S. Furukawa and E. Nakamura, *Heterocycles,* 2015, **90**, 261.

[152] H. Tsuji, Y. Yokoi, C. Mitsui, L. Ilies, Y. Sato and E. Nakamura, *Chem. Asian J.,* 2009, **4**, 655.

[153] G. W. P. Pruissen, E. A. Pidko, M. M. Wienka and R. A. J. Janssen, *J. Mater. Chem. C,* 2014, **2**, 731.

[154] A. P. Dhondge, Y. -X. Huang, T. Lin, Y. -H. Hsu, S. -L. Tseng, Y. -C. Chang, H. J. H. Chen and M. -Y. Kuo, *J. Org. Chem.,* 2019, **84**, 14061.

[155] Z. Zhou, Z. Qiang, T. Sakamaki, I. Takei, R. Shang and E. Nakamura, *ACS Appl. Mater. Interfaces,* 2019, **11**, 22603.

[156] T. Nakamura, S. Furukawa and E. Nakamura, *Chem. Asian J.,* 2016, **11**, 2016.

[157] X. Zhou, F. Kong, Y. Sun, Y. Huang, X. Zhang and R. Ghadari, *J. Energy Chem.,* 2020, **44**, 115.

[158] Y. Liu, Z. Hong, Q. Chen, H. Chen, W. H. Chang, Y. M. Yang, T. B. Song and Y. Yang, *Adv. Mater.,* 2016, **28**, 440.

[159] D. Liu, B. Kan, X. Ke, N. Zheng, Z. Xie, D. Lu and Y. Liu, *Adv. Energy Mater.,* 2018, **8**, 1801618.

[160] H. Yao, Y. Cui, R. Yu, B. Gao, H. Zhang and J. Hou, *Angew. Chem. Int. Ed.,* 2017, **56**, 3045.

[161] X. Ji, T. Zhou, X. Ke, W. Wang, S. Wu, M. Zhang, D. Lu, X. Zhang and Y. Liu, *J. Mater. Chem. A,* 2020, **8**, 5163.

[162] B. X. Zhao, C. Yao, K. Gu, T. Liu, Y. Xiaa and Y. -L. Loo, *Energy Environ. Sci.,* 2020, **13**, 4334.

[163] M. -H. Jung, *J. Mater. Chem. A,* 2019, **7**, 14689.

[164] M. Li, J. Wu, G. Wang, B. Wu, Z. Sun, S. Xue, Q. Qiao and M. Liang, *J. Energy Chem.,* 2020, **47**, 10.

[165] M. Moroni, J. L. Moigne, T. A. Pham and J. Y. Bigot, *Macromolecules,* 1997, **30**, 1964.

[166] D. Khlaifia, F. Massuyeau, C. P. Ewels, J.-L. Duvail, E. Faulques and K. Alimi, *ChemistrySelect,* 2017, **2**, 10082.

[167] J. Qiu, H. Liu, X. Li and S. Wang, *Chem. Eng. J.,* 2020, **387**, 123965.

[168] Y. L. Liao, W. Y. Hung, T. H. Hou, C. Y. Lin and K. T. Wong, *Chem. Mater.,* 2007, **19**, 6350.

[169] P. Gratia, A. Magomedov, T. Malinauskas, M. Daskeviciene, A. Abate, S. Ahmad, M. Grätzel, V. Getautis and M. K. Nazeeruddin, *Angew. Chem. Int. Ed.,* 2015, **54**, 11409.

[170] H. Kim, M. Pei, Y. Lee, A. A. Sutanto, S. Paek, V. I. E. Queloz, A. J. Huckaba, K. T. Cho, H. J. Yun, H. Yang and M. K. Nazeeruddin, *Adv. Funct. Mater.,* 2020, **30**, 1910620.

[171] M. Stolterfoht, C. M. Wolff, J. A. Márquez, S. Zhang, C. J. Hages, D. Rothhardt, S. Albrecht, P. L. Burn, P. Meredith, T. Unold and D. Neher, *Nat. Energy,* 2018, **3**, 847.

[172] Y. K. Wang, H. Ma, Q. Chen, Q. Sun, Z. Liu, Z. Sun, X. Jia, Y. Zhu, S. Zhang, J. Zhang, N. Yuan, J. Ding, Y. Zhou, B. Song and Y. Li, *ACS Appl. Mater. Interfaces,* 2021, **13**, 7705.

[173] S. -C. Chen, D. Wang and Q. Zheng, *Sol. RRL,* 2020, **4**, 2000321.

[174] X. Li, W. Li, Y. Yang, X. Lai, Q. Su, D. Wu, G. Li, K. Wang, S. Chen, X. W. Sun and A. K. K. Kyaw, *Sol. RRL,* 2019, **3**, 1900029.

[175] Y. Dong, V. C. Nikolis, F. Talnack, Y. -C. Chin, J. Benduhn, G. Londi, J. Kublitski, X. Zheng, S. C. B. Mannsfeld, D. Spoltore, L. Muccioli, J. Li, X. Blase, D. Beljonne, J. -S. Kim, A. A. Bakulin, G. D'Avino, J. R. Durrant and K. Vandewal, *Nat. Commun,* 2020, **11**, 4617.

[176] T. D. Kühne, M. Iannuzzi, M. D. Ben, V. V. Rybkin, P. Seewald, F. Stein, T. Laino, R. Z. Khaliullin, O. Schütt, F. Schiffmann, D. Golze, J. Wilhelm, S. Chulkov, M. H. Bani-Hashemian, V. Weber, U. Borštnik, M. Taillefumier, A. S. Jakobovits, A. Lazzaro, H. Pabst, T. Müller, R. Schade, M. Guidon, S. Andermatt, N. Holmberg, G. K. Schenter, A. Hehn, A. Bussy, F.

Belleflamme, G. Tabacchi, A. Gl.., M. Lass, I. Bethune, C. J. Mundy, C. Plessl, M. Watkins, J. VandeVondele, M. Krack and J. Hutter, *J. Chem. Phys.*, 2020, **152**, 194103.

[177] G. S. Han, H. S. Chung, B. J. Kim, D. H. Kim, J. W. Lee, B. S. Swain, K. Mahmood, J. S. Yoo, N.-G. Park, J. H. Lee and H. S. Jung, *J. Mater. Chem. A*, 2015, **3**, 9160-9164.

[178] Q. Hu, J. Wu, C. Jiang, T. Liu, X. Que, R. Zhu and Q. Gong, *ACS Nano*, 2014, **8**, 10161-10167.

[179] F. Han, J. Luo, B. Zhao, Z. Wan, R. Wang and C. Jia, *Electrochim. Acta*, 2017, **236**, 122-130.

[180] J. Zhang, Z. Hu, L. Huang, G. Yue, J. Liu, X. Lu, Z. Hu, M. Shang, L. Han and Y. Zhu, *Chem. Commun*., 2015, **51**, 7047-7050.

[181] D.-X. Yuan, X.-D. Yuan, Q.-Y. Xu, M.-F. Xu, X.-B. Shi, Z.-K. Wang and L.-S. Liao, *Phys. Chem. Chem. Phys.*, 2015, **17**, 26653-26658.

[182] L.-L. Jiang, S. Cong, Y.-H. Lou, Q.-H. Yi, J.-T. Zhu, H. Ma and G.-F. Zou, *J. Mater. Chem. A*, 2016, **4**, 217-222.

[183] L. Zuo, Q. Chen, N. De Marco, Y.-T. Hsieh, H. Chen, P. Sun, S.-Y. Chang, H. Zhao, S. Dong and Y. Yang, *Nano Lett.*, 2017, **17**, 269-275.

[184] K. Wojciechowski, S. D. Stranks, A. Abate, G. Sadoughi, A. Sadhanala, N. Kopidakis, G. Rumbles, C.-Z. Li, R. H. Friend, A. K. Y. Jen and H. J. Snaith, *ACS Nano*, 2014, **8**, 12701-12709.

[185] Z. Liu, S. Li, X. Wang, Y. Cui, Y. Qin, S. Leng, Y.-x. Xu, K. Yao and H. Huang, *Nano Energy*, 2019, **62**, 734-744.

[186] M. Salado, F. J. Ramos, V. M. Manzanares, P. Gao, M. K. Nazeeruddin, P. J. Dyson and S. Ahmad, *ChemSusChem,* 2016, **9**, 2708-2714.

[187] J. Chang, Z. Lin, H. Zhu, F. H. Isikgor, Q.-H. Xu, C. Zhang, Y. Hao and J. Ouyang, *J. Mater. Chem. A*, 2016, **4**, 16546-16552.

[188] X. Li, M. Ibrahim Dar, C. Yi, J. Luo, M. Tschumi, S. M. Zakeeruddin, M. K. Nazeeruddin, H. Han and M. Gratzel, *Nat. Chem.,* 2015, **7**, 703-711.

[189] H. Kim, S.-U. Lee, D. Y. Lee, M. J. Paik, H. Na, J. Lee and S. I. Seok, *Adv. Energy Mater*., 2019, **9**, 1902740.

[190] E. H. Jung, N. J. Jeon, E. Y. Park, C. S. Moon, T. J. Shin, T.-Y. Yang, J. H. Noh and J. Seo, *Nature*, 2019, **567**, 511-515.

[191] A. A. Sutanto, N. Drigo, V. I. E. Queloz, I. Garcia-Benito, A. R. Kirmani, L. J. Richter, P. A. Schouwink, K. T. Cho, S. Paek, M. K. Nazeeruddin and G. Grancini, *J. Mater. Chem. A*, 2020, **8**, 2343-2348.

[192] Y. Lin, L. Shen, J. Dai, Y. Deng, Y. Wu, Y. Bai, X. Zheng, J. Wang, Y. Fang, H. Wei, W. Ma, X. C. Zeng, X. Zhan and J. Huang, *Adv. Mater.*, 2017, **29**, 1604545.

[193] G. Almeida, O. J. Ashton, L. Goldoni, D. Maggioni, U. Petralanda, N. Mishra, Q. A. Akkerman, I. Infante, H. J. Snaith and L. Manna, *J. Am. Chem. Soc.*, 2018, **140**, 14878-14886.

[194] K. T. Munson, C. Grieco, E. R. Kennehan, R. J. Stewart and J. B. Asbury, *ACS Energy Lett.*, 2017, **2**, 651-658.

[195] S. Yang, J. Dai, Z. Yu, Y. Shao, Y. Zhou, X. Xiao, X. C. Zeng and J. Huang, *J. Am. Chem. Soc.*, 2019, **141**, 5781-5787.

[196] F. Palazon, D. P.rez-del-Rey, S. Marras, M. Prato, M. Sessolo, H. J. Bolink and L. Manna, *ACS Energy Lett.*, 2018, **3**, 835-839.

[197] A. Torres and L. G. C. Rego, *J. Phys. Chem. C*, 2014, **118**, 26947-26954.

[198] H.-Y. Cheng, C.-S. Sun and D.-R. Hou, *J. Org. Chem.*, 2007, **72**, 2674-2677.

[199] Q. Zhang, J. Dong, Q. Meng, G. Huang and S. Li, *Russ. J. Gen. Chem.*, 2018, **88**, 2388-2393.

[200] K. Behm, J. B. Essner, C. L. Barnes, G. A. Baker and J. R. Walensky, *Dalton Trans.*, 2017, **46**, 10867-10875.

[201] J.-A. Zhang, N.-F. Yang, L.-W. Yang, S. Wu, Y.-H. Chen and J. Zhang, *Macromol. Res.*, 2013, **21**, 641-648.

[202] K.-S. Lim, D.-K. Lee, J.-W. Lee and N.-G. Park, *J. Mater. Chem. A*, 2020, **8**, 9345-9354.

[203] K. Sun, Z. Hu, B. Shen, C. Lu, L. Huang, J. Zhang, J. Zhang and Y. Zhu, *ACS Appl. Energy Mater.*, 2018, **1**, 2114-2122.

[204] Q. Jiang, Y. Zhao, X. Zhang, X. Yang, Y. Chen, Z. Chu, Q. Ye, X. Li, Z. Yin and J. You, *Nat. Photon.*, 2019, **13**, 460-466.

[205] P. Chen, Y. Bai, S. Wang, M. Lyu, J.-H. Yun and L. Wang, *Adv. Funct. Mater.*, 2018, **28**, 1706923.

[206] C. Rocks, V. Svrcek, P. Maguire and D. Mariotti, *J. Mater. Chem. C*, 2017, **5**, 902-916.

[207] D. H. Wang, Y. Hu, J. J. Zhao, L. L. Zeng, X. M. Tao and W. Chen, *J. Mater. Chem. A*, 2014, **2**, 17415-17420.

[208] S.-S. Dong, W.-Z. Shao, L. Yang, H.-J. Ye and L. Zhen, *RSC Adv.*, 2018, **8**, 28152-28160.

[209] R. Yerushalmi, J. C. Ho, Z. Fan and A. Javey, *Angew. Chem. Int. Ed.*, 2008, **47**, 4440-4442.

[210] G. Biagiotti, V. Lang., C. Ligi, S. Caporali, M. Muniz-Miranda, A. Flis, K. M. Pietrusiewicz, G. Ghini, A. Brandi and S. Cicchi, *Beilstein J. Nanotechnol*., 2017, **8**, 485-493.

[211] Y. Yang, J. Wu, X. Wang, Q. Guo, X. Liu, W. Sun, Y. Wei, Y. Huang, Z. Lan, M. Huang, J. Lin, H. Chen and Z. Wei, *Adv. Mater.*, 2020, **32**, 1904347.

[212] L. Wang, H. Zhou, J. Hu, B. Huang, M. Sun, B. Dong, G. Zheng, Y. Huang, Y. Chen, L. Li, Z. Xu, N. Li, Z. Liu, Q. Chen, L.-D. Sun and C.-H. Yan, *Science*, 2019, **363**, 265-270.

[213] W. Zhang, S. Pathak, N. Sakai, T. Stergiopoulos, P. K. Nayak, N. K. Noel, A. A. Haghighirad, V. M. Burlakov, D. W. deQuilettes, A. Sadhanala, W. Li, L. Wang, D. S. Ginger, R. H. Friend and H. J. Snaith, *Nat. Commun.*, 2015, **6**, 10030.

[214] R. Lindblad, D. Bi, B.-w. Park, J. Oscarsson, M. Gorgoi, H. Siegbahn, M. Odelius, E. M. J. Johansson and H. Rensmo, *J. Phys. Chem. Lett.*, 2014, **5**, 648-653.

[215] H. Kanda, N. Shibayama, A. J. Huckaba, Y. Lee, S. Paek, N. Klipfel, C. Roldan-Carmona, V. I. E. Queloz, G. Grancini, Y. Zhang, M. Abuhelaiga, K. T. Cho, M. Li, M. D. Mensi, S. Kinge and M. K. Nazeeruddin, *Energy Environ. Sci.*, 2020, **13**, 1222-1230.

[216] F. Ambroz, W. Xu, S. Gadipelli, D. J. L. Brett, C.-T. Lin, C. Contini, M. A. McLachlan, J. R. Durrant, I. P. Parkin and T. J. Macdonald, *Part. Part. Syst. Charact.*, 2020, **37**, 1900391.

Appendices

Appendix A: Supporting Information of Chapter 2

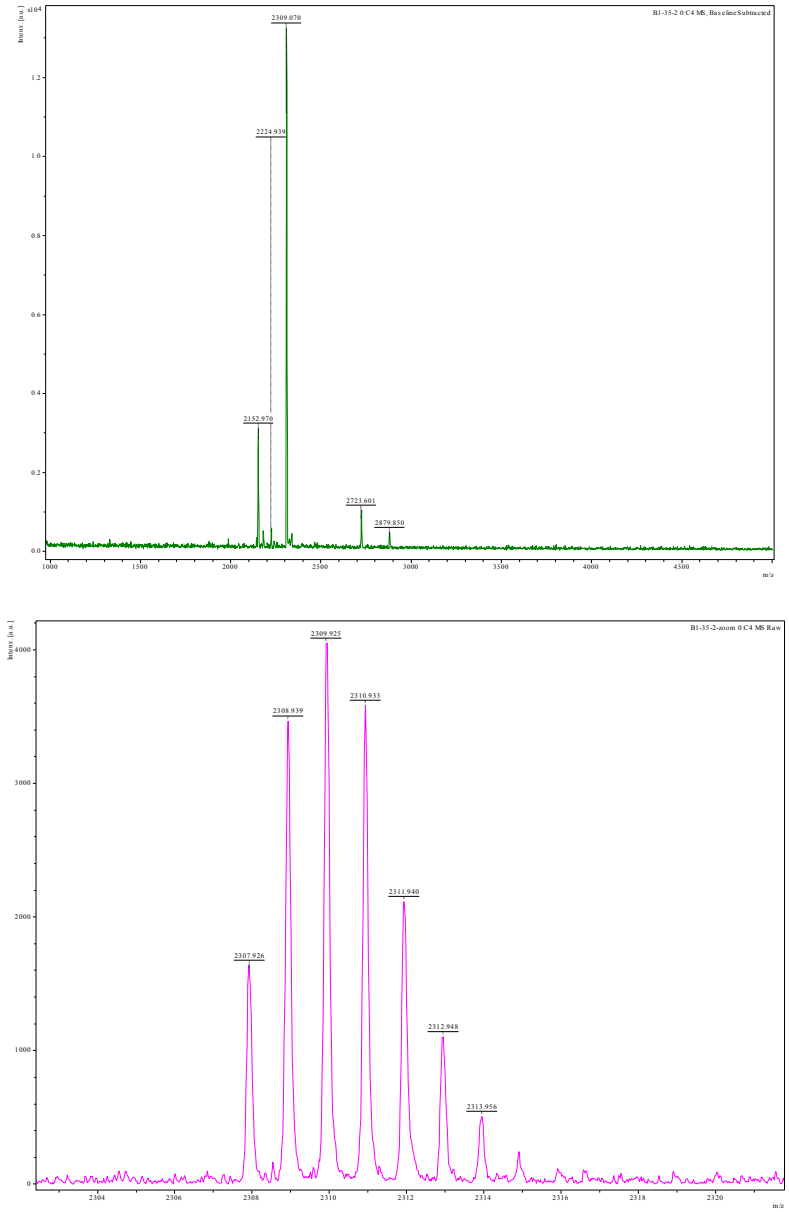

Figure A.1. MALDI-TOF-MS spectra in wide and narrow mass ranges of CI-B1.

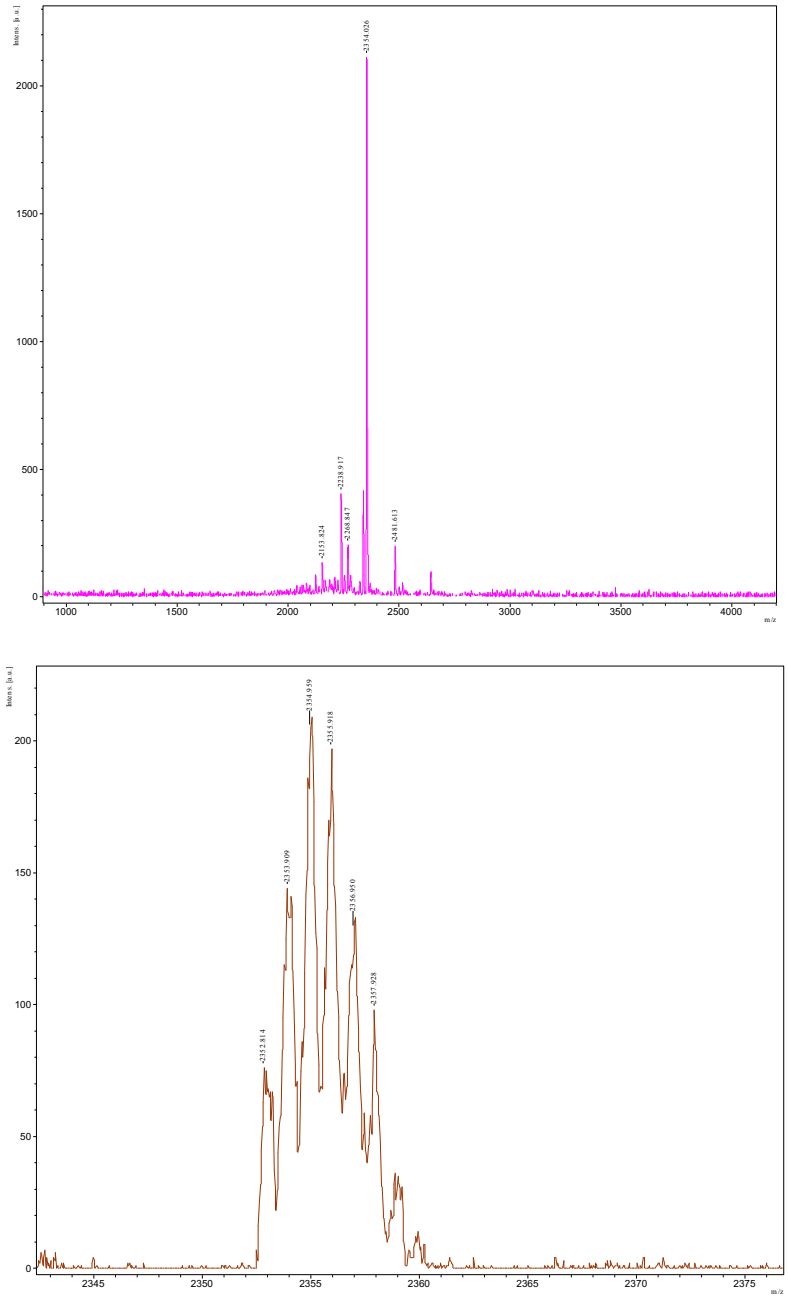

Figure A.2. MALDI-TOF-MS spectra in wide and narrow mass ranges of CI-B2.

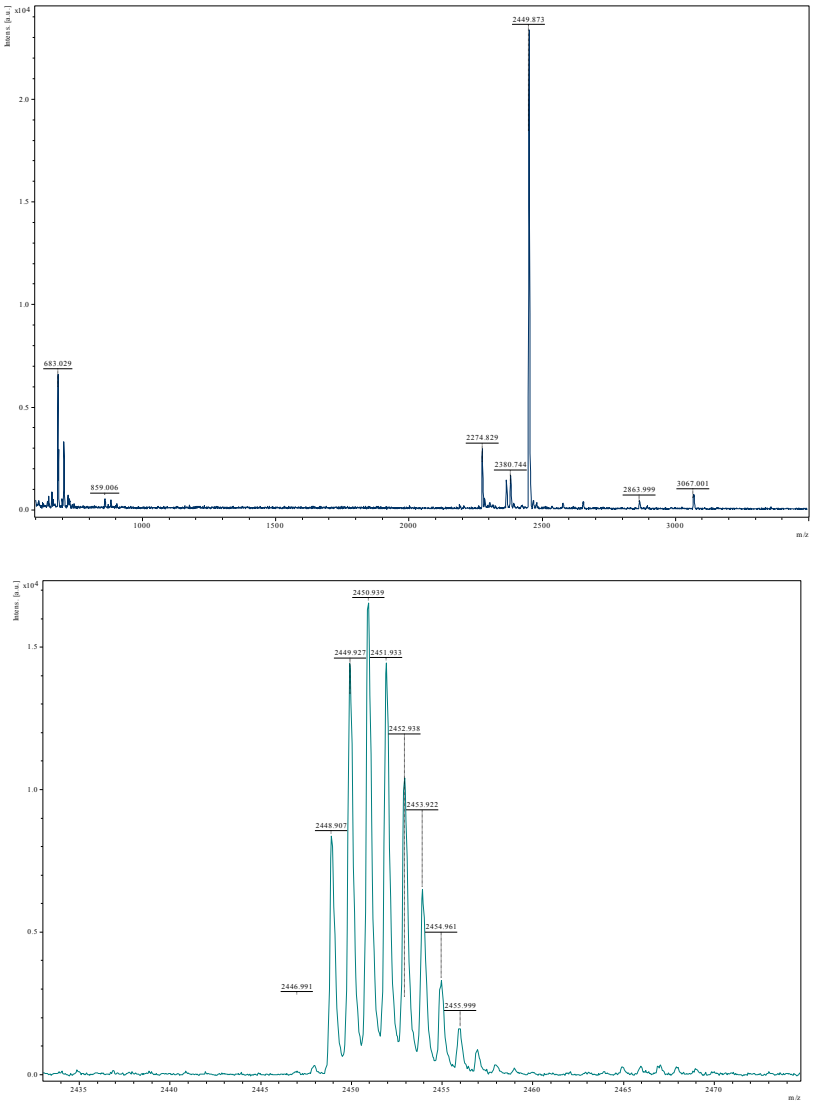

Figure A.3. MALDI-TOF-MS spectra in wide and narrow mass ranges of CI-B3.

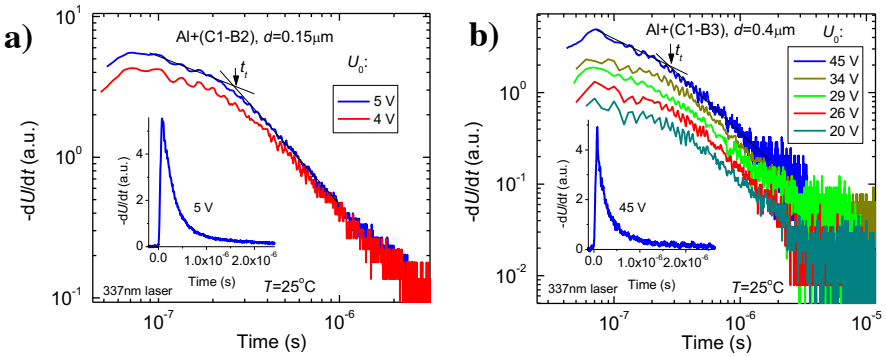

Figure A.4. XTOF discharge transients in thin layers of a) C1-B2 and b) C1-B3.

Experimental Methods

2D GIWAXS measurements

The 2-dimensional grazing incidence wide-angle X-ray scattering (2D GIWAXS) has been measured at an incident angle of 0.12° through a Huber diffractometer and photon energy of 12.39 keV (1.0 Å) by using synchrotron radiation at beamline BL19B2 of SPring-8 with PILATUS 300K 2D X-ray detectors.

PL Measurements

Time-resolved photoluminescence was measured by a time-correlated single photon counting system (Nanofinder 30). The wavelength for excitation was 480 nm. The wavelength for the detector was 791—797 nm. Figure shows the comparison of the PL spectra between the bare perovskite and that containing a thin layer of the HTMs. The TIPL spectra have been registered upon excitation at 450 nm. TRPL measurements were performed of the perovskite/HTM bilayer deposited on non-conductive glass to target exclusively the interfacial behaviour. A two-component exponential decay model was used to obtain the emission lifetimes of the thin films in the nanosecond regime, both deposited in exactly the same conditions as those used in the device stack. The bare perovskite layer, monitored as a reference, showed the longest charge carrier lifetime, which was significantly reduced when the HTMs were employed.

Conductivity measurement

The characterization conductivity of hole transporting materials can be reliably carried out using the organic field-effect transistor (OFET) configuration. The OFET substrates were purchased from Fraunhofer IPMS. It is containing 4 x 4 transistors of different channel length, 2.5 µm, 5 µm, 10 µm and 20 µm. Conductivity measurements were carried out on the 2.5 µm channel. The channel width was 10 mm and the channel height were 40 nm. The gate capacity is 15nF and the probe station used to characterize the transistors is a home-built setup located inside an Argon filled glovebox. The conductivity was calculated from linear fit (Ohm's law). The sample preparation consists in 10min oxygen plasma cleaning of the substrates and subsequent film deposition inside 0.015 м tetrachloroethane solution. The spin coating parameters were 1500 rpm for 10sec and the films were heated at 50°C for 10min before the measurements. The measurement was performed without use of any further additives for spiro-OmeTAD and CI-B HTMs. Lateral thin-film conductivity of CI-B1, CI-B2 and CI-B3 was determined to be 7.98 x 10^{-8}, 5.33 x 10^{-7} and 9.60 x 10^{-7} S cm^{-1}, respectively. In the absence of the additives, conductivity of spiro-OMeTAD was determined to be 1.07 x 10^{-6} S cm^{-1}.

Solar cell fabrication

Solar cell devices were fabricated onto conductive FTO glass substrates (Nippon Sheet Glass) They were cleaned sequentially by sonication in a 2 % Hellmanex solution, deionization water, acetone and ethanol for 30 min, respectively, followed by a 15 min UV-ozone exposure. A 30 nm thick TiO_2 compact layer was deposited by spray pyrolysis from a precursor solution of diluted titanium diisopropoxide bis(acetylacetonate) (TAA) in ethanol at 450 °C. A 150 nm thick mesoporous TiO_2 layer was obtained by spin coating using a commercially available 30 NR-D titanium dioxide paste from Dyesol diluted in ethanol (ratio 1:9 by weight). The substrates were then sintered at 500 °C for 30 min. After cooling down the substrates, a Li-doping of the mesoporous TiO_2 is done by spin coating 50 µL of a solution of lithium tris(bis(trifluoromethylsulfonyl)imide) (Li-TFSI) in acetonitrile (20 mg/mL) onto the mesoporous layer at 3000 rpm for 10 s, followed by sintering at 500 °C for 30 min. The mixed perovskite precursor solution was prepared by dissolving Perovskite precursor solution was prepared by mixing CsI (0.11 M), FAI (1.07 M), PbI_2 (1.23 M), MABr (0.19M) and $PbBr_2$ (0.19 M) in an anhydrous solvent 1:4 mixture of DMSO/DMF. The perovskite precursor solution was spin coated at 2000 rpm

for 10 s, followed by 6000 rpm for 30 s. Trifluorotoluene (110 µl) was dropped on the spinning substrate at the 10 s in the second step. The films were annealed at 100 °C for 60 min in the glove box. The hole-transporting material, consisting of 0.015 M CI-B1, CI-B2 and CI-B3 in tetrachloroethane at 70°C, was spin-coated on the top of the perovskite layer with a spin speed of 4000 rpm. As reference, the devices using spiro-OMeTAD as HTM were prepared consisting of 0.06 M spiro-OMeTAD, 0.03 M LiTFSI, 0.2 M TBP, and 0.002 M of tris(2-(1H-pyrazol-1-yl)-4-tert-butylpyridine) cobalt(III) tris(bis(trifluoromethyl sulfonyl)imide) (FK209) in chlorobenzene, were spin-coated dynamically onto the perovskite layers at 4000 rpm for 25 s. The gold electrodes were deposited by thermal evaporation of 70 nm gold using a shadow mask under high vacuum conditions.

Photovoltaic Characterization

The current–voltage curves were measured under an AM 1.5 simulated light source connected to a source meter (Keithley 2400). The light intensity was calibrated with an NREL- certified KG5 filtered Si reference diode. *J–V* curves were obtained at a scan rate of 50 mV s^{-1}. The devices were measured by using a black mask with an active area of 0.16 cm^2. The IPCE spectra were measured by using a commercially available instrument (ORIEL, IQE 200B).

Appendix B: Supporting Information of Chapter 3

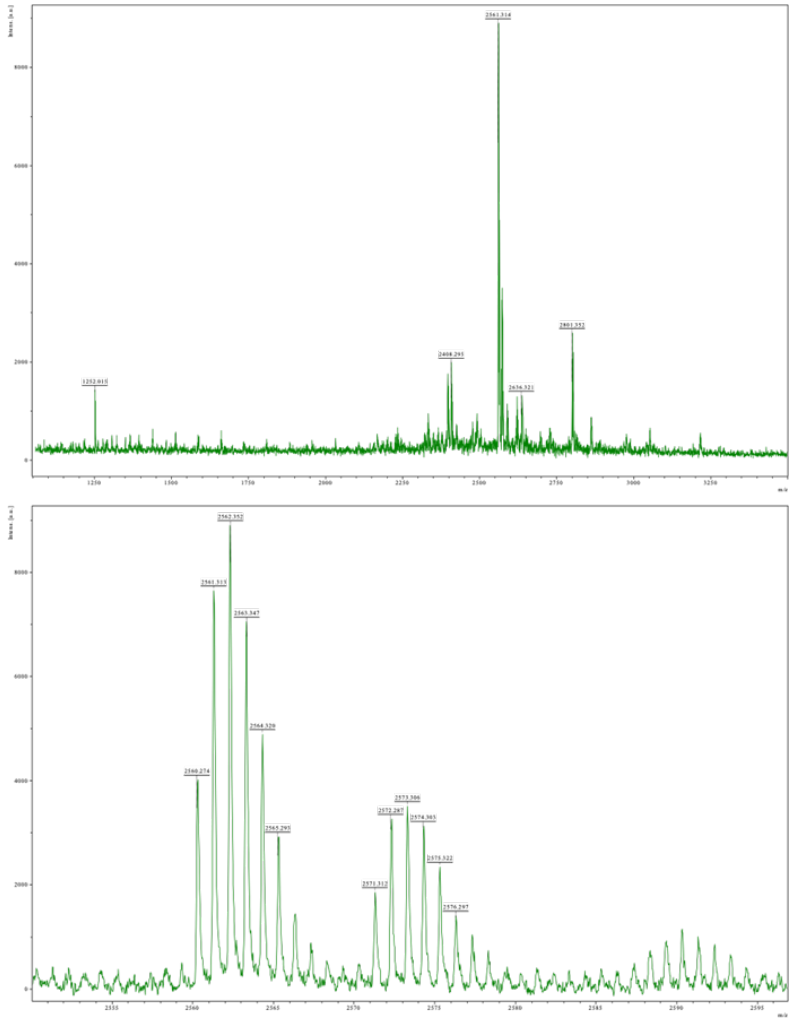

Figure B.1. MALDI-TOF-MS spectra in wide and narrow mass ranges of CI-TTIN-2F.

Experimental Methods

Device Fabrication

The TiO_2 compact layer was firstly deposited on clean FTO substrates by spray pyrolysis from a precursor solution of diluted titanium diisopropoxide bis(acetylacetonate) (TAA) in isopropanol at 450 °C. The 0.6 M $CsPbI_3$ precursor solution was prepared by dissolving stoichiometric CsI and $DMAPbI_3$ with a 1:1 molar ratio in DMF. The precursor solution was spun onto the room-temperature (RT) substrates at 1000 rpm for 10 s with a ramping rate of 500 rpm·s^{-1} and subsequently at 2500 rpm for 30 s with a ramping rate of 1000 rpm·s^{-1}. After spin-coated, the substrates were transferred onto a hotplate with 180°C for 25 min to obtain uniform $CsPbI_3$ films. Dopant-free hole transport materials (HTMs) with the concentration of 15 mg/mL (CI-TTIN-2F in tetrachloroethane or spiro-OMeTAD in chlorobenzene) were subsequently spin-coated at 2000 rpm for 20 s. For comparison, a conventional spiro-OMeTAD with dopants which prepared by dissolving 75 mg spiro-OMeTAD in chlorobenzene solution with 32 µL TBP, 20 µL Li-

TFSI/acetonitrile (1.8 M), and 8 µL FK209/acetonitrile (1 M), was spun to the perovskite substrates at 3500 rpm for 20 s. Finally, the devices were finished by the evaporation of 70 nm Au electrode. For module fabrication, 6.5 cm × 7 cm FTO substrates were patterned by laser with nine sub-cells connected in series. The P1 lines were patterned on FTO substrates first with a width of 50 µm. The film deposition processes were the same with the small solar cells. Then the laser scribing was performed twice before (P2, 500 µm) and after (P3, 200 µm) gold evaporation to complete the module fabrication.

Device characterization

The *J-V* characteristics of the photovoltaic devices were measured in ambient air with RH ~30% under an AM 1.5 simulated light source connected to a source meter (Keithley 2400), calibrated by an NREL- certified KG5 filtered Si reference diode. A black metal mask defined the device area as 0.16 cm^2. EQE was characterized by an Enli Technology EQE measurement system with a dual xenon/quartz halogen light source. Steady-state PL and TRPL were performed by Edinburgh FLS-980 fluorescence spectrometer (Edinburgh Instruments, UK). Confocal PL intensity maps were recorded with a laser confocal Raman spectrometer (Princeton Instruments, Acton Standard Series SP-2558) and a 485 nm laser (PicoQuant LDH-P-C-485, 0.4 mW with a 1% optical density filter) using a home-built confocal microscope. The EIS was performed with an SP-200 potentiostat (BioLogic) in the dark condition with bias of 0.8 V. The thermal admittance spectroscopy was conducted at a frequency range of 1 Hz to 1 MHz at a temperature of 300 K. The GIWAXS was measured through a Huber diffractometer and photon energy of 12.39 keV (1.0 Å) at a fixed incident angle on the order of 0.12° through a Huber diffractometer by using synchrotron radiation at beamline BL19B2 of SPring-8 with PILATUS 300K 2D X-ray detectors. Cyclic voltammetry (CV) was measured with a Biologie SP-200 cyclic voltammeter with a standard three-electrode configuration. Thermogravimetric analysis (TGA) data were collected using TGA 4000 from PerkinElmer. MS were recorded on 6530 Accurate-Mass Q-TOF LC/MS (Agilent Technologies) using electrospray ionization (ESI) and atmospheric pressure photoionization (APPI) techniques or Axima-CFR plus (Shimadzu) using matrix-assisted laser desorption/ionization (MALDI) technique.

Computational details

All simulations are performed within the density functional theory using CP2K code, employing localized atomic DZVP-MOLOPT basis sets, auxiliary plane wave basis set with 600 Ry cut-off for interfaces, and 450 Ry for isolated molecules and Goedecker-Teter-Hutter pseudopotentials for the description of the core region. The interaction of the HTM was modelled with PbI_2-terminated perovskite surface, obtained from the bulk structure of the tetragonal β-$CsPbI_3$ phase having the space group P4/mbm, as reported by Marronnier *et al*. For this purpose, Born-Oppenheimer molecular dynamics simulations of the CI-TTIN-2F molecule deposited on top of perovskite slab were performed employing the Perdew-Burke-Ernzerhof (PBE) density functional with Grimme's dispersion correction. The molecule was allowed to freely relax on top of the perovskite surface at the constant temperature of 300 K, maintained by the velocity rescaling algorithm. PBE-D3, B3LYP, HSE06 and PBE0 density functionals were benchmarked to describe the electronic structure of isolated HTM molecules. Auxiliary density matrix method (ADMM) was used for the calculations with the hybrid or range-separated functionals. The structures were visualized with VESTA and VMD programs.

Appendix C: Supporting Information of Chapter 4

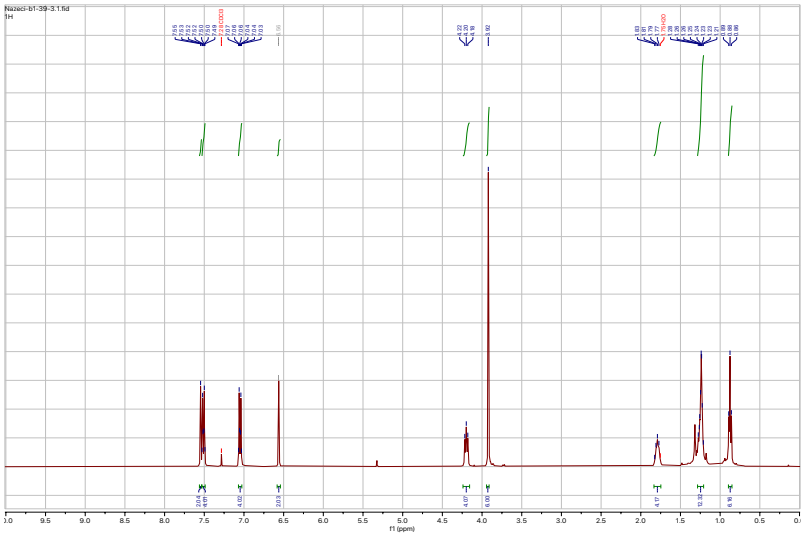

Figure C.1. ^{1}H NMR spectrum of CB-1 recorded in $CDCl_3$.

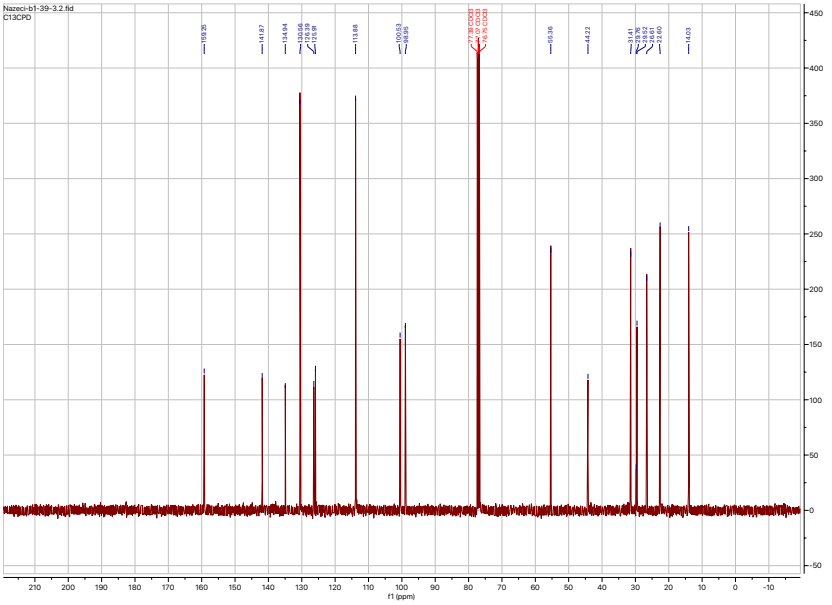

Figure C.2. ^{13}C NMR spectrum of CB-1 recorded in $CDCl_3$.

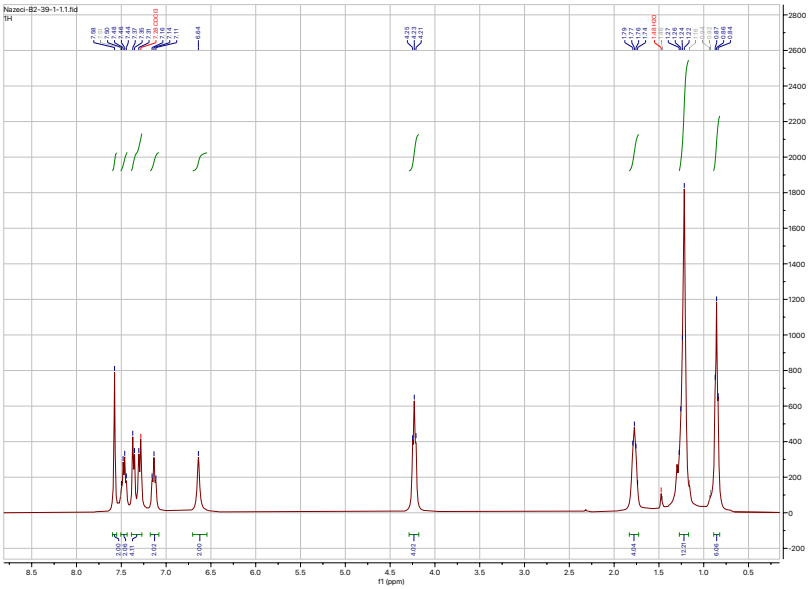

Figure C. 3. ^{1}H NMR spectrum of CB-2 recorded in $CDCl_3$.

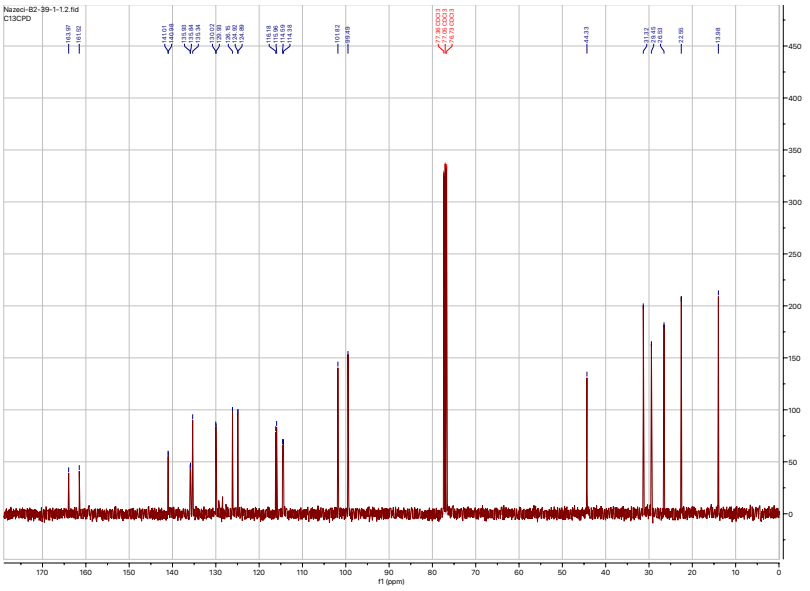

Figure C.4. ^{13}C NMR spectrum of CB-2 recorded in $CDCl_3$.

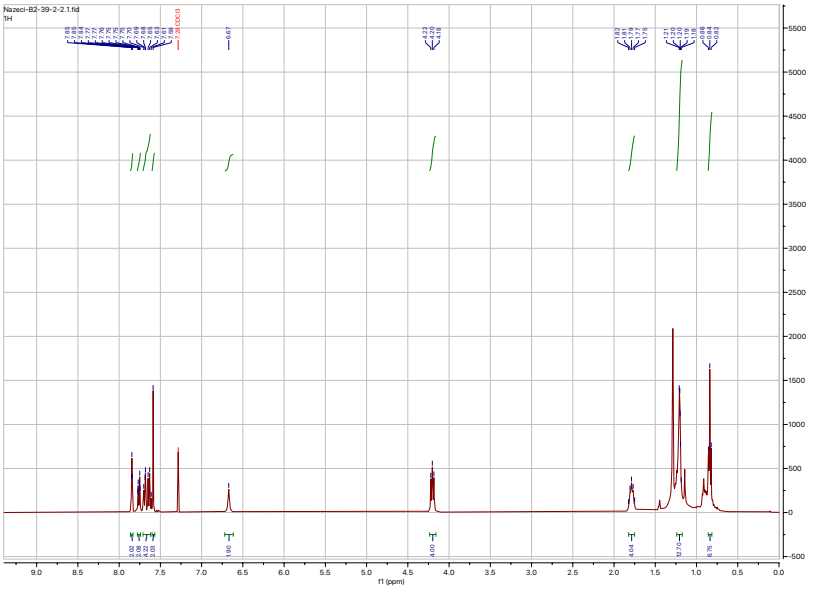

Figure C. 5. ^{1}H NMR spectrum of CB-3 recorded in $CDCl_3$.

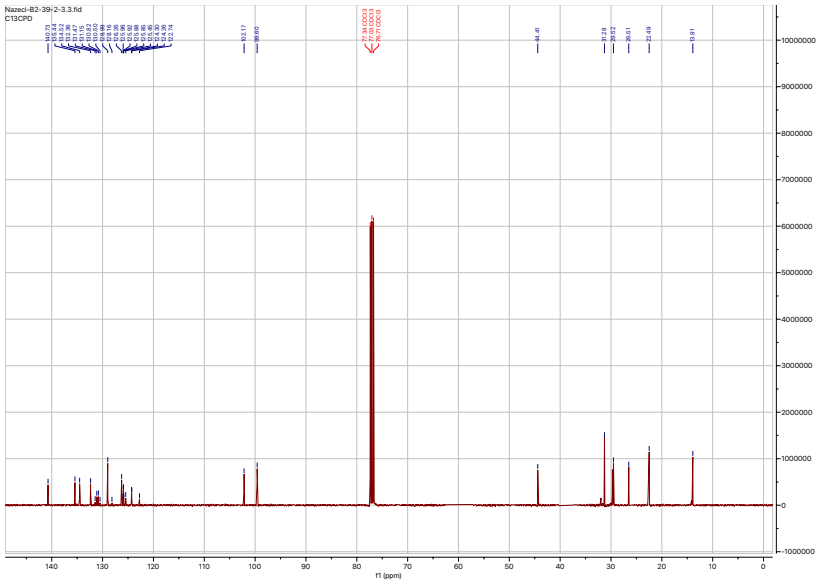

Figure C. 6. ^{13}C NMR spectrum of CB-3 recorded in $CDCl_3$.

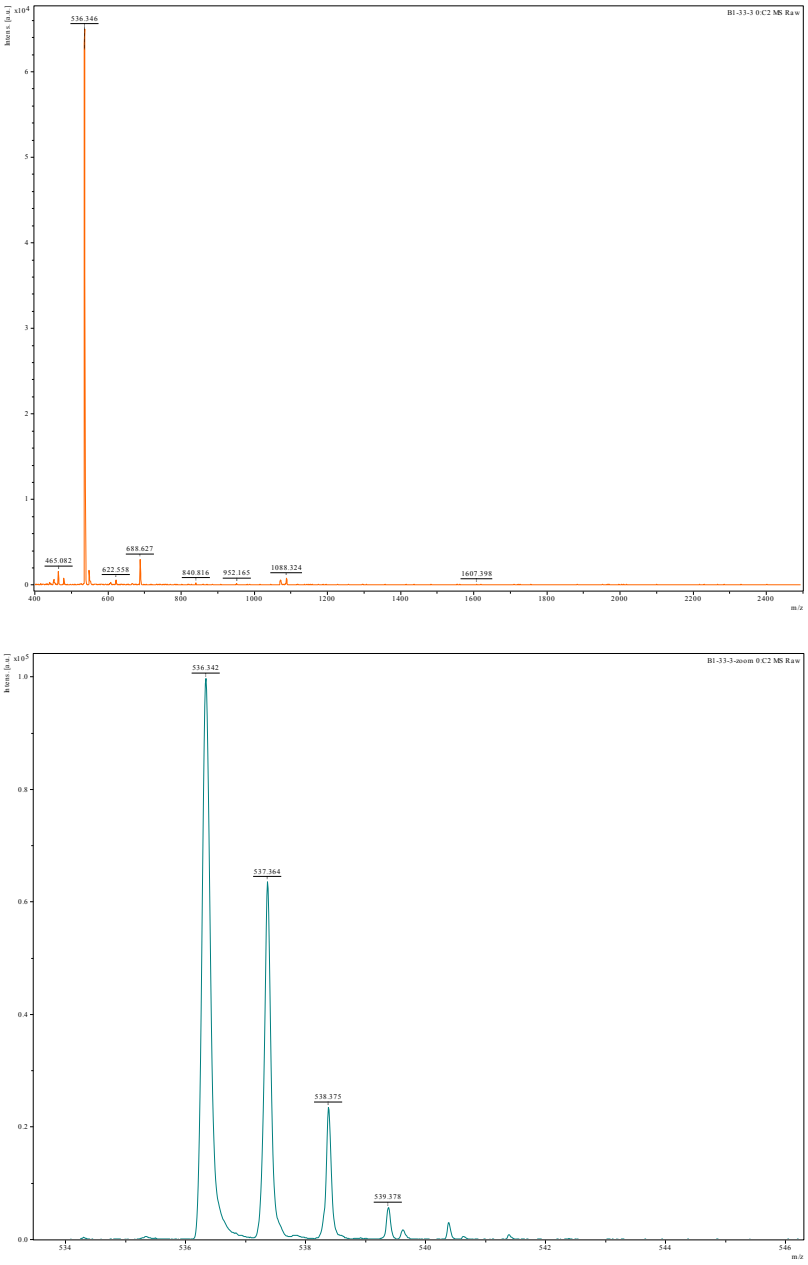

Figure C. 7. MALDI-TOF-MS spectra in wide and narrow mass ranges of CB-1.

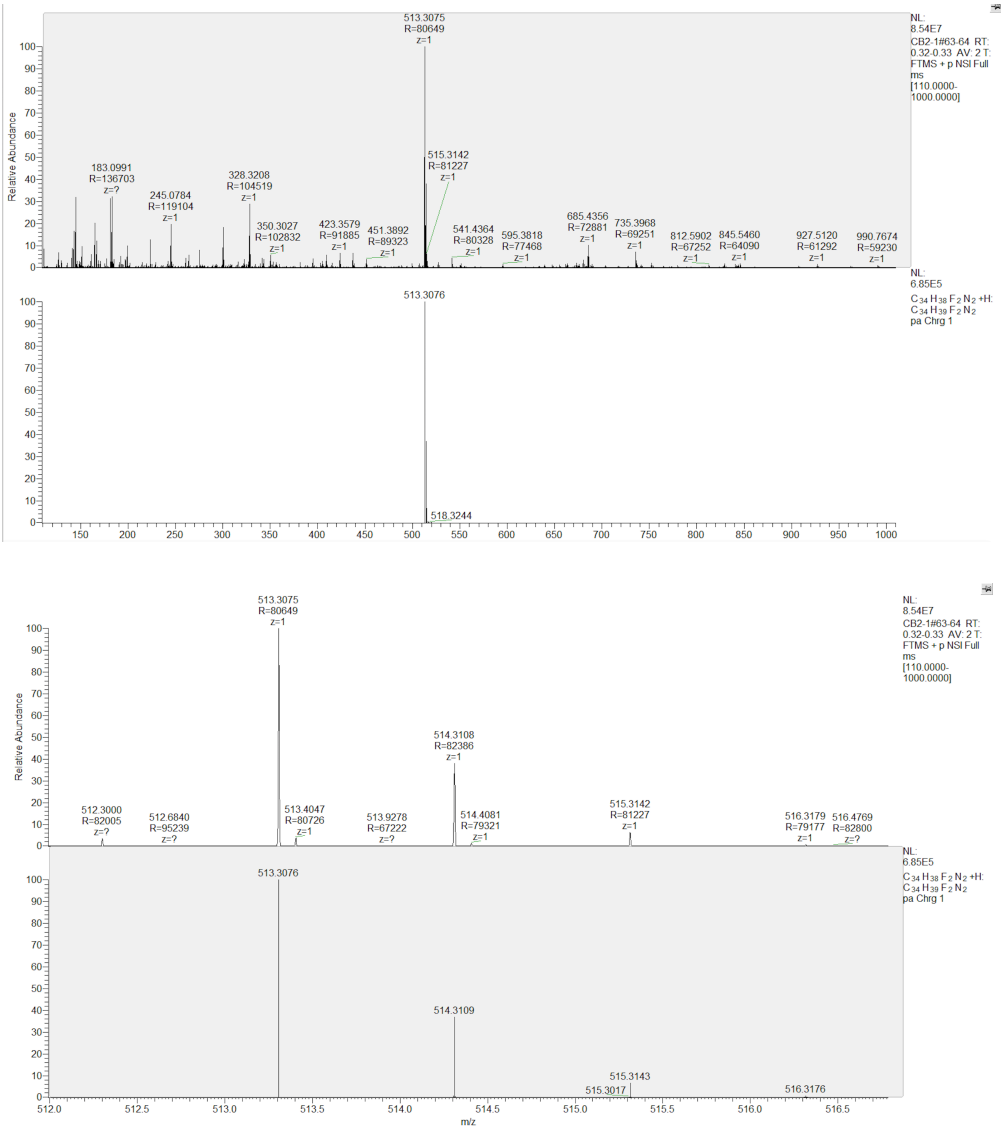

Figure C. 8. MALDI-TOF-MS spectra in wide and narrow mass ranges of CB-2.

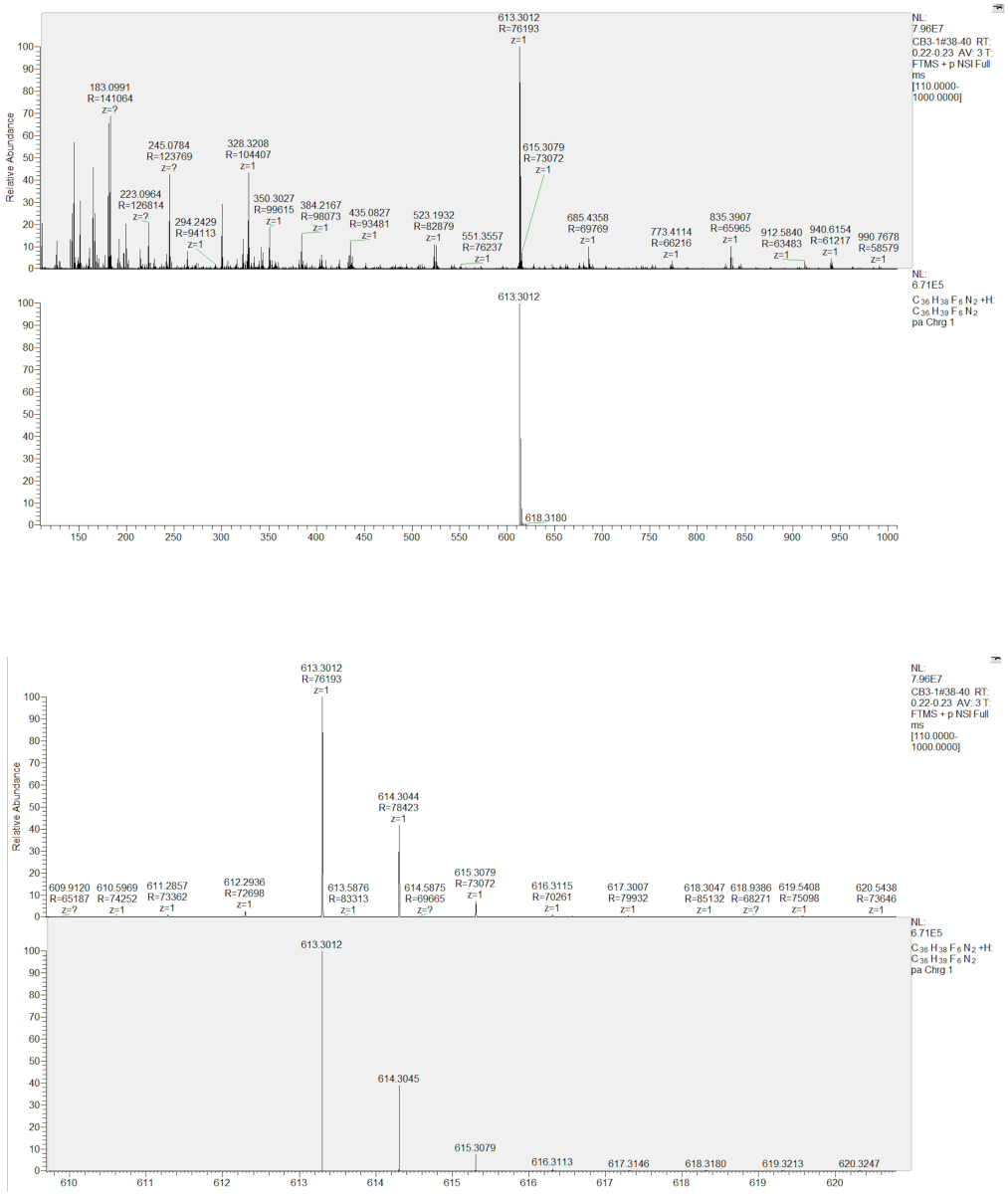

Figure C. 9. MALDI-TOF-MS spectra in wide and narrow mass ranges of CB-3.

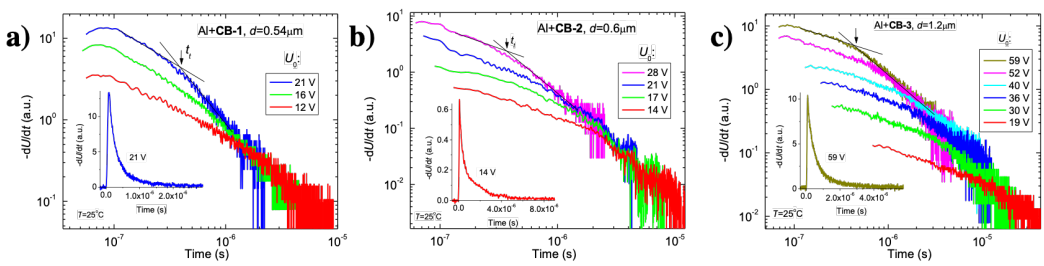

Figure C. 9. XTOF transients for the (a) CB-1, (b) CB-2 and (c) CB-3 samples. Arrow marks a transit time of holes.

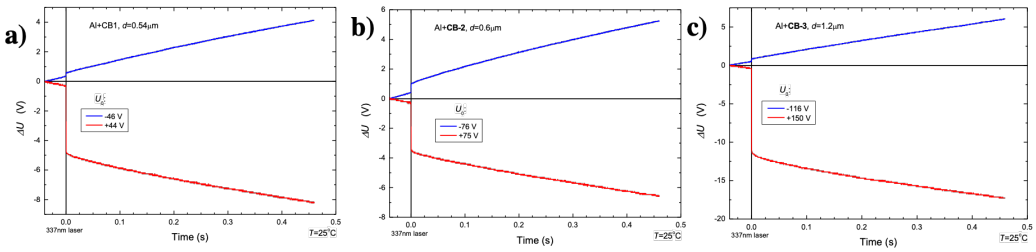

Figure C. 10. The integral XTOF measurements in (a) CB-1, (b) CB-2 and (c) CB-3 samples for charge transport.

Experimental Methods

Perovskite thin-films and solar cells fabrication

FTO glass substrates were cleaned with acetone and isopropyl alcohol (IPA) to use as a conducting electrode. On the FTO glass substrates, a compact TiO_2 layer was deposited by spray pyrolysis using titanium diisopropoxide bis(acetylacetonate) (Sigma-Aldrich) dissolved in isopropanol (1: 15 in volume), which was followed by thermal annealing at 450 °C for 30 min. A mesoporous TiO_2 layer was deposited on top of the compact TiO_2 layer using a diluted TiO_2 paste (Greatcell Solar 30 NR-D) in ethanol (1: 9 in volume). The solution was spin-coated at 5000 rpm for 20 s followed by sintering at 500 °C for 30 min. On the mesoporous TiO_2 layer, a SnO_2 layer was formed by spin-coating 0.1 M $SnCl_4$ solution (Acros) dissolved in water and subsequent annealing at 190 °C for 1 h. To deposit perovskite, the substrates were transferred into a glove box. The perovskite precursor solution was prepared by mixing FAI (1.04 M), PbI_2 (1.19 M), MABr (0.16 M), $PbBr_2$ (0.16 M), and CsI (0.10 M) in a mixed solvent of DMF: DMSO (78: 22 in volume). The solution was spin-coated at 2000 rpm for 10 s followed by 5000 rpm for 30 s. During the high rpm step of the spin-coating, 125 µL of ethyl acetate was dropped on the substrate. The films were annealed at 100 °C for 60 min. After cooling down the substrates, HTMs were deposited on top of the perovskite layer. 20 mM of CB series and 63 mM of spiro-OMeTAD were prepared by using chlorobenzene as a solvent. The HTMs were doped with Li-bis (trifluoromethanesulphonyl) imide, FK 209 Co(III) TFSI and 4-*tert*-butylpyridine at the ratio of 0.53 : 0.055 : 0.0033 in molar concentration compared to that of both CBs or spiro-OMeTAD. The devices were completed with 70 nm-thick gold electrodes by thermal evaporation.

Device characterization

Current density-Voltage (*J-V*) characteristics were measured under 1-sun AM 1.5G illumination generated by xenon lamp solar simulator (450 W, Oriel Sol3A, AAA class). The light intensity was calibrated using a Si reference equipped with an IR-cut-off (KG5) filter prior to the measurement. The active area of 0.16 cm^2 was defined by a black metal mask with the aperture of 4x4 mm. The J-V curves were scanned under the scan rate of 50 mV/s with 2 s pre-illumination time. During the J-V scan, an external voltage bias was applied and the current response was recorded with a digital source meter (Keithley 2400). The incident photon to current conversion efficiency (IPCE) of the solar cells devices was measured IQE200B (Oriel).

Photoluminescence (PL)

PL spectra of the perovskite thin-films were acquired using Fluorolog, Horiba Jobin Yvon fluorescence spectrometer upon excitation at 625 nm for the steady-state PL measurement and 635 nm for the transient PL measurement.

Scanning electron microscopy (SEM)

The top-view and cross-section images were obtained using FEI Teneo scanning electron microscope. The measurements were performed under the accelerating voltage of 2-3kV. In lens detector and Everhart-Thornley detector were used to acquire the cross-section and top-view images, respectively.

Lateral conductivity

Conductivity measurement of BDP-based HTMs and spiro-OMeTAD were carried out using the organic field-effect transistor (OFET) configuration with two-contact electrical conductivity set-up. The OFET substrates were purchased from Fraunhofer IPMS. The substrates were prepared first washing with acetone and ethanol then with 20 min oxygen plasma cleaning. BDP-based HTMs and spiro-OMeTAD were deposited from a chlorobenzene solution (20 mM and 63 mM, respectively) chemically doped with FK-209, Li-TFSI, *t*-BP as additives by spin-coating (at 4000 rpm for 30 s). Conductivity measurements were carried out on the 2.5 µm channel by sweeping from -10 to 10 V (source-drain voltage) at a scan rate of 1 V s^{-1} with a Keithley 2612A. The data was recorded with the KickStart software program. The channel width and height are 10 mm and 40 nm, respectively, and the gate capacity is 15nF.

Hole-drift mobility

The xerographic time-of-flight (XTOF) technique was used to characterize charge transport in the films of CB-1, CB-2, CB-3 transporting materials (HTM). Samples are prepared under drop casting technique on Al coated glass plates using CB as solvent, sample thickness was 0.54–1.2 µm. The corona charging used to create electric fields in the HTM layer. Charge carriers were generated at the layer surface by illumination with pulses of nitrogen laser (pulse duration was 1 ns, wavelength 337 nm). The layer surface potential decrease as a result of pulse illumination was about 5 % of initial potential and so was ensured small charge mode in XTOF measurement. The capacitance probe deposited over the sample and connected to the wide frequency band electrometer measured the speed of the surface potential decrease d*U*/d*t*, which is equivalent to a current in widely known TOF technique. The transit time t_t was determined by the kink on the curve of the d*U*/d*t* transient in double logarithmic plot and investigated materials are characterized by dispersive hole transport. The drift mobility was calculated by the formula $\mu_0 = d^2/U_0 t_t$, where d is the layer thickness and U_0 is the surface potential at the moment of illumination.

Water contact angle

Water contact angle on the top of thin layers of BDP-based HTMs was measured using the KRUSS DSA100 optical contact angle instrument. Measurements were conducted using the sessile drop program with 0.5 mm needle size. Drops of water at a rate of 0.01 mL/min and a volume of 12 µL were created. Substrates were prepared by spin coating 20 mM HTM solutions onto perovskite layers. The image was recorded 1 second after the interaction of the water drop with the HTM layer.

Computational details

All calculations are performed within the Density Functional Theory (DFT), as implemented in CP2K code. The atomic DZVP-MOLOPT atomic basis set, auxiliary plane wave basis set with 450 Ry cut-off for the isolated molecules and 600 Ry for interfaces, as well as Goedecker-Teter-Hutter (GTH) pseudopotentials have been employed in the calculations. The interactions at the interface have been studied using Perdew-Burke-Ernzerhof (PBE) density functional including Grimme's dispersion correction, required for the description of non-covalent interactions at the interface. To ensure the consistency of the description, the bulk perovskite cell parameters corresponding to stoichiometry $([FAPbI_3]_{0.87}[MAPbBr_3]_{0.13})_{0.92}(CsPbI_3)_{0.08}$ and atomic positions were optimized at PBE-D3 level of theory as well. The energy and spatial distribution of frontier molecular orbitals of CB-1, CB-2 and CB-3 was analyzed using PBE-D3, B3LYP and PBE0 density functionals. To accelerate hybrid functional calculations, auxiliary density matrix method (ADMM) is used. Structures were visualized with VESTA and VMD codes.

Appendix D: Supporting Information of Chapter 5

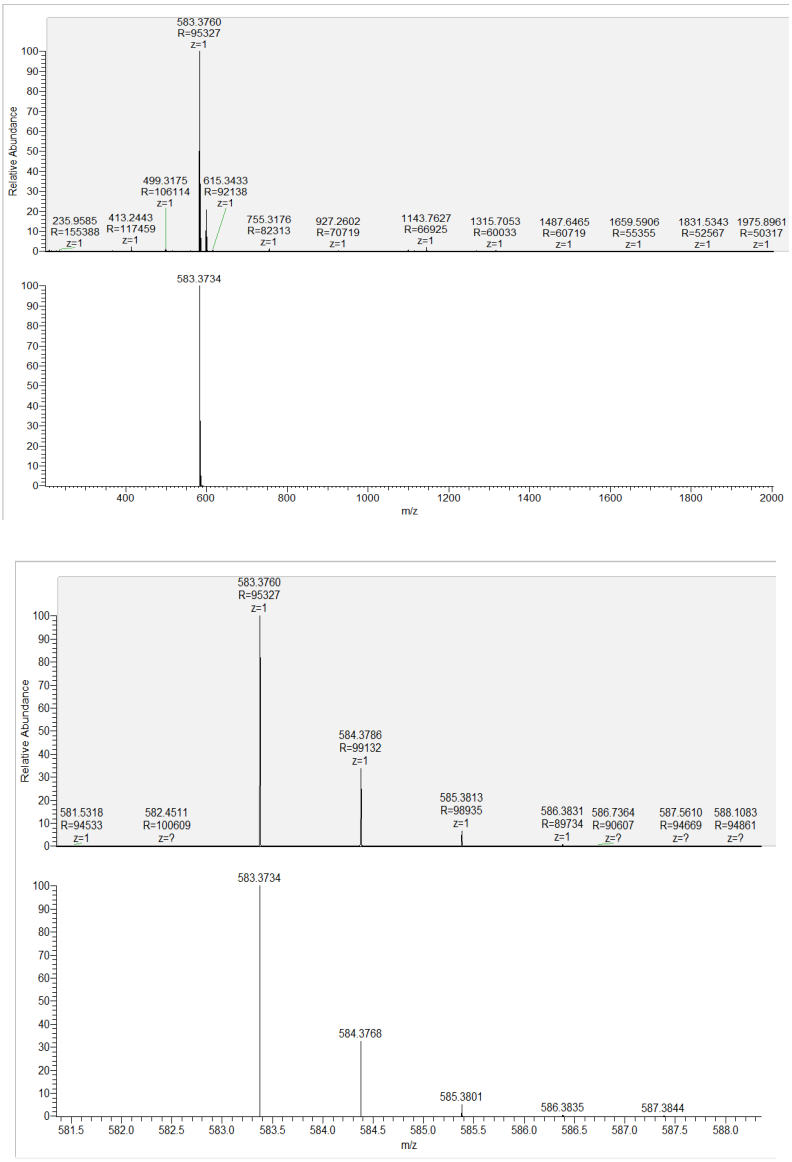

Figure D. 1. ESI-QTOF-MS spectra in wide and narrow mass ranges of THPPO.

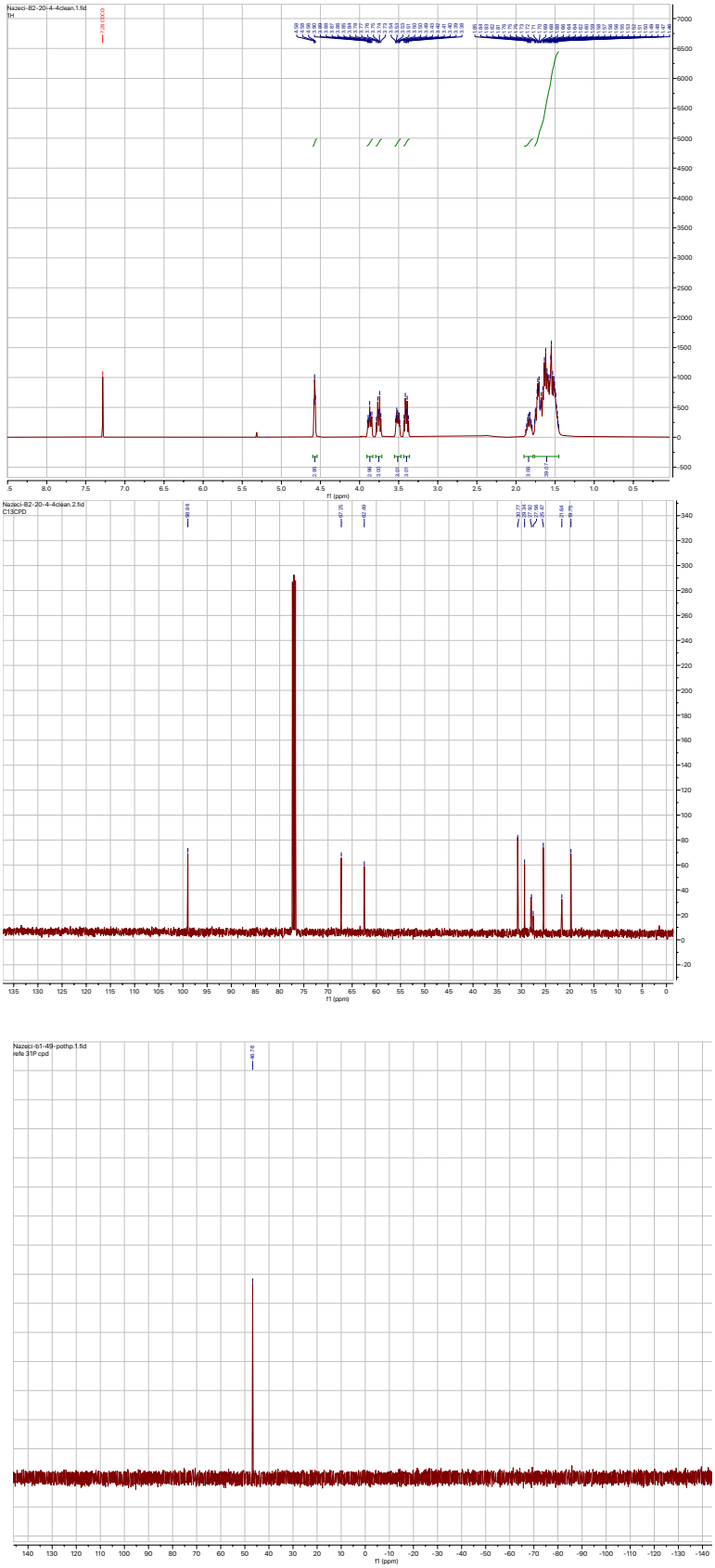

Figure D. 2. ^{1}H, ^{13}C and ^{31}P NMR ($CDCl_3$) spectrum of THPPO.

Experimental Methods

Perovskite thin-films and solar cells fabrication

Fluorine-doped tin oxide coated glass (FTO, Nippon Sheet Glass) was used as the conducting electrode. Prior to each use, FTO glass was patterned by chemical etching using Zn powder and aqueous HCl solution (3.0 M), then it was cleaned with detergent (Helmanex), deionized water, acetone, and isopropanol in an ultrasonic bath. A 30 nm-thick compact-TiO_2 layer was used as the electron transporting material and deposited on top of FTO glass via spray pyrolysis of titanium diisopropoxide bis(acetylacetonate) (Sigma Aldrich, diluted to 1:15 v/v in isopropanol) at 450°C. A 100 nm-thick mesoporous TiO_2 layer was then deposited by spin coating the ethanolic solution (1:8 v/v) of TiO_2 paste (GreatCellSolar, 30NR-D) at 5000 rpm for 20 s, followed by heating at 10 min and sintering at 500 °C for 20 min. A 20 nm-thick passivating tin oxide was spin coated on top of mesoporous TiO_2 layer by dissolving tin (IV) chloride (Acros) solution (12 µL in 988 µL water) at 3000 rpm for 30 s, followed by annealing at 100 °C for 10 min and 190 °C for 1 h. UV-ozone treatment was carried out for 15 minutes before perovskite layer deposition. A triple cation-based perovskite precursor solution $[(FAPbI_3)_{0.87}(MAPbBr_3)_{0.13}]_{0.92}(CsPbI_3)_{0.08}$ with a concentration of 1.3 M was prepared by mixing FAI (GreatCellSolar), MABr (GreatCellSolar), CsI (ABCR), PbI_2 (TCI), and $PbBr_2$ (TCI) in DMF and DMSO (0.78:0.22 v/v). An excess concentration of PbI_2 was used in the precursor solution (PbI_2: FAI= 1.05:1). The perovskite solution was then deposited on top of the prepared substrates at 2000 rpm for 12 s and 5000 rpm for 30 s. Chlorobenzene was dropped at 15 s before the end of the spin coating process. Perovskite film was annealed inside the glovebox for 60 minutes. A various concentration of THPPO solution (0.005, 0.010, 0.020, and 0.030 M) in chlorobenzene was deposited on top of the perovskite films at 4000 rpm for 30 s. For the HTL-based device, 2,2′,7,7′-tetrakis-(*N*,*N*-di-p-methoxyphenyl-amine)-9,9′-spirobifluorene (spiro-OMeTAD) is incorporated as the HTL. spiro-OMeTAD (Merck) with the concentration of 0.06 M was dissolved chlorobenzene. For 1 mL solution, it is doped with 18.57 µL of Li-bis (trifluoromethanesulphonyl) imide (Aldrich) from the stock solution (196 mg in 379 µL acetonitrile), 13.69 µL of FK 209 Co (III) TFSI (GreatCellSolar) from the stock solution (99 mg in 263 µL acetonitrile), and 31.28 µL of 4-*tert*-butylpyridine (Sigma-Aldrich). For a complete PSC device, a 70 nm-thick gold counter electrode was deposited by physical vapor deposition under high vacuum condition.

Device characterization

The current density-voltage (*J-V*) characteristics were measured under xenon lamp solar simulator (450 W, Oriel Sol3A, AAA class). The light intensity was calibrated to 1 sun illumination by using a Si reference equipped with an IR-cut-off (KG5) filter. The *J-V* curves then recorded with a digital source meter (Keithley 2400) by applying an external voltage bias and measuring the current response. The active area was defined by using a black metal mask with the aperture of 0.16 cm^2. The *J-V* curves were scanned under the rate of 50 mV/s without any preconditioning. External quantum efficiency (EQE) spectra were recorded using IQE200B (Oriel). Long-term stability test was carried out under continuous 1 sun illumination and maximum power point (MPP) tracking with LED lamps in an inert (Ar) atmosphere without any encapsulation.

Thin-films characterization

UV-VIS absorption: The absorption spectra of the thin films were measured using an ultraviolet, visible, near-infrared spectrophotometer (PerkinElmer Lambda 950S).

Photoluminescence: Steady-state photoluminescence spectra of the perovskite thin films were measured using Fluorolog3-22 spectrofluorometer by exciting the films at 550 nm. Transient photoluminescence spectra were measured and recorded by a time-correlated single photon counting system (Nanofinder 30) at the excitation wavelength of 480 nm. The detection wavelength was set on 763-770 nm.

X-ray Diffraction (XRD): XRD measurements were performed on Bruker D8 Advance diffractometer and non-monochromated Cu Kα radiation at the ambient atmosphere and temperature.

Scanning Electron Microscopy (SEM): Cross-section and top surface SEM images were recorded by in-lens detector of FEI Teneo scanning electron microscope at the accelerating voltage of 3 kV and 5 kV.

Grazing incidence wide angle X-ray scattering (GIWAXS) measurements: GIWAXS measurements were performed at SPring-8 on beamline BL19B2. The X-ray irradiation with an energy of 12.39 keV (λ = 1 Å) was used on the sample at a fixed incident angle on the order of 0.12° through a Huber diffractometer. A two-dimensional image detector (Pilatus 300K) were used to record the 2D-GIWAXS patterns.

Ultraviolet photoelectron spectroscopy (UPS) measurements: The ultraviolet photoelectron spectroscopy (UPS) were measured using He-I source ($h\nu$ = 21.22 eV) (AXIS Nova, Kratos Analytical Ltd., UK) in order to determine the valence band energy and Fermi-level. Gold (Au) which is in electrical contact with the sample is used as a reference for the Fermi-level of the samples.

X-ray photoelectron spectroscopy (XPS): The X-ray photoelectron spectroscopy (XPS) measurements were performed using VersaProbe II (Physical Electronics Inc) with a monochromator and Al-Kα source of 1486.6 eV. The spectrum was referenced using the C-C bound component of the adventitious carbon.

Acknowledgements

First of all, I would like to thank my thesis director, Prof. Mohammad Khaja Nazeeruddin, for giving me the opportunity to pursue my doctoral studies in the Group for Molecular Engineering of Functional Materials (GMF). Thank to him for allowing me to work with so much freedom in carrying out my research and to collaborate with many great scientists in the field. He was always very patient and open to discussions; his experience and insightful feedback pushed me to sharpen my thinking and have certainly been my academic success determinants.

I would like to acknowledge all jury members: Prof. Kevin Sivula, Prof. Wendy Lee Queen, Prof. Emilio Palomares and Prof. Gianluca Pozzi for devoting their precious time to read, to give feedback and to evaluate my thesis.

There is a tremendous amount of people who have contributed to my growth, broadened my horizons and inspired me over the past four years, this work would not have been possible without their help and I would like to express my gratitude to all of them. Specially, I am very grateful to Dr. Kasparas Rakstys, Dr. Sanghyun Paek, Dr. Hobeom Kim, Dr. Albertus Adrian Sutanto, Dr. Cheng Liu, Dr. Yi Yang and Dr. Cristina Momblona for all of their hard work and fruitful collaboration. The daily life at the university includes numerous discussion and stories around lunches, coffee breaks, drinks, ski sessions and trips. The main actors of this wonderful and necessary equilibrium between work and leisure are Albert, Cristina, Nadja, Mousa Hiroyuki, Alex, Ines, Nikita, Sadig, So-Min and Valentino. I sincerely acknowledge my colleagues in GMF for having a great fun time and for creating a pleasant atmosphere in the lab and office.

I owe a great deal of thanks to my parents and my sister were always supportive and enthusiastic about whatever I chose to do. You are always there for me. Their love and encouragement while growing up made all the difference in shaping who I am and where I am today. Also, I would like to thank all my old times friends, who understood and accepted my hermit working-mode and brought me back to reality when I needed. Special thanks to İrem, Sarp, Selin, Özge and Gizem who provided stimulating discussions as well as happy distractions to rest my mind outside of my research.

I do not have words to express my gratitude to Berkay Kose, without whose love, support and encouragement this thesis would not have been possible. He has definitely been my rock for the past 11 years. I appreciate him for trusting me, even more than myself with strong faith. I am extremely lucky to have met and married you and I thank you for everything you have done for me.

Cansu Igci

Lausanne, November 2021

Curriculum Vitae

C A N S U I G C I

EPFL ISIC-Valais, CH-1950 Sion, Switzerland

cansu.igci@epfl.ch ; cansuigci1@gmail.com

https://www.linkedin.com/in/cansu-igci-50387a84/

https://bit.ly/IgciCansu

E D U C A T I O N

École Polytechnique Fédérale de Lausanne (EPFL), Lausanne, Switzerland
Ph.D. in Chemistry and Chemical Engineering **11/2017 – 12/2021**
Advisor: Prof. Md. K. Nazeeruddin
Thesis: Molecularly Engineered Functional Materials for High Performance Perovskite Solar Cells

Middle East Technical University (METU), Ankara, Turkey
M.Sc. in Chemistry **9/2015 – 8/2017**
Advisor: Assist. Prof. Dr. Gorkem Gunbas
Thesis: From Supramolecular Chemistry to Fundamental Organic Chemistry: Bis-Rosette Nanatubes and Novel Molecular Frameworks

Middle East Technical University (METU), Ankara, Turkey
B.Sc. in Chemistry **9/2011 – 6/2015**

P U B L I C A T I O N S

1. **Igci**, **C.**; Kanda, H.; Yoo, S.-M.; Sutanto, A. A.; Syzgantseva, O.; Syzgantseva, M.; Jankauskas, V.; Rakstys, K.; Mensi M.; Kim, H.; Asiri, A. M.; Nazeeruddin, M. K. Highly Planar Benzodipyrrole-based Hole Transporting Materials with Passivation Effect for Efficient Perovskite Solar Cells. *Sol. RRL* **2021**, 2100667.

2. Klipfel, N.; Kanda, H.; Sutanto, A. A.; Mensi, M.; **Igci, C.**; Leifer, K.; Kinge, S.; Roldán-Carmona, C.; Momblona, C.; Dyson, P. J.; Nazeeruddin M. K. Mechanistic insights into the role of the bis(trifluoromethanesulfonyl)imide ion in co-evaporated p-i-n perovskite solar cells. *ACS Appl. Mater. Interfaces* **2021**, *13*, 52450–52460.

3. Klipfel, N.; Alvarez, A.; Kanda, H.; Sutanto, A. A.; **Igci, C.**; Roldan-Carmona, C.; Momblona, C.; Fabregat Santiago, F.; Nazeeruddin, M. K. C_{60} thin films in perovskite solar cells: efficient or limiting charge transport layer. *Manuscript under review in ACS Applied Energy Materials.*

4. Dessimoz, M.; Yoo, S-M.; Kanda, H.; Igci, C.; Kim, H.; Nazeeruddin M. K. Phase Pure Quasi-2D Perovskite by Protonation of Neutral Amine. *J. Phys. Chem. Lett.* **2021**, *12*, 11323–11329.

5. Liu, C.;† **Igci, C.**;† Yang, Y.;† Syzgantseva, O. A.; Syzgantseva, M. A.; Rakstys, K.; Kanda, H.; Shibayama, N.; Ding, B.; Zhang, X.; Jankauskas, V.; Ding, Y.; Dai, S.; Dyson, P.J. and Nazeeruddin, M. K. Dopant-Free Hole Transport Materials Afford Effi-

cient and Stable Inorganic Perovskite Solar Cells and Modules. *Angew. Chem. Int. Ed.* **2021**, *60*, 2–11. *(†Equal contribution)*

6. Vaitukaityte, D.; Momblona, C.; Rakstys, K.; Sutanto, A. A.; Ding, B.; **Igci, C**.; Jankauskas, V.; Gruodis, A.; Malinauskas, T.; Asiri, A. M.; Dyson, P. J.; Getautis, V.; Nazeeruddin M. K. Cut from the Same Cloth: Enamine-Derived Spirobifluorenes as Hole Transporters for Perovskite Solar Cells. *Chem. Mater.* **2021**, *33*, 6059–6067.

7. Joseph, V.; Sutanto, A. A.; **Igci, C.**; Syzgantseva, O. A.; Jankauskas, V.; Rakstys, K.; Queloz, V. I. E.; Huang, P.-Y.; Ni, J.-S.; Kinge, S.; Chen, M.-C; Nazeeruddin M. K. Stable Perovskite Solar Cells Using Molecularly Engineered Functionalized Oligothiophene as Low-Cost Hole Transporting Materials. *Small* **2021**, 2100783.

8. Sutanto, A.; Joseph, V.; **Igci, C.**; Syzgantseva, O. A.; Syzgantseva, M. A.; Jankauskas, V.; Rakstys, K.; Queloz, V. I. E.; Huang, P.-Y.; Ni, J.-S.; Kinge, S.; Asiri, A. M.; Chen, M.-C.; Nazeeruddin M. K. Isomeric carbazole-based hole-transporting materials: Role of linkage position on the photovoltaic performance of perovskite solar cells. *Chem. Mater*. **2021**, *33*, 3286–3296.

9. Kanda, H.; Usiobo, O. J.; Momblona, C.; Abuhelaiqa, M.; Sutanto, A. A.; **Igci, C.**; Gao, X.-X.; Audinot, J.-N.; Wirtz, T.; Nazeeruddin M. K. Light Stability Enhancement of Perovskite Solar Cells Using 1*H*,1*H*,2*H*,2*H*-Perfluorooctyltriethoxysilane Passivation. *Sol. RRL* **2021**, *5*, 2000650.

10. Sutanto, A. A.;† **Igci, C.**;† Kim, H.; Kanda, H.; Shibayama, N.; Mensi, M.; Queloz, V. I. E.; Momblona, C.; Yun, H. J.; Bolink, H. J.; Huckaba, A. J. and Nazeeruddin M. K. Phosphine Oxide Derivative as a Passivating Agent to Enhance the Performance of Perovskite Solar Cells. *ACS Appl. Energy Mater*. **2021**, *4*, 1259–1268. *(†Equal contribution)*

11. Illicachi, L. A.; Urieta-Mora, J.; Calbo, J.; Aragó, J.; **Igci, C**.; García-Benito, I.; Momblona, C.; Insuasty, B.; Ortiz, A.; Roldán-Carmona, C.; Molina-Ontoria, A.; Ortí, E.; Martín, N.; Nazeeruddin, M. K. *Chem.—Eur. J.* **2020**, *26*, 11039.

12. **Igci, C.**; Paek, S.; Rakstys, K.; Kanda, H.; Shibayama, N.; Jankauskas, V.; Roldán-Carmona, C.; Kim, H.; Asiri, A. M. and Nazeeruddin, M. K. D–π–A-Type Triazatruxene-Based Dopant-Free Hole Transporting Materials for Efficient and Stable Perovskite Solar Cells. *Sol. RRL* **2020**, *4*, 2000173.

13. Rakstys, K.; **Igci, C**.; Nazeeruddin, M. K. Efficiency vs. stability: dopant-free hole transporting materials towards stabilized perovskite solar cells. *Chem. Sci.* **2019**, *10*, 6748.

14. **Igci, C.**; Karaman, O.; Fan, Y.; Gonzales III, A. A.; Fenniri, H.; Gunbas, G. Synthesis of N-bridged pyrido[4,3-*d*]pyrimidines and self-assembly into twin rosette cages and nanotubes in organic media. *Sci*. *Rep*. **2018**, *8,* 15949.

C O N F E R A N C E S

1. Igci, C., Paek, S., Rakstys, K., Kanda, H., Shibayama, N., Jankauskas, V., Roldán-Carmona, C., Kim, H., Asiri, A. M. and Nazeeruddin, M.K. "D–π–A-Type Triazatruxene-Based Dopant-Free Hole Transporting Materials for Efficient and Stable Perovskite Solar Cells." Poster presentation, The 5th International Conference on Perovskite Solar Cells and Optoelectronics, Lausanne, Switzerland.

2. Igci, C., Fan, Y., Gonzales, A., Temburnikar, K., Fenniri, H., Gunbas, G., "Synthesis of Self-Assembled Bisrosette Supramolecules." Poster presentation, 253rd American Chemical Society National Meeting and Exposition, San Francisco, USA.